Workshop III

Solar System Bodies

Chairmen:

Dr. Theodor Kostiuk (NASA GSFC, USA)
Prof. Vitalii Kruchynenko (AO KNU, Ukraine)
Prof. Yuri Shkuratov (AO KhNU, Ukraine)
Prof. Leonid Shulman (MAO NASU, Ukraine)

Session 1. Planets, Satellites, and Asteroids

UNIQUE INFRARED STUDIES OF PLANETARY ATMOSPHERES: THE CASSINI/HUYGENS MISSION AND GROUND–BASED STUDIES

T. Kostiuk

NASA Goddard Space Flight Center, Greenbelt, MD 20771, USA
e-mail: `Theodor.Kostiuk@gsfc.nasa.gov`

Space flight missions have been in the forefront of astronomical discoveries in recent years and will continue to play an even greater role in astronomical and planetary studies in the year 2000 and beyond. Astronomical Space science missions require a great deal of supporting work to achieve their successes. Different disciplines of astronomy and space science, ground-based observations, laboratory and theoretical studies are needed to plan and execute the mission and to interpret measured data. They also provide a great opportunity for international cooperation and participation. Figure 1 illustrates the components that go into the planning and execution of space science missions. Ground-based studies play an important role in identifying measurement goals, and in providing complementary studies at higher spectral resolution, spectral coverage, and long term temporal coverage not possible with spacecraft. The NASA/ESA Cassini/Huygens mission to the Saturnian system and ground-based infrared heterodyne spectroscopic measurements provide an excellent example of the need and complementary nature of ground-based and space-based studies.

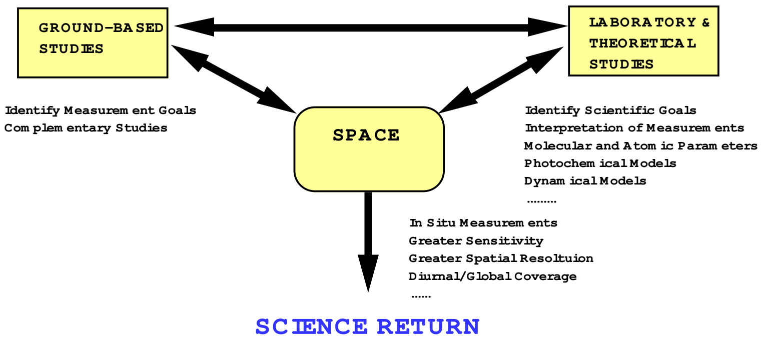

Figure 1: Components of space science missions

The Cassini/Huygens mission was launched October 15, 1997 with a scheduled encounter with Saturn July 1, 2004. Among the major goals of the mission is to study the composition, temperature structure and winds in the atmospheres of Saturn and Titan. En route to Saturn the spacecraft swings by Jupiter within $\sim$140 Jovian radii ($\sim 10^7$ km) on December 30, 2000 providing a unique opportunity to study Jupiter, its atmosphere and intense aurora.

The Composite Infrared Spectrometer, (Kunde *et al.*, 1996), on the Cassini spacecraft is a Fourier Transform Spectrometer covering the 3–1000 μm spectral region with three focal planes. The 9–16 μm region is covered by a 10-element linear array in focal plane 3, FP3 with a spectral resolution of 0.5 cm^{-1}. During the Jupiter flyby CIRS will be used to determine Jupiter's temperature distribution, hydrocarbon abundances, distribution of CO_2, $^{15}N/^{14}N$ ratio, and to study Jupiter's mid-infrared aurora. The CIRS field of view (FOV) on Jupiter

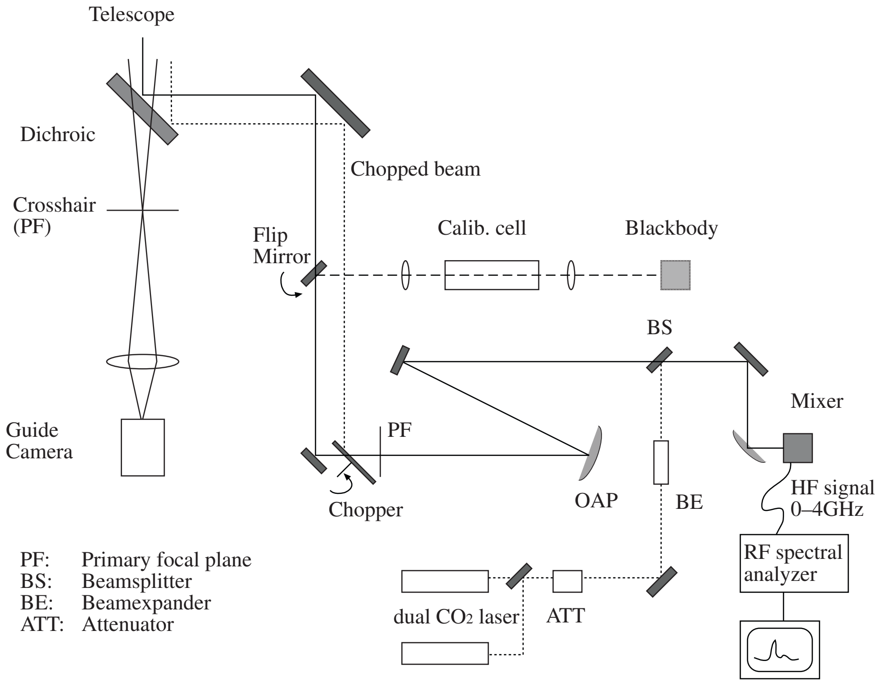

Figure 2: HIPWAC optical schematic

varies with distance, but at the time of closest approach is ~1 arcsec.

Ground-based measurements of Jupiter will be made during the flyby period using the Goddard Space Flight Center infrared heterodyne spectrometer, Heterodyne Instrument for Planetary Wind And Composition, HIPWAC (Schmuelling *et al.*, 2001). The instrument will cover the 9–12 μm spectral region with a much higher spectral resolution 0.00086 cm^{-1} and 0.00017 cm^{-1} than CIRS. Fully resolved spectral lines of ethane C_2H_6 and ethylene C_2H_4 near 12 and 10.5 μm, respectively, will provide complementary data on molecular abundances, temperature, and their altitude and north-south distribution, as well as the mid-infrared aurora. The HIPWAC spectral resolution permits the measurement of true line shapes and thus enables the retrieval of both abundance and temperature information, particularly in the hot auroral regions. The mid-infrared aurora has been studied in this way over a long-term period (*e.g.*, Kostiuk *et al.*, 1987; Kostiuk *et al.*, 1993; Livengood *et al.*, 1993). The FOV on Jupiter is 1 arcsec throughout the period and thus will provide higher spatial information at times before and after the closest approach, supporting the CIRS measurements. The schematic of the HIPWAC optical front end is given in Fig. 2. The telescope source beam is collimated and combined with an expanded CO_2 laser local oscillator beam at the ZnSe beam splitter and the combined beams are focused onto a HgCdTe photodiode mixer (Spears, 1977). The difference frequency between the laser and source beam generated in the photomixer is in the radio frequency (RF) region of the spectrum and preserves the intensity and frequency information of the source within ~4 GHz of the laser frequency. This RF signal is amplified and fed into a RF filter bank where it is analyzed and the data stored on a computer. A detailed description of the heterodyne technique and its application is given in Kostiuk (1994).

An example of the retrieval of both abundance and temperature information from infrared heterodyne spectra is given in Fig. 3. Ethane emission lines from the north auroral region are shown at 25 MHz (0.00086 cm^{-1}) resolution (right side). The solid line is a model fit to the data (histogram). In the upper plots a nominal thermal profile shown on the left was used and the C_2H_6 abundance was varied. Even with an unreasonably large abundance, mole fraction $= 25 \pm 8 \times 10^6$ a good fit can not be obtained. Modifying the thermal profile as shown in the lower plots as well as abundance, a good fit is obtained. Results show that the auroral emission is dominated by a significant increase in temperature in the upper stratosphere. Some chemical effects may also be present as indicated by the near two-fold increase in ethane abundance over the $\sim 3\times 10^6$ global quiescent mole fraction. The contribution functions indicating the pressure altitude regions contributing to the emission are shown on the left. CIRS observations can measure changes in ethane emission, but can not discriminate between temperature and abundance contribution to the measured emission spectra.

The science goals on Jupiter for CIRS and HIPWAC during the Cassini flyby period are given in Table 1.

Once at the Saturn system Titan's atmosphere and surface are primary targets of the Cassini mission and its

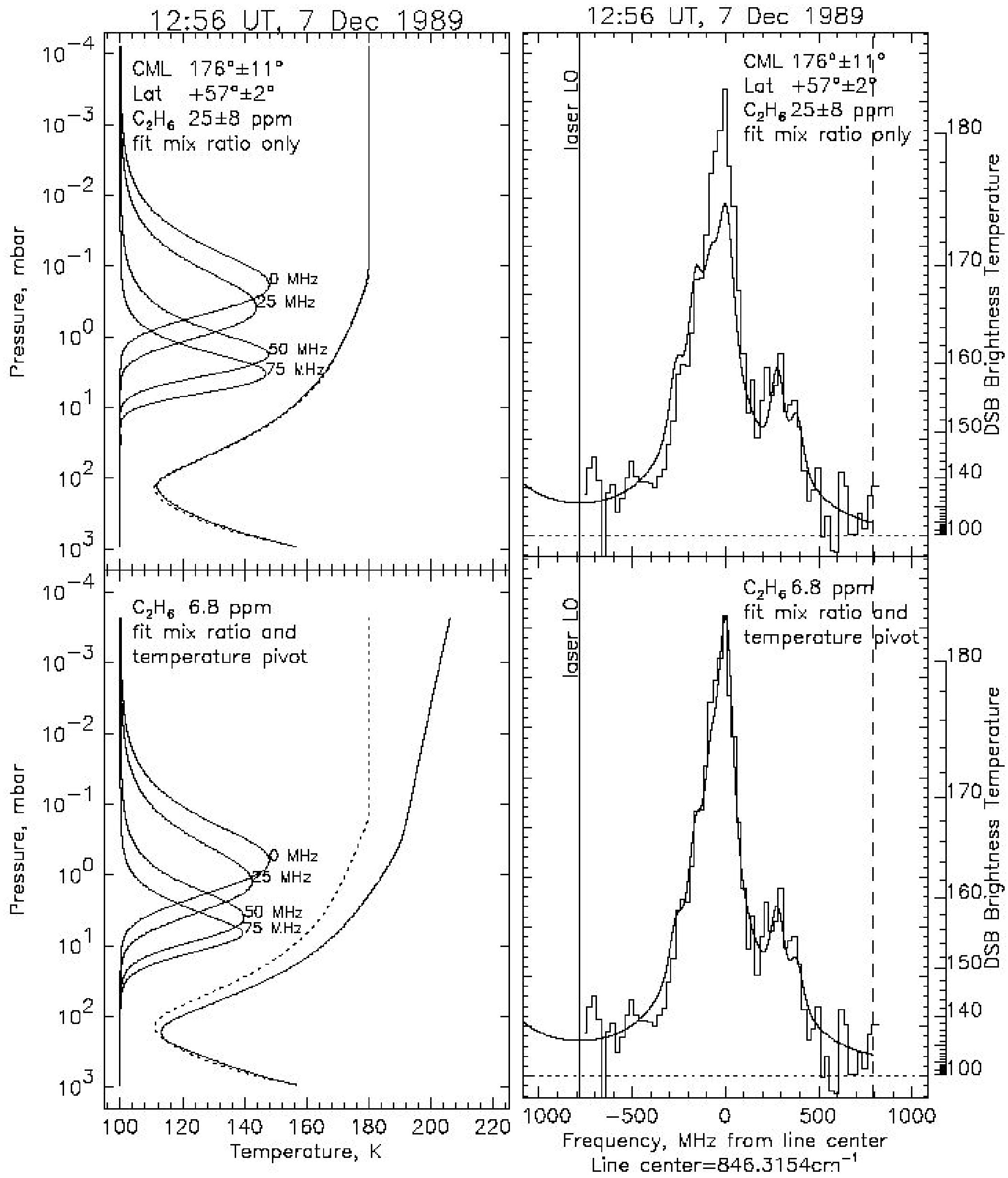

Figure 3: Jupiter's north ethane aurora

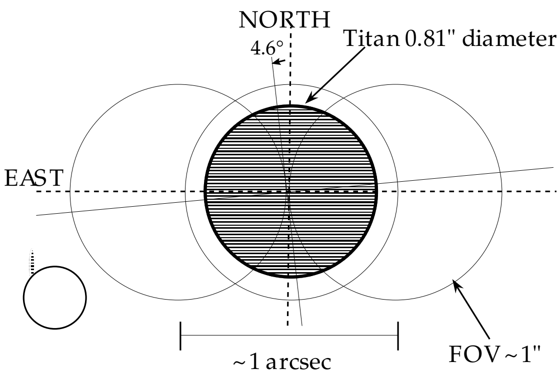

Figure 4: Titan observing geometry

Table 1:

CIRS FP3 SCIENCE GOALS ON JUPITER	HIPWAC SCIENCE GOALS ON JUPITER
Determine temperature distribution 10 to 1 mBar	Determine temperature distribution to < 0.1 mBar
Abundance and distribution of hydrocarbons *e.g.*, C_nH_m	Determine abundance and temperature from single line C_2H_6, C_2H_4
Sources of higher order HC's photochemistry *vs.* aurora	Equator *vs.* pole measurements
Mid-IR aurora	Temperatures and variability – additions to long term study; probe to 10 μBar
Determine $^{15}N/^{14}N$ ratio in NH_3	–
Meridional distribution of CO_2	–

PERFORMANCE PARAMETERS		
Spectral coverage	9 – 16 μm	9 – 12 μm
Spectral resolution	0.5 cm^{-1}	< 0.0008 cm^{-1}
FOV	Dec. 16, 2000: 2 arcsec Dec. 30, 2000: 1 arcsec	1 arcsec on 3-meter telescope $\sim$0.3 arcsec on 10-meter telescope

Huygens Probe (Lebreton, 1997). Knowledge of global circulation on Titan is particularly important. Titan's rotation period is long 16 days, making it the second slowest rotator (next to Venus) in our Solar System. Dynamics in atmospheres of slowly rotating bodies is poorly understood. The magnitude and direction of the resultant cyclostrophic circulation can not be determined from theory and indirect methods using thermal field data (Flasar, 1998) and stellar occultation (Hubbard *et al.*, 1993) can not determine wind direction. Direct measurements are needed to constrain theories of atmospheric dynamics in slowly rotating bodies (Hourdin *et al.*, 1995; Del Genio and Zhou, 1996). In addition, winds will transport the Huygens Probe horizontally during its parachute descent, determining its ultimate landing site and the length of time that communications can

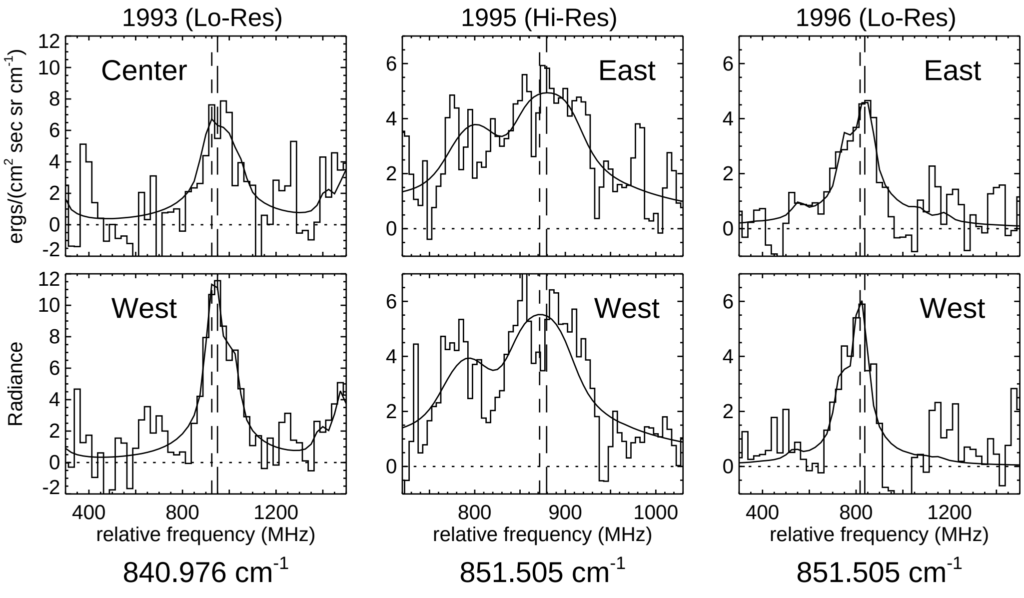

Figure 5: Doppler shift of ethane lines on Titan

be maintained and data transferred between the Orbiter and the landed Probe. Because the wind direction has not previously been determined, the direction of transport cannot be predicted with sufficient confidence to plan for it. Current mission plans attempt to mitigate the winds' effect on communication time by establishing a conservative error ellipse symmetric about zero wind velocity. This approach will limit the length of time for surface investigations. Knowing the magnitude and sense of the winds, the orbiter antenna pointing with respect to the probe entry point can be optimized for the longest possible communications and for surface studies, thus increasing the scientific information that can be retrieved from Titan.

Infrared heterodyne spectroscopy (IRHS) measurements of Doppler-shifted ethane (C_2H_6) emission line shapes from Titan's stratosphere (Kostiuk *et al.*, 1997) can be used to directly measure the direction and magnitude of Titan's zonal winds. Observations of the C_2H_6 emission lines near 11.8 μm from the ν_9 band were made in August 1993, in October 1995, and in September 1996, using the Goddard IRHS instrument at the Coude focus of the NASA Infrared Telescope Facility (IRTF) on Mauna Kea, Hawaii. The observing geometry is given in Fig. 4. Ethane line shapes and frequency positions were measured with the FOV positioned at the east limb and at the west limb on Titan's disc. Differences in the retrieved east and west line frequency positions (Fig. 5) after removing effects of systematic errors are attributed to Doppler shifts from a zonal wind field projected along the respective lines-of-sight. A prograde zonal wind with speed 210 ± 150 m/s, in the direction of Titan's rotation, was retrieved with 94% probability (Kostiuk *et al.*, 2001). The uncertainty, due primarily to the large 1 arcsec FOV on the limb of a 0.81 arcsec Titan (see Fig. 4), is too large for modification of the Huygens Probe release scenario. Since the heterodyne FOV is diffraction limited, using an 8-meter telescope (*e.g.*, Gemini North) would reduce the FOV to $\sim$0.3 arcsec and decrease the wind uncertainty by a factor of $\sim$5 in an equivalent integration time. This is the next goal of HIPWAC observations in support of the Cassini/Huygens mission. Besides data for the Huygens Probe release, results will provide complementary data for the Doppler Wind Experiment on Huygens (Bird *et al.*, 1997) and constraints on dynamical models for slowly rotating atmospheres.

REFERENCES

[1] *Bird M. K., et al.* The Huygens Doppler Wind Experiment. // Huygens: Science, Payload and Mission / Ed. J.-P. Lebreton.–European Space Agency SP-1177, 1997.–P. 139–162.

[2] *Del Genio A. D., Zhou W.* Simulations of superrotation on slowly rotating planets: sensitivity to rotation and initial conditions // Icarus.–1996.–**120**.–P. 332–343.

[3] *Flasar F. M.* The dynamic meteorology of Titan // Planet. and Space Sci.–1998.–**46**.–P. 1125–1147.

[4] *Hourdin F. P., et al.* Numerical simulation of the general circulation of the atmosphere of Titan // Icarus.–1995.–**117**.–P. 358–374.

[5] *Hubbard W. B., et al.* The occultation of 28 Sgr by Titan // Astron. and Astrophys.–1993.–**269**.–P. 541–563.

[6] *Kostiuk T., et al.* Variability of ethane on Jupiter // Icarus.–1987.–**72**.–P. 394–410.

[7] *Kostiuk T., Romani R., Espenak F., et al.* Temperature and abundances in the jovian auroral stratosphere 2. Ethylene as a probe of the microbar region // J. Geophys. Res.–1993.–**98**.–P. 18823–18830.

[8] *Kostiuk T.* Physics and chemistry of upper atmospheres of planets from infrared observations // Infrared Phys. Technol.–1994.–**35**.–P. 243–266.

[9] *Kostiuk T., et al.* Ethane abundance on Titan // Planet. and Space Sci.–1997.–**45**.–P. 931–939.

[10] *Kostiuk T., et al.* Direct Measurement of Winds on Titan // Geophys. Res. Lett.–2001.–**28**.–P. 2361.

[11] *Kunde V., et al.* Cassini Infrared Fourier Spectroscopic Investigation // Proc. SPIE.–1996.–**2803**.–P. 162–177.

[12] Huygens: Science, Payload and Mission / Ed. J.-P. Lebreton.–European Space Agency SP-1177, 1997.

[13] *Livengood T. A., Kostiuk T., Espenak F., Goldstein J. J.* Temperature and abundances in the Jovian auroral stratosphere 1. Ethane as a probe of the millibar region // J. Geophys. Res.–1993.–**98**.–P. 18813–18823.

[14] *Schmuelling F., Kostiuk T., et al.* Heterodyne Instrument for Planetary Wind And Composition // Applied Optics.–2001.–in preparation.

[15] *Spears D. L.* Planar HgCdTe quadrantal heterodyne arrays with GHz response at 10.6 μm // Infrared Phys.–1977.–**17**.–P. 5–8.

WEAK PHOTON LOCALIZATION AND OPPOSITION PHENOMENA IN PLANETARY ASTROPHYSICS

M. Mishchenko and N. Zakharova

NASA Goddard Institute for Space Studies
2880 Broadway, New York, NY 10025, USA
e-mail: crmim@giss.nasa.gov

Coherent backscattering of light by discrete random media, otherwise known as weak photon localization, is a remarkable optical phenomenon caused by constructive interference of waves propagating along the same light-scattering paths but in opposite directions. This paper briefly reviews manifestations of coherent backscattering and the use of this phenomenon as a remote sensing tool.

INTRODUCTION

Coherent backscattering is a remarkable phenomenon caused by constructive interference of waves propagating along reciprocal multiple-scattering paths in a discrete random medium [2, 7]. A well-known manifestation of coherent backscattering is an intensity peak centered at exactly the backscattering direction. The magnitude of the peak relative to the incoherent background depends on the polarization states of the incident and reflected beams and can be as large as a factor of 2 when the scattering particles are spherically symmetric, the incident beam is circularly polarized, and the intensity of the reflected beam is measured in the same-helicity channel [9]. Another manifestation of coherent backscattering can be observed when the incident beam is unpolarized. In this case the backscattering intensity peak is accompanied by a sharp asymmetric peak of negative polarization with a minimum centered at a very small phase angle (the angle between the reflected beam and the backscattering direction) [10]. This phenomenon has been called the polarization opposition effect [10] and has the same physical origin as the so-called spatial anisotropy of the backscattering intensity peak in the case of a linearly polarized incident beam [21].

It has been suggested that coherent backscattering could be a contributor to some effects observed for Solar System bodies in visible light and at radiowave frequencies [15, 17, 19]. However, accurate theoretical computations of weak localization are difficult and have been used in analyses of observational data in only a handful of publications. In this paper we briefly review the exact theory of coherent backscattering and its remote sensing applications.

THEORY

To explain the physical origin of weak photon localization, let us consider a layer composed of discrete, randomly positioned scattering particles and illuminated by a parallel beam of light incident in the direction $\hat{n}_{ill}$ (Fig. 1). The observer measures the intensity of light reflected by the layer in the direction $\hat{n}_{obs}$. The reflected signal is contributed to by waves scattered along various paths inside the layer involving different combinations of particles. Let us consider two conjugate scattering paths shown in Fig. 1 by solid and dashed lines. These paths go through the same group of N particles, denoted by their positions $\mathbf{r}_1$, $\mathbf{r}_2$, ..., $\mathbf{r}_N$, but in opposite directions. The waves scattered along the two conjugate paths interfere, the interference being constructive or destructive depending on the phase difference $\mathrm{k}(\mathbf{r}_N - \mathbf{r}_1)(\hat{n}_{ill} + \hat{n}_{obs})$, where k is the wave number in the surrounding medium. If the observation direction is far from the exact backscattering direction given by $-\hat{n}_{ill}$, then the waves scattered along conjugate paths involving different groups of particles interfere in different ways, and the average effect of interference is zero due to the randomness of particle positions. Consequently, the observer measures some average, incoherent intensity well described by the classical radiative transfer theory. However, at exactly the backscattering direction ($\hat{n}_{obs} = -\hat{n}_{ill}$), the phase difference between conjugate paths involving any group of particles is identically equal to zero and the interference is always constructive, thereby resulting in a coherent backscattering intensity peak [2]. Kuga and Ishimaru [6] were the first to measure this effect in a controlled laboratory experiment, although it may have been unknowingly observed by Lyot [8] in the form of the so-called coherent polarization opposition effect [10, 14].

Exact computation of the coherent backscattering effect based on solving the Maxwell equations is feasible only for few-particle clusters and is complicated by several factors. First, the scattering pattern for a monodisperse cluster in a fixed orientation is always heavily burdened by multiple interference maxima and minima and by an intricate resonance structure typical of single monodisperse spheres. Second, the scattering pattern is further affected by near-field effects that result from component spheres in a closely packed cluster not being in the far-field zones of each other. Third, simple trigonometry shows that the angular width of the coherent backscattering intensity peak is of the order of $1/k\langle d\rangle = \lambda/2\pi\langle d\rangle$, where $\langle d\rangle$ is the average distance between the cluster components and λ is the wavelength in the surrounding medium. Therefore, this peak may be too broad to be reliably identified unless the cluster components are separated widely enough. However, increasing the distance between the cluster components diminishes the contribution of multiple scattering and, thus, the amplitude of the coherent backscattering peak, thereby making it difficult to detect. To smooth the effect of the first factor out and make the backscattering peak detectable, the scattering pattern must be averaged over particle sizes, cluster orientations, and distances between the components. Furthermore, the average distance between the cluster components must be much larger than the size of the components and the wavelength, but yet small enough so that the multiple-scattering contribution to the total signal be still significant.

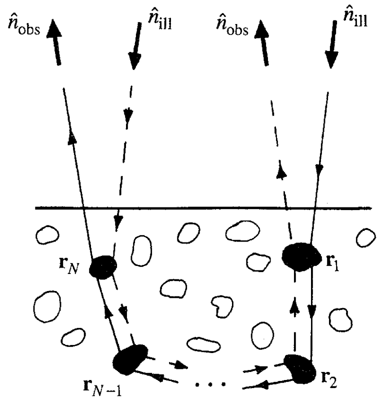

Figure 1: Schematic explanation of coherent backscattering

Ismagilov and Kravtsov [5] studied analytically the simplest case of two widely separated spheres with diameters much smaller than the wavelength, but found that the amplitude of the coherent backscattering intensity peak was extremely small because of the weakness of the multiple-scattering contribution to the total scattered signal. Mishchenko [12] applied the exact superposition T-matrix method to polydisperse, randomly oriented clusters composed of two equal wavelength-sized spheres. He computed the ratio of intensities scattered by the clusters and by two independent spheres of the same size assuming that the incident light was unpolarized. Figure 2 shows this ratio versus scattering angle (angle between the incident and scattered beams) calculated for $k\langle d\rangle = 25$, average component sphere size parameter $k\langle a\rangle = 5$, where a is the sphere radius, and relative refractive index $m = 1.2$. The curve clearly shows an enhancement of intensity with an angular width comparable to $1/k\langle d\rangle$ and an amplitude of about 1.03. Mishchenko [12] found that this feature persisted with varying $k\langle d\rangle$, $k\langle a\rangle$, and refractive index, thereby indicating that it was indeed caused by coherent backscattering.

The amplitude of the coherent backscattering peak can be significantly greater for very large collections of particles [21, 11]. Unfortunately, the exact theory of coherent backscattering for such collections is extremely complicated and has been developed only for the case of reflection of light by a semi-infinite layer composed of particles with sizes much smaller than the wavelength [1]. Mishchenko *et al.* [14] used this theory to compute the characteristics of coherent backscattering. They assumed unpolarized incident light and defined the intensity enhancement factor as the ratio of the total reflected intensity to the incoherent background value. The degree of linear polarization was defined as minus the ratio of the total reflected second Stokes parameter to the total reflected intensity. Figure 3 shows both quantities as functions of a dimensionless angular parameter q. The upper panel demonstrates the renowned intensity peak centered at exactly the opposition. The amplitude of the peak is ≈ 1.5368 and its half-width at half-maximum is ≈ 0.597. The lower panel of Fig. 3 shows that the reflected polarization is zero at opposition, which is a consequence of azimuthal symmetry in the case of normal illumination and unpolarized incident light. However, with increasing q, polarization becomes negative, rapidly grows in absolute value, and reaches its minimal value $P_{min} \approx -2.765\%$ at a reflection direction very close to opposition ($q_P \approx 1.68$). The peak of negative polarization is highly asymmetric so that the half-minimal polarization value -1.383% is first reached at $q_{P,1} \approx 0.498$, which is even smaller than the value

$q_\zeta \approx 0.597$ corresponding to the half-width at half-maximum of the backscattering intensity peak, and then at a much larger $q_{P,2} \approx 7.10$. This unusual behavior of polarization at near-backscattering angles was called in [10] the polarization opposition effect (POE).

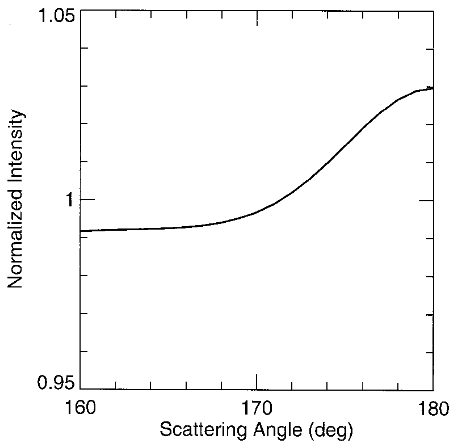

Figure 2: Coherent backscattering by polydisperse, randomly oriented two-sphere clusters

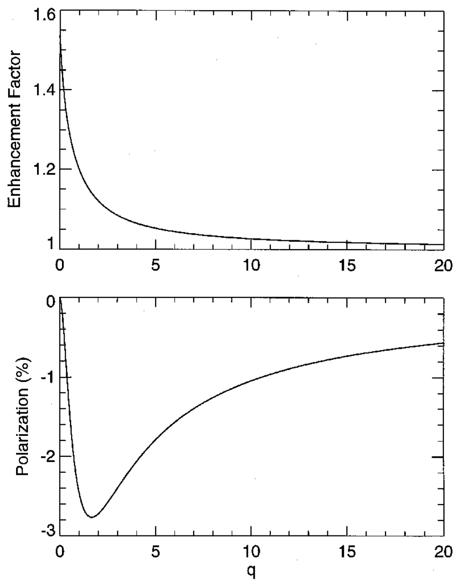

Figure 3: Theoretical angular profiles of the intensity enhancement factor and the degree of linear polarization of the reflected light for a half-space of nonabsorbing Rayleigh particles illuminated by an unpolarized beam of light incident normally to the boundary of the scattering medium

A useful exact result was obtained by Mishchenko [9], who showed that the photometric and polarization characteristics of coherent backscattering at exactly the backscattering direction as well as outside the backscattering peak can be expressed in terms of the solution of the classical radiative transfer equation. This result allows the use of realistic models of polydisperse, arbitrarily sized and arbitrarily shaped particles with any refractive indices. Other theoretical approaches are based on the so-called diffusion approximation [18] and Monte Carlo computations [20]. Because the angular width of the intensity peak caused by coherent backscattering from optically thick layers is proportional to the ratio wavelength/(photon mean free path), it is negligibly small for sparse particle collections and does not affect the results of remote sensing observations of such tenuous objects as clouds, aerosols, and precipitation. However, measurements of coherent backscattering can be a valuable characterization tool in laboratory and remote sensing studies of layers of closely spaced particles such as dense particle suspensions and natural and artificial particulate surfaces [2, 11, 15].

DISCUSSION AND APPLICATIONS

Because lasers are the most frequently used sources of illumination and usually generate linearly or circularly polarized light, explicit laboratory demonstrations of POE have been extremely rare. Apparently, the first laboratory observation of POE was made by Lyot as long ago as in 1920s [8], although the physical explanation of this phenomenon was, of course, unknown at that time. POE may have also been observed in more recent laboratory measurements by Geake and Geake [3] for fine alumina powders, although the smallest phase angle in their experiments was 2° and may be too large for definitive conclusions to be made. These measurements may suggest that POE weakens and ultimately disappears with increasing particle size, which would be consistent with the similar disappearance of the spatial anisotropy of the backscattering intensity peak in the case of a linearly polarized incident beam observed by van Albada *et al.* [21].

Sharp peaks of negative polarization at phase angles considerably less than 1 deg were observed for Saturn's rings and the Galilean satellites of Jupiter [10, 16]. Because these peaks were distinctly different from the symmetric, nearly parabolic negative polarization branch commonly observed for many Solar System bodies [3, 15], they were interpreted in terms of POE caused by coherent backscattering of sunlight by a surface layer composed primarily of microscopic ice particles [10, 16]. The fact that the same objects exhibit comparably narrow intensity peaks centered at exactly the opposition [4, 10] provides strong support for this interpretation. Weak localization is also the likely cause of the unusually strong and narrow photometric opposition effect observed for bright E type asteroids [13].

REFERENCES

[1] *Amic E., Luck J. M., Nieuwenhuizen Th. M.* Multiple Rayleigh scattering of electromagnetic waves // J. Phys. I.–1997.–**7**.–P. 445–483.

[2] *Barabanenkov Yu. N., Kravtsov Yu. A., Ozrin V. D., Saichev A. I.* Enhanced backscattering in optics // Progr. Opt.–1991.–**29**.–P. 65–197.

[3] *Geake J. E., Geake M.* A remote-sensing method for sub-wavelength grains on planetary surfaces by optical polarimetry // Mon. Notic. Roy. Astron. Soc.–1990.–**245**.–P. 46–55.

[4] *Helfenstein P., Currier N., Clark B. E., et al.* Galileo observations of Europa's opposition effect // Icarus.–1998.–**135**.–P. 41–63.

[5] *Izmagilov F. M., Kravtsov Yu. A.* Backscattering enhancement polarization effects on a system of two small randomly oriented scatterers // Waves Random Media.–1993.–**3**.–P. 17–24.

[6] *Kuga Y., Ishimaru A.* Retroreflectance from a dense distribution of spherical particles // J. Opt. Soc. Am. A.–1984.–**1**.–P. 831–835.

[7] *Lagendijk A., van Tiggelen B. A.* Resonant multiple scattering of light // Phys. Rep.–1996.–**270**.–P. 143–215.

[8] *Lyot B.* Recherches sur la polarisation de la lumiere des planetes et de quelques substances terrestres // Ann. Obs. Paris.–1929.–**8**.

[9] *Mishchenko M. I.* Enhanced backscattering of polarized light from discrete random media // J. Opt. Soc. Am. A.–1992.–**9**.–P. 978–982.

[10] *Mishchenko M. I.* On the nature of the polarization opposition effect exhibited by Saturn's rings // Astrophys. J.–1993.–411.–P. 351–361.

[11] *Mishchenko M. I.* Diffuse and coherent backscattering by discrete random media // JQSRT.–1996.–**56**.–P. 673–702.

[12] *Mishchenko M. I.* Coherent backscattering by two-sphere clusters // Opt. Lett.–1996.–**21**.–P. 623–625.

[13] *Mishchenko M. I., Dlugach J. M.* Coherent backscatter and the opposition effect for E-type asteroids // Planet. and Space Sci.–1993.–**41**.–P. 173–181.

[14] *Mishchenko M. I., Luck J.-M., Nieuwenhuizen T. M.* Full angular profile of the coherent polarization opposition effect // J. Opt. Soc. Am. A.–2000.–**17**.–P. 888–891.

[15] *Muinonen K.* Coherent backscattering by solar system dust particles // Asteroids, Comets, Meteors.–1993.–P. 271–296.

[16] *Rosenbush V. K., Avramchuk V. A., Rosenbush A. E., Mishchenko M. I.* Polarization properties of the Galilean satellites of Jupiter: Observations and preliminary analysis // Astrophys. J.–1997.–**487**.–P. 402–414.

[17] *Shkuratov Yu. G.* Light backscattering by the solid surfaces of celestial bodies: Theoretical models of the opposition effect // Solar Syst. Res.–1994.–**28**.–P. 418–431.

[18] *Stephen M. J., Cwilich G.* Rayleigh scattering and weak localization: Effect of polarization // Phys. Rev. B.–1986.–**34**.–P. 7564–7572.

[19] *Tishkovets V. P.* Light scattering by clusters of spherical particles // Kinematics and Physics of Celestial Bodies.–1994.–**10**, N 2.–P. 50–54.

[20] *van Albada M. P., Lagendijk A.* Vector character of light in weak localization // Phys. Rev. B.–1987.-**36**.–P. 2353–2356.

[21] *van Albada M. P., van der Mark M. B., Lagendijk A.* Polarization effects in weak localization of light // J. Phys. D.–1988.–**21**.–P. S28–S31.

TEMPERATURE DISTRIBUTION IN A SEMI–INFINITE ATMOSPHERE SUBJECTED TO COSINE COLLIMATED RADIATION

T. Viik

Tartu Observatory 61602, Tõravere, Tartumaa, Estonia
e-mail: viik@jupiter.aai.ee

Accurate numerical solutions are presented for the radiation field in a semi-infinite, two-dimensional, plane-parallel, absorbing-emitting but non-scattering gray atmosphere subjected to cosine-varying collimated incident boundary radiation. We approximate the kernel of the integral equation for the emissive power by a sum of exponents. After this approximation the integral equation can be solved exactly. The solution contains the well-known Ambartsumian-Chandrasekhar $H-$function. This approach allowed us to find the accurate values for the emissive power and the radiative flux at arbitrary optical depths in the atmosphere. The calculations have shown that the radiative flux may have a maximum at certain values of the spatial frequency in the atmosphere and that the region, where the emissive power reaches a constant value, may lie very deep in the atmosphere.

INTRODUCTION

An one-dimensional model for radiative transfer in different media has been extensively studied. Many problems in one-dimensional transfer allow rigorous mathematical solutions which may serve as benchmarks for more complicated cases or as first approximations to two-dimensional problems.

However, there are many problems in astrophysics where the results of the one-dimensional model of radiative transfer are not accurate enough and we have to apply models of two- or three-dimensional radiative transfer. This enormously complicates the solution and thus only a few exact studies exist and they deal mostly with scattering of a narrow pencil of radiation incident on a scattering medium (*cf.* the references in [1]).

There is a group of two-dimensional problems for which an exact solution can be found. One of these problems is connected with non-scattering media with the cosine varying incident collimated radiation. In this case the two-dimensional problem can be reduced to one-dimensional integral equation as shown by Breig and Crosbie [2]. However, their approach allowed to determine only the external radiation field.

In this report we generalize the results of Breig and Crosbie by applying the method of approximating the kernel of the integral equation for the Sobolev resolvent function (respective Green function) by a series of exponents. The resulting approximate equation has an exact solution which is also represented by a series of exponents. This allows us to define the auxiliary functions g and h through the resolvent function Φ and thus define all the relevant functions.

In one-dimensional media the described approach gave very accurate results [3]. It appeared that for the problem on hand we were able to find both the external and internal radiation field.

The full-scale presentation of this problem is given in [1] and for the optically finite atmosphere in [4].

SOLUTION OF THE EQUATION OF RADIATIVE TRANSFER

We are looking for the emissive power in a homogeneous non-scattering plane-parallel two-dimensional gray atmosphere which is in local thermodynamic equilibrium. The radiative transfer in such an atmosphere is described by the following equation

$$\cos\theta \frac{\partial I}{\partial \tau_z} + \sin\theta \sin\phi \frac{\partial I}{\partial \tau_y} + I = \frac{\sigma}{\pi} T^4, \tag{1}$$

where I is the intensity; θ is the polar angle measured from the inward normal to the atmosphere; ϕ is azimuthal angle measured from the τ_x-axis; σ is the Stefan-Boltzmann constant; T is the temperature in the atmosphere; σT^4 is the emissive power. The optical depth τ_z is measured downward from the boundary of the atmosphere and together with τ_x and τ_y they form a right-hand rectangular co-ordinate system. We require that the energy is transferred only by radiation, *i.e.*, there is no heat conduction or convection in the atmosphere.

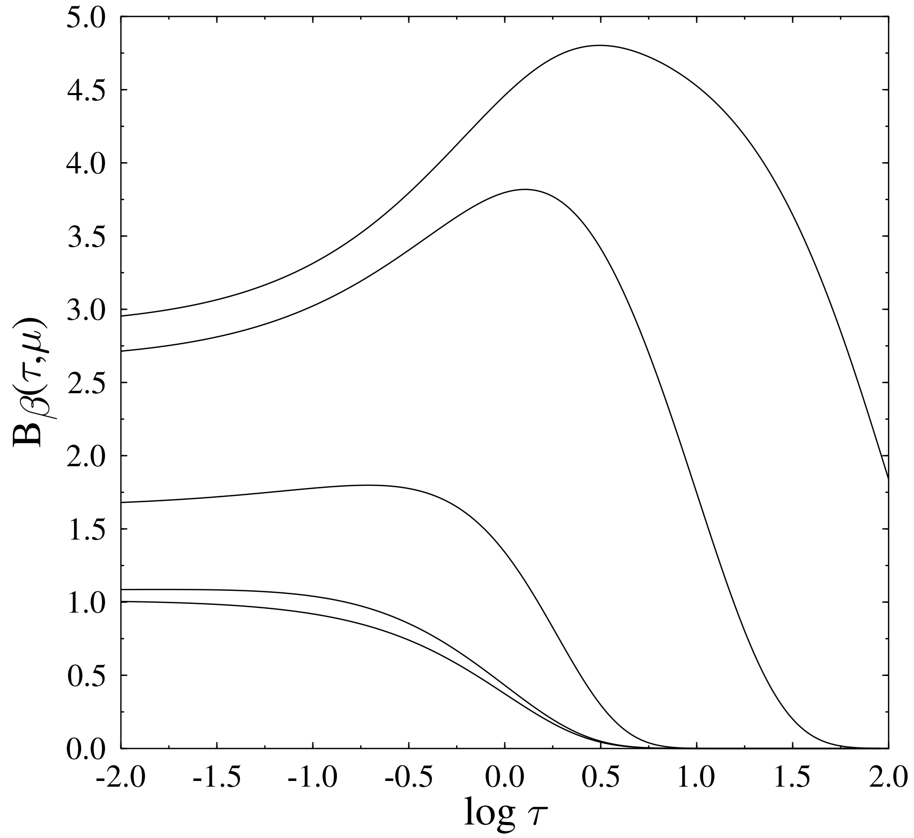

Figure 1: The dimensionless emission power as a function of the optical coordinate τ_z for different values of spatial frequency β while the angle of incidence is zero. Starting from above: $\beta = -2, -1, 0, 1, 2$

Taking this fact into account we obtain the equation for the emissive power

$$4\sigma T^4(\tau_y, \tau_z) = \int_{2\pi} I_0^+(\tau_y^+) \exp(-\tau_z/\mu) \mathrm{d}\omega + \frac{1}{\pi} \int_0^{2\pi} \int_0^1 \int_0^\infty \sigma T^4(\tau_y', \tau_z') \exp(-|\tau_z - \tau_z'|/\mu) \mathrm{d}\tau_z' \mathrm{d}\mu/\mu \mathrm{d}\phi, \tag{2}$$

where $\tau_y^+ = \tau_y - \tau_z \tan\theta \sin\phi$, $\tau_y' = \tau_y + (\tau_z' - \tau_z) \tan\theta \sin\phi$, $\mu = \cos\theta$ and I_0^+ is the intensity incident on the boundary of the atmosphere [2]. According to our assumption the incident intensity may be expressed as

$$I_0^+(\tau_y^+) = I_0 \left[1 + \epsilon \exp(i\beta\tau_y^+)\right] \delta(\mu - \mu_0)\delta(\phi), \tag{3}$$

where I_0 is a constant, $(\mu_0 = \cos\theta_0, \phi)$ defines the direction of the incident collimated radiation, ϵ is the amplitude of the cosine wave and δ is the Dirac delta function. Boundary condition (3) means that the top of the atmosphere is strip-wise illuminated by a parallel beam at an angle θ_0 while the strips are parallel to the x-axis and their widths are defined by the spatial frequency β as π/β in units of optical length τ_y^+. The illumination in the direction parallel to the y-axis varies according to the cosine law. Next we apply the concept of separation of variables to Eq. (2) by assuming that

$$\sigma T^4(\tau_y, \tau_z) = \frac{1}{4} I_0 \left[B_{\beta=0}(\tau, \mu_0) + \epsilon B_\beta(\tau, \mu_0) \exp(i\beta\tau_y)\right], \tag{4}$$

where B_β is the dimensionless emissive power and $\tau = \tau_z$. Using Eq. (4) in Eq. (2) gives us a simple integral equation for B_β in the form

$$B_\beta(\tau, \mu_0) = \exp(-\tau/\mu_0) + \frac{1}{2} \int_0^\infty \mathcal{E}_1(\tau - \tau') B_\beta(\tau', \mu_0) \mathrm{d}\tau', \tag{5}$$

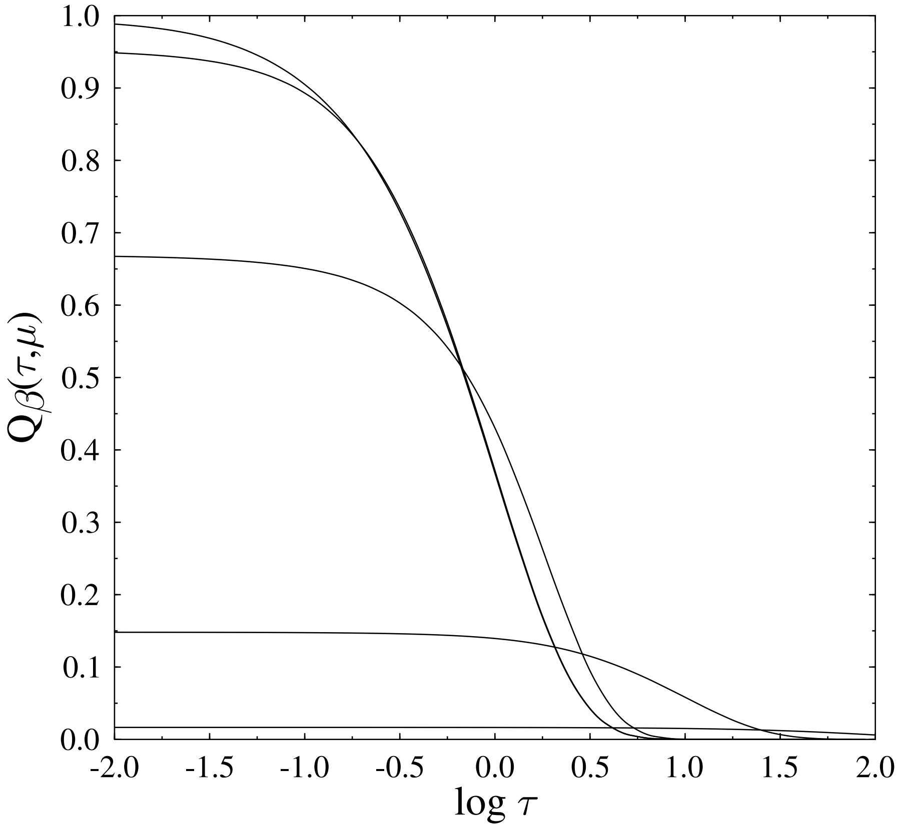

Figure 2: The dimensionless flux as a function of the optical coordinate τ_z for different values of spatial frequency β while the angle of incidence is zero. Starting from above: $\beta = -2, -1, 0, 1, 2$

where the generalized exponential integral $\mathcal{E}_1$ is defined as [2]

$$\mathcal{E}_1(\tau, \beta) = \int_1^\infty \exp(-|\tau| \sqrt{u^2 + \beta^2}) \frac{\mathrm{d}u}{\sqrt{u^2 + \beta^2}}. \tag{6}$$

Sobolev has shown that the non-singular part of the Green function for Eq. (5) – often called the Sobolev resolvent function Φ satisfies the following equation [5]

$$\Phi_\beta(\tau) = \frac{1}{2}\mathcal{E}_1(\tau, \beta) + \frac{1}{2}\int_0^\infty \mathcal{E}_1(\tau - \tau')\Phi_\beta(\tau')\mathrm{d}\tau'. \tag{7}$$

Next we introduce two functions $h(\tau, \mu)$ and $g(\tau, \mu)$ as follows [3]

$$h_\beta(\tau, \mu) = 1 + \int_\tau^\infty \Phi_\beta(t) \exp(-(t - \tau)/\mu)\mathrm{d}t, \tag{8}$$

$$g_\beta(\tau, \mu) = \exp(-\tau/\mu) + \int_0^\tau \Phi_\beta(t) \exp(-(\tau - t)/\mu)\mathrm{d}t. \tag{9}$$

Sobolev [5] has shown that the solution of Eq. (5) may be written in our notation in the form

$$B_\beta(\tau, \mu_0) = B_\beta(0, \mu_0) g_\beta(\tau, \mu_0). \tag{10}$$

Formally, this completes the solution of the problem.

In order to find the functions $h_\beta(\tau, \mu_0)$ and $g_\beta(\tau, \mu)$ at an arbitrary optical depth we have to solve Eq. (7). This can be easily done if we approximate the kernel of Eq. (7) by a sum of exponents. After that the integral equation can be solved exactly and we may find the functions $h(\tau, \mu)$ and $g(\tau, \mu)$ by simple integration. This procedure is described in detail in [3].

NUMERICAL RESULTS

Due to the facts that for large β the characteristic function of the problem increases rapidly towards the end of the domain of its definition and that the generalized exponential integral has a logarithmic singularity at $\tau \to 0$ we have to be careful in using the Gaussian rule in approximating the kernel of Eq. (7). For better accuracy we divided the integration range into four subintervals and in each subinterval we used the Gaussian rule with $N/4 = 21$ points. This scheme ensured at least five significant digits both for the dimensionless flux and the emissive power in the region of $0 \leq \beta \leq 10000$.

Fig. 1 shows the behaviour of the dimensionless emissive power for $\mu = 1.0$. According to calculations for small angles of incidence the dimensionless emissive power decreases monotonically for all the values of β. This does not take place in the case of perpendicular incidence where such a monotonous decrease is present only for $\log \beta \geq 0.5$. For smaller values of β the dimensionless emissive power has a maximum at a definite τ.

The influence of the spatial frequency β and the optical depth τ (optical coordinate in z-direction) on the dimensionless flux of energy $Q_\beta(\tau, \mu = 1)$ is illustrated in Fig. 2. The dimensionless flux decreases from its maximum value (which is equal to μ) at large values of spatial frequency and small values of optical depth towards smaller values of spatial frequency and larger values of optical depth but curiously enough there appears a maximum in the $Q_\beta - \log \tau$ plane in the region where $\log \tau \geq -0.75$.

REFERENCES

[1] *Viik T.* Temperature Distribution in a Semi-Infinite Atmosphere Subjected to Cosine Varying Collimated Radiation // Proc. Estonian Acad. Sci. Phys. Math.–2000.–**49**.–P. 40–57.

[2] *Breig W. F., Crosbie A. L.* Two-dimensional radiative equilibrium: A semi-infinite medium subjected to cosine varying radiation // J. Quant. Spectrosc. Radiat. Transfer.–1973.–**13**.–P. 1395–1419.

[3] *Viik T., Rõõm R., Heinlo A.* A method of the resolvent function approximation in radiative transfer // Tartu Teated.–1985.–N 76.–P. 3–131. (in Russian).

[4] *Viik T.* Temperature Distribution in a Finite Atmosphere Subjected to Cosine Varying Collimated Radiation // Proc. Estonian Acad. Sci. Phys. Math.–2000.–**49**.–P. 108–121.

[5] *Sobolev V.V.* Light Scattering in Planetary Atmospheres.–Moscow: Nauka, 1972. (in Russian).

ESTIMATION OF RANDOM ERRORS OF PHOTOMETRIC METHOD FOR PLANET RELIEF DETERMINATION

I. Dulova, Yu. Kornienko, V. Pugach

Institute of Radiophysics and Electronics, NAS of Ukraine
12 Ak. Proskury, 61085 Kharkiv, Ukraine
e-mail: pvv@ire.kharkov.ua

The effect of detection noise on accuracy of the surface relief determination by surface images obtained in the optical or radar ranges has been investigated. The method is based on the brightness dependence on the local normal to the surface. In the frame of proposed technique, statistical estimation of the relief is shown to be not biased. Expressions for variance and spectral density of the error of relief determination have been obtained.

The method of determination of the surface relief according to a series of its optical or radio-images was developed in the work [1]. In [2] it was shown that this method can be applied to determine the surface relief according to its radio-brightness measured by means of the radar with a synthetic aperture (SAR). In [3] the experimental investigation of errors of this method was carried out by computer simulation. These researches have confirmed the efficiency of this method and the acceptable magnitude of its errors. In spite of this it is desirable to study theoretically the errors of this method and to receive analytic expressions for them.

The errors arising when determining the relief by the photometric method described in [1, 2] have a dual origin. Firstly, the signal reception is accompanied by noise of different nature. It causes a random error in the issue; and the higher is the noise level, the larger is the magnitude of error. Secondly, in [1, 2] the equation determining the optimum filter is solved only approximately that finally causes a systematic error, and the steeper surface slopes and the more variations of its parameters are, the larger is the magnitude of error. In the given work we investigate the random error of the photometric method. And in order to avoid bulk calculations, a simplified problem of determination of only the surface relief without determination of its photometric parameters, which are considered as known and constant over all the surface under investigation, is solved.

For examination we shall take, as introduced in [1, 2], the following assumptions. The required relief $H(x,y)$ (*i.e.*, the function describing the dependence of the height H above a mean plane on the Cartesian x, y coordinates) represents the realization of a stationary Gaussian process with the spectral density $1/\alpha(\mathbf{k})$, where $\mathbf{k}$ is two-dimensional vector of spatial frequency. The angle, at which it is possible to see the investigated place from the point of observation, is rather small, so that the direction on the observer can be approximately considered the same in all points of this place. The brightness of the surface element in the j-th image depends on the orientation of the normal $\mathbf{n}$ to the element by the law

$$I_j = F_j\left(\mathbf{n}\right), \tag{1}$$

where F_j is an known function describing the properties of the scattering surface. Assuming that the surface inclinations are small, it is possible to expand $F_j\left(\mathbf{n}\right)$ into a Taylor series in terms of $\mathbf{n}$ and the average normal to the surface $\mathbf{n}_0$. Keeping the first expansion term one can write:

$$I_j = I_{0j} + \mathbf{c}_j \cdot \left(\mathbf{n} - \mathbf{n}_0\right). \tag{2}$$

When $|\mathbf{n} - \mathbf{n}_0|$ is small, this relation within the accuracy of second order infinitesimals can be written as

$$I_j = I_{0j} + \mathbf{c}_j \cdot \mathbf{t}\left(x,y\right), \tag{3}$$

where

$$\mathbf{t}\left(x,y\right) = \nabla H\left(x,y\right) \tag{4}$$

is the two-dimensional vector of the surface inclination, ∇ is the two-dimensional gradient, and $\mathbf{c}_j$ is the two-dimensional vector constant determined by properties of the surface and the actual geometry. Each realization of the relief $H(x,y)$ is characterized by its own value of the prior density

$$\rho_h(H) \cong exp\left(-\int\limits_{-\infty}^{\infty} \tilde{H}^*(\mathbf{k})\ \alpha(\mathbf{k})\ \tilde{H}(\mathbf{k})\ d^2\mathbf{k}\right) \tag{5}$$

(note that the normalizing factor does not play any important role, because it does not enter into the final result). Similarly for noise

$$\rho_n(N) \cong exp\left(-\int\limits_{-\infty}^{\infty} \tilde{N}^*(\mathbf{k})\ \beta(\mathbf{k})\ \tilde{N}(\mathbf{k})\ d^2\mathbf{k}\right). \tag{6}$$

Here $\tilde{H}(\mathbf{k})$ and $\tilde{N}(\mathbf{k})$ are Fourier-images of the relief and noise accordingly, $\beta(\mathbf{k})$ is the value inverse to the noise spectral density, the asterisk means complex conjugation.

The images received in an experiment and described by the brightness distribution $J_j(x,y)$ are related with $I_j(x,y)$ by the relation

$$J_j(x,y) = \int\limits_{-\infty}^{\infty}\int\limits_{-\infty}^{\infty} g_j(x-x',y-y')\ I_j(x',y')\ dx'\,dy' + N_j(x,y), \tag{7}$$

where $g_j(x-x',y-y')$ is the kernel describing the j-th image diffusion caused by phase distortions in the propagation medium and other disturbing factors, $N_j(x,y)$ is an arbitrary realization of the stationary additive Gaussian noise. This relation is more convenient *ad referendum* to write in the frequency representation expanding both parts into a Fourier series

$$\tilde{J}_j(\mathbf{k}) = \tilde{g_j}(\mathbf{k})\ \tilde{I}_j(\mathbf{k}) + \tilde{N}_j(\mathbf{k}). \tag{8}$$

Let us have m of such images received from different points of the trajectory of an aircraft. It is required to find the most probable relief.

The expression for *a posteriori* density of the relief $H(x,y)$ is generated by the Bayes' formula [4] taking into account (12), (14), (15). Later it will be more convenient to use its logarithm

$$L(H) = \int \tilde{H}^*(\mathbf{k})\ \alpha(\mathbf{k})\ \tilde{H}(\mathbf{k})\ d^2\mathbf{k} +$$

$$+\sum_j \int \left[\tilde{J}_j(\mathbf{k}) - i\,\tilde{g_j}(\mathbf{k})\ \mathbf{c}_j\cdot\mathbf{k}\ \tilde{H}^*(\mathbf{k})\right]^* \beta(\mathbf{k}) \left[\tilde{J}_j(\mathbf{k}) - i\,\tilde{g_j}(\mathbf{k})\ \mathbf{c}_j\cdot\mathbf{k}\ \tilde{H}^*(\mathbf{k})\right] d^2\mathbf{k}. \tag{9}$$

The maximum of this functional determines the most probable relief $H_m(x,y)$ for the given set of original images $J_j(x,y)$ $(i = 1,\ \ldots\ ,\ m)$.

When equating to zero the derivative of this expression with respect to $\tilde{H}(\mathbf{k})$, one shall receive the equation for the most probable relief

$$\left[\alpha(\mathbf{k}) + \sum_j (\mathbf{k}\,\mathbf{c}_j)^2\ \tilde{g_j}^*(\mathbf{k})\ \tilde{g_j}(\mathbf{k})\ \beta(\mathbf{k})\right] \tilde{H}(\mathbf{k}) = i\sum_j \mathbf{k}\,\mathbf{c}_j\ \tilde{g_j}^*(\mathbf{k})\,\beta(\mathbf{k})\,\tilde{J}_j(\mathbf{k}), \tag{10}$$

its solution is

$$\tilde{H}_m(\mathbf{k}) = \left[\alpha(\mathbf{k}) + \sum_j (\mathbf{k}\,\mathbf{c}_j)^2\ \tilde{g_j}^*(\mathbf{k})\ \tilde{g_j}(\mathbf{k})\ \beta(\mathbf{k})\right]^{-1} i\sum_j \mathbf{k}\,\mathbf{c}_j\ \tilde{g_j}^*(\mathbf{k})\,\beta(\mathbf{k})\,\tilde{J}_j(\mathbf{k}). \tag{11}$$

This expression determines the optimum filter, which translates whole set of images $J_j(x,y)$ received as a result of the experiment into the most probable relief $H_m(x,y)$. It is a particular case of the result received in [1, 2], and comes out from it if all its photometric parameters are considered as constants.

Let the true relief be described by the function $H_0(x,y)$. Then, as a result of the experiment, we shall get according to (7), (3), (4) a set of images

$$J_j\left(x,y\right)=\int\limits_{-\infty}^{\infty}\int\limits_{-\infty}^{\infty} g_j\left(x-x',y-y'\right)\ \mathbf{c}_j\,\nabla H_0\left(x',y'\right)dx'\,dy'+N_j\left(x,y\right), \tag{12}$$

where $N_j\left(x,y\right)$ are independent realizations of noise during recording. Processing it with the optimum filter (11), we shall obtain the most probable relief for the given set of images $J_j\left(x,y\right)$, which in the frequency representation can be written as follows

$$\tilde{H}_m\left(\mathbf{k}\right)=P\left(\mathbf{k}\right)\ \tilde{H}_0\left(\mathbf{k}\right)+\sum_j Q_j\left(\mathbf{k}\right)\ \tilde{N}_j\left(\mathbf{k}\right), \tag{13}$$

where

$$P\left(\mathbf{k}\right)=\frac{\sum\limits_j\left(\mathbf{k}\,\mathbf{c}_j\right)^2\tilde{g_j}^*\left(\mathbf{k}\right)\ \tilde{g_j}\left(\mathbf{k}\right)}{\dfrac{\alpha\left(\mathbf{k}\right)}{\beta\left(\mathbf{k}\right)}+\sum\limits_j\left(\mathbf{k}\,\mathbf{c}_j\right)^2\tilde{g_j}^*\left(\mathbf{k}\right)\ \tilde{g_j}\left(\mathbf{k}\right)}, \tag{14}$$

$$Q\left(\mathbf{k}\right)=\frac{i\,\mathbf{k}\,\mathbf{c}_j\tilde{g_j}^*\left(\mathbf{k}\right)}{\dfrac{\alpha\left(\mathbf{k}\right)}{\beta\left(\mathbf{k}\right)}+\sum\limits_j\left(\mathbf{k}\,\mathbf{c}_j\right)^2\tilde{g_j}^*\left(\mathbf{k}\right)\ \tilde{g_j}\left(\mathbf{k}\right)}. \tag{15}$$

Thus, we have received the relationship between the true relief and the statistical estimation of the most probable relief, in which unknown realizations of noise $N_j\left(x,y\right)$ are present, and because no one of these realizations $\tilde{H}_m\left(\mathbf{k}\right)$ is equal to $\tilde{H}_0\left(\mathbf{k}\right)$. The difference

$$\delta\left(x,y\right)=H_m\left(x,y\right)-H_0\left(x,y\right) \tag{16}$$

is the error of determination of the relief, the random nature of which is caused by the influence of the presence into (12) realizations of noise $N_j\left(x,y\right)$ and by random nature of the required relief (which also contributes to the error beyond the filter passband). Writing down (16) as a frequency representation and substituting (3) and (12) in it, we shall get

$$\delta\left(\mathbf{k}\right)=\left(P\left(\mathbf{k}\right)-1\right)\ \tilde{H}_0\left(\mathbf{k}\right)+\sum_j Q_j\left(\mathbf{k}\right)\ \tilde{N}_j\left(\mathbf{k}\right). \tag{17}$$

From this expression one can see that two components of essentially different nature make a random error of the relief definition. The addend linearly depends on noise realizations and as a matter of fact it represents the noise, which runs through the filter and forms the relief from original images. The augend comes from the signal itself, depends linearly on it and is related to the smoothing nature of the forming filter. Both components depend on the frequency nature of the filter, and so on statistical properties of the relief and noise. However, the augend does not depend on specific realizations of noise $N_j\left(x,y\right)$, and the addend is independent on the true relief $H_0\left(x,y\right)$.

As $H_0\left(x,y\right)$ and $N_j\left(x,y\right)$ are stationary Gaussian processes, owing to (17) this concerns $\delta\left(x,y\right)$ as well. Consequently, values of $\delta\left(\mathbf{k}\right)$ for different $\mathbf{k}$ are not correlated with each other. Therefore, statistical properties of the error $\delta\left(x,y\right)$ are completely characterized by the function

$$\tilde{D}\left(\mathbf{k}\right)=\overline{\tilde{\delta}^*\left(\mathbf{k}\right)\ \tilde{\delta}\left(\mathbf{k}\right)}, \tag{18}$$

where the line means the ensemble averaging of signal and noise realizations. Substituting $\delta\left(\mathbf{k}\right)$ from (17) in this expression and considering that noise realizations $\tilde{N}_j\left(\mathbf{k}\right)$ are not correlated with the relief and with each other, we receive

$$\tilde{D}\left(\mathbf{k}\right)=\left(P\left(\mathbf{k}\right)-1\right)^2\ \overline{\tilde{H}_0^*\left(\mathbf{k}\right)\tilde{H}_0\left(\mathbf{k}\right)}\ +\ \sum_j Q_j^*\left(\mathbf{k}\right)Q_j\left(\mathbf{k}\right)\ \overline{\tilde{N}_j^*\left(\mathbf{k}\right)\tilde{N}_j\left(\mathbf{k}\right)}. \tag{19}$$

This expression represents the error spectral density $\delta\left(x,y\right)$. Substituting here $1/\alpha(\mathbf{k})$ and $1/\beta(\mathbf{k})$ instead of the average in the addend and the augend accordingly with the account of (14) and (15) we shall obtain

$$\tilde{D}\left(\mathbf{k}\right)=\frac{1}{\alpha\left(\mathbf{k}\right)+\beta\left(\mathbf{k}\right)\sum\limits_{j}\left(\mathbf{k}\,\mathbf{c}_j\right)^2\tilde{g_j}^{*}\left(\mathbf{k}\right)\tilde{g_j}\left(\mathbf{k}\right)}\,. \tag{20}$$

The function $D\left(x,y\right)$, the Fourier-image of which is $\tilde{D}\left(\mathbf{k}\right)$, represents the autocorrelation function of this error. The existence of this function is provided by that for the smooth relief the augend in the denominator (20) tends to infinity when $\mathbf{k}$ approaches infinity. As the addend in the denominator usually decreases quickly at infinity owing to the limited spatial passband of the section (what is expressed by the fast decrease of $\tilde{g}\left(\mathbf{k}\right)$ with the increase of the module $\mathbf{k}$, the function $\tilde{D}\left(\mathbf{k}\right)$ tends to zero at infinity according to the same law as the spectral density of the relief (the tending of the latter to zero at infinity is supposed because of the true relief regularity). It follows, in particular, that $D\left(x,y\right)$ has the same degree of smoothness (has the same quantity of derivative) as the autocorrelation function of the relief.

When analyzing (19) it is easy to see that, as one would expect, on a set of arbitrary frequency characteristics of the filter, which forms the relief from original images, the error dispersion $\tilde{D}\left(\mathbf{k}\right)$ reaches minimum for all $\mathbf{k}$, if this filter is determined by the equation (11). Thus, the filter (11) being optimal to the effect that gives the most probable relief is the optimum at the same time to the effect that provides the minor root-mean-square error of determination of each Fourier-component of the relief.

REFERENCES

[1] *Kornienko Yu. V., Dulova I. A., Nguyen Xuan Anh* Wiener approach to determination of optical characteristics of planet surface by photometrical observation results // Kinematics and Physics of Celestial Bodies.–1994.–**10**, N 5.–P. 69–76.

[2] *Kornienko Yu. V., Nguyen Xuan Anh* Determination of relief and radiooptical parameters of planet surface region by SAR // Radiofisika i Electronika.–1996.–N 1.–P. 129–133. (in Russian).

[3] *Diggelen I.* // B. A. N.–1951.–**11**.–P. 283–423.

[4] *Parusimov V. G., Kornienko Yu. V.* On determination of most probable relief of planet surface by its optical image // Astrometry and astrophysics.–1973.–N 19.–P. 20–24. (in Russian).

[5] *Dulova I. A., Kornienko Yu. V., Nguyen Xuan Anh, Pugach V. V.* Photometric Method for Determination of Planet Surface Relief By Means of Synthetic Aperture Radar // Abstracts of papers submitted to The 30th Microsymposium on Comparative Planetology, Moscow, Oct. 8–9, 1999, Vernadsky-Brown Microsymp. 30.–P. 15–16.

GLOBAL STRUCTURE OF THE VENUSIAN CLOUD LAYER

E. G. Yanovitskij, J. M. Dlugach

Main Astronomical Observatory, NAS of Ukraine
27 Akademika Zabolotnoho, 03680 Kyiv, Ukraine
e-mail: yan@mao.kiev.ua, dl@mao.kiev.ua

This work is based on the results obtained by the authors with colleagues during a period of more than last ten years and presented in [3–8]. The main objective of this presentation is to summarize these long-term investigations, which have resulted in discovering of *global, horizontal, and regular inhomogeneity of the Venusian cloud layer.*

INTRODUCTION

By now, an approximately four-day revolution of the upper part of the Venusian cloud layer in the near-equatorial zone (superrotation), which was found in the ultraviolet spectral range both from the ground-based [1] and space born measurements, has been studied well. In addition, a 4-day variation in the R "line strength" of the 8689 Å CO_2 absorption band was also observed [11]. Discovery of approximately the same period in variations of different characteristics of the atmosphere observed at the ends of a rather wide wavelength range from 3500 to 9000 Å, suggests that a single mechanism (a superrotation of the upper part of the cloud layer) is responsible for these oscillations. This upper layer is likely showing a global horizontal inhomogeneity. To check this hypothesis, we reviewed the results of numerous measurements of stellar magnitude m of Venus in the visible spectral range [2]. These data were processed using the standard procedure of time-series analysis [3]. A series of 70 measurements separated by approximately equal time interval, which were performed by Danjon in 1943, were found to be the most suitable for the analysis.

The autocorrelation function (Fig. 1a) and power spectrum (Fig. 1b) were calculated. One can see from the figures that the series has a distinct harmonic constituent with a period of about 3.5 days (the peak in the power spectrum corresponding to a period of 3.75 days is statistically significant at a level of 92%).The amplitude of oscillations Δm was found to be $0.^{m}03 \pm 0.^{m}01$ [3], that is, the entire range of variation of m is $0.^{m}06 \pm 0.^{m}02$.

An analysis of possible causes of the periodic variations in m [3, 4] leads to conclusion that this effect can be explained by the global asymmetry of the upper part of the cloud layer revolving due to superrotation with a period of 4 days (Fig. 2a). The corresponding velocity of zonal wind is 100 m/s. Computations [3] show that if the mean optical thickness of the cloud layer is assumed to be equal to 30, then this value for one Venusian hemisphere will be 1.41 ± 0.16 times greater than that for the opposite one.

By analysing the data of the ground-based measurements of equivalent widths of the R(0) lines for four weak CO_2 absorption bands in the near-infrared region ($\tilde{\lambda}$ = 7820, 7883, 8689, 10627 Å) [10], particular estimates of the mean optical thickness for the corresponding hemispheres of Venus were obtained in [5]. In these computations a model of the Venusian atmosphere given in Fig. 3 was used. The altitude of the lower boundary of the cloud layer was adopted to be constant and equal to ~50 km, according to the data from most of the landers. These optical thicknesses were found to be 34.4 and 24.4. The ratio 1.41 between these values is in good agreement with the above-mentioned independent estimate. The altitudes of the upper boundary of the cloud layers proved to be equal to 75.8 and 68.4 for the opposite hemispheres.

Thus, all the available results of observations confirm the existence of a global horizontal regular inhomogeneity of the Venusian cloud layer. Note that this phenomenon could not be found before from the majority of space experiments performed because of their local character, while the ground-based observations enable one to study the planet as a whole and reveal its global characteristics.

We believe that the existence of the global regular horizontal inhomogeneity of the Venusian cloud layer can shed light on such a puzzling, in many respects, phenomenon as superrotation. According to the data on distribution of wind velocity in the Venusian atmosphere with height, this velocity is of about 100 m/s near the upper boundary of the cloud layer and approaches zero near the planet's surface. However, the atmosphere is not rotating as a solid body. As a consequence, sooner or later the interior friction of the atmospheric layers would terminate the superrotation (or, at least, make the motion of atmospheric layers irregular). As far as we know, the mechanism of this regular phenomenon has not been established precisely by now.

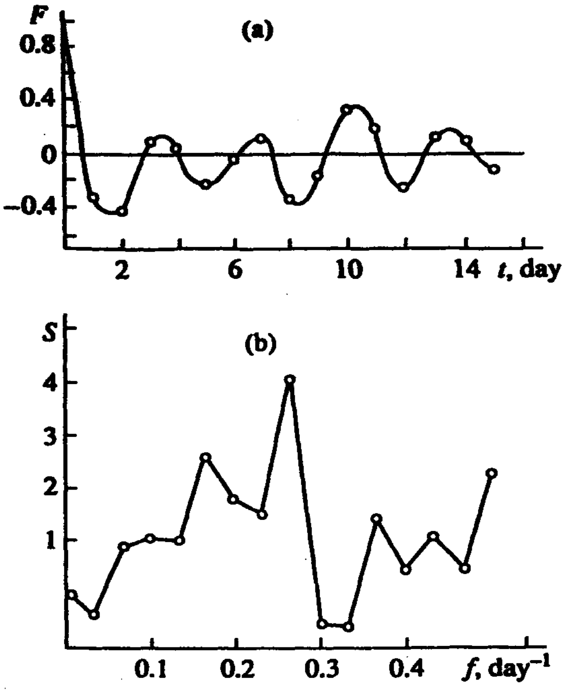

Figure 1: (a) Autocorrelation function and (b) power spectrum of the time series representing the variation in stellar magnitude of Venus

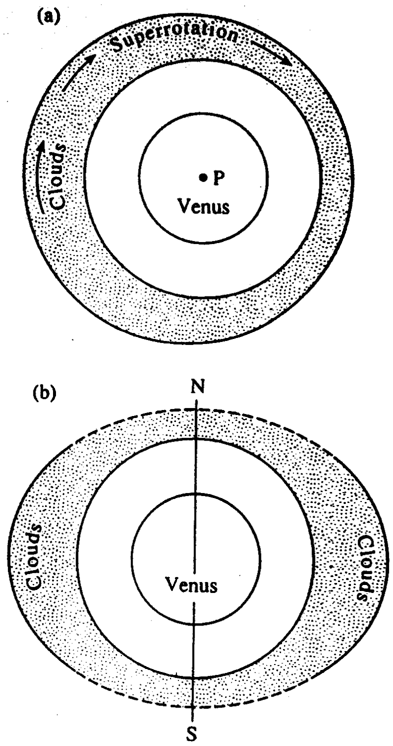

Figure 2: Schematic view of the structure of the Venusian cloud layer: (a) projection onto the equatorial plane and (b) projection onto the plane of the sky

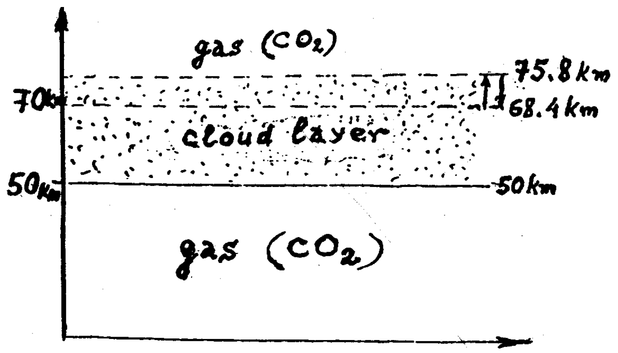

Figure 3: The applied model of the Venusian atmosphere

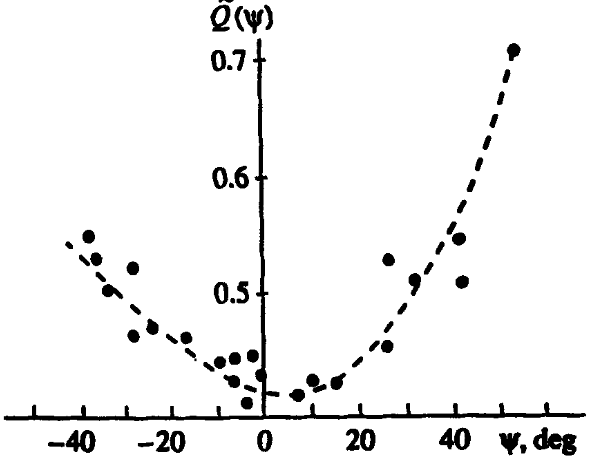

Figure 4: Distribution with latitude ψ of the observed values (dots) of the quantity $\tilde{Q}(\psi)$ for the 7820 Å CO_2 absorption band. Dashed line represents the result of fitting

We think that it is asymmetry of the cloud layer that offers a macroscopic explanation of this phenomenon. Indeed, since the mean optical thickness of an atmosphere over a planetary hemisphere oscillates with a period of about 4 days, its reflectivity (or stellar magnitude) and, consequently, the amount of light energy absorbed in visible and transformed into heat should also oscillate with the same period. On the one hand, this absorbed energy supports the superrotation. On the other hand, the periodic variation of the absorbed energy acts as a peculiar "anchor mechanism" providing this periodicity.

GLOBAL STRUCTURE OF THE CLOUD LAYER AT DIFFERENT LATITUDES

Young *et al.* [9] studied the behaviour of the R(0) lines for 7820, 7883 and 8689 Å CO_2 absorption bands at a period from September 17 to October 7, 1972. The observations were carried out almost daily (only three days were skipped). As it is mentioned above, these observations revealed an approximately four-day periodicity in the variation of the so-called relative R "line strength".

In this work not only the R "line strengths" were given for all the above absorption bands, but also, in the majority of cases, the positions of the spectrograph slit with the respect to the intensity equator or central meridian of the planet were described. This allowed us to study in [6], at least qualitatively, variations of global optical characteristics of the Venusian atmosphere both with latitude ψ and longitude ω.

As an example Fig. 4 shows the $\tilde{Q}(\psi)$ dependence for the absorption band 7820 Å (points). The dashed line in Fig. 4 represents the result of fitting. The quantity $\tilde{Q}(\psi) \sim R(\psi) \sim W(\psi)$, where $W(\psi)$ is the equivalent line width. Analogous curves were plotted for two other absorption bands. The obtained dependences [6] show that, at least up to the latitude $\psi = \pm 50°$, the value of $\tilde{Q}(\psi)$, and therefore $W(\psi)$, increases with increasing $|\psi|$, and that the optical properties of the atmosphere are highly symmetric with respect to the intensity equator.

On the other hand, the equivalent line width W decreases with increasing the optical thickness of the cloud layer [5]. There is a simple physical explanation for this effect: the cloud layer acts as a shield hindering the penetration of photons into the subcloud layer, where photons are mainly absorbed owing to the high abundance of CO_2. Thus, the curve in Fig. 4 indicates that the optical thickness of the Venusian cloud layer decreases essentially from the equator to poles. So, the structure of this layer observed from the Earth can be schematically shown in Fig. 2b.

The latitude structure of the cloud layer shown in Fig. 2b can be easily explained from thermodynamic standpoint. It is well known that the deep layers of the Venusian atmosphere are in local thermodynamic equilibrium. To keep this equilibrium, the "heat machine" of the atmosphere should rearrange the cloud layer to decrease the incoming radiation energy in the deep layers in near-equatorial zone, where the insolation of the upper layer is maximal.

Finally, a *quantitative* analysis of the R "line strength" and equivalent width W of the R(0) line in the CO_2 absorption bands at 7820 and 8680 Å was performed in [8]. It was based on the data obtained in 1972 and published in [9]. All the observations were preliminary *approximately* reduced to a wavelength of 7820 Å and then to the spectrograph slit position along the intensity equator of Venus. As well as above, we considered a two-layer model of the atmosphere (Fig. 3). The equivalent width W of the R(0) line in the CO_2 absorption band at 7820 Å was calculated for this model by the invariant imbedding method. The calculations were made for the spectrograph slit position along the intensity equator, the phase angle $\alpha = 70°$, the optical thickness τ_0 ranging from 20 to 45, two values of the single scattering albedo λ in the continuum (1 and 0.9997), and two heights h_{cl} of the upper boundary of the cloud layer (68 and 75 km). Our calculations confirm a nearly 4-day period of oscillations in the equivalent width and hence in the mean optical thickness of the cloud layer. The average peak-to-peak amplitude is proved to be equal 3-4, and its maximum value in the course of observations was about 7, which corresponded to the variation of h_{cl} from 75 to 70 km. The mean optical thickness of the cloud layer was found to vary with latitude from 37 (at the intensity equator) to 25 (at $\psi = 50°$), and this corresponded to the variation of h_{cl} from 75 to 67 km.

So, we obtained a qualitative confirmation and quantitative estimations of the global structure of the Venusian cloud layer. Result is represented schematically in Fig. 2. However, an important problem remains unsolved: what microscopic mechanism is responsible for the permanent spatial rearrangement of the cloud layer? The solution of this problem is likely to be found at the joint of such sciences as kinetics, dynamics, and thermodynamics of the atmosphere, and this would be done in future.

REFERENCES

[1] *Boyer C. H., Camichel H.* Observations photographiques de la planete Venus // Ann. Astrophys.–1961.–**24**.–P. 531–535.

[2] *Danjon M. A.* Photometrie et Colorimetrie des lanetes Mercure et Venus // Bull. Astronom. Publ. pour L'Observatoire de Paris.–1949.–**14**.–P. 315–345.

[3] *Klimenko V. M., Fomin N. N., Yanovitskij E. G.* Global variations of the optical thickness of the Venus atmosphere. I. Analysis of observations of the integrated brightness // Kinematics and Physics of Celestial Bodies.–1989.–**5**.–P. 33–38.

[4] *Fomin N. N., Yanovitskij E. G.* Global variations of the optical thickness of the cloudy layer of Venus. II. Analysis of equivalent widths of CO_2 lines // Kinematics and Physics of Celestial Bodies.–1990.–**6**.–P. 10–18.

[5] *Fomin N. N., Yanovitskij E. G.* Global variations of the optical thickness of the cloudy layer of Venus. III. Analysis of the behavior of equivalent widths of CO_2 lines for the model of the nonuniform atmosphere // Kinematics and Physics of Celestial Bodies.–1993.–**9**.–P. 30–42.

[6] *Yanovitskij E. G., Dlugach J. M.* On the effect of the width and orientation of the spectrograph slit on the observable spectrum of Venus // Kinematics and Physics of Celestial Bodies.–1995.–**11**.–P. 20–35.

[7] *Yanovitskij E. G.* Global horizontal regular inhomogeneity of the Venusian cloudy layer: a macroscopic analysis of causes of this phenomenon // Solar System Res.–1999.–**33**.–P. 452–455.

[8] *Yanovitskij E. G., Dlugach J. M.* Global horizontal regular inhomogeneity of the Venusian cloud layer: a numerical analysis of the 1972 spectroscopic observations // Kinematics and Physics of Celestial Bodies.–1999.–**15**.–P. 291–303.

[9] *Young A. T., Woszczyk A., Young L. G.* Spectroscopic observations of spatial and temporal variations on Venus // Acta Astron.–1974.–**24**.–P. 55–68.

[10] *Young L. D. G.* High resolution spectra of Venus – A review // Icarus.–1972.–**17**.–P. 632–658.

[11] *Young L. G., Young A. T., Young J. W., Bergstralh J. T.* The planet Venus: a new periodic spectrum variable // Astrophys. J. Lett.–1973.–**181**.–P. L5–L8.

A NEW METHOD FOR REGISTRATION OF OSCILLATIONS IN ATMOSPHERES OF JOVIAN PLANETS

A. P. Vid'machenko

Main Astronomical Observatory, NAS of Ukraine
27 Akademika Zabolotnoho, 03680 Kyiv, Ukraine
e-mail: vida@mao.kiev.ua

Our analysis shows that a change of gas and aerosol vertical speed in the range of $w = (10-50)$ cm/s determines the volume of top layers of visible clouds of giant planets, and therefore, may allow to find the reflectance characteristics of an observable cloud layer. In the presence of the certain factors, causing a change of a value of an air vertical moving speed as well as direction of such moving, it will modulate processes of cloudy formation and/or their destruction. In this connection we assume that the fluctuation processes of cloudy creation and their disintegration can serve as a preferable method for registration of possible giant planetary atmosphere oscillations.

INTRODUCTION

Vorontsov, Zharkov and Lubimov [16] were the first who predicted theoretically that the atmospheres of Jupiter and other giant planets can oscillate just like the solar photosphere. In [7, 8, 11] a significant work was performed to recalculate oscillation periods, using two different approaches to the technique of calculations and the newest models of the internal structure of the giant planets [4].

Detection and continuous observation of the oscillations in planetary atmospheres would be a very powerful tool for study of internal structures of these planets. Theoretical (analytic) researches showed that the analysis of the pressure modes of low orders allows to determine the radius of planetary nucleus. Really, the periods of free oscillations of the giant planets are sensitive to their internal structure. To be "zond" for testing the internal planetary structures these waves should exist during a time as long as several oscillation periods. In this case these waves must overcome the attenuation and have a sufficiently large amplitude to be registered as atmospheric line shift by using:

1) the Doppler displacement of spectral lines [12];
2) temperature oscillation during a geterodin observation of infrared hydrocarbon's bands [11];
3) planetary brightness oscillations in spectral range 390–420 nm offered below.

The P-modes of Jupiter's atmosphere have been most intensively studied during the last ten years. Some of them may have significant amplitudes near the upper edge of the visible cloud layer. Each oscillation mode produces perturbations of the equilibrium density, pressure and other atmospheric parameters. It was found [9] that in the upper troposphere some of propagating $P - modes$ produce a vertical air mass shift with a velocity about $w = (10–30\,\mathrm{cm/s})$.

FUNDAMENTALS OF THE METHOD

Several cloud layers are known to be present in the Jovian atmosphere. The Jupiter's tropospheric clouds consist of an upper layer of ammonia clouds at a 200–300 mbar level, and of a deeper water layer located at a 2–5 bar level and others. It is known that elementary processes are extremely important in formation of cloudiness. Microphysical properties of the Jovian clouds were studied by Carlson *et al.* [1]. It was found that the value of atmospheric vertical velocity, temperature profile and some other parameters of the clouds determine their dynamical properties, and determine the height of the top of a cloud and the maximal updrafts. They are the reason of cloud's creations also. Therefore, studying dynamic and thermal atmospheric structure we can study the law of occurrence and evolution of cloudy structures. On the other hand, studying cloud fields and distribution of their microphysical parameters we can obtain certain information about the degree of turbulization of a layer, intensity of vertical and horizontal movements of gas and aerosol, radiation mode, *etc.*

Ibragimov [5], Solodovnic [13], Yair *et al.* [17] and some other authors have shown that in atmospheres of giant planets all the macrostructurian parameters of water and ammonia condensation clouds are rather sensitive to dynamic factors of the atmospheric layer studied. The computations show that increase of the vertical speed of the atmospheric gas transfer results in the growth of volume both of water and ammonia cloudiness [6]. But the influence of these atmospheric factors on deeper water and upper ammonia clouds are essential distinguished [5]. So, inside a water cloud both the concentration of the arising cloudy particles and their average sizes are more sensitive to the turbulent atmospheric fluctuations. But in an ammonia cloud the change of the value and direction of the vertical velocity gives considerable variations of the number density of arising cloudy particles and their average sizes. Our computation has shown that increase of w results in growth of size and amount of condensed cloud particles at all altitudinal levels (hence, to increasing the integral characteristics of the observable cloudiness).

Thus, any change of the gas and aerosol vertical velocity determines significantly the volume of the top layer of visible cloud of the giant planets. So, it determines visible reflection characteristics of an observable cloudy layer. Therefore, existence of the certain factors changing the value and direction of vertical motions in atmosphere, will modulate processes of formation and/or destruction of clouds.

From the general equations of meteorology and approximate dynamic and kinematic evaluations of physical parameters of atmosphere [10] it follows that clouds in atmospheres of the giant planets are to be formed in the presence of ordered movements of gaseous masses with a vertical speed from units up to some hundreds of cm/s [5, 17].

In the general case, for Jupiter and Saturn the geometrical thickness of a cloud changes with value and direction of the vertical velocity of atmospheric masses:

1) the geometrical thickness of a cloud increases with increasing w;

2) in the most of modeling cases the specific content of condensed phase in clouds decreases when the sign of the vertical speed is changing, *i.e.*, their disintegration takes place;

3) if there are atmospheric movements with a $w = -(10\text{–}15)$ cm/s (falling air masses), a gradual slowing down of cloud growth is observed initially, and only later a cloud development is replaced by its disintegration;

4) if $w = 20$ cm/s the cloud formation or its disintegration begins practically at once when the sign of vertical speed changes; the time of cloud occurrence and/or beginning of its disappearance decreases with increase of the air mass vertical speed.

Since the Jupiter and Saturn tropospheres have a rich chemical composition [5, 17], a change of some component (especially water, methane, and ammonia), which are condensed at certain levels in atmosphere, results in variation of brightness of the cloud layer. Therefore, if a periodic variation of the vertical speed produced by oscillations of planetary atmospheres is present, we should observe periodical variations both of reflection and absorption of visible cloud layer too.

We have evaluated the changes of gas and aerosol optical parameters for Saturn's atmosphere. For our calculations we used the multilayer multiple scattering program developed by Dlugach [2]. We adopted the following assumption about the upper layers of Saturn's atmosphere: (1) aerosol scattering plays the dominant role in the process of radiative transfer; (2) cloud particles are nonabsorbing homogeneous spheres and the observed absorption is due to gas; (3) in spectral range of 300–600 nm the reflected radiation originates in the part of atmosphere, which may be represented by two homogeneous layers: the upper one is an optically thin gas layer and the lower one is a gas-aerosol semi-infinite medium.

For Saturn's Equatorial Zone at a wavelength of 316 nm the calculations have shown that an air mass lifting with a vertical speed $w = 30$ cm/s results in absolute reflectivity increasing equal to 0.0035 (for its average value of 0.200) in a time around two hours. At a wavelength of 600 nm for EZ this change is equal only to 0.00007 for its average value of 0.550. At the same time, our estimations of the spectral transmission coefficients for the Earth's atmosphere [3] as well as our observations concerning changes of spectral absolute reflectivity of different Saturn's disk features permit us to conclude that the observations in spectral interval 390–420 nm are the most preferable for registration of possible Saturn's atmosphere oscillations. Just for these wavelengths the spectral transmission coefficients of the Earth's atmosphere do not already deform a useful signal from planets so strongly (as it occurs in ultraviolet at 316 nm), so the light flux from the planet becomes high enough for its reliable registration by the photometrical method with photon counting.

As it has been shown by our calculations, for Saturn's EZ at 400 nm an air mass lifting with a vertical speed $w = 30$ cm/s can give absolute reflectivity increasing of 0.001 for its average value of 0.200 (the amplitude of these variations is about 5 mma) approximately in two hours. Analogously, for Jupiter's EZ this increment is equal to 0.0012 for an average value of 0.390 (the amplitude is about 3.3 mma). In this connection we assume that the fluctuation processes of cloud creation and disintegration can serve as a preferable method for registration of the optical characteristic of the oscillations in a planetary atmosphere, especially for the registration of possible free oscillations of a giant planet atmosphere. In the considered spectral range obtained values of changes of planetary atmosphere brightness [15] are quite accessible for their registration using the photon counter at Mount Maidanak Observatory [14].

REFERENCES

[1] *Carlson B. E., Rossov W. B., Orton G. S.* Cloud microphysics of the giant planets // J. Atmos. Res.–1988.–**45**.–P. 2067–2081.

[2] *Dlugach Zh. M.* Reflection of the light by multilayer planetary atmosphere // Astron. Vestnik.–1982.–**17**, N 2.–P. 234–239.

[3] *Dlugach Zh. M., Morozhenko A. V., Yanovitskiy E. G., Vid'machenko A. P.* Investigations of the optical properties of Saturn's atmosphere carried out at the Main astronomical observatory of the Ukrainian Academy of sciences // Icarus.–1983.–**54**, N 2.–P. 319–336.

[4] *Hubbard W. B., Marley M. S.* Optimized Jupiter, Saturn and Uranus models // Icarus.–1989.–**78**, N 1.–P. 102–118.

[5] *Ibragimov K. Yu.* Numerical modeling of stratifirm clouds in atmospheres of the planets-giants.–Alma-Ata: Nauka, 1990.–237 p. (in Russian).

[6] *Ibragimov K. Yu., Kirienko G. A., Solodovnic A. A.* Modeling of multilayer clouds in the Jovian atmosphere // Astron. Vestnik.–1986.–**20**, N 3.–P. 228–234.

[7] *Marley M. S.* Nonradial oscillation of Saturn // Icarus.–1991.–**94**, N 3.–P. 420–435.

[8] *Marley M. S., Hubbard W. B.* Low degree nonradial oscillation spectre of the Jovian planets // Bull. Amer. Astron. Soc.–1988.–**20**.–P. 870.

[9] *Marley M. S., Hubbard W. B.* Thermodynamics of dense molecular hydrogenhelium mixtures at high pressure // Icarus.–1988.–**73**, N 3.–P. 536–544.

[10] *Matveev L. T.* General meteorology.–Moscow: Gidrometeoizdat, 1980.–568 p. (in Russian).

[11] *Mosser B.* The pressure mode oscillation spectrum of a rotating gaseous sphere: Application to Jupiter // Icarus.–1990.–**87**, N 2.–P. 198–209.

[12] *Severnyi A. B.* Some problems in the Solar physics.–Moscow: Nauka, 1988.–288 p. (in Russian).

[13] *Solodovnik A. A.* Peculiarities of formation of multiplier cloudiness in the atmospheres of Jupiter and Saturn // Kinematics and Physics of Celestial Bodies.–1985.–**1**, N 6.–P. 24–28.

[14] *Vid'machenko A. P.* Brightness variations of celestial objects in astronomical observations at the Maidanak mountain // Kinematics and Physics of Celestial Bodies.–1994–**10**, N 5.–P. 62–68.

[15] *Vid'machenko A. P., Klimenko V. M., Morozhenko A. V.* The transparency of Earth's atmosphere on Mount Maidanak at the autumn-winter period of 1977-1978 // Astromet. Astrophys.—-1979.–**39**.–P. 84–87. (in Russian).

[16] *Vorontsov S. V., Zharkov V. N., Lubimov V. M.* The free oscillations of Jupiter and Saturn // Icarus.–1976.–**27**, N 1.–P. 109–118.

[17] *Yair Y., Levin Z., Tzivion S.* Water-Cumulus in Jupiter's Atmosphere: Numerical Experiments with an Axisymmetric Cloud Model // Icarus.–1992.–**98**, N 1.–P. 72–89.

PHOTOMETRIC AND POLARIMETRIC OPPOSITION EFFECTS OF SIMULATED PLANETARY REGOLITHS

Yu. Shkuratov[1], **A. Ovcharenko**[1], **O. Rack**[1], **V. Rosenbush**[2], **R. Nelson**[3], **W. Smythe**[3], **K. Muinonen**[4], **J. Piironen**[4], **S. Kaasalainen**[4], **P. Helfenstein**[5]

[1] *Kharkiv Astronomical Observatory, 35 Sumska St., 61022 Kharkiv, Ukraine*
e-mail: `Shkuratov@astron.kharkov.ua`

[2] *Main Astronomical Observatory, NAS of Ukraine, 27 Akademika Zabolotnoho, 03680 Kyiv, Ukraine*

[3] *Jet Propulsion Laboratory, 4800 Oak Grove Drive, Pasadena, CA 91101, USA*

[4] *Helsinki Astronomical Observatory, FIN-00014 U. Helsinki, Finland*

[5] *Center for Radiophys. and Space Res., Cornell University, Ithaca, NY 14853-6801, USA*

We present results from simultaneous photometric and polarimetric laboratory measurements of samples that have different microcrystalline structures and albedos. The studies were conducted using the Kharkiv Observatory laboratory polarimeter at a wavelength of 0.65 μm and phase angles covering $0\overset{\circ}{.}1 - 3\overset{\circ}{.}5$. This polarimeter was calibrated with a comparable instrument at JPL NASA. Surfaces formed by smoked deposits of MgO and carbon soot show similar prominent negative branches of polarization with minima near $2\overset{\circ}{.}0$ and depths near 1%, despite the fact that they have extremely different albedos and brightness opposition effects. The results for carbon soot allow to predict a narrow negative polarization branch for some dark asteroids. A strong particle-size dependence of the negative polarization parameters for powdered dielectric surfaces was found. Particle-size separates of Al_2O_3 (0.1, 0.5, 1, 7, and 12 μm) with almost the same albedo were studied. For grain larger than 1 μm the depth of negative polarization does not exceed 0.2%. It is maximal (0.8%) for the 0.1 and 0.5 μm fractions. The angular width of the opposition spikes of all the separates are very similar. These data are important to interpret photometric and polarimetric opposition effects of icy satellites of outer planets and bright asteroids.

INTRODUCTION

Many bright airless Solar System bodies exhibit two phenomena observed near opposition: opposition brightening and negative linear polarization. These effects are observed over both narrow ($< 2°$) and wide ($2°$–$20°$) ranges of phase angles. Photometric and polarimetric opposition effects, both with very narrow angular widths, are observed in Saturn rings, some icy satellites of outer planets (*e.g.*, Europa, Titania), and also bright asteroids. The photometric and polarimetric opposition effects accompany each other in laboratory experiments as well as in planetary observations. Characteristic opposition effects are illustrated by photometric observations of Harris *et al.* (1989) and polarimetric measurements (Rosenbush *et al.*, 2000) of the asteroid 64 Angelina (see Figs. 1 and 2). To date, most planetary studies suggest that the strength of the photometric opposition effect and the depth of the negative branch of polarization are correlated with one another – surfaces with strong photometric opposition effects often exhibit larger negative polarizations than surfaces with weak photometric opposition effects. Their simultaneous occurrence is predicted by coherent backscatter enhancement theory (*e.g.*, Shkuratov, 1985; Muinonen, 1990; Mishchenko, 1993).

Most laboratory studies of the photometric and polarization opposition effects cover a wide range of phase angle with the minimum angle extending down to a few degrees in phase. However, measurements of both effects at phase angles smaller than a few degrees are very rare. For instance, polarimetric measurements at phase angles $< 1°$ were first carried out by Lyot (1929), but included only a sample of smoked deposit of MgO. To better understand the photometric and polarimetric opposition effects and to interpret available telescopic and anticipated (*e.g.*, Cassini) spacecraft observational data, more laboratory measurements of regolith simulants are necessary. In this paper we present first results of such measurements for samples that exhibit different albedos and microstructure.

EQUIPMENT AND SAMPLES

To study the phase dependence of the degree of linear polarization from light scattered by samples of simulated regolith, we used the Kharkiv Astronomical Observatory laboratory photometer-polarimeter (Shkuratov *et al.*, 1999). This instrument allows us to measure the reflectance and degree of linear polarization at phase angles covering $\alpha = 0^\circ\!.1 - 3^\circ\!.5$. In this study, we used only one spectral band 0.65 μm. All measurements were done at a standard observation/illumination geometry such that the samples were viewed by the detector at normal emission angle and motion of the light source changes the incidence and phase angles. Sample albedo was determined relative to a Halon reflectance standard at $\alpha = 2^\circ$. The estimated accuracy of our measurements is 0.05%, including random and systematic errors. The Kharkiv photometer-polarimeter was calibrated against a comparable JPL NASA instrument (Nelson *et al.*, 1999). Table 1 provides a description of our laboratory samples. We studied smoked-deposits of MgO and carbon soot (*i.e.*, samples with extremely different albedo), ultra-disperse powdered SiO_2, and particulate size-separates of Al_2O_3 powder. Results of our preliminary studies are presented in Figures 1 and 2.

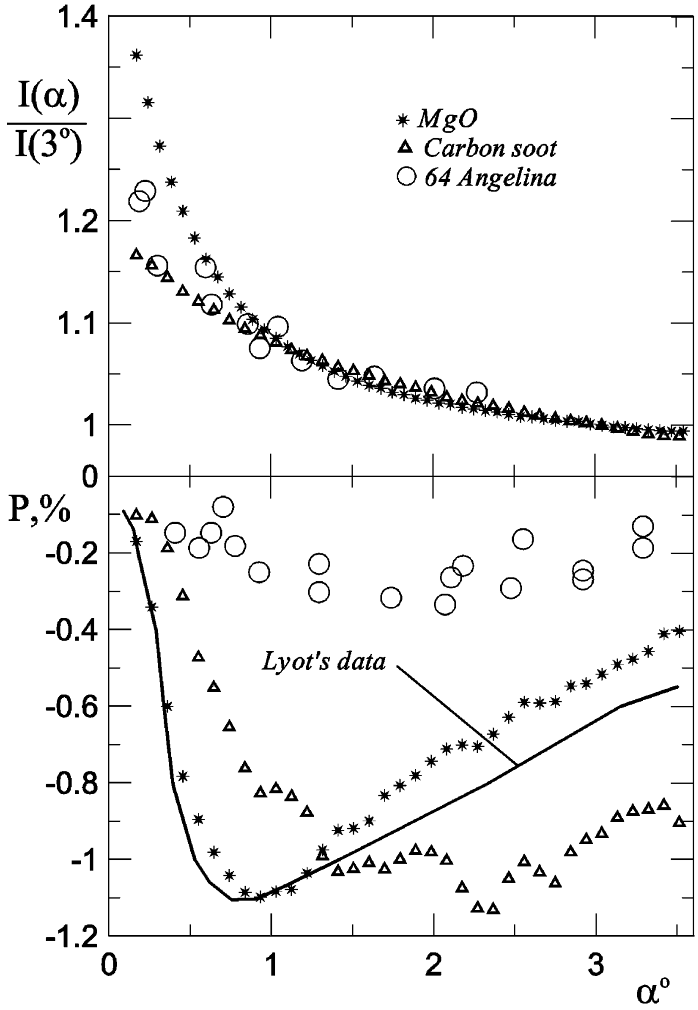

Figure 1: The photometric and polarimetric opposition effects for the asteroid 64 Angelina (the opposition spike is obtained after removal of a linear component of the phase curve) and for carbon soot and MgO smoked deposits. Lyot's (1929) data are presented by line

RESULTS AND DISCUSSION

Figure 1 shows the phase dependences of brightness and the degree of linear polarization for smoked surfaces that exhibit different albedo, MgO and carbon soot. The strengths of the photometric opposition effects clearly depend on albedo: The opposition spike for bright MgO is about 20% stronger than for dark soot deposits. Because coherent-backscatter enhancement relies upon the presence multiply-scattered light, the observed behavior is consistent with its occurrence in our samples. However, in this example, photometric and polarimetric effects

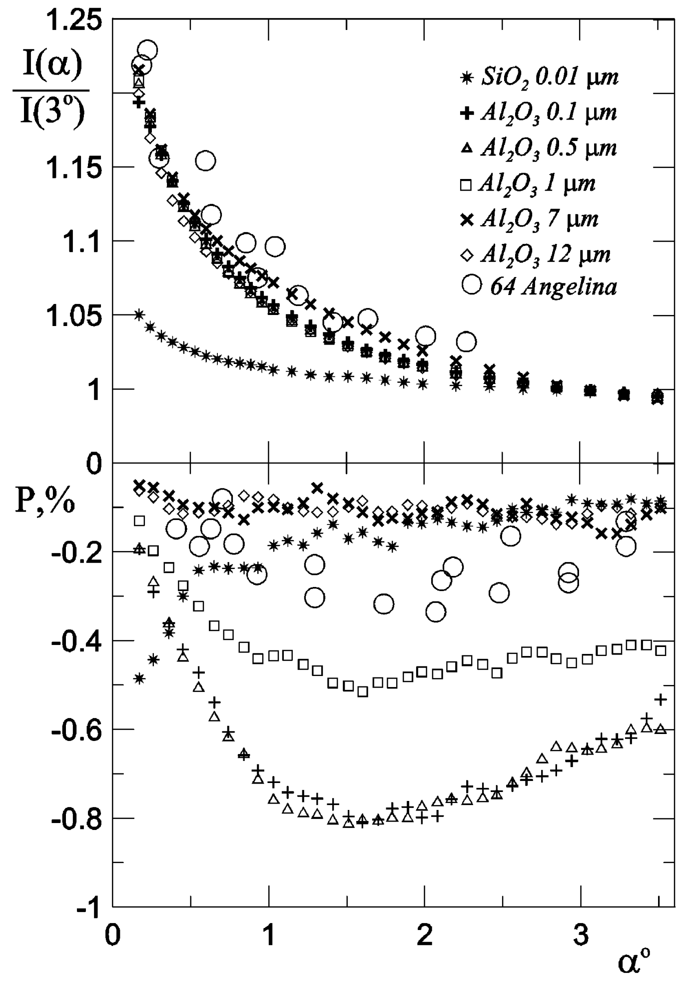

Figure 2: Phase dependence of brightness and polarization degree for nanodisperse powder of SiO_2 and for Al_2O_3 separates with different size of particles. Data for the asteroid 64 Angelina are also given here

are not strictly correlated with one another, in contrast to what might be expected if coherent-backscatter is responsible for the negative polarization and the brightness opposition effects. Figure 1 shows that while both samples clearly exhibit different brightness opposition surges they each have similar negative polarization branches. The results for carbon soot allow to expect a narrow negative polarization branch for some dark asteroids, if they have fluffy submicron structure of the surface. Figure 1 also allows a comparison of our measurements of smoked-MgO to those of Lyot; the dependences are almost the same. Some mutual deviations are likely related to differences in preparation of the samples. Note also that the depth of the negative branch of polarization for the samples and asteroid 64 Angelina is very different.

Figure 2 shows the photometric and polarimetric behavior of SiO_2 powder with very small particles that are only a few nanometers in size. This sample exhibits an extremely narrow negative polarization branch. While the plot can be seen to approach a definite minimum as phase angle decreases to 0.°1, our experimental measurements do not extend downward to small enough phase angles to observe the polarization as it becomes zero. The nanodisperse SiO_2 powder appears to exhibit no significant brightness opposition spike over our measured phase angle range.

A strong particle-size dependence in the negative polarization branch for powdered dielectric surfaces was found (see Figure 2). Particle-size separates of Al_2O_3 (0.1, 0.5, 1, 7, and 12 μm) with almost the same albedo were studied. For grain-sizes larger than 1 μm the depth of the negative polarization does not exceed 0.2%. It is maximal (near 0.8%) for the 0.1 and 0.5 μm fractions. The brightness phase dependencies of the samples are remarkably similar. The angular-width of the opposition spike is slightly broader for the 4 μm fraction than for the other size-fractions. Our measurements of Al_2O_3 particle-size separates thus provide an additional example

Table 1: Characteristics of samples

name	albedo at 2°, %	particle size, μm
MgO	98	< 1
soot	3	< 1
SiO_2	98	~ 0.01
Al_2O_3	100	~ 0.1
Al_2O_3	100	~ 0.5
Al_2O_3	97	~ 1
Al_2O_3	95	~ 7
Al_2O_3	95	~ 12

for which the photometric and polarimetric opposition effects are not strictly correlated. Among measured samples, only the 1 μm fraction of Al_2O_3 yields both photometric and polarimetric opposition effects that are more or less mutually comparable to those of 64 Angelina. We note that qualitatively similar results with polarimetry of Al_2O_3 powders have been obtained by Geake and Geake (1990). However, they were able to measure only at phase angles larger 1° and they did not study the photometric properties of the samples.

In summary, we have found laboratory examples of samples whose photometric and polarimetric behaviors do not strictly follow to the coherent backscatter enhancement model. In particular, the photometric and polarimetric opposition effects are not neither correlated among bright and dark samples of the same particle microstructure structure and in the case of particle-size separates of Al_2O_3.

CONCLUSION

1. We have found examples for which both photometric and polarization opposition effects are not strictly correlated to one another, contrary to the predictions of coherent-backscatter theory. In particular, MgO and carbon soot smoked-deposits have closely matching negative polarization branches, but exhibit different photometric behavior at small phase: a prominent opposition spike for MgO and comparatively small surge in the case of soot.

2. Surfaces composed of particles having a characteristic structure scale on the order of a wavelength of light reveal the negative polarization at the range $0\overset{\circ}{.}1 - 3\overset{\circ}{.}5$. This effect disappears at larger structure scales. The negative polarization branch is transformed to a very asymmetric one for fluffy surfaces consisting of nanometer-sized (Rayleigh) particles and the brightness opposition spike becomes too narrow to be measured in our experiments ($< 1°$).

REFERENCES

[1] *Geake J., Geake M.* A remote-sensing method for subwavelength grains on planetary surfaces by optical polarimetry // Mon. Notic. Roy. Astron. Soc.–1990.–**245**.–P. 46–55.

[2] *Harris A., et al.* Phase relations of high albedo asteroids: the unusual opposition brightening of 44 Nysa and 64 Angelina // Icarus.–1989.–**81**.–P. 365–374.

[3] *Lyot B.* Recherches sur la polarisation de la lumiere des planetes et de queldues substances terrestres // Ann. Obs. Meudon.–1929.–**8**.–P. 1–161.

[4] *Mishchenko M. I.* On the nature of the polarization opposition effect exhibited by Saturn's rings // Astophys. J.–1993.–**411**.–P. 351–361.

[5] *Muinonen K.* Light scattering by inhomogeneous media: backward enhancement and reversal of polarization // PhD-thesis.–University of Helsinki.–1990.

[6] *Nelson R., Hapke B., Smyth W., et al.* The reflectance phase curves at very small phase angle: a comparative study of two goniometers // Lunar and Planet. Sci.–30th. Abstract N 2068.–LPI Houston, 1999.

[7] *Rosenbush V. K., Kiselev N. N., Jockers K., et al.* Optical polarimetry of the Galilean satellites, Iapetus, and 64 Angelina near opposition // this issue.–P. 227–230.

[8] *Shkuratov Yu. G.* On the origin of the opposition effect and negative polarization for cosmic bodies with solid surface // Astron. Circular.–Moscow: Shternberg State Astron. Inst., 1985.–N 1400.–P. 3–6.

[9] *Shkuratov Yu., Kreslavsky M., Ovcharenko A., et al.* Opposition effect from Clementine data and mechanisms of backscatter // Icarus.–1999.–**141**.–P. 132–155.

WHAT PHYSICAL PROPERTIES OF NEAR–EARTH ASTEROIDS TELL US ABOUT SOURCES OF THEIR ORIGIN?

D. F. Lupishko[1], M. Di Martino[2], and T. A. Lupishko[1]

[1] *Astronomical Observatory of Kharkiv National University*
35 Sumska St., 61022 Kharkiv, Ukraine
e-mail: lupishko@astron.kharkov.ua

[2] *Astronomico Osservatorio di Torino*
10025 Pino Torinese, Italy
e-mail: dimartino@to.astro.it

It is generally recognized that main-belt asteroids (MBAs) and nuclei of extinct comets are two main sources for the near-Earth asteroids (NEAs) replenishment. Theoretical studies of NEA dynamics and numerical modelling of their orbital motions showed that so-called resonance mechanism for supplying NEAs is quite sufficient to sustain this population. The physical properties of NEAs and MBAs (and partly of comet nuclei) were compared to understand what the physical properties of NEAs can tell us about sources of their origin. The results of the comparison are given in this paper. The principal results of such a comparative analysis can be reduced to the following. All the NEAs have the small sizes, almost the same variety of their taxonomic classes and mineralogy, predominance of differentiated assemblages among them, approximately similar shape and rotation, optical properties and surface structure as compared to those of MBAs. All these conclusions clearly indicate that the main asteroid belt is the principal source of NEA, and comet nuclei contribution to the total NEA population does not exceed 10%. The NEAs 2100 Ra-Shalom, 2101 Adonis, 2201 Oljato, 2212 Hephaistos, 3200 Phaethon, 3552 Don Quixote and 4015 Wilson-Harrington are the most probable candidates for the cometary origin.

INTRODUCTION

According to available estimates a median lifetime of Aten-Apollo-Amor asteroids in unstable orbits, which approach or cross the Earth orbit, is relatively short and approximately equal to 10^6–10^7 years. As far as the population of Earth-approaching asteroids still exists it appears to be continuously supplied by new objects. It is generally recognized that there are two sources of near-Earth asteroids (NEAs) replenishment: main-belt asteroids (MBAs) and dormant or extinct cometary nuclei. Recent studies certainly suggest that the main asteroid belt is the dominant source of NEAs, *i.e.*, the near-Earth asteroids are the fragments of MBAs coming to the current orbits through collisional processes and chaotic dynamics. These results have been obtained mainly on the basis of theoretical studies of the NEA dynamics and numerical simulations of their orbital motions [3]–[6], [14].

In this study we tried to compare all the relevant physical properties of near-Earth and main-belt asteroidal populations and partly of cometary nuclei to extract the information on the sources of NEA origin.

TAXONOMY AND MINERALOGY

Almost all taxonomic classes of main-belt asteroids are presented among the classified NEAs except one or two low-albedo classes that are located in the outer part of the main belt. One of the important results of the NEA taxonomy is quite different relative abundance of two most numerous classes C and S. About a half of the classified near-Earth objects belongs to the S-class and the number of S-types exceeds that of low-albedo types by a factor of three, while among the MBAs the ratio is inverse, about 1:5 [20]. Taking into account the results of modelling of the selection effects in observations of both NEAs and MBAs [13] Lupishko and Di Martino [11] showed that the relative number of C and other low-albedo objects among the NEA population is approximately 2.5 times less than in the main asteroid belt. This could be an important constraint for the possible sources of NEA replenishment. The most immediate explanation could be that NEAs are coming preferentially from the inner regions of the main belt where the relative abundance of C and other low-albedo asteroids is much lower.

Most NEAs for which mineralogical information exists represent differentiated assemblages. Among them there are objects with monomineral silicate composition (1915 Quetzalcoatle, 3199 Nefertity) and purely metalic ones (6178 1986 DA). The variety of taxonomic classes among NEAs reflects the diversity of their surface mineralogy and an overall analogy with the MBAs. Taking into account their small sizes, one might infer that they are fragments of much larger differentiated bodies.

SIZE, SHAPE AND ROTATION

Size, shape as well as rotation of asteroid are the fundamental characteristics related to its origin and collisional history. There are size estimates for all discovered NEAs, but more or less exact determinations of their diameters have been obtained for less than 10% of those objects. Amor-asteroid 1036 Ganymed (D = 38.5 km) is the largest among NEAs, two other asteroids (433 Eros and 3552 Don Quixote) are of about 20 km in size, all others are of about or less than 10 km and approximately 3/4 of them are less than 3 km. The smallest known NEAs are of about 3–6 m across. The absence of NEA-objects larger than 40 km in diameter is usually interpreted as an evidence that near-Earth objects are not primordial, but they are collisional fragments of larger MBAs.

Table 1 contains the mean values of observed and corrected (reduced to 0° phase angle) asteroid amplitudes for NEAs and small-sized MBAs. Almost the same corrected mean amplitudes for both the NEAs and small-sized MBAs are an indication of the indentical shape elongations of these asteroid populations on the average. An irregular shape of an asteroid can be approximated by a three dimensional ellipsoid with an $a > b > c$ axial ratio. In this case, the mean light curve amplitude of 0.28–0.29 mag is characterized by an axial ratio $a : b = 1.3$. The data available show that comet axial ratios usually lie in the range from 1.6 to 2.5, that is, cometary nuclei have more elongated shapes than NEAs (see [7, 12]).

Table 1: Mean values of asteroid amplitudes and rotation rates

Population	$\bar{D}$, km	Observed amplitude, mag	N	Reduced amplitude, mag	Rotation rate, rev/day	N
NEAs	2.7 ± 0.4	0.53 ± 0.04	113	0.29	4.80 ± 0.29	119
MBAs ($D < 12$ km)	6.8 ± 0.3	0.35 ± 0.03	102	0.28	4.34 ± 0.23	100
MBAs ($D > 130$ km)	185.8 ± 0.9	0.22 ± 0.01	100	0.19	2.90 ± 0.12	100

The rotation rate distributions of the NEAs and comparable sized MBAs are characterized by close mean values of the rotation rates as well as their standard deviations (see Table 1). At the same time the mean rotation rate and reduced amplitude of large main-belt asteroids (Table 1, the last line) differ essentially. Thus, we can conclude that on the average NEAs as well as the comparable sized MBAs rotate in a similar manner. It should be added that according to the data available cometary nuclei rotate much slower than NEAs [1, 7]. Analyzing the rotation periods of 47 cometary nuclei Whipple [19] found out that the periods of only four comets lie in the range of 3.9 to 5.7 hrs, the rest of cometary nuclei rotate slower, thereby the mean value of comet rotation periods (15.0 hrs) more than two times exceeds the mean value for NEAs.

OPTICAL PROPERTIES AND SURFACE STRUCTURE

NEAs have relatively small sizes and, hence, relatively small masses and so the gravitational forces that determine compactness of the particles in the surface layer. Due to their location NEAs also differ from MBAs in terms of cratering rates and solar wind flux, both of which affect asteroid surfaces. Therefore, one may expect that if distinctions in optical properties and surface structure between two asteroid populations really exist they are even more prominent between NEAs and large MBAs.

Table 2 lists the mean values of optical parameters of NEAs and MBAs: the polarimetric and radiometric albedos, color indexes, phase coefficients β_V and polarimetric parameters such as the depth of negative polarization $P_{\min}$, the polarization slope h, and the inversion angle $\alpha_{\rm inv}$. As it can be seen the NEA polarimetric and radiometric albedos are somewhat higher than those of MBA, though the distinctions lie in the limits of accuracy. If these distinctions really exists, they may be caused by smaller contamination of S-type NEA surfaces by material of low-albedo asteroids, as compared with the situation in the main belt where relative abundance of low-albedo asteroids (as note above) is more than that among NEA population by a factor of 2.5. The difference between the mean radiometric albedos can be explained using the standard thermophysical model for some NEAs, which are the best fit for so-called "rotating" model as far as the standard (nonrotating) thermal model often overestimates albedos of "nonstandard" asteroids. In general, the whole range of NEA geometric albedos is in complete agreement with that of MBAs.

Table 2: Mean optical parameters of S-type asteroids (V-band)

Parameter	NEAs	N	MBAs ($D > 100$ km)	N
Albedo polarimetric	0.183 ± 0.011	9	0.177 ± 0.004	28
Albedo radiometric	0.190 ± 0.014	23	0.166 ± 0.006	27
U-B (mag)	0.445 ± 0.013	30	0.453 ± 0.008	28
B-V (mag)	0.856 ± 0.013	31	0.859 ± 0.006	28
β (mag/deg)	0.029 ± 0.002	9	0.030 ± 0.006	18
$P_{\min}$ (%)	0.77 ± 0.04	3	0.75 ± 0.02	28
h (%/deg)	0.098 ± 0.006	9	0.105 ± 0.003	23
$\alpha_{\rm inv}$ (deg)	20.7 ± 0.2	6	20.3 ± 0.2	18

The rest of the optical characteristics in Table 2 are basically the same for both asteroid samples. Since the near-Earth and main-belt asteroids have on the average the same albedos and similar surface composition, a strict similarity of their phase coefficients and polarimetric parameters suggests that at least majority of NEAs should have the same surface porosity and roughness at the scale length of submicrons [9].

Thus, it can be concluded that NEA surfaces display the same optical properties as those of MBAs, and it seems that they possibly have the same microstructure.

One of the characteristics of an asteroid reflecting surface is its radar albedo, which is related to a bulk density, that is, to the density and porosity of the surface material. The available data show that the mean radar albedos of small NEAs and large MBAs (S-type), in spite of the fact that they differ in sizes by a factor 25–30, are practically the same (0.161 ± 0.020 for NEAs and 0.147 ± 0.011 for MBAs). It can be explained by the similar composition (mineralogy) and the bulk density of surface materials of both asteroid populations.

CONCLUSIONS

The small sizes of NEAs, almost the same diversity of their taxonomic classes and reflectance spectra, the relative abundance of C and S objects, the same average shape and rotation, as compared to those of MBAs, clearly indicate that the main asteroid belt is the principal source of NEA population replenishment. On the other hand, the identification of some asteroids (and among them an Apollo asteroid 4015 Willson-Harrington) with extinct or dormant comets supports cometary origin for some of them. Thus, there is no doubt that some of NEAs may be extinct cometary nuclei, although the estimates of their abundance are controversial. Öpik [15] believed that most NEAs are extinct cometary nuclei. Levin and Simonenko [10] argued against cometary origin for most NEAs, because the latter are parent bodies of the meteorites which could not be formed in cometary nuclei. Wetherill [18] estimated that extinct comets could provide about 40% of NEAs, and Binzel *et al.* [1] constrained the fraction of cometary nuclei between 0 and 40% of total NEA population. Tedesco and Gradie [16] concluded that extinct cometary nuclei are rare among NEAs, if they exist at all.

The candidates for cometary origin, as a rule, should satisfy the following conditions: (a) they should be low-albedo objects of D, P and C-types [8]; (b) their rotational rates should be lower than the mean rates of NEAs [2, 7, 17]; (c) they should also be evolved on unstable orbits, and should be associated with meteor streams [17].

The data available (NEA taxonomy, shapes and rotation parameters, associations with meteors streams) show that less than 10% of known NEAs satisfy these conditions. Among the NEAs the most probable candidates for cometary origin are the following objects:

Asteroid	Type	Period of rotation (hrs)	D (km)	Comments
2100 Ra-Shalom	C	19.79	3.4	Meteor stream
2101 Adonis	?	?	?	Meteor stream, anomalous radar echo
2201 Oljato	S	24	2	Meteor stream, chaotic orbit
2212 Hephaistos	SG	> 20	5.7	Meteor stream, cometary orbit
3200 Phaethon	F	3.6	6.9	Geminid meteor stream
3552 Don Quixote	D	7.7	19	Comet orbit
4015 Willson-Harring	CF	6.1	2.0	Comet activity in the past

Thus, we can conclude that the main asteroid belt is the principal source of NEA replenishment and the fraction of NEAs of cometary origin does not exceed 10%. This conclusion does not contradict to the recent results of dynamic considerations, according to which the main asteroid belt can supply a few hundred km-sized NEAs per 1 Myr that is well enough to sustain the current NEA population [14].

REFERENCES

[1] *Binzel R. P., Xu S., Bus S. J., Bowell E.* Origin for the near-Earth asteroids // Science.–1992.–**257**.–P. 779–782.

[2] *Degewij J., Tedesco E. F.* Do comets evolve into asteroids? Evidence from physical studies // Comets / Ed. L. L. Wilkening.–Tucson: Univ. of Arizona Press, 1982.–P. 665–695.

[3] *Farinella P., Gonczi R., Froeschle Ch., Froeschle C.* The injection of asteroid fragments into resonances // Icarus.–1993.–**101**.–P. 174–187.

[4] *Froeschle Ch., Michel P., Froeschle C.* Dynamical transport mechanisms of planet-crossing bodies // Evolution and Source Regions of Asteroids and Comets: Proc. 173 Coll. IAU, Tatranska Lomnica, Slovak Republic, 1998 Aug. 24–28 / Eds J. Svoren, E. M. Pittich, H. Richman.–1999.–P. 87–96.

[5] *Froeschle Ch., Morbidelli A.* The secular resonances in the Solar system / Asteroids, Comets, Meteors 1993: Proc. 160 Symp. IAU, Belgirate Italy, 1993 June 14–18 / Eds A. Milani, M. Di Martino, A. Cellino.–1994.–P. 189–204.

[6] *Gladman B. J., Migliorini F., Morbidelli A., et al.* Dynamical lifetime of objects injected into asteroid belt resonances // Science.–1997.–**277**.–P. 197–201.

[7] *Hartmann W. K., Tholen D. J.* Comet nuclei and Trojan asteroids: a new link and a possible mechanism for comet splittings // Icarus.–1990.–**86**, N 2.–P. 448–454.

[8] *Hartmann W. K., Tholen D. J., Cruikshank D. P.* The relationship of active comets, “extinct” comets, and dark asteroids // Icarus.–1987.–**69**, N 1.–P. 33–50.

[9] *Helfenstein P., Veverka J.* Physical characterization of asteroid surfaces from photometric analysis // Asteroids II / Eds R. P. Binzel, T. Gehrels, M. S. Matthews.–Tucson: Univ. of Arizona Press, 1989.–P. 557–593.

[10] *Levin B. Yu., Simonenko A. N.* On the implausibility of a cometary origin for most Apollo-Amor asteroids // Icarus.–1981.–**47**.–P. 487–491.

[11] *Lupishko D. F., Di Martino M.* Physical properties of near-Earth asteroids // Planet. and Space Sci.–1998.–**46**.–P. 47–74.

[12] *Luu J.* Comets disguised as asteroids // Publs Astron. Soc. Pacif.–1994.–**106**, N 699.–P. 425–435.

[13] *Luu J., Jewitt D.* On the relative number of C types and S types among near-Earth asteroids // Astron. J.–1989.–**98**.–P. 1905–1911.

[14] *Menichella M., Paolicchi P., Farinella P.* The main belt as a source of near-Earth asteroids // Earth, Moon, and Planets.–1996.–**72**.–P. 133–149.

[15] *Öpik E. J.* The stray bodies in the solar system. Part I. Survival of cometary nuclei and the asteroids // Adv. Astron. and Astrophys.–1963.–**2**.–P. 219–262.

[16] *Tedesco E. F., Gradie J.* Discovery of M class objects among the near-Earth asteroid population // Astron. J.–1987.–**93**, N 3.–P. 738–745.

[17] *Weissman P. R., A'Hearn M. F., MacFadden L. A., Rickman H.* Evolution of comets into asteroids // Asteroids II / Eds R. P. Binzel, T. Gehrels, M. S. Matthews.–Tucson: Univ. of Arizona Press, 1989.–P. 880–920.

[18] *Wetherill G. W.* Where do Apollo objects come from? // Icarus.–1988.–**76**.–P. 1–18.

[19] *Whipple F. L.* The rotation of comet nuclei // Comets / Ed. L. L. Wilkening.–Tucson: Univ. of Arizona Press, 1982.–P. 227–250.

[20] *Zellner B.* Asteroid taxonomy and the distribution of the compositional types // Asteroids / Ed. T. Gehrels.–Tucson: Univ. of Arizona Press, 1979.–P. 783–806.

FOLLOW–UP CCD OBSERVATIONS OF NEAR–EARTH ASTEROIDS IN 1999

Yu. N. Krugly, I. N. Belskaya, V. G. Chiorny, and V. G. Shevchenko

Astronomical Observatory of Kharkiv National University
35 Sumska St., 61022 Kharkiv, Ukraine
e-mail: krugly@astron.kharkov.ua

INTRODUCTION

It is very important from the point of view of asteroid hazard problem both timely to discover "dangerous" body and to know its main physical properties. To a middle of 2000 the total amount of these objects with good known orbits exceeded 1000. However, study of physical properties of near-Earth asteroids (NEA) falls considerably behind from the speed of their discovering. Today the data of rotations and shapes have been obtained for less then 20% of known NEA.

In 1996 at Astronomical Observatory of Kharkiv University the regular CCD observations of NEA were started. The observations were carried out in collaboration with the DLR Institute for Planetary Exploration (Berlin) within the framework of European NEA discovery projects. The observation program includes obtaining both NEA lightcurves for a study of their rotation and shapes, and astrometric follow-up observations for newly discovered objects. For the observations we usually had 5–7 nights per month close to a new moon. Since these bodies have diameters about some kilometers or less the discovery occurs in a moment of their close approaching to Earth. This period of maximal visible brightness is most suitable to study physical properties, and we try to do our observations of asteroids just after their discoveries.

OBSERVATIONS

We discussed the results of follow-up photometric observations of NEA carried out in 1999. The 70-cm telescope equipped with a CCD camera SBIG ST-6 UV was used. Usually the observations were done through the R or V filters close to the standard Johnson-Cousins photometric system. The ASTPHOT package developed by S. Mottola (Mottola *et al.*, 1995) was used for reduction of CCD frames.

In 1999 we observed nine NEA and one Mars-crosser just after their discoveries. Namely they are listed in Table 1. It includes the asteroid orbit type, the calculated absolute magnitude H and the asteroid diameter. The absolute magnitude of each asteroid was calculated for its primary lightcurve maximum by using the HG-function (Bowell *et al.*, 1989) and assuming $G = 0.15$.

Table 1: Magnitudes and diameters of observed asteroids

Name of asteroid	Orbit type	H (mag)	Diameter (km)
1999 CV3	Apollo	15.0	3.0–5.5
1999 GU3	Amor	19.28	0.6
1999 HF1	Aten	14.54	3.7–6.8
1999 JM8	Aten	15.63	2.2–4.1
1999 JO8	Aten	16.77	1.3–2.4
1999 LF6	Apollo	18.02	0.7–1.4
1999 ND43	Amor	18.9	0.5–0.9
1999 RH27	Amor	16.83	1.3–2.4
1999 RQ36	Apollo	20.72	0.2–0.4
1999 US3	Mars-Crosser	13.61	5.7–10.4

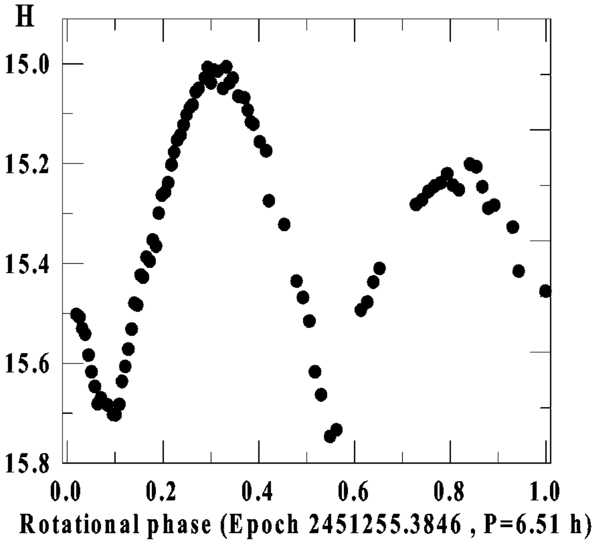

Figure 1: Composite lightcurve of asteroid 1999 CV3

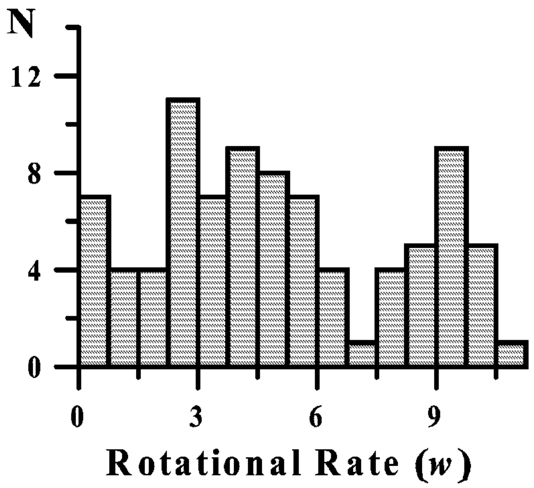

Figure 2: Distribution of NEA rotational rates

RESULTS

The composite lightcurve of asteroid **1999 CV3** observed during three nights in March 1999 is shown as an example in Fig. 1. The lightcurve is characterized by two pairs of extrema with unequal level of maxima and amplitude of 0.74 mag. Such large brightness variations give an evidence on a rather asymmetric elongated shape of the asteroid.

We determined unambiguously rotational periods for 6 of 10 asteroids. Three asteroids are characterized by fast rotation with periods less than 2.5 hours. One of these fast rotating asteroids, namely **1999 HF1**, is supposed to be a binary system (Pravec, 1999). Four observed NEA showed long-period brightness variations with periods more than 12 hours. Additional observations are needed to determine the accurate values of their rotational periods. Our data of the long-period asteroid **1999 GU3** were combined with the photometric data obtained at Ondrejov and Table Mountain Observatories and with the radar observations carried out using the Goldstone's radar system. As result the periodicity was thoroughly analysed and the period was determined (Pravec *et al.*, 2000). Lightcurves of asteroid **1999 ND43** did not show variations more than 0.1 mag and we did not find any period which could fit the data.

A distribution of NEA rotational rates is shown in Fig. 2. The sample includes 86 near-Earth asteroids with well-determined rotational periods. Asteroids can be divided into three groups according to their rotation: fast ($P < 3.5\,\mathrm{h}$), middle ($3.5 - 12\,\mathrm{h}$) and slow ($> 12\,\mathrm{h}$) rotation. Our observations presented here give a contribution into statistics for each group.

REFERENCES

[1] *Bowell E., Hapke B., Domingue D., et al.* Application of photometric models to asteroids // Asteroids II / Eds R. Binzel, T. Gehrels, M. S. Matthews.–Tucson: Univ. of Arizona Press, 1989.–P. 524–556.

[2] *Mottola S., De Angelis G., Di Martino M., et al.* The Near-Earth objects follow-up program: first results // Icarus.–1995.–**117**.–P. 62–70.

[3] *Pravec P.* 1999. Personal communication.

[4] *Pravec P., Sarounova L., Benner L. A. M., et al.* Slowly rotating asteroid 1999 GU3 // Icarus.–2000.–submitted.

THE DIVERSITY OF THE OPPOSITION EFFECT AMONG ASTEROIDS

I. N. Belskaya and V. G. Shevchenko

Astronomical Observatory of Kharkiv National University
35 Sumska St., 61022 Kharkiv, Ukraine
e-mail: irina@astron.kharkov.ua

INTRODUCTION

The sharp increase in asteroid brightness near opposition called the opposition effect (OE) was firstly discovered by Gehrels (1956) for the S-type asteroid 20 Massalia. Further observations proved that it is a general phenomenon for asteroids. At first the opposition effect was considered to be very similar among different types of asteroids (Gehrels and Taylor, 1977; Gehrels and Tedesco, 1979). Scaltriti and Zappala (1980) performed a thorough analysis of phase curves of 26 asteroids. They concluded that similarity of the opposition effect amplitudes among asteroids is independent of their albedo. Later special observational campaigns were organized to enlarge the observational data set (*e.g.*, Harris *et al.*, 1989; Shevchenko *et al.*, 1997). Harris *et al.* (1989) discovered a very sharp and narrow opposition effect peak for the high-albedo E-type asteroids. On the other hand, some low albedo asteroids show an almost linear magnitude-phase dependence down to a phase angle of 2 deg (French, 1987; Harris and Young, 1989; Shevchenko *et al.*, 1996). The purpose of the present work is to summarize and critically analyze the available observational data on the asteroid opposition effect.

MEAN VALUES OF THE ASTEROID OPPOSITION EFFECT

For this analysis we have chosen the asteroid magnitude-phase curves which have a good phase angle coverage and small scattering within the observational data. At present there are 37 asteroids observed at least three times at small phase angles including subdegree range. All the data were obtained in the V band and were reduced to the standard geometry of observations if it was necessary. The absolute magnitudes were taken at the primary maximum of an asteroid lightcurve which is known to be slightly influenced by the asteroid shape elongation (Surdej and Surdej, 1978). Although the number of asteroids under consideration has not greatly changed as compared to previous analyses of asteroid phase curves, the quality of the data considered here has essentially improved.

To provide quantitative estimates of observed differences among phase curves for asteroids of different composition it is important to be clear about the taken definition of OE. There are two different conventions typically used to define the OE: the absolute increase in brightness, *e.g.*, I(1°)/I(7°), or the relative excess above the extrapolation of the linear part of phase curve. In the second definition the OE is considered as a separate phenomenon caused by a mechanism distinct from the rest of the phase curve. We will use both definitions of the OE and it will be shown below that our conclusions do not depend on a chosen OE definition.

Table 1 summarizes the mean values of opposition effect parameters and their standard deviations calculated for different asteroid types.

Table 1: Mean values of opposition effect parameters for different asteroid types

Type	N	Geometric albedo (p_V)	OE amplitude at $\alpha = 0.^\circ 3$ (mag)	Ratio of intensities: I(0°.3)/I(5°)	Angle of the OE beginning (deg)
P	5	0.04 ± 0.01	0.10 ± 0.04	1.30 ± 0.03	3.0 ± 1.3
C	8	0.07 ± 0.01	0.16 ± 0.05	1.34 ± 0.05	4.4 ± 1.2
M	7	0.16 ± 0.04	0.34 ± 0.04	1.45 ± 0.04	5.9 ± 0.7
S	10	0.21 ± 0.04	0.35 ± 0.04	1.44 ± 0.03	5.3 ± 1.2
E	4	0.51 ± 0.03	0.23 ± 0.03	1.28 ± 0.03	3.2 ± 1.2

The first two columns of the table gives asteroid compositional types according to Tholen (1989) and the number of asteroids taken inside each type. The mean albedo was calculated using the IRAS albedo database

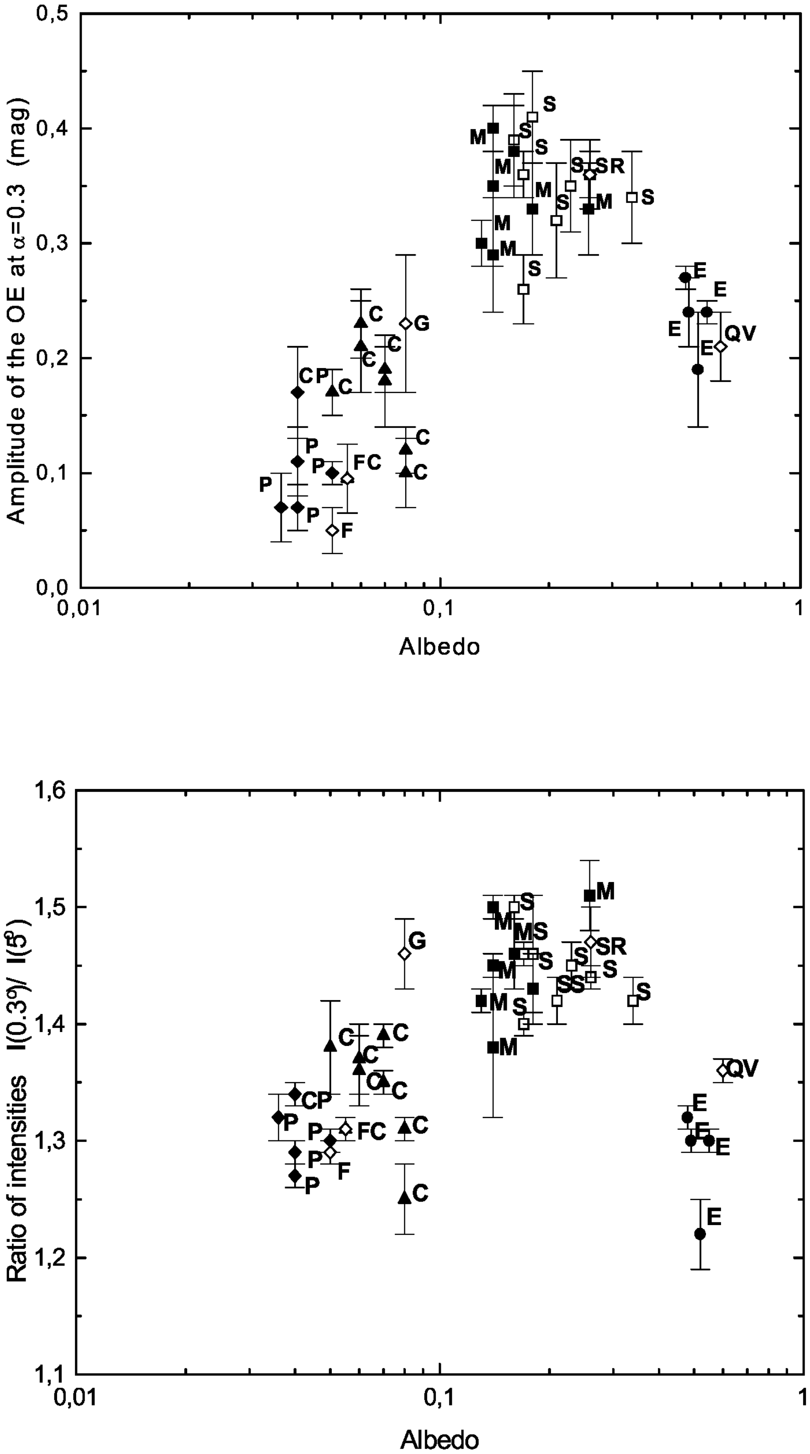

Figure 1: Dependences of the opposition effect calculated as the excess in magnitude at $\alpha = 0\overset{\circ}{.}3$ relatively to the extrapolated linear part of phase curve (top) and as the ratio of intensity at $\alpha = 0\overset{\circ}{.}3$ to that at $\alpha = 5^\circ$ (bottom) versus albedo for asteroids of various types

(Tedesco *et al.*, 1992). The OE amplitude was measured at a phase angle of 0.3 deg relative to the extrapolation of the linear part of magnitude-phase curve. The ratio of intensity at 0.3 deg of phase angle measured relative to that at 5 deg characterizes the absolute increase in asteroid brightness near opposition. The mean value of the angle at which non-linear increase in magnitude-phase dependence begins was calculated using the composite magnitude-phase curves for each asteroid type. We consider this angle as an important characteristic of the opposition effect phenomenon. Unfortunately, the value of the angle is often uncertain for an individual asteroid because of poor phase angle coverage in the range of interest.

We have chosen 0.3 deg as the phase angle at which the value of the OE amplitude was determined for two reasons: 1) very few observations of asteroid brightness are available at smaller phase angles ($\alpha = 0^\circ\!.3$ is the mean minimal phase angle of observations for the considered data set). The extrapolation depends strongly on the assumed approximating function; 2) the influence of the finite angular size of the solar disk (*e.g.*, Shkuratov, 1991) which is difficult to take into account based on available observational data.

The diversity of phase curves are clearly seen for the main asteroid types. The OE amplitudes differ for both absolute and relative measurements. Asteroids of the S and M types show the largest values of the OE amplitude. Note that differences in the OE amplitude within a particular type are relatively small, not exceeding 0.1 mag. For most types the differences between individual phase curves are on the order of the observational scatter. For the C-type asteroids there are systematic differences in the opposition effect steepness for phase curves of different low-albedo asteroids.

The angle at which non-linear increase of a magnitude-phase dependence begins also varies among asteroid types. The largest angles of the OE beginning typically occur for the M and S types which have albedos in the range of 0.1–0.3. It decreases both for high albedo E type and for low albedo C and P types. For some of them the magnitude-phase dependence remains linear down to 2–3 deg. For our entire data set, the mean value of the angle of OE beginning is 4.6 deg. This result is rather unexpected since previously it was considered that the OE of asteroids begins at phase angles of 7–9 deg (Scaltriti and Zappala, 1980).

ALBEDO DEPENDENCE OF OPPOSITION EFFECT AMPLITUDE

Understanding of the opposition effect phenomena of atmosphereless bodies has considerably improved last decade. Now it is obviously that there are two main mechanisms; namely shadow hiding and coherent backscatter causing the OE phenomena. Detailed descriptions of the OE mechanisms can be found in Hapke (1993), Muinonen (1993), and Shkuratov (1994). Mishchenko and Dlugach (1993) demonstrated quantitatively that the coherent backscattering can explain observed narrow opposition effect for the E-type asteroids. Available theoretical models give a number of predictions. In particular, the dependence of OE amplitude on albedo is of a great importance. According to Hapke (1993) the coherent backscatter effect can be distinguished observationally from the shadow-hiding effect with a help of the OE amplitude dependence on albedo.

Dependence of the OE amplitude on albedo for asteroids of various types is shown in Fig. 1. The amplitude of OE clearly varies with asteroid albedo in a non-monotonic way. Values of the OE amplitude defined both as absolute and as relative increases in magnitude show a similar dependence on albedo. The amplitude of the OE decreases both for dark and high albedo asteroids. The largest amplitude occurs with moderate albedo asteroids (about 20% of albedo). According to Hapke (1993) the contribution of the shadow-hiding effect decreases as albedo increases while that for coherent-backscatter increases as albedo increases. If Hapke's conclusion is true then the observed non-monotonic dependence of the OE amplitude on albedo cannot be explained by a single mechanism.

CONCLUSIONS

The amplitude and width of OE depends on asteroid albedo in a non-monotonic way with the maximum for the moderate-albedo asteroids. Relative to this maximum, the amplitude of the OE decreases both for low and high albedo asteroids, which can be caused by combined influence of both shadow-hiding and coherent-backscatter mechanisms.

Acknowledgements. This study was supported by Ukrainian foundation of fundamental science and technology (grant N 2.4/314).

REFERENCES

[1] *French L. M.* Rotation properties of four L5 Trojan asteroids from CCD photometry // Icarus.–1987.–**72**.–P. 325–341.

[2] *Gehrels T.* Photometric studies of asteroids: V. The lightcurve and phase function of 20 Massalia // Astrophys. J.–1956.–**123**.–P. 331–335.

[3] *Gehrels T., Taylor R. C.* Minor planets and related objects: XXII. Phase function for 6 Hebe // Astron. J.–1977.–**82**.–P. 229–232.

[4] *Gehrels T., Tedesco E. F.* Minor planets and related objects: XXVIII. Asteroid magnitudes and phase relations // Astron. J.–1979.–**84**.–P. 1070–1087.

[5] *Hapke B.* Theory of reflectance and Emittance Spectroscopy.–New York: Cambridge University Press, 1993.

[6] *Harris A. W., Young J. W.* Two dark asteroids with very small opposition effects // Lunar and Planet Sci.–1989.–XIX **2**.–P. 447–448.

[7] *Harris A. W., Young J. W., Contreiras L., et al.* Phase relations of high albedo asteroids: the unusual opposition brightening of 44 Nysa and 64 Angelina // Icarus.–1989.–**81**.–P. 365–374.

[8] *Mishchenko M. I., Dlugach J. M.* Coherent backscatter and the opposition effect for E-type asteroids // Planet. and Space Sci.–1993.–**41**.–P. 173–181.

[9] *Muinonen K.* Coherent backscattering by Solar System dust particles // Asteroids, Comets, Meteors 1993 / Eds A. Milani, M. Di Martino, A. Cellino.–1993.

[10] *Scaltriti F., Zappala V.* The similarity of the opposition effect among asteroids // Astron. and Astrophys.–1980.–**83**.–P. 249–251.

[11] *Shevchenko V. G., Chiorny V. G., Kalashnikov A. V., et al.* Magnitude-phase dependences for three asteroids // Astron. and Astrophys. Suppl. Ser.–1996.–**115**.–P. 1–6.

[12] *Shevchenko V. G., Belskaya I. N., Chiorny V. G., et al.* Asteroid observations at low phase angles. I. 50 Virginia, 91 Aegina and 102 Miriam // Planet. and Space Sci.–1997.–**45**.–P. 1615–1623.

[13] *Shkuratov Yu. G.* Estimating the effect of finite angular light source dimensions on the opposition brightness effect in atmosphereless celestial bodies // Sol. Syst. Res.–1991.–**25**, N 1.–P. 54–57.

[14] *Shkuratov Yu. G.* Study of the backscatter of light by solid surfaces of celestial bodies: theoretical models of the opposition effect // Sol Syst. Res.–1994.–**28**, N 4-5.–P. 155–171.

[15] *Surdej A., Surdej J.* Asteroid lightcurves simulated by the rotation of a three-axes ellipsoid model // Astron. and Astrophys.–1978.–**66**.–P. 31–36.

[16] *Tedesco E. F., Veeder G. J., Flower J. W., Chillemi J. R.* The IRAS Minor Planet Survey Data Base.–National Space Science Data Center, Greenbelt, Maryland, 1992.

[17] *Tholen D. J.* Asteroid taxonomic classification // Asteroids II / Eds R. P. Binzel, T. Gehrels, M. S. Matthews.–Tucson: Univ. of Arizona Press, 1989.–P. 1139–1150.

THE FIRST RESULTS OF THE OBSERVATIONS OF THE KUIPER BELT ASTEROIDS AT THE TERSKOL OBSERVATORY

L. V. Rykhlova[1], M. A. Smirnov[1], G. T. Bologova[1] V. K. Tarady[2], A. V. Sergeev[2], N. V. Karpov[2], I. Kulyk[3]

[1]*Institute of Astronomy, Russian Academy of Science*
23 Piatnitskaia, Moscow, Russia

[2]*International Center for Astronomical and Medico-Ecological Research*
27 Akademika Zabolotnoho, 03680 Kyiv, Ukraine

[3]*Main Astronomical Observatory, NAS of Ukraine*
27 Akademika Zabolotnoho, 03680 Kyiv, Ukraine
e-mail: leda@mao.kiev.ua

The astrometric positions of two Kuiper Belt asteroids in the USNO-2A catalogue system are presented. The estimations of the inner accuracy and a comparison with the ephemeris were made.

I. INTRODUCTION

In recent years many efforts have been made to understand the nature and dynamics of the Kuiper Belt (Jewitt 1999). Observational programs to look for this trans-Neptunian population have been highly successful (Irwin *et al.*, 1995; Jewitt *et al.*, 1998; Davies *et al.*, 1997). Now the orbital elements are available for near the 250 objects (*http://cfa–www.harvard.edu/~graff/Ephemerides/Distant*). Many of them are derived from a single opposition and needed in new astrometric observations.

We present the first results of astrometry of two Kuiper Belt asteroids with the goal to test the obsevational method and its positional precision.

II. OBSERVATIONS AND RESULT

The observations were made with the IC AMEI 2-m Zeiss Telescope at the Terskol Observatory. In July 1999 six frames with the images of the asteroid 1998TO66 and in October eight frames with the images of the asteroid 1995SM55 were obtained using the Two-Channel Focal Reducer of the Max-Planck-Institute for Aeronomy (Küppers and Jockers, 1997). The lens from the red channel was placed in blue channel to increase the field of

Table 1: Derived astrometric positions of two Kuiper Belt asteroids

	Date (1999, UT)	$\alpha_{2000.0}$			$\delta_{2000.0}$			rms α	error δ	(O–C) α	(O–C) δ	Object
July	$10^d.96198$	00^h	04^m	$14^s.743$	$+03°$	$54'$	$48''.22$	$0''.34$	$0''.47$	$-1''.32$	$-0''.19$	1996TO66
	12.92413	00	04	12.804	03	54	55.30	0.30	0.44	−1.25	0.03	($21^m.8$ V)
	13.94635	00	04	11.680	03	54	57.88	0.27	0.28	−1.17	−0.18	
	13.95581	00	04	11.655	03	54	57.63	0.37	0.37	−1.38	−0.46	
	14.98704	00	04	10.405	03	55	00.55	0.29	0.52	−1.79	0.19	
	15.00399	00	04	10.410	03	55	00.70	0.29	0.40	−1.39	0.31	
October	07.96569	01	40	06.042	14	17	55.29	0.36	0.29	−5.4	−0.6	1995SM55
	07.96765	01	40	06.037	14	17	55.22	0.32	0.33	−5.4	−0.6	($21^m.5$ V)
	07.98731	01	40	05.931	14	17	54.79	0.32	0.33	−5.6	−0.2	
	07.99168	01	40	05.888	14	17	54.72	0.33	0.38	−6.1	−0.5	
	07.99737	01	40	05.882	14	17	55.03	0.32	0.39	−5.4	−0.2	
	08.00477	01	40	05.836	14	17	54.52	0.35	0.38	−6.0	−0.7	
	08.00919	01	40	05.821	14	17	54.50	0.35	0.36	−5.4	−0.7	
	08.01680	01	40	05.783	14	17	54.42	0.32	0.39	−5.1	−0.2	

view. The red filter Gunn R ($\lambda = 680$ nm, FWHM = 111 nm) was used for all the observations. Twilight sky was acquired for the flatfield frames. The integration time was from 300 to 900 sec. The coordinates of image centres were estimated using a two-component Gaussian fit. Astrometric positions were derived with respect to USNO-2A catalogue. The number of the reference stars was of about 25 in the range of the magnitudes from $16\overset{m}{.}0$ to $21\overset{m}{.}0$. The six constants model was used for determination of an asteroid position. The internal error was evaluated from the residuals of the reference stars. The astrometric positions are presented in Table 1.

III. CONCLUSIONS

A good inner accuracy of the astrometric positions demonstrates that successful astrometry may perform with 2-m Telescope equipped with the Two-Channel Focal Reducer for such faint objects as the Kuiper Belt asteroids.

REFERENCES

[1] *Davies J., McBride N., Green S. F.* Optical and infrared photometry of Kuiper Belt object 1993SC // Icarus.–1997.–**125**, N 1.–P. 61–66.

[2] *Irwin M., Tremaine S., Zytkow A. N.* A Search for slow-moving objects and the luminosity function of the Kuiper Belt // Astron. J.–1995.–**110**.–P. 3082–3093.

[3] *Jewitt D.* Kuper Belt objects // Annu. Rev. Earth. Planet. Sci.–1999.–**27**.–P. 287–312.

[4] *Jewitt D., Luu J., Trujillo C.* Large Kuiper Belt objects: the Mauna Kea 8K CCD survey // Astron. J.–1998.–**115**.–P. 2125–2135.

[5] *Küppers M., Jockers K.* A Multi-emission imaging study of the Io plasma torus // Icarus.–1997.–**120**, N 1.–P. 48–71.

OBSERVATIONS OF ASTEROIDS WITH CCD TELESCOPES ACCORDING TO THE PROGRAMME OF INTERNATIONAL CO–OPERATION BETWEEN MYKOLAIV ASTRONOMICAL OBSERVATORY (MAO), INSTITUTE OF APPLIED ASTRONOMY (IAA), AND BORDEAUX ASTRONOMICAL OBSERVATORY (BAO)

A. Ivantsov[1], A. Kovalchuk[1], M. Martynov[1], G. Pinigin[1], V. Pishnenko[1], Zh. Pozhalova[1], A. Shulga[1], Yu. Chernetenko[2], V. Shor[2], M. Rapaport[3], B. Viateau[3]

[1] *Mykolaiv Astronomical Observatory, 54030 Mykolaiv, Ukraine*
[2] *Institute of Applied Astronomy, 191187, Saint-Petersburg, Russia*
[3] *Bordeaux Astronomical Observatory, B.P. 89-33270, Floirac, France*

INTRODUCTION

Observations in the MAO are carried out with the Zone astrograph (ZA) (objective aperture D = 160 mm with a 120 mm diaphragm, focal length F = 2044 mm) and the Axial meridian circle (AMC) (D = 180 mm, F = 2480 mm) equipped with similar CCD cameras (ISDO17, 1040×1160 pixels, pixel size 16×16 mkm). The observations in the BAO are carried out with the Bordeaux meridian circle (BMC) (D = 190 mm, F = 2370 mm) equipped with a CCD camera (1024×1024 pixels, pixel size 19×19 mkm).

I. LIST OF THE OBSERVED OBJECTS

The co-ordinated Programme includes observations of small Solar System bodies up to 16 magnitude in the following areas.

1. Uniform observation series of selected minor planets along all their visual tracks as far from the opposition as possible (IAA programme). The aims of the research are as follows: a) to compare the accuracy of the photographic observations with that of CCD and to estimate their possible systematic differences, b) to estimate the minimal Solar elongation angle at which minor planets yet can be observed, c) to use these observations for determination of the mutual orientation of the dynamical frame and ICRF, d) to select an adequate scattering law accounting for phase effect.

2. Observation of asteroids in order to determine the masses of some minor planets. The IAA programme list includes 30 sufficiently bright asteroids and the BAO programme includes 10 additional ones. The proposed observations during a 4–5 year period with an accuracy not worse than 60 mas will be used for improvement of the masses of Ceres (1), Vesta (4) and others.

3. The Programme includes also observations of near-Earth objects (NEO) for determining their positions and brightness. The list of objects compiled in IAA for 2000 includes more than 20 NEO up to 16 magnitude which encounter to the Earth at the distance less than 0.3 AU. Only five asteroids among them have minimum magnitudes less than 15.

II. OBSERVATIONS AT THE MYKOLAIV ASTRONOMICAL OBSERVATORY

1. Universal CCD camera

The camera with ISDO17 detector made by Optron-Electronic Corporation (Saint-Petersburg) was made at the MAO in 1999 [1]. It can work either in the drift-scan mode (exposure time 103/cos δ seconds, field of view (FOV) $23'\times26'$ for AMC) or in the drift-scan and stare mode (exposition from 1 ms to 30 min, limiting magnitude is about 15 min by a 5 min exposition and FOV $28'\times31'$ for ZA). The instrumental accuracy of coordinate determination with the CCD camera is presented in the Figure 1.

2. Observations of minor planets at the Zone astrograph

Trial CCD observations were carried out with ZA in autumn 1999 and the regular ones started in April 2000. More than 100 observations of 12 minor planets were performed. It was used such an observational procedure: there were taken series from 5 to 9 CCD frames for every planet during each night, exposition for a single CCD frame was from 2 till 4 minutes. Part of the observational data was preliminary reduced using the "Astrometrica

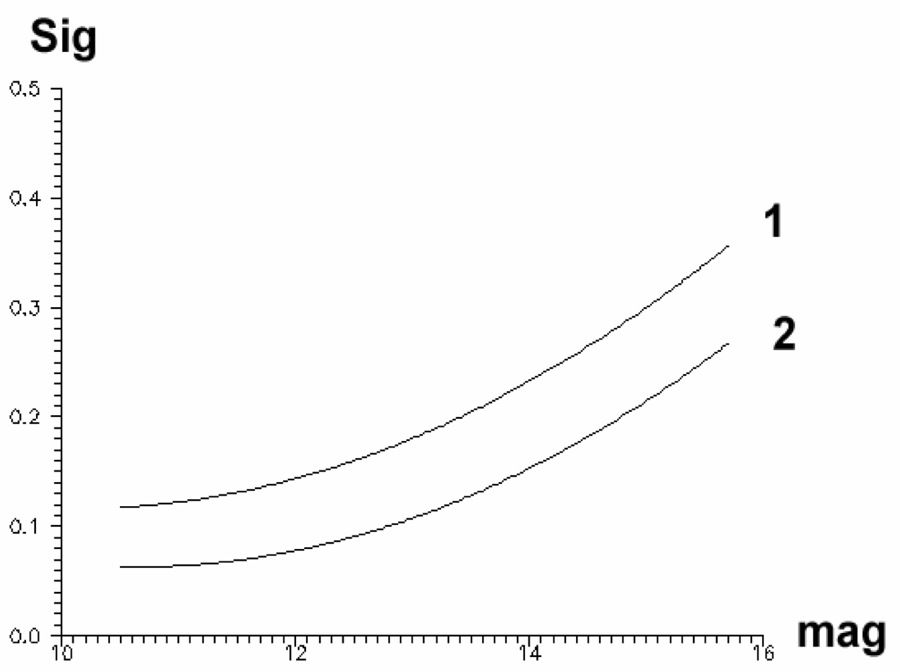

Figure 1: The instrumental accuracy of coordinate determination with CCD as a function of magnitude (in arcseconds)

programme" [2] in the system of USNO-A2.0 Catalogue. An internal accuracy for one minor planet position is of $0.''03 \div 0.''1$. The calculations of (O–C) were fulfilled for the series of observations of Thetis (17) and Vesta (4) only. The external error for one observation is about $0.''38$ in right ascension and $0.''51$ in declination. Our calculations were confirmed by similar ones which have been made O. P. Bykov (Pulkovo Observatory) using the "Epos" software. It is to be noted that observations of the planets have been carried out at a zenith distance $60° - 70°$.

3. Observations of minor planets with AMC in 1997-1998

First observations of minor planets with AMC were carried out using the previous CCD (288×256 pixels, pixel size 24×32 mkm). According to the list of selected minor planets by the IAA programme, 136 observations of 27 minor planets were fulfilled. A standard error for one determination of (O–C) in the GSC system was of $0.''22 \div 0.''51$. After modernization and installation of a new universal CCD camera the AMC will provide regular observations in 2001.

CONCLUSIONS

The first results of minor planets observations with MAO CCD telescopes show that these observations are to be perspective [3]. There are many appropriate methods to improve their accuracy. It permits to hope that the proposed Programme can be fulfilled during 4–5 years both by using of traditional methods and combining them with those developed for the complex of AMC and Zone astrograph of the MAO [4].

REFERENCES

[1] *Kovalchuk A.* Universal CCD-micrometer in Astronomy // Kinematics and Physics of Celestial Bodies. Suppl. Ser.–1999.–N 1.–P. 97–100. (in Ukrainian).

[2] *Raab H.* *http://www.astrometrica.at.*

[3] *Bykov O.* Positional observations of the Small Solar System Bodies: state and the nearest perspectives // Proc. IV Conf. Astron. Soc., Moscow, November 19–29, 1997.–Moscow, 1998.–P. 73–81.

[4] *Kovalchuk A., Pinigin G., Protsyuk Yu., et al.* The use of AMC in Nikolaev in combined observations with the telescope in parallactic mounting // Kinematics and Physics of Celestial Bodies. Suppl. Ser.–1999.–N 1.–P. 79–83. (in Russian).

OPTICAL POLARIMETRY OF THE GALILEAN SATELLITES, IAPETUS, AND 64 ANGELINA NEAR OPPOSITION

V. K. Rosenbush[1], **N. N. Kiselev**[2], **K. Jockers**[3],
V. V. Korokhin[2], **N. M. Shakhovskoy**[4], **and Yu. S. Efimov**[4]

[1] *Main Astronomical Observatory, NAS of Ukraine*
27 Akademika Zabolotnoho, 03680 Kyiv, Ukraine
e-mail: rosevera@mao.kiev.ua

[2] *Kharkiv Astronomical Observatory, Kharkiv, Ukraine*

[3] *Max–Planck–Institut für Aeronomie, Katlenburg-Lindau, Germany*

[4] *Crimean Astrophysical Observatory, Naukove, Ukraine*

Detailed measurements of polarization of the Galilean satellites of Jupiter, Saturn's satellite Iapetus and the asteroid 64 Angelina in the UBVRI filters around opposition, which were obtained at the Kharkiv, Crimean, and Pik Terskol Observatories in 1998–1999, are presented. Undoubtedly, there is a sharp peak of negative polarization centered at a very small phase angle which is superimposed on the negative branch of the regular phase angle dependence of polarization. Detection of the photometric opposition spike and polarization opposition peak for the researched objects suggests that at least partially their surfaces are covered with an optically thick layer composed of nonabsorbing (or weakly absorbing) submicrometer–sized grains.

INTRODUCTION

There are two interesting phenomena observed for some atmosphereless Solar System bodies near opposition: the photometric opposition effect and negative linear polarization. Their study attracts particular interest because of a great importance not only for understanding properties of the scattering surface but also for understanding the physics of the radiation scattering process itself. These effects may be observed in both wide (as linear increase of brightness and the regular negative polarization branch) and narrow (as a very sharp brightness spike and peak of negative polarization at phase angles less than 1°–2°) ranges of phase angles.

The main purpose of our investigations is the study of behavior of polarization of different cosmic bodies near opposition. We present new, detailed measurements of polarization of the Galilean satellites, the Saturn's satellite Iapetus and the asteroid 64 Angelina.

OBSERVATIONS

Galilean satellites. Imaging polarimetry of satellites of Jupiter was carried out with the 70–cm reflector of the Astronomical Observatory of Kharkiv National University on September 9–25, 1998 at phase angles ranging from $-1\overset{\circ}{.}41$ to $2\overset{\circ}{.}28$. The one–channel polarimeter with a quasi–continuous rotating polaroid was used. CCD camera has 752×582 pixels (60×60 arcsec). To reduce the influence of a background of Jupiter the 15×15 arcsec area was selected for observations of satellites. The observations were carried out in the V standard band. The photopolarimeter and the program complex IRIS developed for automation of observations and initial processing of digital images are described in more detail in paper [5].

Iapetus and 64 Angelina. Observations of Iapetus and the asteroid 64 Angelina were carried out with the five–channel UBVRI photopolarimeter attached to the 1.25–m telescope of the Crimean Astrophysical Observatory. Iapetus was observed from October 11, 1998 to January 18, 1999 in the phase angle range from $-1\overset{\circ}{.}38$ to $6\overset{\circ}{.}1$. Observations of 64 Angelina were carried out on October 17–23, 1995 and September 3 – October 16, 1999. They covered the phase angle ranges from $0\overset{\circ}{.}75$ to $-2\overset{\circ}{.}59$ and from $-3\overset{\circ}{.}3$ to $13\overset{\circ}{.}0$ in 1995 and 1999, respectively. A description of the equipment is given in [4].

Observations of Iapetus and the asteroid 64 Angelina were also made with the 2–m telescope of Pik Terskol Observatory (Northern Caucasus) equipped with two–channel focal reducer of the Max–Planck Institute for Aeronomy (Germany). Simultaneously two images are received in passbands close to the B ($\lambda = 0.43/0.09\ \mu$m) and R ($\lambda = 0.68/0.11\ \mu$m) filters. The technique of polarimetric measurements and description of a device are given by [3]. The CCD images were processed using the MIDAS reduction package.

Standard unpolarized and polarized stars have been observed together with the program objects to determine the instrumental polarization and the zero–point of position angle of the polarization plane, respectively. The total errors (the mean square error and the error of the instrumental system) in the degree of polarization are: 0.1–0.2% in the U filter, 0.03–0.07% in the R filter and 0.06–0.15% in others.

RESULTS AND DISCUSSION

Galilean satellites. The phase dependence of polarization for Io, Europa, Ganymede and Callisto is shown in Fig. 1. In spite of the significant scatter of the data points, it is obvious that Io, Europa and Ganymede have a sharp peak of negative polarization centered at a very small phase angle ($< 1°$) and superimposed on the regular negative polarization branch. There is no such effect for Callisto.

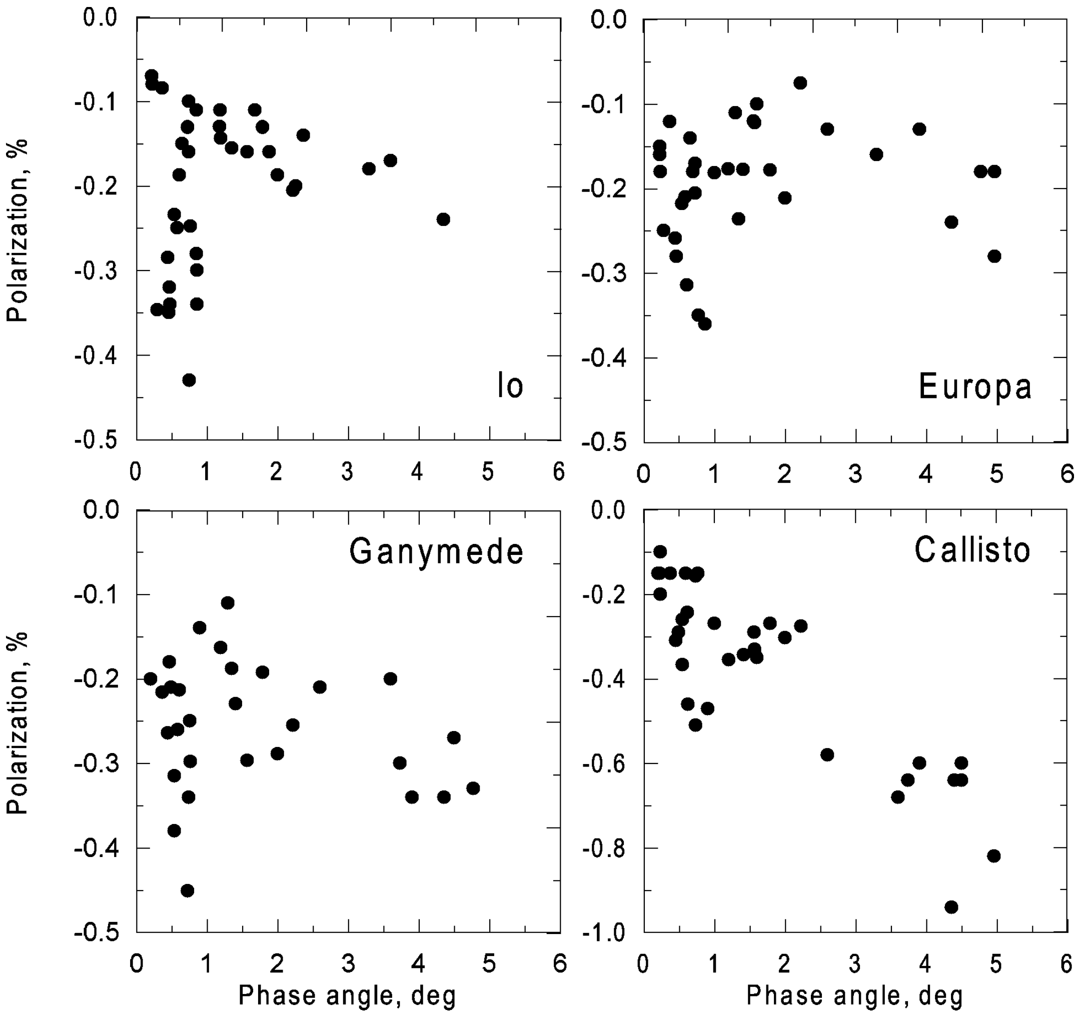

Figure 1: The polarization opposition effect for the Galilean satellites in the V filter

64 Angelina. The results of observations of 64 Angelina in the B and V bands are presented in Fig. 2. There is the regular phase dependence of polarization with the parameters $P_{min} = -0.28\%$ at $\alpha_{min} = 7\overset{\circ}{.}1$ and $P_{min} = -0.33\%$ at $\alpha_{min} = 8\overset{\circ}{.}9$) in the B and V bands, respectively. Noticeable increase of the negative polarization is observed at the phase angles less than 4°. Amplitude of P_{min} in the B filter is somewhat larger than that in the V filter. For both bands, the parameters P_{min} differ for before and after opposition.

Iapetus. The phase dependence of polarization for Iapetus in the B and R filters is presented in Fig. 3. One can see a high degree of polarization within the phase angle range $1\overset{\circ}{.}5$ to $0\overset{\circ}{.}3$. However, the lack of observations outside of this range does not allow to make any certain conclusions about the presence of the polarization opposition effect at phase angles less than 1°.

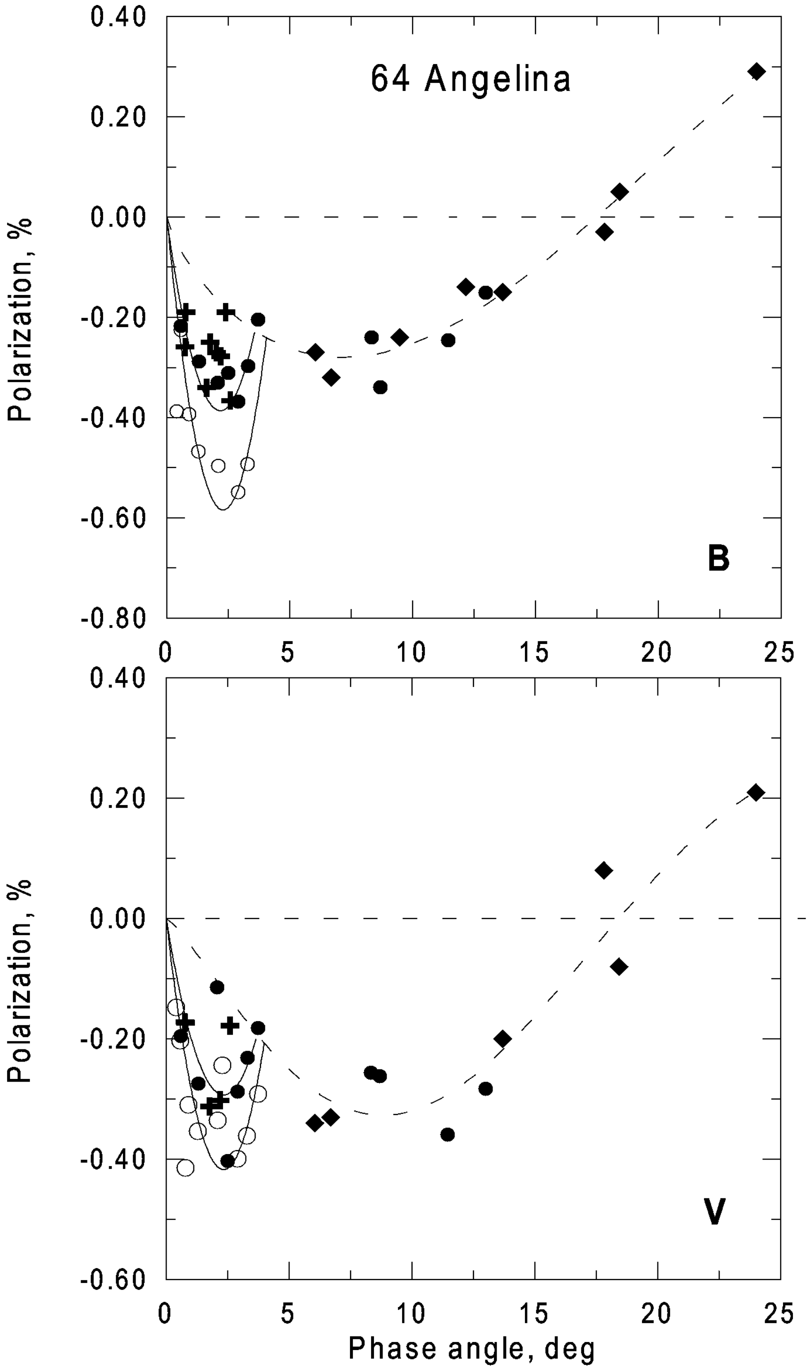

Figure 2: The regular negative polarization branch (dashed curve) and the negative polarization peak produced by coherent backscattering (solid curve) for the asteroid 64 Angelina. The data are shown separately for before (open circles) and after (filled circles) opposition of 1999. The data for opposition 1995 are marked by pluses. The measurements made by Zellner and Gradie [8] are designated by diamonds

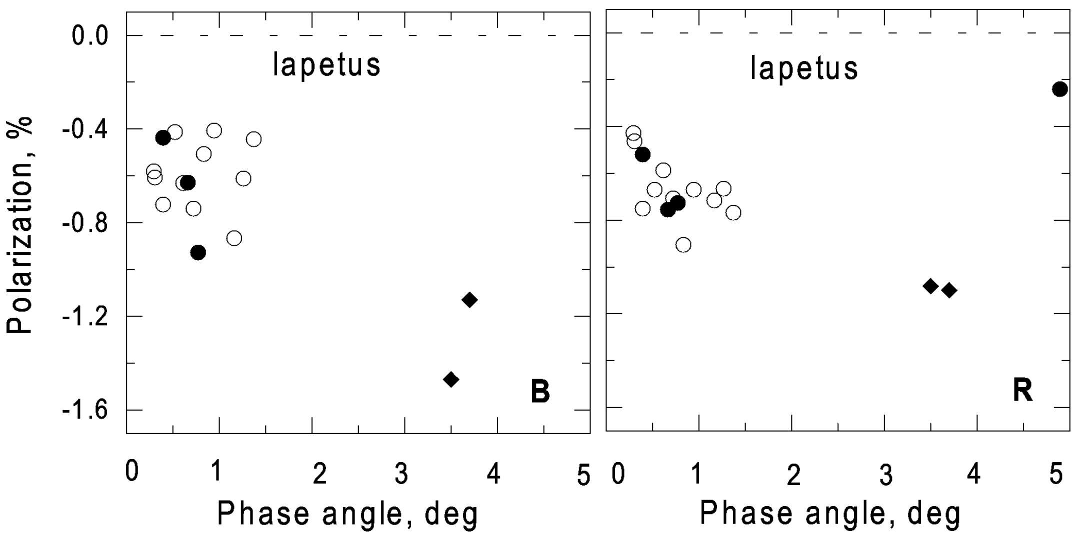

Figure 3: Phase-angle dependence of the degree of linear polarization for Iapetus in the B, and R filters. The Crimean data are shown by the filled (before opposition) and open (after opposition) circles and the Terskol data by diamonds

Our observations as a whole do not contradict the theory of the coherent backscattering enhancement [6]. According to this theory, the objects with a high albedo should exhibit the photometric opposition spike at small phase angles ($< 1°$). Besides, the theory predicts that the photometric opposition effect should be accompanied by polarization opposition peak. All objects, for which we have discovered a sharp peak of the negative polarization, have a high albedo (64 Angelina – 0.55; Io – 0.61; Europa – 0.64; Ganymede – 0.42) and show the brightness spikes [2, 1, 7]. Albedo of Callisto is only 0.2 and it exhibits neither the photometric opposition spike nor a polarization opposition peak. The angular semiwidth and the position of polarization peak exactly at the backscattering direction are comparable to that of the photometric opposition spike. This indicates that the same submicron-sized grains and the same optical mechanism of coherent backscattering are responsible for both effects. Since the surfaces can be covered by grains of different size, the coherent peak produced by smallest grains can be superposed on the regular negative polarization branch produced by larger grains and by surface irregularities. At the same time, the position and amplitude of the observed polarization peak and brightness spike for the satellite Europa and the asteroid 64 Angelina are different. Therefore, it is reasonable to assume that even within the framework of the same mechanism of the coherent backscattering enhancement the influence of different properties of particles (albedo, size, refractive index, porosity) may be different for the photometric and polarimetric opposition effects.

REFERENCES

[1] *Domingue D., Hapke B., Lockwood G. W., Thompson D. T.* Europa's phase curve: Implication for surface structure // Icarus.–1991.–**90**.–P. 30–42.

[2] *Harris A., Young J. W., Contreiras L., et al.* Phase relations of high albedo asteroids: the unusual opposition brightening of 44 Nysa and 64 Angelina // Icarus.–1989.–**81**.–P. 365–374.

[3] *Jockers K., Rosenbush V. K., Bonev T., Credner T.* Images of polarization and colour in the inner coma of Comet Hale-Bopp // Earth, Moon, and Planets.–1999.–**78**, Issue 1/3.–P. 381–386.

[4] *Korhonen T., Piirola V., Reiz A.* Polarization measurements at La Silla // ESO Messenger.–1984.–**38**.–P. 20–24.

[5] *Korokhin V. V., Beletsky S. A., Velikodsky Yu. I., et al.* The experience of CCD–photodetectors using on Kharkiv Observatory // Kinematics and Physics of Celestial Bodies.–2000.–**16**.–P. 80–86.

[6] *Mishchenko M. I.* On the nature of the polarization opposition effect exhibited by Saturn's rings // Astrophys. J.–1993.–**411**.–P. 351–361.

[7] *Thompson D. T., Lockwood G. W.* Photoelectric photometry of Europa and Callisto 1976-1991 // J. Geophys. Res.–1992.–**97**.–P. 14761–14772.

[8] *Zellner B., Gradie J.* Minor planets and related objects. XX. Polarimetric evidence for the albedos and compositions of 94 asteroids // Astron. J.–1976.–**81**.–P. 262–280.

NEAR–INFRARED PHOTOMETRIC OBSERVATIONS OF THE INNER JOVIAN SATELLITES

I. Kulyk[1], **K. Jockers**[2], **N. Karpov**[3], **A. Sergeev**[3]

[1] *Main Astronomical Observatory, NAS of Ukraine*
27 Akademika Zabolotnoho, 03680 Kyiv, Ukraine
e-mail: leda@mao.kiev.ua

[2] *Max-Planck-Institut für Aeronomie*
D-37191 Katlenburg-Lindau, Germany
e-mail: jockers@linmpi.mpg.de

[3] *International Center for Astronomical and Medico-Ecological Research*
27 Akademika Zabolotnoho, 03680 Kyiv, Ukraine

The Galileo spacecraft observations reveal the inner moons of Jupiter as sources for the Jovian ring. Therefore, the question of existence and nature of regolith on the surface of these moons should paid more attention. We present the first results of an attempt to observe the opposition surge of these satellites with the 2-m Zeiss RCC telescope of the Terskol Observatory in October and November 1999. Images of Amalthea, Thebe, and Metis were acquired at solar phase angles from –3.3 to +2.5 degrees.
We present the results of the analysis of about 50 images obtained in the methane absorption band and provide absolutely calibrated magnitudes for these three satellites at small solar phase angles.

1. INTRODUCTION

During the Voyager mission, three of four small inner Jovian satellites were discovered.

Following the spacecraft observations, the main Jovian ring and small satellites were detected from the Earth, but these observations were limited because of difficulties caused by the light scattered by Jupiter (Beclin and Wynn-Williams, 1979; Jewitt *et al.*, 1981; Neugebauer *et al.*, 1981; Nicholson *et al.*, 1991). Spacecraft observations were continued with Galileo and HST and our knowledge about sizes, shapes, reflectances of these satellites and the ring structure was improved (Ockert-Bell *et al.*, 1999; Thomas *et al.*, 1998; Meier *et al.*, 1999).

Nevertheless, many specific problems connected with the alteration of the satellite surfaces by interaction with magnetospheric plasma, meteoroid impacts or by implantation of the sulfur ions from Io remain unresolved (Veverka *et al.*, 1986; Thomas *et al.*, 1998). An investigation of the inner moons brightness near their opposition can indicate the differences in their regolith and thus provide information about their environment. We present the first results of photometric CCD observations of Amalthea, Thebe, Metis made at small phase angles from –3.3 to 2.5 degrees.

2. OBSERVATION

We used the 2-m Telescope of the Terskol Observatory equipped with the Two–Channel Focal Reducer of the Max-Planck-Institute for Aeronomy (Küppers and Jockers, 1997). The number of images, the phase angles, and the orbital longitudes covered by the satellites are presented in Table 1.

All observations were performed with red channel of the device. The red channel has a CCD array with 576×406 pixel, the image scale is approximately $0''.83$ per pixel for an overall field of view of $7'.8\times5'.2$. To reduce the flux from Jupiter and the Galilean satellites, a filter consisting of Schott glasses NG1 (1 mm thick) and BG39 (0.3 mm thick) was placed in the Cassegrain focus to cover whole Jupiter's disk (see Küpper and Jockers, 1997). The observations were performed in the methane absorption band at 0.89 μm where the disk of Jupiter is comparatively dark. Each night, the spectrophotometric reference stars ζ Pegasi, $\pi2$ Orioni, $\xi2$ Ceti were observed at different airmasses in order to make the absolute photometric calibration as well as to measure extinction coefficient. Twilight sky was acquired for the flatfield frames. The integration time was from 120 to 300 sec for the frames with satellite images.

The satellite precise positions for the purpose of image identifications were taken from the Horizons Ephemeris System (*horizons@ssd.jpl.nasa.gov*).

Table 1: Summary of Images

Satellite	Date (UT, 1999)	Number of images	Phase angle (deg)	Longitudes covered (deg)
Thebe	23 October	7	0.31	102.9–115.3
	25 October	6	0.57	91.2–106.1
	2 November	5	2.25	290.1–310.1
	2 November	5	2.30	43.9–62.0
Amalthea	13 October	7	–2.27	46.7–82.4
	23 October	2	0.31	110.9–112.8
	2 November	6	2.27	57.2–72.9
Metis	8 October	7	–3.30	90.9–111.31
	2 November	1	2.26	263.1
	2 November	3	2.30	101.0–113.4

3. PROCESSING AND RESULTS

At the first step of image processing we made bias subtraction and flatfield correction for each frame. As it is well known, one of the main difficulties in observing the inner satellites and processing their images is the scattered light from the planet. The light diffracted by the support structure of the secondary mirror was removed by a Lyot stop that placed at the exit pupil of the focal reducer. The remaining aureole has circular symmetry and its brightness depends on the angular distance from the Jupiter's center. To account this part of the scattered light we recalculate each image into polar coordinates. Afterwords the linear interpolation was performed along diameters connecting the background fields on either side of the ring's system with the satellites. Interpolated background was transformed back in to rectangular coordinates and removed from the original image.

For each frame we examined how the total intensity of satellite's or star's image varies as a function of the distance from their center. The center of any image was estimated by two-component Gaussian fit. Aperture photometry was performed on all satellite and reference star images. A round aperture, 10 pixels in the radius, is the most suitable for stars, satellites Amalthea and Thebe. For the innermost satellite Metis it was necessary to decrease the aperture to a radius of 4 pixel. After this we estimated a residual background from an annular aperture with inner and outer radii 12 and 14 pixels respectively and subtracted this background from the total number of counts of a satellite. We performed an absolute photometry by comparing the integrated brightness of each moon image with the brightness of the standard star. The variation of the satellite/star atmospheric extinction is taken into account by means of the extinction coefficient.

The absolute energy distribution for reference stars was taken by Bessel (Bessel, 1999). To account for the filter width, the area of the stellar spectrum under the filter transmission curve was integrated and divided by the width of the filter's pass band.

The satellite magnitudes were reduced to the $r = 1\,\mathrm{AU}$. They are given in Table 2. The internal standard error was calculated by averaging the several frames obtained in the same night neglecting the satellite orbital variations. These errors are included in the table too.

Table 2: Absolute magnitude for Thebe, Amalthea, Metis

Satellite	Elongation	Phase angle (°)	$M(1,\varphi)$ (mag)	rms (mag)
Thebe	E	0.31	7.86	0.05
	E	0.57	7.83	0.06
	W	2.25	8.31	0.10
	E	2.30	7.92	0.08
Amalthea	E	–2.27	6.19	0.04
	E	0.31	6.11	–
	E	2.27	6.24	0.03
Metis	E	–3.30	8.24	0.15
	W	2.26	8.56	–
	E	2.30	8.22	0.17

To derive the phase coefficients of satellite brightness we used all the data available for Amalthea and the images of Thebe obtained near the eastern elongation of the satellite.

The value of the phase coefficient for Amalthea 0.046 ± 0.015 mag/degree is in a good agreement with that obtained by Voyager images for phase angles 0.8–40 degrees and an effective wavelength near 0.48 μm (Veverka *et al.*, 1981). The phase coefficient for Thebe is 0.043 ± 0.021 mag/degree. Both values are comparable with those measured for other objects with rough, very dark surfaces (Clark *et al.*, 1999).

We did not estimate the phase variations of brightness of Metis because lack of the data near opposition. The absolute magnitudes for Metis indicate that the leading side for this satellite is brighter then the trailing one in agreement with Galileo data, but our estimates of the absolute magnitudes point to a higher geometric albedo for 0.89 μm then those derived from Galileo images (Thomas *et al.*, 1998).

4. CONCLUSIONS

Our results are in a good agreement with early measurements that indicate on the increase of a brightness of Thebe and Amalthea from the visible to 0.9 μm (Pascu *et al.*, 1992; Thomas *et al.*, 1998). The phase dependences of brightness at small solar phase angles are similar for Thebe and Amalthea.

The estimations of the brightness of Metis have a preliminary character due to insufficient photometric data for this satellite.

REFERENCES

[1] *Becklin E. E., Wynn-Williams C. G.* Detection of Jupiter ring at 2.2 μm // Nature.–1979.–**279**.–P. 400–401.

[2] *Bessel M. S.* Spectrophotometry: Revised Standards and Techniques // Publs Astron. Soc. Pacif.–1999.–**111**.–P. 1426–1433.

[3] *Clark B. E., Veverka J., Helfenstein P., et al.* NEAR Photometry of Asteroid 253 Mathilde // Icarus.–1999.–**140**.–P. 53–65.

[4] *Jewitt D. C., Danielson E., Terrile R. J.* Groundbased observations of the Jovian rings and inner satellites // Icarus.–1981.–**48**.–P. 536–539.

[5] *Küppers M., Jockers K.* Multi-emission imaging study of the Io plasma torus // Icarus.–1997.–**129**.–P. 48–71.

[6] *Meier R., Smith B. A., Owen T. C., et al.* Near Infrared Photometry of the Jovian Ring and Adrastea // Icarus.–1999.–**141**.–P. 253–262.

[7] *Neugebauer G., Beclin E. E., Jewitt D. C., et al.* Spectra of the Jovian Ring and Amalthea // Astron. J.–1981.–**86**.–P. 607–610.

[8] *Nicholson P. D., Matthews K.* Near-Infrared Observations of the Jovian Ring and Small Satellites // Icarus.–1991.–**93**.–P. 331–346.

[9] *Ockert-Bell M. E., Burns J. A., Daubar I., et al.* The Structure of Jupiter's Ring System as Revealed by the Galileo Imagin Experiment // Icarus.–1999.–**138**.–P. 188–213.

[10] *Pascu D., Panassian S. P., Schmidt R. E., et al.* B, V Photometry of Thebe (JXIV) // Icarus.–1992.–**98**.–P. 38–42.

[11] *Thomas P. C., Burns J. A., Rossier L., et al.* The Small Inner Satellites of Jupiter // Icarus.–1998.–**135**.–P. 360–371.

[12] *Veverka J., Thomas P., Davies M., Morrison D.* Amalthea: Voyager Imaging Results // J. Geophys. Res.–1981.–**86**.–P. 8675–8692.

[13] *Veverka J., Thomas P., Johnson T. V., et al.* The Physical Characteristics of Satellite Surfaces // Satellites / Eds J. A. Burns, M. S. Matthews.–1986.–P. 342–403.

ANALYSIS OF THE SOLAR PHASE CURVES OF THE GALILEAN SATELLITE CALLISTO

V. I. Shavlovskij

Main Astronomical Observatory, NAS of Ukraine
27 Akademika Zabolotnoho, 03680 Kyiv, Ukraine
e-mail: svitaly@mao.kiev.ua

Using long-term photoelectric observations by Shavlovskij and Lockwood *et al.* [7] for solar phase angles from 0 to 12 degree we have obtained Hapke's parameters w, g, h, B_0 of the solar phase functions for the leading and trailing hemispheres of the Jupiter's satellite Callisto. The curve, with parameters determined from the $\lambda\,0.54\,\mu$m ground-based observations in the small range of α, agrees well with the total solar phase functions for both hemispheres measured in the large interval of α (from 10 to 140 degree) during space probe missions.

During past decade many authors (Buratti [1, 2], Domingue *et al.* [3]) have used the photometric observations of the Galilean satellites for determination of such physical properties of the surface of the atmosphereless celestial bodies as porosity, roughness, regolith size distribution. Photometric modeling also describes such material properties as the average single scattering albedo and single scattering functions. Hapke's theory [4, 5, 6] is currently accepted for these purposes. Within the framework of this theory the parameters of the solar phase function are expressed in terms of the physical characteristics of the surface layer. At the same time the characteristics of the leading and trailing hemispheres of Callisto obtained by several authors (Buratti [2], Domingue *et al.* [3]) applying the Hapke's theory are not in agreement. It can be explained by the lack of observations near opposition, the heterogeneity of the data, and the formal procedure of separation of solar and orbital brightness variations.

From 1980 to 1985 years author obtained an extensive set of homogeneous high accurate photometric observations of the Galilean satellites in eleven spectral bands. The observations processed by Lockwood *et al.* [7] have been also used. It should be noted that many observations were carried out near opposition that allows to find reliable parameters of the solar phase functions for the leading and trailing hemispheres of Callisto in four spectral regions.

We introduced an approach to correct the orbital brightness variations. Within this approach it was assumed that surfaces of the leading and trailing hemispheres differ by their (w, g, B_0, h) parameters. We used [2] to estimate the values of the roughness parameters. The contribution of each hemisphere to the total light flux scattered by the surface is accepted to be proportional to the square of the projection of the hemisphere on the image plane. This contribution may be calculated using the Hapke's theory equations for the taken set of the parameters and α, θ values for time of observation. The fact that the geometric albedo value for each hemisphere is directly determined from the observations near α=0° simplifies the search for other parameters. The w, g, B_0, and h parameters were derived from the condition of the best accordance between the model and the observed reflectivity values. The derived values of parameters are presented in Table 1. The data presented in the lines 1–3 are obtained from the observational data by Shavlovskij, those in the lines 4, 5 from Lockwood's data, and finally the data in the line 6 are derived by combining the data in [7] and author's ones.

Analysis of the results in Table 1 shows that the surface of the leading side of Callisto, on the contrary to the surface of the trailing side, consists of particles with more strong backscattering and more porous state. The observational data and model curves at $\lambda = 0.54\,\mu$m are presented in Fig. 1 and Fig. 2. It can be seen in Fig. 3 that the curve with parameters derived from ground-based observations within a small range of α ($< 12°$) reproduces well the solar phase functions of both hemispheres obtained over a large range of α (up to 140°) during space probe missions [2]. This fact confirms the reality of the values of parameters derived by using the high quality ground-based observations.

Table 1: Hapke model parameters for Callisto

hemisphere	Hapke model parameters				λ
	B_0	h	w	g	μm
leading					
1	0.900	0.020	0.350	-0.225	0.346
2	0.925	0.025	0.400	-0.275	0.540
3	1.000	0.040	0.450	-0.200	0.792
4	0.950	0.030	0.337	-0.300	0.470
5	0.900	0.030	0.375	-0.300	0.550
6	0.925	0.025	0.400	-0.275	0.540
trailing					
1	0.800	0.055	0.450	-0.150	0.346
2	0.975	0.045	0.500	-0.175	0.540
3	0.800	0.045	0.600	-0.100	0.792
4	0.975	0.055	0.400	-0.225	0.470
5	0.900	0.045	0.450	-0.225	0.550
6	0.900	0.045	0.500	-0.175	0.540

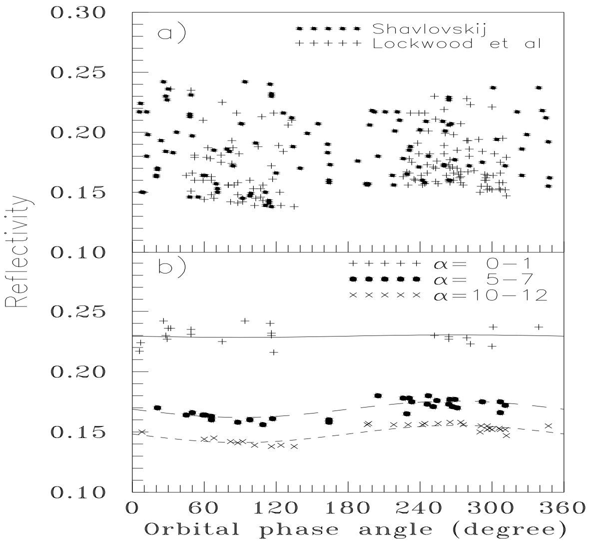

Figure 2: The reflectivity of Callisto at 5400 Å as a function of orbital phase angle. a) Total set of observational data. b) Observational data for a several fixed ranges of the solar phase angle and corresponding model predictions

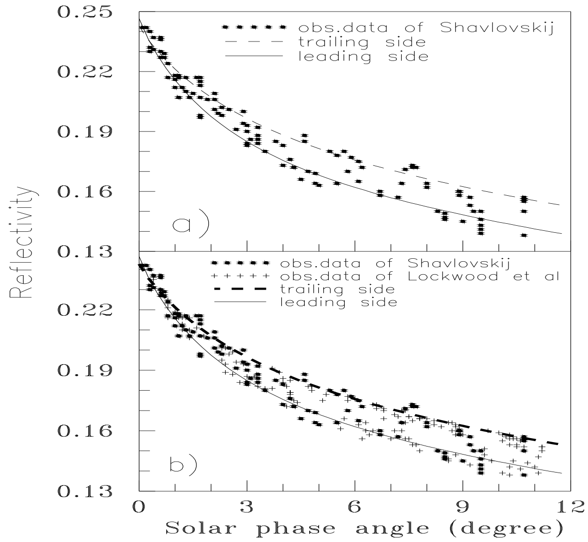

Figure 1: a) The observed reflectivity (points) of Callisto at 5400 Å as a function of solar phase angle. The model predictions are shown by the solid (leading side) and dashed (trailing side) lines. b) The same as in a) but for more extensive observational data set

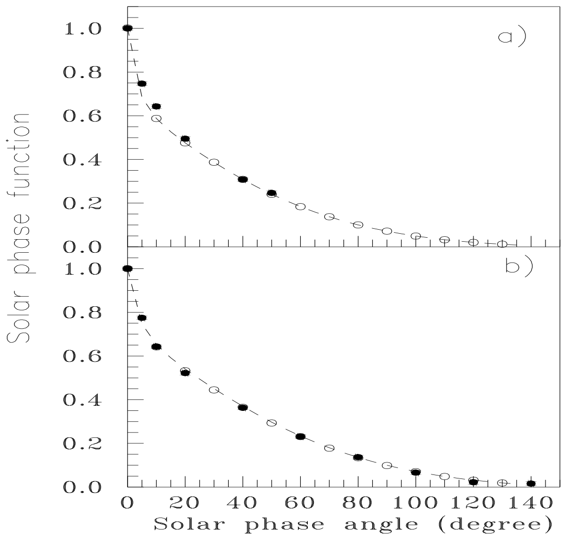

Figure 3: The solar phase function versus solar phase angle for leading (a) and trailing (b) hemispheres of Callisto at 5400 Å. Predictions of two models are shown by the dashed lines. Their parameters are derived by using the observational data by Shavlovskij, the parameters of the model presented by the open circles are based on Shavlovskij & Lockwood data. The Voyager data (filled circles) are shown for comparison

REFERENCES

[1] *Buratti B. J.* Callisto: New evidence for a hemispheric difference in surface texture // Bull. Amer. Astron. Soc.–1989.–**21**, N 3.–P. 983.

[2] *Buratti B. J.* Ganymede and Callisto: surface textural dichotomies and photometric analysis // Icarus.–1991.–**92**, N 2.–P. 312–323.

[3] *Domingue D., Verbiscer A.* Re-analysis of the solar phase curves of the icy galilean satellites // Icarus.–1997.–**89**, N 1.–P. 49–74.

[4] *Hapke B. W.* Bidirectional reflectance spectroscopy. 1. Theory // J. Geophys. Res.–1981.–**86**, N B4.–P. 3039–3054.

[5] *Hapke B. W.* Bidirectional reflectance spectroscopy. 3. Correction for macroscopic roughness // Icarus.–1984.–**59**, N 1.–P. 41–59.

[6] *Hapke B. W.* Bidirectional reflectance spectroscopy. 4. The extinction coefficient and opposition effect // Icarus.–1986.–**67**, N 2.–P. 264–280.

[7] *Lockwood G. W., Thompson D. T.* Photoelectric photometry of Europa and Callisto 1976-1991 // J. Geophys. Res.–1992.–**97**, N E9.–P. 14761–14772.

PRELIMINARY ANALYSIS OF THE SOLAR PHASE CURVES OF THE JUPITER'S SATELLITE GANYMEDE

V. I. Shavlovskij

Main Astronomical Observatory, NAS of Ukraine
27 Akademika Zabolotnoho, 03680 Kyiv, Ukraine
e-mail: svitaly@mao.kiev.ua

The Hapke's model parameters (w, g, h and B_0) were obtained separately for leading and trailing hemisphere of the Jupiter's satellite Ganymede by using the ground-based narrow band photoelectric observations at λ 0.346, 0.540 and 0.792 μm. The values of the obtained parameters confirm existence of hemispherical dichotomies in the photometric characteristics of Ganymede surface. The values of average single scattering albedo w and parameters of the opposition amplitude B_0 increase with increasing wavelength of observation.

The physical properties of the surface of Ganymede have been studied by several authors: Buratti [1], Domingue and Verbiscer [2]. The solar phase curves of Ganymede have been modeled by using the Hapke's theory [3, 4, 5].

Buratti [1] used a combination of telescopic observations and measurements from the Voyager images. She did not find any hemispherical differences on Ganymede. Buratti [1] attributed these results to a balance of magnetospheric interactions on the trailing hemisphere with micrometeoritic bombardment on the leading hemisphere.

Reanalysis of the solar phase curves of Ganymede by Domingue and Verbiscer [2] demonstrates that the trailing hemisphere of satellite is rougher than the leading hemisphere by about 6°. The results of Domingue and Verbiscer [2] indicate that the leading hemisphere of Ganymede is much more porous than the trailing hemisphere; at 0.55 μm both hemispheres are predominately backscattering with a little difference between them. These conclusions disagree with Buratti [1] results.

A possible reason of the discrepancy between the parameters derived by Domingue and Verbiscer [2] and those by Buratti [1] is that their curves are based on a few number of observations near opposition.

During 1980–1985 years the author obtained an extensive set of homogeneous high accurate photometric observations of Ganymede by using 11 narrow band filters. We have carried out quite a number of observations

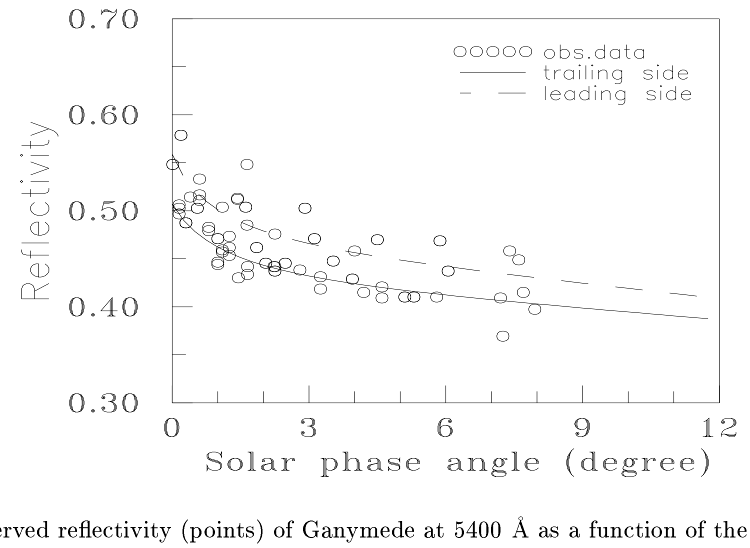

Figure 1: The observed reflectivity (points) of Ganymede at 5400 Å as a function of the solar phase angle. The model predictions are shown by the solid (trailing side) and dashed (leading side) lines

Table 1: Hapke model parameters for Ganymede

hemisphere	Hapke model parameters					λ
	B_0	h	w	g	$\bar{\theta}°$	μm
leading	0.330	0.008	0.890	-0.230	28	0.346
	0.360	0.008	0.866	-0.250	29	0.346
	0.400	0.010	0.910	-0.270	28	0.540
	0.467	0.009	0.943	-0.217	29	0.540
	0.470	0.008	0.920	-0.240	28	0.792
	0.470	0.010	0.910	-0.250	29	0.792
trailing	0.300	0.010	0.878	-0.140	35	0.346
	0.300	0.012	0.878	-0.140	29	0.346
	0.450	0.012	0.920	-0.200	35	0.540
	0.533	0.014	0.930	-0.158	29	0.540
	0.450	0.014	0.930	-0.160	35	0.792
	0.450	0.014	0.930	-0.150	29	0.792

near opposition. A new approach to correct the observed orbital brightness variations has been proposed by the author.

The surfaces of the leading and trailing hemispheres differ by their properties, therefore an individual set of Hapke's parameters was taken for every side. The contribution of each hemisphere to the total light flux scattered by the surface is accepted to be proportional to the square of the projection of the hemisphere on the image plane. This contribution may be calculated by using the Hapke's theory equations for any sets of parameters and α, θ values during the observation.

The w, g, B_0, and h parameters were derived from the condition of the best fit of this model with observed values of the reflectivity. The derived values of parameters are presented in Table 1. The values of the roughness parameters $\bar{\theta}$ have been taken for leading and trailing hemisphere by Buratti [1] (29° and 29°) and by Domingue and Verbiscer [2] (28° and 35°).

The observational data and model curves of leading and trailing sides at λ 0.54 μm are presented in Fig. 1.

Analysis of the results in Table 1 shows that the surface of the leading side of Ganymede consists of particles with more strong backscattering and more porous state then those on the surface of the trailing side. The values of the average single scattering albedo (w) and the parameters of the opposition amplitude (B_0) increase with increasing the wavelength of observation.

Our results contradict to Buratti [1] conclusions and confirm the existence of hemispherical dichotomies in the photometric characteristics of the Ganymede surface [2].

REFERENCES

[1] *Buratti B. J.* Ganymede and Callisto: surface textural dichotomies and photometric analysis // Icarus.–1991.–**92**, N 2.–P. 312–323.

[2] *Domingue D., Verbiscer A.* Re-analysis of the solar phase curves of the icy galilean satellites // Icarus.–1997.–**128**, N 1.–P. 49–74.

[3] *Hapke B. W.* Bidirectional reflectance spectroscopy. 1. Theory // J. Geophys. Res.–1981.–**86**, N B4.–P. 3039–3054.

[4] *Hapke B. W.* Bidirectional reflectance spectroscopy. 3. Correction for macroscopic roughness // Icarus.–1984.–**59**, N 1.–P. 41–59.

[5] *Hapke B. W.* Bidirectional reflectance spectroscopy. 4. The extinction coefficient and opposition effect // Icarus.–1986.–**67**, N 2.–P. 264–280.

FRICTION EFFECT IN A SPHEROIDAL ENVELOPE ON THE MODIFICATION OF ORBITAL ELEMENTS OF PARTICLES

A. A. Tereshchenko

Uman' Pedagogical University
2 Sadova St., 20300 Uman', Ukraine

Effect of a spheroidal spinning envelope on the modification of orbital elements of a particle moving in a central gravitational field is considered. The resistance force is considered as a small perturbation; the envelope's self-gravitating is negligible.

The self-gravitating systems during their evolution may be separated into a central body and a peripherals in the form of rings, disks or spheroidal envelopes as a result of a global instability. Such phenomena are observed in galaxies, globular stellar clusters, and interstellar medium clouds [2, 3, 5]. The Oort's cloud is likely a formation of such a kind [1, 6]. If a particle moves around a central body and crosses a spheroidal envelope, which surrounds this body, then a friction caused by the envelope matter have to act on the particle. In this connection we consider the problem of influence of the friction on the orbital elements of a particle moving in the central gravitational field.

As a simplest model let's take a central body as a point gravitating center, mass M of which is much greater than the envelope mass, which is negligible. Let's image the envelope as a spheroidal stratum having the internal and external radii r_1 and r_2, respectively (see Fig. 1). Such on equilibrium form can be supported by self-rotation of the envelope, gravitational forces, intrinsic pressure, and magnetic fields. Let us suppose the friction force to be depended on the relative velocity $\vec{v}$ of a particle and envelope's matter as well as on the distance r between the particle and the gravitating center: $\vec{R} = -c\dfrac{v^\alpha}{r^\beta}\dfrac{\vec{v}}{v}$, where α, β are constants, c is a coefficient that is small enough to consider the friction force as a small perturbation in comparison with the gravitational force.

Let's consider firstly a stationary (*i.e.*, non-rotating) envelope. Since the resistance force is tangent directional to the particle's trajectory then the Lagrange equation for the major semi-axis a and the eccentricity e can be converted to the form [4]:

$$\frac{da}{dr} = -\frac{2Ra^2\sqrt{r\,(2a-r)}}{GM\cdot\xi}, \quad \frac{de}{dr} = -\frac{2Ra\left(1-e^2\right)\sqrt{r}}{GM\cdot e\xi\sqrt{2a-r}}, \tag{1}$$

where $\xi = \sqrt{(ae)^2 - (a-r)^2}$; R is the value of the resistance force, M is the mass of the central body.

Since friction is considered as a small perturbation then values of a and e vary weakly inside the envelope and can be regarded as constants while $r_1 < r < r_2$. Substituting the values of a and e that describe the orbit before the particle enters the envelope and integrating the right parts of (1) one can obtain the first approximation of modifications of a and e after passing the envelope by the particle:

$$\Delta a \approx \int_{r_1}^{r_2} -\frac{2Ra^2\sqrt{r\,(2a-r)}}{GM\cdot\xi}dr, \quad \Delta e \approx \int_{r_1}^{r_2} -\frac{2Ra\left(1-e^2\right)\sqrt{r}}{GM\cdot e\xi\sqrt{2a-r}}dr. \tag{2}$$

Thus, Δa and Δe depend on the resisting force, size of the envelope and initial values of a and e. Antiderivatives of definite integrals (2) are represented in Table 1.

If the particle passes consequently through the envelope then it lose its energy and major semi-axis of the orbit decreases, but the intersection point of the orbit and the envelope moves to the orbit's apocenter. Thus, any stage of decreasing of eccentricity down to some critical value have to become the stage of its continuous increasing.

Table 1: Modification of the major semi-axis and the eccentricity in a case of non-rotating envelope

$R=cv$	$\Delta a = k\,a^{3/2}\left(a\eta-\xi\right),$	$\Delta e = k\gamma^2\xi e^{-1}$
$R=cvr^{-1}$	$\Delta a = ka^{3/2}\left(2\zeta\gamma^{-1}-\eta\right),$	$\Delta e = k\sqrt{a}\left(1+e\right)\,e^{-1}\left(\zeta-\eta\gamma\right)$
$R=cvr^{-2}$	$\Delta a = k\sqrt{a}\left(1+e^2\right)\,\gamma^{-2}\left(\zeta\gamma^{-1}+2\xi r^{-1}\right),$	$\Delta e = ka^{-1/2}e^{-1}\left(e^2\gamma^{-1}\zeta-\xi r^{-1}\right)$
$R=cv^2$	$\Delta a = 2ace^{-1}\left(E\left(e,x\right)-2F\left(e,x\right)-\tau\right),$	$\Delta e = ce^{-2}\gamma^2\left(2E\left(e,x\right)-2F\left(e,x\right)-\tau\right)$
$R=cv^2r^{-1}$	$\Delta a = ce^{-1}\left[6F\left(e,x\right)-8E\left(e,x\right)\,\gamma^{-2}+\tau+8\lambda\sqrt{1-ex}\,\chi\,\gamma^{-2}e^{-1}\right]$	$\Delta e = -ce^{-2}a^{-1}\left[4E\left(e,x\right)-4F\left(e,x\right)\,\gamma^2-\gamma^2\tau-4\lambda\sqrt{1-ex}\,\chi e\right]$
$R=cv^2r^{-2}$	$\Delta a = \frac{2}{3}ca^{-1}\gamma^{-4}\left[\left(3e^2+5\right)\gamma^2e^{-1}F(e,x)-8\left(1+e^2\right)e^{-1}E(e,x)-4\chi\sqrt{1+ex}\left(2ex\gamma^2+e^2+3\right)\lambda^{-3}\right]$	$\Delta e = -\frac{2}{3}c\,\left(ea\gamma\right)^{-2}\,\left[E\left(e,x\right)\,\left(1+7e^2\right)-F\left(e,x\right)\,\left(3e^2+1\right)+e\chi\,\left(1-ex\right)^{-1}\,\lambda^{-1}\,\left(7e^3x-5e^2+ex-3\right)\right]$

Used designations: $\xi=\sqrt{\left(ae\right)^2-\left(a-r\right)^2}$; $\zeta=\arcsin\left(\frac{r+a\,\left(1-e^2\right)}{re}\right)$; $\eta=\arcsin\left(\frac{a-r}{ae}\right)$; $k=-\frac{2c}{\sqrt{GM}}$; $\gamma=\sqrt{1-e^2}$; $x=(1-r/a)/e$; $\chi=\sqrt{1-x^2}$; $\lambda=\sqrt{1-\left(ex\right)^2}$; $\tau=\ln 2-\ln\left(2ex^2-e-e^{-1}+2\chi\lambda\right)$; $F\left(...\right)$ and $E\left(...\right)$ are elliptical integrals of the first and second kinds.

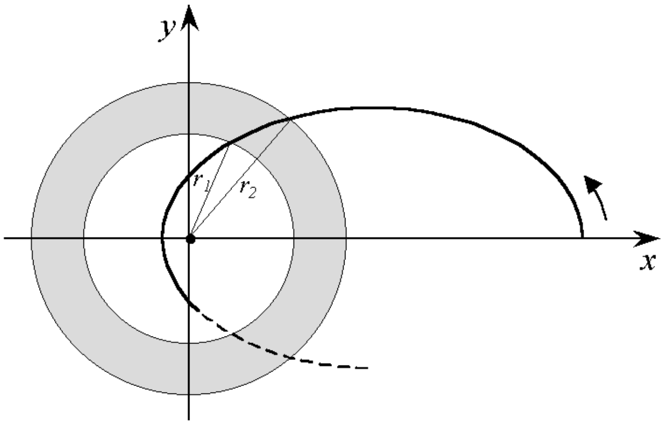

Figure 1: Particle passes trough the envelope

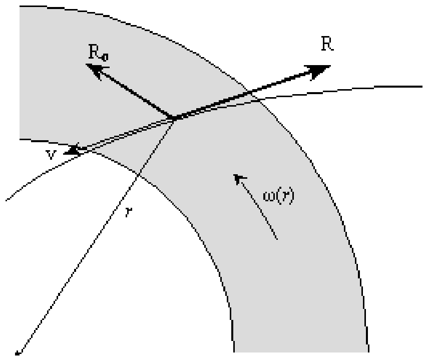

Figure 2: Resistance force components

Now we consider passing of a particle through a self-rotating envelope. Such an envelope acquires its spheroidal form due to self-rotation, but if one limits oneself with orbits lying in the equatorial plane then nonsphericity is negligible. A new transversal force appears due to the axial rotation (see Fig. 2). It produces the additional increments of the major semi-axis and eccentricity that can be found from the Lagrange's equations:

$$\Delta a^*\approx-\int\limits_{r_1}^{r_2}\frac{2a^3R'_\varphi\sqrt{1-e^2}}{GM\cdot\xi}\,dr,\quad \Delta e^*\approx\int\limits_{r_1}^{r_2}\frac{R'_\varphi\sqrt{1-e^2}\left(r^2-a^2\left(1+e^2\right)\right)}{GM\cdot\xi}dr. \tag{3}$$

Thus, now the full modifications of a and e are equal to $\Delta a+\Delta a^*$ and $\Delta e+\Delta e^*$. The force component

Table 2: Additional modification of the major semi-axis and the eccentricity in case of rotating envelope

$R = cv$	$\omega\ (r) = \sqrt{GM} \cdot r^{-3/2}$	$\Delta a^* = -\frac{1}{3}\, k\, a^{5/2} e^{-1} \sqrt{1-e}\,[-E\,(\rho_1, \sigma_1)\ (3e+1) + F\,(\rho_1, \sigma_1)\ (1-e) - (E\,(i\rho_1, i\sigma_2)\ (3e+1)\ (e-1) + F\ (i\rho_1, i\sigma_2)\ (1+e)\ (5e+1))\ \gamma^{-2}]$ $\Delta e^* = -\frac{1}{3}\, k\, \gamma\, a^{3/2}\, e^{-1}\ \left[3\ (1+e)^{3/2}\, E\,(\rho_1, \sigma_1) - E\,(i\rho_2, i\sigma_1)\ \sqrt{1-e}\,(1-3e) + 3F\,(\rho_1, \sigma_1)\ \sqrt{1+e}\,(e-1) + F\,(i\rho_1, i\sigma_2)\ \sqrt{1-e}\,(1+e) + \sqrt{r}\ \xi\right]$
	$\omega\ (r) = \omega_0 \cdot r^{-1}$	$\Delta a^* = -2c\mu^{-1}\omega_0 a^3 \gamma\eta,$ $\Delta e^* = \frac{1}{2}\, c\ (\mu e)^{-1}\ \gamma\, \omega_0 \left[\, (r+3a)\ \xi + 3a^2 e^2 \eta\right]$
	$\omega\ (r) = \omega_0 = const$	$\Delta a^* = -2c\mu^{-1}\omega_0 a^3\ (\xi + a\eta)\,,$ $\Delta e^* = -\frac{1}{6}\, c\, \omega_0\, (\mu e)^{-1}\ \gamma\ \left[\, 15a^3 e^2 \eta + \xi\ \left(r\ (2r+5a) + 5a^2\ \left(1+2e^2\right)\right)\right]$
$R = cv^2$	$\omega\ (r) = \sqrt{GM} \cdot r^{-3/2}$	$\Delta a^* = 2ca^2\zeta, \quad \Delta e^* = -ce^{-1}\gamma\ (a\eta - a\zeta\gamma - \xi)$
	$\omega\ (r) = \omega_0 \cdot r^{-1}$	$\Delta a^* = 2c\mu^{-1} a^3 \omega_0^2 \gamma\eta,$ $\Delta e^* = -\frac{1}{2}\, c\, \omega_0^2\, \gamma\ (\mu\, e)^{-1}\ \left[(r+3a)\ \xi + 3a^2 e^2 \eta\right]$
	$\omega\ (r) = \omega_0 = const$	$\Delta a^* = -c\mu^{-1}\gamma\, a^3 \omega_0^2\ \left[\, a^2\ \left(e^2+2\right)\ \eta + \xi\ (r+3a)\right]$ $\Delta e^* = \frac{1}{8}\, c\, (\mu e)^{-1}\ \omega_0^2 \gamma\ \left[7a^4 e^2\ \left(4+e^2\right)\ \eta + \frac{1}{3}\, \xi\ \left(6r^3 + 14a\ \left(r^2 + ra + a^2\right)\right) + 7a^2 e^2\ (13a+3r)\right]$
Used designations: $\rho_1 = \sqrt{\frac{2e}{1+e}}$; $\rho_2 = \sqrt{\frac{2e}{1-e}}$; $\sigma_1 = \sqrt{\frac{a\,(1+e)-r}{2ae}}$; $\sigma_2 = \sqrt{\frac{r-a\,(1-e)}{2ae}}$.		

R'_φ depends on the additional relative velocity of the particle and envelope's matter introduced by rotation: $R'_\varphi = c\ (\omega\,(r)\, r)^\alpha \cdot r^\beta$, where $\omega\,(r)$ is the distribution of the angular velocity of envelope's matter in the equatorial plane. Table 2 gives antiderivatives for the integrals in (3).

If the envelope's matter rotates by the Keplerian law $\omega\,(r) \sim r^{-3/2}$ then the orbit changes and the particle can be rotating by on a circular orbit inside the envelope. In the case of rotation by the law $\omega\,(r) \sim r^n\ (-3/2 < r < 0)$ the orbit turns into a quasi-stationary state when modifications of the major semi-axis and the eccentricity become small, but the orbit become elliptical and its apocenter lies inside the envelope.

REFERENCES

[1] *Vitiazev A. V., Pechernikova G. V., Safronov V. S.* The Earth-like planets: origin and early evolution.–Moscow, 1990.–296 p. (in Russian).

[2] *Efremov Yu. N.* Star formation zones in galaxies: star complexes and spiral arms.–Moscow: Nauka, 1989.–248 p. (in Russian).

[3] *Ogorodnikov K. F.* Dynamics of stellar systems .–Moscow: Gos. izd. fiz.-mat. lit., 1958.–627 p. (in Russian).

[4] *Roy A. E.* Orbital motion.–Bristol: Adam Hilger Ltd, 1978.–544 p.

[5] *Thompson J. M. T.* Instabilities and catastrophes in science and engineering.–Chichester–New York–Brisbane–Toronto–Singapore: A Wiley-Interscience Publ., 1982.–254 p.

[6] *Churyumov K. I.* The comets and its observation.–Moscow, 1980. (in Russian).

EXTERNAL GRAVITATIONAL POTENTIAL OF GIANT PLANETS WITH THE POTENTIAL OF THE SYSTEM OF INHOMOGENEOUS SELF–GRAVITATING DISKS

O. V. Zavizion

Uman' Pedagogical University
2 Sadova St., 20300 Uman', Ukraine

We introduce parameters of the systems of inhomogeneous disks, which can describe the external gravitational potentials of giant planets. Dynamical characteristics of giant planets were taken from the astronomical observational data. We assumed that giant planets have figures close to equilibrium ones.

There are various methods of description of gravitational potentials of volume bodies [1]. The description based on the potential of a simple fiber (disk) is quite effective. When using such a model, number of dimensions of a body reduces in fact that allows to simplify the expression for the gravitational potential. If one applies this method to planets of the solar system then it's necessary to divide the planet's figure into some ellipsoidal strata. Then, according to the potential theory, one have to find an equivalent disk for each stratum and collect all the disks into a system.

It's known [6, 7] that the external gravitational potential of a homogenous oblate ellipsoid of revolution can be exactly described like the external potential of a real inhomogeneous circular thin disk having the radius

$$R_x = \left(a^2 - c^2\right)^{1/2} \tag{1}$$

and surface density distribution

$$\sigma(R) = \sigma_0 \left(1 - \frac{R^2}{R_x^2}\right)^{1/2}, \tag{2}$$

where $\sigma_0 = \dfrac{2a^2 c\rho}{a^2 - c^2}$; a and c are the major and minor semi-axes of ellipsoid, ρ is the volume density.

If one divides the planet's figure into some homogenous ellipsoidal strata having their own densities ρ_i and oblatenesses f_i, *i.e.*, as a figure composed of some homogenous ellipsoids of revolution, then it will be possible to describe the external gravitational potential of a planet exactly as a sum of the external potentials of inhomogeneous circular disks obtained by fitting the disks' parameters.

According to the proposed algorithm, let us compose a multi-layer ellipsoidal model of a planet using parameters of the internal structure of giant planets [2, 3, 5]. Let divide the planet's figure into some homogenous strata and satisfy the condition of mass parity

$$M = \sum_{i=1}^{n} M_i, \tag{3}$$

where M is the planet's mass; $M_i = \dfrac{4\pi}{3}\left(\rho_i - \rho_{i+1}\right) R_i^3$, $\rho_{n+1} = 0$ are the masses of the homogenous ellipsoids of revolution composed the planet's figure; $R_i = \sqrt[3]{a_i^2 c_i}$ is the equivalent radius of a sphere; n is the number of strata. Then let us determine geometrical oblateness of each stratum from the solution of the Clairaut equation (4). Equilibrium planets' figures have to satisfy it but the figures of giant planets are only closed to equilibrium ones [8].

$$\frac{d^2 f}{dr^2} + \frac{6}{r}\frac{\rho}{D}\frac{df}{dr} - \frac{6}{r^2}\left(1 - \frac{\rho}{D}\right) f = 0, \tag{4}$$

where $D = D(r) = \frac{3}{r^3}\int\limits_0^r \rho r'^2 dr'$ is the average density of a sphere of radius r.

The initial conditions on the external surface for finding the oblateness f are following:

$$f\,|_{r=R} = f_0, \quad \left.\frac{df}{dr}\right|_{r=R} = \frac{1}{R}\left(\frac{5}{2}m - 2f_0\right),$$

where f_0 is the surface oblateness of a planet; $m = \dfrac{\omega^2 R^3}{GM}$; ω is the angular velocity of the planet's self-rotation.

The defined model parameters are given in Table 1 (columns from 1 to 4).

Table 1: Parameters of models of giant planets

Stratum number i	Average radius R_i, km	ρ_i, g/cm^3	F_i	Disk number m	R_{xm}, km	σ_{0m}, 10^{11} g/cm^2
			Jupiter			
1	4893	12.60	0.00429	1	453.17	4.678
2	9086	8.50	0.00976	2	1270.72	5.900
3	53818	2.15	0.03431	3	14139.60	2.105
4	63604	0.80	0.05102	4	20409.00	0.531
5	69894	0.37	0.06487	5	25462.36	0.390
			Saturn			
1	5247	9.08	0.00874	1	694.25	2.361
2	18073	5.14	0.02132	2	3738.31	2.855
3	28267	1.76	0.04829	3	8919.32	0.287
4	39644	1.27	0.07168	4	15108.85	0.595
5	58300	0.18	0.09500	5	25639.85	0.108
			Uranus			
1	8122	4.37	0.00902	1	1091.85	1.681
2	19543	2.50	0.01350	2	3214.77	3.438
3	25380	0.12	0.02070	3	5192.48	0.145
			Neptune			
1	12311	4.99	0.01197	1	1907.08	2.422
2	19205	2.63	0.01500	2	3330.47	3.130
3	24622	0.18	0.01710	3	4560.24	0.258

Using obtained results, one can compute parameters of inhomogeneous disks by formulas:

$$R_{xm} = \sqrt{a_m^2 - c_m^2}, \quad \sigma_{0m} = \frac{2a_m^2 c_m\left(\rho_m - \rho_{m+1}\right)}{a_m^2 - c_m^2}, \quad \rho_{n+1} = 0, \quad m = 1,\,\ldots,\,n. \tag{5}$$

Then models of systems of inhomogeneous self-gravitating disks can be composed to describe the external gravitational potentials of planets (see Table 1, columns from 5 to 7).

A criteria of the estimated accuracy of description of the external gravitational potentials of planets is a correspondence of the dynamical characteristics (6)–(7) of the models [4] and the data of astronomical observations (see Table 2).

$$V = \frac{GM}{r}\left\{1 - \sum_{k=1}^{\infty} J_{2k}\cdot P_{2k}\left(\cos\theta\right)\cdot\left(\frac{a_e}{r}\right)^{2k}\right\}, \tag{6}$$

$$J_{2k} = (-1)^{k+1}\,\frac{3}{(2k+1)\,(2k+3)}\,\frac{\sum\limits_{i=1}^{n} M_i\left(a_i^2 - c_i^2\right)^k}{Ma^{2k}}, \tag{7}$$

where $P_{2k}(\cos\theta)$ are the odd Legendre's polynomials; J_{2k} are the odd gravitational moments of the models; (r, φ, θ) are the spherical coordinates of the point where such a potential is found.

Table 2: Dynamical characteristics of giant planets (J_{2n} are the observational values; J^*_{2n} are the values computed from composed models)

Parameter	Jupiter	Saturn	Uranus	Neptune
$M, 10^{26}$ kg	18.97	5.68	0.8687	1.0243
a_e, km	71492	60268	25559	24764
m	0.083	0.139	0.0285	0.0259
$J_2 \cdot 10^2$	1.4697±0.0001	1.6331±0.0018	0.351323±0.000032	0.3539±0.0010
$J^*_2 \cdot 10^2$	1.47	1.63	0.351	0.353
$J_4 \cdot 10^4$	–5.84±0.05	–9.14±0.61	–0.319±0.005	$-0.28 \begin{smallmatrix} +0,12 \\ -0,20 \end{smallmatrix}$
$J^*_4 \cdot 10^4$	–5.85	–9.12	–0.322	–0.313
$J_6 \cdot 10^5$	3.1±2.0	10.8±5.0	0.021÷0.067	
$J^*_6 \cdot 10^5$	3.475	8.03	0.04784	

It follows from the fulfilled computations that the description of the external gravitational potential as the potential of a system of inhomogeneous self-gravitating disks is an effective method to be applied for problems of celestial mechanics and astronomical geodesy. The appeared discrepancies between the values of gravitational moments are explained by heterogeneity of internal structure and by absence of information about geometrical oblateness of internal strata of giant planets. The mean relative error of determination of the first gravitational moments is as follows $\delta(J_2) = 0.02\%$, $\delta(J_4) = 0.17\%$ for Jupiter, $\delta(J_2) = 0.19\%$, $\delta(J_4) = 0.22\%$ for Saturn, $\delta(J_2) = 0.09\%$, $\delta(J_4) = 0.94\%$ for Uranus, $\delta(J_2) = 0.25\%$ for Neptune. They were calculated by comparison with the astronomical observational data. It is impossible to check the calculated higher gravitational moments because of the lack of reliable astronomical data.

REFERENCES

[1] *Antonov V. A., Timoshkova E. I., Kholshevnikov K. V.* Introduction to the Newton's theory of potential.–Moscow: Nauka, 1988.–272 p. (in Russian).

[2] *Gudkova T. V., Zharkov V. N.* // Pis'ma v Astron. Zh.–1993.–**19**, N 2.–P. 153–159. (in Russian).

[3] *Gudkova T. V., Zharkov V. N.* // Pis'ma v Astron. Zh.–1996.–**22**, N 1.–P. 66–80. (in Russian).

[4] *Duboshin G. N.* The theory of attraction.–Moscow: Fizmatgiz, 1961.–288 p. (in Russian).

[5] *Zharkov V. N.* // Astron. Vestnik.–1991.–**25**, N 6.–P. 627–649. (in Russian).

[6] *Zavizion O. V.* // Astron. School's Rep.–2000.–**1**, N 1.–P. 82–85. (in Ukrainian).

[7] *Meshcheriakov G. A.* Problems of the theory of potential and the generalized Earth.–Moscow: Nauka, 1991.–216 p. (in Russian).

[8] *Morits G.* The Earth's figure: theoretical geodesy and the inner structure of the Earth.–Kyiv, 1994.–240 p. (in Russian).

ON THE NATURE OF REGULARITIES IN THE RADIAL STRUCTURE OF SATURNIAN RINGS

Yu. K. Gulak[1], **I. A. Dichko**[2]

[1] *Gravimetrical Observatory, NAS of Ukraine, 36029 Poltava, Ukraine*
[2] *Poltava Military Institute of Communication, Poltava, Ukraine*

The theory [1] based on the consideration of a cosmic planetary system (PS) as a spatially limited oscillating system with many degrees of freedom predicts the formation of annular features of the type of radial standing waves (SW). The gravitating matter consisting bodies (satellites) of different sizes accumulates itself in the SW nodes and loops as in peculiar traps. The matter of Saturnian system that consists of different bodies is of undoubted interest from this point of view. The theory permits to obtain a wave length (WL) of the principal mode of SW in dependence on the central body's mass M: $a = \beta M^{7/9}$, where β is the integrating constant. In particular for the system of Saturn $a_h = 74739$ km. A radial matter distribution in the Saturnian rings corresponds to the SW properties adduced below:

1. WL of the structural features and their nodes and loops positions are stable during a long time. The D, C, B and A Rings can be considered as harmonics with a wave length $a_5 = a_h/5 = 14948$ km. Its nodes coincide with the edges of the A, B and C Rings and with the B Ring middle, which separates the inner and outer halfs of that Ring essentially different by the optical depth and structure [4] (see table). Analogous structures are appeared within the asteroidal belt [2].

2. Within the principal mode of SW a set of all higher harmonics is generated. SW with the WL $a_{70} = a_h/70 \approx 1000$ km is displayed within the C Ring and with the WL $a_{180} \approx 400$ km within the Cassini Gap. Though, these small structures have to be formed also as independent SW within the limiting bounds of the larger features (including C Ring and Cassini Division too). Under such conditions more small structures are divided into more and more finest ones. Such peaked oscillations of the optical depth (W-features) are observed through the whole width of the Rings down to the resolution limit of the Voyager TV system (Fig. 1). The F Ring displays more than ten fine density waves within 60 km width and its denser part has the same

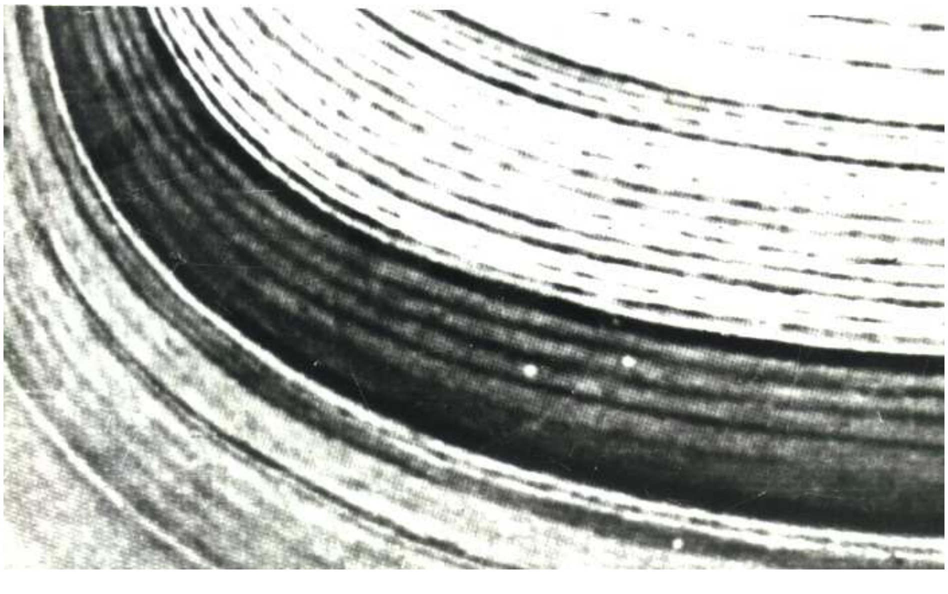

Figure 1: Image of the part of Saturnian rings composed by computer according to Voyager-2 data. Cassini Division is more dark

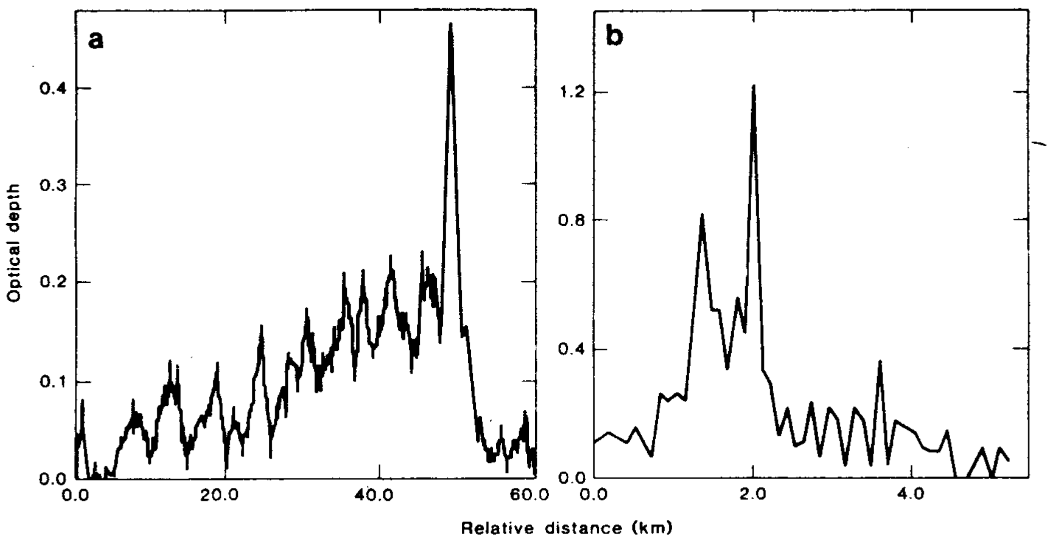

Figure 2: Optical depth of the F Ring (a) and its thickest part (b) [6]

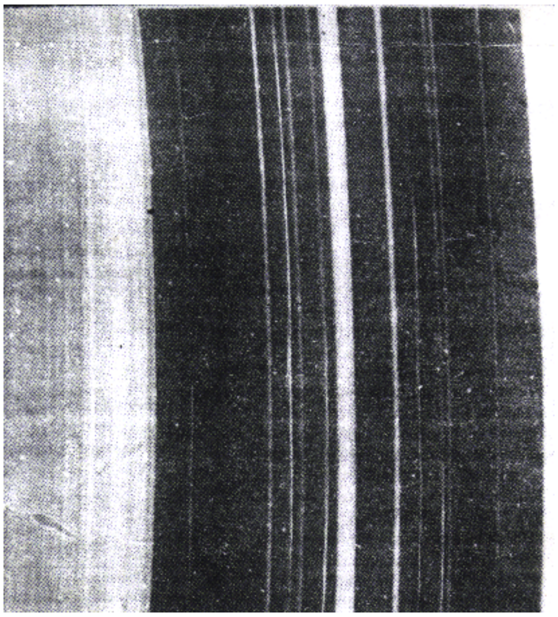

Figure 3: Encke Division with the inner ringlets [6]

quantity of the thickenings and rarities (Fig. 2) within 5 km. There are an evident dense central ringlet and many fine ringlets on the commensurable distances in the Encke Division (328 km width) (Fig. 3).

3. Wherever polydisperse matter is to be presented, its separation have to take place in accordance with its pliability (inertness) to perturbations. Analysis [4] of the Voyager observations shows an increase of the number of fine particles on the edges of the A and B Rings. Ultra-violet's absorption is found within the Cassini Gap in the nodes of the above mentioned a_{180} wave, while a radio signal passes it without losses [5, 7]. A dusty substance is seen as bright belts outside the A and B Rings and in the Cassini Gap on the images obtained by Pioneers on the dark side in the diffused light. Analogous separation of the large and small matter fractions are appeared also within the asteroidal belt [3].

	n	$a_t = a_h + na_h/5$, 10^3 km	Obs	$a_0 - a_t$
D Ring inner edge	–0.5*	67.2	67.0	–0.2
C Ring inner edge	0	74.7	74.5	–0.2
B Ring inner edge	1	89.7	92.0	2.3
B Ring middle	2	104.6	104.0	–0.6
A Ring inner edge (Cassini Gap middle)	3	119.6	119.8	–0.2
A Ring outer edge	4	134.5	136.8	2.3

* – Mode of the higher degree.

We explain some discrepancies by the influence of other structural mechanisms, *e.g.*, by tides and resonances with the satellite's distances. That's why SWs are not displayed clearly everywhere or displayed with broken regularities.

REFERENCES

[1] *Gulak Yu. K.* On Commensurabilities (Resonances) in the Solar System // Sov. Astron.–1980.–**24**, N 1.–P. 84–90. (in Russian).

[2] *Fedij P. M., Gulak Yu. K., Eremin V. I.* Statistical analysis of gravitating substance distribution in the Solar System // this issue.–P. 248–250.

[3] *Gulak Yu. K.* // Astron. Tsircular.–1982.–N 1233.–P. 4–8. (in Russian).

[4] *Esposito L. W., Cuzzi J. N., Holberg J. B., et al.* Saturn's Rings. In: Saturn (Eds T. Gehrels, M. S. Matthews).–Tuscon, Arisona Univ. Press, 1984.–P. 463–543.

[5] *Esposito L. W., O'Callaghan M., Simmons K. E., et al.* Voyager Photopolarimeter Stellar occultation of Saturn's Rings // J. Geophys. Res.–1983.–**88**, N A11.–P. 863–869.

[6] *Lane A. L., Hord W., West R., et al.* Photopolarimetry from Voyager 2 // Science.–1982.–**215**, N 4532.–P. 537–543.

[7] *Tyler G. L., Marouf E. A., Simpson R. A., et al.* The Microwave Opacity of Saturn's Rings // Icarus.–1983.–**54**.–P. 160–188.

STATISTICAL ANALYSIS OF GRAVITATING SUBSTANCE DISTRIBUTION IN THE SOLAR SYSTEM

P. M. Fedij[1], **Yu. K. Gulak**[2], **V. I. Yeremin**[3]

[1] *Pedagogical University, Poltava, Ukraine*
[2] *Gravimetrical Observatory, NAS of Ukraine, Poltava, Ukraine*
[3] *Institute of Magnetism, NAS of Ukraine, Kyiv, Ukraine*

The article presents a statistic estimation of the correlation between the existing radial distribution of gravitating substance in the Solar System and the series of the $a_n = na_0/2$ values ($n = 2, 3, 4, \dots$). This correlation has been predicted theoretically by Gulak (1980). The average orbital semi-major axes by Bretagnon were used for eight planets (except Pluto) while for 11 statistically significant asteroidal complexes (AC), which we have found out throughout the whole asteroidal belt by three independent methods of restoring the probability density function, maxima of this function were taken. These methods are: 1) the Parsen-Rozenblatt's algorithm with exponential kern (Milen'kiy, 1983); 2) the method of separation of distributions in a mixture (Ayvasian, 1974); 3) the method of non-parametrical estimation of unknown probability density function (Vapnik, 1984). There is a good agreement of all the received results. Fig. 1 represents results of the first method used. For the final analysis we prefer the values of maxima derived by the second method, which are as more adequate, in our opinion, to the classification problem.

The optimal value $a_0 = 0.2726$ AU of the commensurable element was found by minimizing two different norms of deviation. A comparison of the empirical values a_* of the orbital semi-major axes with those of "theoretical" a as well as the corresponding quantum integers n with the empirical fractional values $n_* = 2a_{*n}/a_0$ for the planets and asteroidal complexes of the Solar System are shown in the table.

Deviations Δn of the fractional empirical values n_* from the expected quantum integers n are normally distributed ($P(\tilde{\chi}^2 > \tilde{\chi}_0^2) > 70\%$, $\tilde{\chi}_0^2 = 0.08$) with the average value $\overline{\Delta n} = 0.056$ and standard deviation of $\sigma = 0.19$. The statistical hypothesis about the zero-value of the average (expected value) was proved. The standard deviation can be considered sufficiently small in comparison with 0.29 (for the uniform distribution in the case when any regularities are absent) and also with a maximal possible deviation of 0.5. It is important to note that six consequent quantum rates correspond to 6 AC of the main belt, which contains a sufficient number of individual objects.

Object	a_*	a	Δa	n_*	n	Δn
Mercury	0.39	0.41	–0.02	2.84	3	–0.16
Venus	0.72	0.68	0.04	5.31	5	0.31
Earth	1.00	0.95	0.05	7.34	7	0.34
Mars	1.52	1.50	0.02	11.18	11	0.18
AC	1.89	1.91	–0.02	13.86	14	–0.14
AC	2.23	2.18	0.05	16.37	16	0.37
AC	2.39	2.45	–0.06	17.57	18	–0.43
AC	2.59	2.59	–0.01	18.98	19	–0.02
AC	2.71	2.73	0.01	19.91	20	–0.09
AC	2.87	2.86	0.01	21.05	21	0.05
AC	3.01	3.00	0.01	22.11	22	0.11
AC	3.15	3.14	0.01	23.08	23	0.08
AC	3.42	3.41	0.01	25.06	25	0.06
AC	3.96	3.95	0.01	29.05	29	0.05
Jupiter	5.2026	5.18	0.02	38.17	38	0.17
AC	5.2032	5.18	0.02	38.17	38	0.17
Saturn	9.55	9.54	0.01	70.10	70	0.10
Uranus	19.22	19.22	0.00	141.00	141	0.00
Neptune	30.11	30.13	–0.01	220.91	221	–0.09

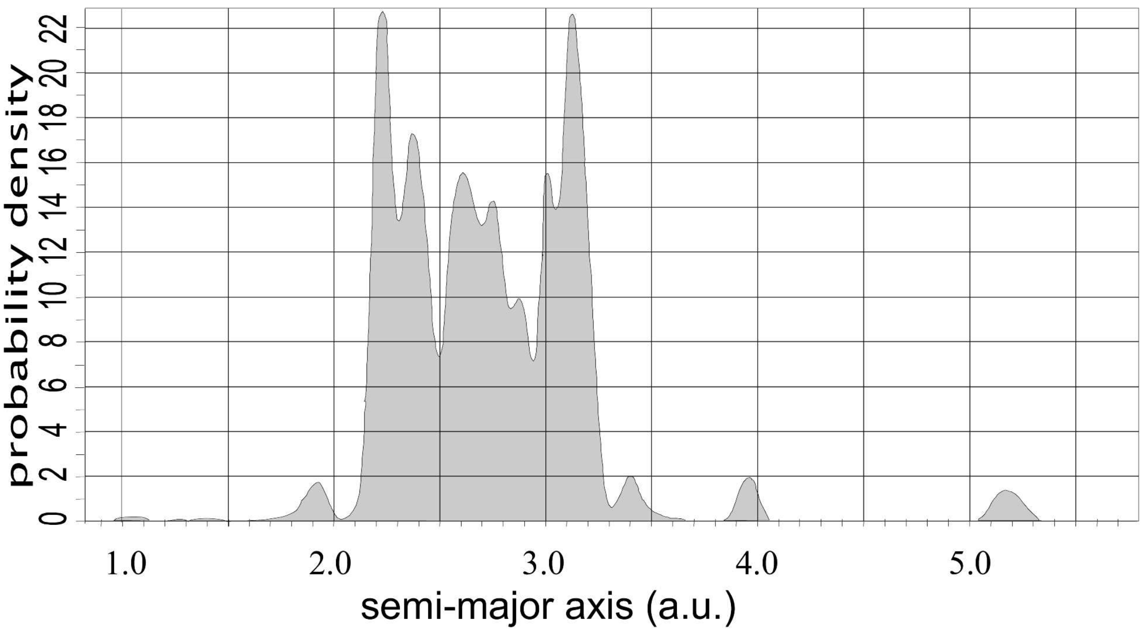

Figure 1: Probability density function of asteroidal semi-major axes distribution by the Parsen-Rozenblatt method

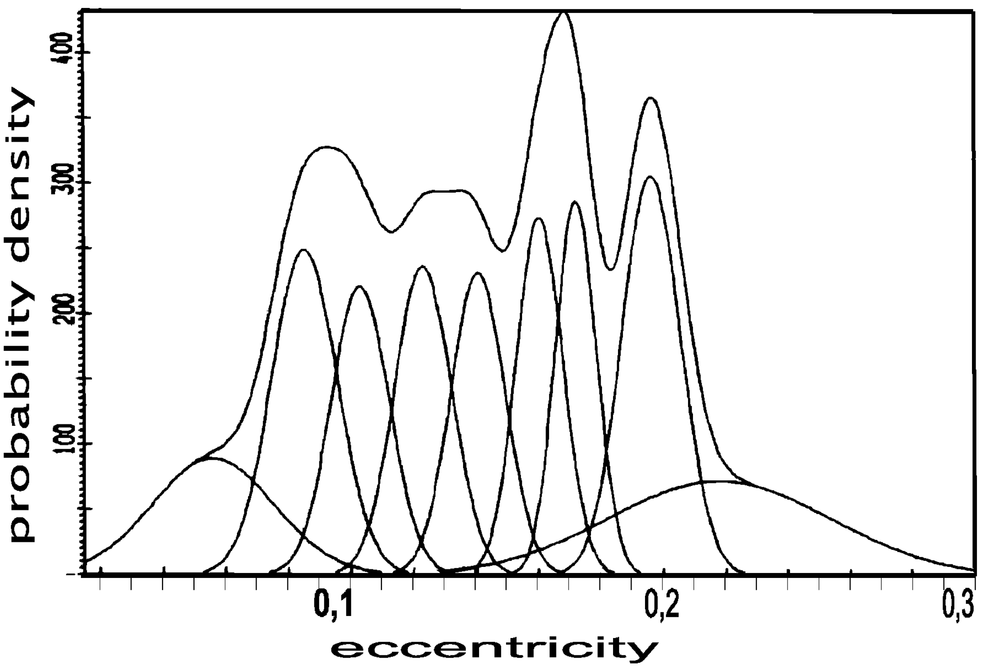

Figure 2: Probability density function of asteroidal orbits eccentricities distribution inside of AC with $2.10 < a < 2.31$ AU obtained by the second method

Thus, we can state that the theory is consistent with the observed distribution of gravitating matter complexes in the Solar System. It is necessary to note that such a distribution means a quantization of the specific total energy of the complexes:

$$E_n = -\frac{GM}{a_n} = -\frac{2GM}{na_0} = -\frac{E_0}{n},$$

where GM is the "gravitational charge" of the Sun.

We have also studied the distribution of orbital eccentricities and inclinations inside of each AC. As a result of this consideration the discrete structure has been found that corresponds qualitatively to the theoretical predictions (for example see Fig. 2).

REFERENCES

[1] *Gulak Yu. K.* On Commensurabilities (Resonances) in the Solar System // Sov. Astron.–1980.–**24**, N 1.–P. 84–90. (in Russian).

[2] *Milen'kiy M. A.* Classification of Signals under Conditions of Indetermination.–Moscow: Radio i Svyaz', 1983. (in Russian).

[3] *Ayvasian S. A.* Classification of Multi-dimensioned Observations.–Moscow: Statistika, 1974. (in Russian).

[4] Algorithms and Programs for Dependences Restoring / Ed. N. W. Vapnik.–Moscow: Nauka, 1984. (in Russian).

THE TITIUS LAW AND ITS PHYSICAL FUNDAMENTALS

Yu. K. Gulak[1], **I. A. Dichko**[2]

[1] *Gravimetrical Observatory, NAS of Ukraine, 36029 Poltava, Ukraine*
[2] *Poltava Military Institute of Communication, Poltava, Ukraine*

A cosmic planetary system (PS) having a sufficient enough number of the satellites moving eccentrically and interacting one with another within a $R - r$ layer (R – outer and r – inner boundaries) is the spatially limited oscillating system with many degrees of freedom. There is a set of the remotest apocentres of PS satellites (at the first approximation it is a sphere of R radius) at outer boundary of such a system. An inner boundary of PS is a set of the pericentres of the satellites, which are the nearest from the gravitating centre (GC). They are moving eccentrically as if they are reflected from these boundaries. In such a system: 1) the virial theorem works, *i.e.*, there is the relationship between the time averaged potential (gravitational) U and kinetic E energy: $-\langle U\rangle = 2\langle E\rangle$; 2) the radial standing waves are formed; 3) the initial gravitational energy decreases during the relaxation of PS to its stable state. So, if the outer satellites' layer R loses the equilibrium as result of some perturbation only a half of its gravitational energy, *i.e.*, $-GM/(R/2) = -2GM/R$, remains in PS according to the virial theorem. The another half of energy either runs away from PS by the energy-bearing satellites or transforms into positive kinetic energy of a new satellite belt at the $R/2$ vicinity from GC. If this new state of PS is to be broken by an outer or inner reason, then a part of the $R/2$-layer satellites migrates toward GC and their specific energy will be equal to $-2^2GM/R$ at the $R/2^2$ distance. When such events are repeated by n times the distance of the middle of an n-th layer from GC will be equal to $R_n = R/2^n$ with the energy of $U_n = -2^nGM/R$. By using the inverse geometric ratio and denoting $R_n = 2^na$ we have $U_n = -GM/(2^na)$, which reminds a quantum energy level of the Bohr atom model. If the distance of the lowest layer is b (this retreats from the symmetry could be explained by some GC influence such as tides or/and the magnetic moment) we obtain the known formula:

$$a_n = 2^na + b. \tag{1}$$

In the Titius Law $a = 0.3$ AU and $b = 0.4$ AU. Distances of the giant satellites of Jupiter, Saturn and Uranus can be described approximately by the (1) formula [1]. Inexact fitting of planetary and satellites distances to the Titius Law is explained by the influence of another mechanisms (*e.g.*, radial standing waves [2], tides, resonances, *etc.*), which takes place in the process of a PS formation and its relaxation to the stable state. Therefore, radial standing wave structures [2] (the Titius structures) must prevail in the rings and near stellar nebulae at the some stages as well as in the systems of the giant satellites formed by accreting mechanism.

REFERENCES

[1] *Nieto M. M.* The Titius-Bode Law.–Oxford, New York, Toronto, Sydney, Braunsccheig: Pergamon Press, 1972.– P. 190.

[2] *Gulak Yu. K., Dichko I. A.* On the nature of regularities in the radial structure of Saturnian rings // this issue.– P. 245–247.

Session 2. Comets, Meteors, and Meteoroids

INFLUX OF SPACE BODIES TO THE EARTH (LA–UR–00–1575)

D. O. ReVelle[1], V. G. Kruchynenko[2]

[1] *Los Alamos National Laboratory*
Los Alamos, New Mexico, USA
e-mail: dor@vega.lanl.gov

[2] *Astronomical Observatory, Taras Shevchenko National University*
3 Observatorna St., 04053 Kyiv-53, Ukraine
e-mail: kruch@aoku.freenet.kiev.ua

Small bodies from within our Solar System enter the atmosphere from space constantly. There is also apparently a small component of this flux ($<\sim 2\%$) entering from Interstellar Space as well. The sources of these objects include both asteroids and comets. Over the full spectrum of masses from $\sim 10^{-20}$ to 10^{15} kg, numerous methods have been employed to observe these materials. These include EM radar, photographic techniques, telescopes, satellite impacts and microphone recordings, infrasound, hydroacoustic and seismic detection techniques, spectral recordings, meteorite falls/finds, *etc.* Very bright and quite large bolides have also been routinely detected globally by US DoD satellites both optically and in the infrared. ReVelle (1997) has analyzed the AFTAC (U.S. Air Force Technical Applications Center, Patrick AFB, Florida) infrasound data and has predicted an influx rate of large bolides as a function of their source energy and compared it with the satellite derived influx estimates. Kruchynenko (1998) also recently presented an independent assessment of the integrated density of the influx of space bodies to the Earth over a much wider range of masses than considered by ReVelle. His results are more similar to the findings of Ceplecha *et al.* (1998), but with a curve fit of each of the various regimes of material and a separate integrated curve fit for the entire range of masses of space bodies impacting the Earth. ReVelle (1999) has also analyzed a more complete set of infrasound bolide detections for a much wider range of energies considered earlier. This set included observations made in Los Alamos, Russia, Sweden, Australia, *etc.* from 1990–1999 (ReVelle and Whitaker, 1996; ReVelle *et al.*, 1997; ReVelle *et al.*, 1998; ReVelle and Whitaker, 1999). This new analysis corroborates the 1997 results with relatively minor slope changes. For Tunguska ($=10$ Mt source energy), we can expect a reoccurrence, on the average, once every 90–220 years on the Earth (nominal value $=112$ yr). Similar estimates are made for other source energies as well.

I. INTRODUCTION

A. Large Bolides in the Near-Earth Environment: NEO's

There are several type of asteroids that make-up the near-Earth bolide influx. These include the Apollos, the Amors and the Atens (ReVelle and Ceplecha, 1994). All of these types can be seggregated by their orbital parameters. The near-Earth object population is also comprised of meteorite fragments from both asteroidal as well as cometary sources (Ceplecha and McCrosky, 1976; Wetherill and ReVelle, 1981a; 1981b). Since only the strongest objects can penetrate deeply enough to generate a blast wave source, the infrasonic detections are probably a lower limit to the "true" influx rate (ReVelle and Whitaker, 1999).

B. Detection Techniques for Large Bolides

There are three well-known methods for determining the large meteoroid influx, including:

a) Photographic fireball networks: (Panchromatic passband emulsions, requires knowledge of the luminous efficiency to deduce the intial mass of the body).
b) Satellite detection: Visible and infrared light emissions.

c) Infrasound detection: Blast wave generation and detection in the atmospheric waveguide. Arrays of infrasonic sensors provide the elevation and azimuth angle of the plane wave arrivial.

Each of these methods has its optimum size range, detection threshold, *etc.* They each compliment one-another however, in terms of providing a reliable, time-averaged influx rate as is seen in Figures 1 and 2.

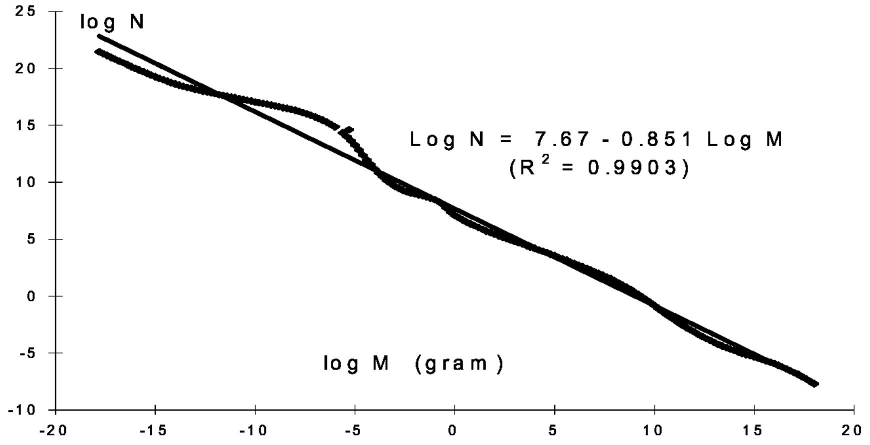

Figure 1: Results from Kruchynenko (on the basis Ceplecha *et al.*, 1998)

II. ANALYSIS

In this section we refer to recent work by Ceplecha *et al.* (1998), by Kruchynneko (1998) and by ReVelle (1997, 1999, *etc.*) on the integral mass influx calculation for the Earth. The work of Ceplecha and Kruchynenko consider nearly the same data sources and seek a curve fit of the data versus mass. The former approach uses a cubic spline interpolation technique, whereas the latter approach uses a single power law, least squares, curve fit over the entire mass range available. In contrast, ReVelle utilized only infrasound data for his source energy influx calculation with his 1997 paper dealing only with historic data sources (from 1960–1974) whereas his 1999 paper also utilized, in addition, the most recent bolides detected infrasonically by Los Alamos National Laboratory and other research groups from 1995–1999. A summary of some of the most recent events used in the analysis of ReVelle (1999) is given below:

1: 11/21/1995, Colorado Springs, Colorado (38.6 N, 104.6 W) – 0918 UTC
ReVelle and Whitaker (1996): US satellite DoD detection, Also, local video/audio on a security camera in Colorado Springs, Colorado, Source energy, E_s = 5.3e^{-02} kt, Max. amp. wave period = 2.0 s (detected at the Los Alamos infrasonic research array in Los Alamos).

2: 10/4/1996, Little Lake, California (36.1 N, 117.6 W) – 0344 UTC
ReVelle *et al.* (1997): US DoD satellite detection, E_s = 0.538 kt, Max. amp. wave period = 4.0 s (NTS, Nevada Test Site array opertaed by Los Alamos) and E_s = 1.136 kt, Max. amp. wave period = 5.0 s (detected at the Los Alamos array in Pinedale, WY at the PSRF-Pinedale seismic research facility).

3: 10/9/1997, El Paso, Texas (31.8 N, 106.1 W) – 1847:15 UTC
ReVelle *et al.* (1998): US satellite DoD detection, E_s = 0.293 kt, Max. amp. wave period = 3.33 s (detected at the CTBT IMS infrasound array in Los Alamos; Also detected infrasonically by the SMU (Southern Methodist University) infrasonic array at Lajitas, Texas, E. Herrin, Geology Department, SMU, Dallas, Texas).

4: 12/9/1997, Southwestern Greenland (62.9 N, 50.9 W) – 0811:55 UTC
Unpublished, L. Liszka, Swedish Isntitute of Space Physics (IRF), Umea, Sweden: US DoD satellite detection, E_s = 0.112 kt, Max. amp. wave period = 2.5 s (detected at the IRF Uppsala infrasound array in Uppsala, Sweden).

5: 8/11/1998, Alice Springs, Australia (19.93 S, 134.3 E) – 1017:36 UTC detection time, not event origin time
Unpublished, D. Christie (CTBTO, Vienna, Austria and K. Muirhead, Australian National University), E_s = 9.3 kt, Lamb wave period = 11.9 s, Max. amp. wave period = 9.4 s (detected at the Waramunga CTBT IMS infrasound array).

III. RESULTS

We first present the graphs of the predicted influx from Kruchynenko (1998), which are based upon essentailly the same data set used in Ceplecha *et al.* (1998). Next we consider the graph of the predictions of ReVelle (1999), since they are quite similar to ReVelle (1997).

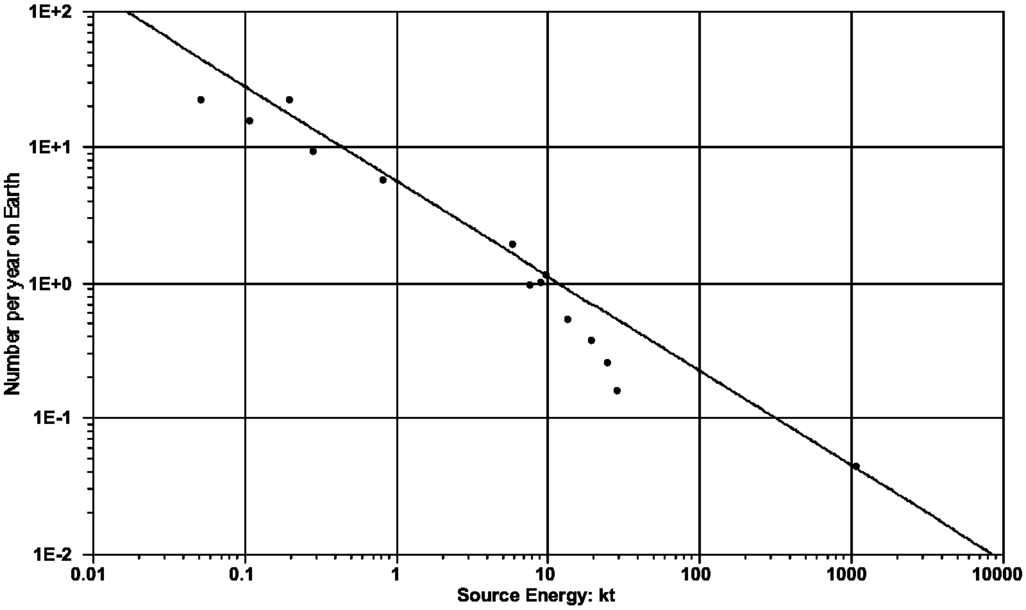

Figure 2: Results from ReVelle (1999)

The various influx relations developed by ReVelle (1999) using this data includes the following:

a) Original relation from ReVelle (1997) for 10 events detected by AFTAC from 1960–1974.
b) New relation using only data recorded since 1995 including five new bolide events.
c) New relation using only data since 1995, but omitting the Alice Springs bolide.
d) All of the infrasound data (15 events) recorded through early 1999 (including Alice Springs).

Using these energy influx relations we can also estimate the influx rate for specific energy sources, with the Tunguska energy clearly an extrapolation beyond the source energies previously detected since the time of event.

a) 1 kt: 7.17/year over Earth
15 kt: 0.99/year over Earth
10 Mt (Tunguska): One every 117.1 years

b) 1 kt: 6.44/year over the Earth
15 kt: 0.765/year over the Earth
10 Mt (Tunguska): One every 217.8 years

c) 1 kt: 7.53/year over the Earth
15 kt: 1.12/year over the Earth
10 Mt (Tunguska): One every 87.7 years

d) 1 kt: 5.61/year over the Earth
15 kt: 0.844/year over the Earth
10 Mt (Tunguska): One every 111.9 years

These estimates are in good agreement with those provided by the US DoD satellite community (Tagliaferri *et al.*, 1994) and also with those of Ceplecha *et al.* (1998) and evaluated independently by Kruchynenko (1998).

Acknowledgements. One of the authors (D. O. R.) would like to acknowledge the generous time and support provided by the Los Alamos infrasound research team, headed by Dr. Rodney W. Whitaker. Dr. ReVelle would also like to thank Dr. L. Liszka and Dr. D. Christie for access to their bolide infrasound data prior to publication. Since the summer of 1999, there are also a number of new bolides that will also be considered in future evaluations of the bolide energy influx rate as well.

REFERENCES

[1] *Ceplecha Z., Borovicka J., Elford W. G., et al.* Meteor phenomena and bodies // Space Sci. Rev.–1998.–**84**.–P. 327–471.

[2] *Ceplecha Z., McCrosky R. E.* Fireball end heights: A diagnostic for the structure of meteoric material // J. Geophys. Res.–1976.–**81**.–P. 6257–6275.

[3] *Kruchynenko V. G.* Integrated density of influx of space bodies onto Earth for a wide range of masses // METEOROIDS 1998.–Bratislava, Slovakia; Astron. Instit. Slovak Academy of Sciences, 1999.–P. 329–332.

[4] *Krychynenko V. G.* Supplement to integrated density of influx of space bodies onto Earth for a wide range of masses. (In printing).

[5] *ReVelle D. O.* Historical detection of atmospheric impacts of large bolides using acoustic-gravity waves // Near-Earth Objects / Ed. J. L. Remo.–New York, 1997.–(Annals of the New York Academy of Sciences.–1997.–**822**.–P. 284–302).

[6] *ReVelle D. O.* Infrasound from bolides: Revised influx estimates // ACM (Asteroids, Comets, Meteors) Conf.; Session: On the Trail of Meteors and Large Bolides, Cornell University, July 26–30, 1999.

[7] *ReVelle D. O., Ceplecha Z.* Analysis of identified iron meteoroids: Possible relations with M-type Earth-crossing asteroids? // Astron. and Astrophys.–1994.–**292**.–P. 330–336.

[8] *ReVelle D. O., Whitaker R. W.* Detection of large meteoroid/NEO flux using infrasound: Recent detection of the November 21, 1995 Colorado fireball // Characteristics and Consequences of Orbital Debris and Natural Space Impactors. Session 1. Detection and Measurement: SPIE Conf., Denver, Colorado, August 8–9, 1996.–1996.–**2813**.–P. 57–68. (LA-UR-96-2236).

[9] *ReVelle D. O., Whitaker R. W.* Infrasonic detection of a Leonid bolide, 17 November 1998 // Meteoritics and Planet. Sci.–1999.–**34**.–P. 995–1005.–(Special Leonid MAC Issue).

[10] *ReVelle D. O., Whitaker R. W., Armstrong W. T.* Infrasonic observations of bolides on October 4, 1996 // Characteristics and Consequences of Orbital Debris and Natural Space Impactors II. Session 4. Environmental Observations and Monitoring: SPIE Conf., San Diego, California, July 27–28, 1997 / Eds F. A. Allahdadi, E. Kane Casani, T. D. Maclay.–1997.–**3116**.–P. 156–167. (LA-UR-97-2481).

[11] *ReVelle D. O., Whitaker R. W., Armstrong W. T.* Infrasound from the El Paso superbolide of October 9, 1997 // Characteristics and Consequences of Space Debris and Near Earth Objects. Session 6. Observation and Tracking: SPIE Conference, Denver, Colorado, July 23, 1998 // Eds C. Bruce Johnson, T. D. Maclay, F. A. Allahdadi.–1998.–**3434**.–P. 66–77. (LA-UR-98-2893).

[12] *Tagliaferri E., Spalding R., Jacobs C., et al.* Detection of meteoroid impacts by optical sensors in Earth orbit // Hazards due to Comets and Meteoroids / Ed. T. Gehrels.– Tucson: Univ. of Arizona Press, 1994.–P. 199–220.

[13] *Wetherill G. W., ReVelle D. O.* Which fireballs are meteorites? A study of the Prairie Network photographic meteor data // Icarus.–1981.–**48**.–P. 308–328.

[14] *Wetherill G. W., ReVelle D. O.* Relationships between comets, large meteors and meteorites // Comets / Ed. L. Wilkening.–Tucson: Univ. of Arizona Press, 1981.–P. 297–319.

VARIATIONS OF LINES SELECTED IN THE COMET HALLEY SPECTRUM

S. A. Borysenko

Main Astronomical Observatory, NAS of Ukraine
27 Akademika Zabolotnoho, 03680 Kyiv, Ukraine
e-mail: borisenk@mao.kiev.ua

Some results of processing the spectrophotometry of Comet Halley are presented in this paper. At the end of preperihelion period the spectral observations of Comet Halley had been performed at the 6-m telescope (SAO, Russia) to ensure a good combination of the spectral (less than 0.1 nm per channel), angular (4 arcsec) and time (5–10 min) resolution. Autocorrelational and crosscorrelational functions and Fourier transformations for the main lines are obtained. We have determined two periods of variations and showed an uniformity of chemical composition of ejecting comet material.

INTRODUCTION

The TV-scanner in the Nasmyth's focus of the 6-m telescope was used as the spectral device for dynamical spectroscopy of Comet Halley. The applied diffraction grate gave the inverse dispersion of 5 nm/mm. The length of a spectrum on the inlet of the image intensifier was equal to 18 mm. The scanner gave the number of photoelectron events in each of 1024 spectral channels. Thus, the width of the channel was of about 0.09 nm. The whole covered spectral region was of 332–660 nm. The spectrograph with a long ($>$ 40 arcsec) slit was used. The width of the slit was set in the range 0.2–1.5 arcsec. A special mask was attached to the slit to cut from it two rectangular diaphragms. The height of each was equal to 4 arcsec. So, we had two space channels separated by 40 arcsec and every exposure gave two one-dimension spectra of two different points of the comet atmosphere.

Four modes of the diaphragm pointing were used: N – the nucleus and the region at 40 arcsec from it; C – two regions of the coma each at 20 arcsec from the nucleus between its; NN – the near-nuclear region at 4 arcsec from the nucleus and the point in the atmosphere at the nucleocentric distance 36 arcsec; S – one of the diaphragms was accompanying the occulted star, while another was tracing the coma.

A total number of obtained spectra is of about 500. Observations are described in detail in [1, 3]. The primary processing the spectra has been carried out by H. K. Nazarchuk with the software developed in SIPRAN-language in SAO. This processing removed the effect of geomagnetic field on the image intensifier and the atmospheric extinction. In this paper we study only N mode in the spectral region of 400–510 nm.

CALCULATIONS

The autocorrelation functions and Fourier transformations for some lines are shown in Figs. 1–4. The correlation function is

$$K(\tau) = \int_{-\infty}^{+\infty} F(t)F(t+\tau)dt, \tag{1}$$

where $F(t) = \sum_{k=1}^{N} A(t)\delta(t-\tau_i)$ and from this after some transformations [2] we have

$$K(\tau) = \frac{1}{T}\sum_{i=1}^{N} C_k\delta(t-\tau_k), \tag{2}$$

where $\tau_k = t_j - t_i$, $C_k = A_iA_j$, $K(\tau)$ is a discrete value of the autocorrelation function. To obtain the continuous function instead of the discrete one we used the smoothing by the convolution it with the Gauss core.

$$y(\tau) = C\sum_{i=1}^{N} K(\tau)_i exp(-(x(i)-X)^2/d), \tag{3}$$

where $d = 2\sigma^2$, $C = 1/(\sigma\sqrt{2\pi})$, $N = 28$ – number of measurements in series, σ – the constant for smoothing of oscillations on the frequency of sampling. This method is described in detail in [3, 4].

Three types of crosscorrelations are under investigation here: a) crosscorrelation between lines of the same element for the nucleus and coma at 40 arcsec from nucleus separately (Fig. 5); b) crosscorrelations between lines of different elements for the nucleus and coma at 40 arcsec from nucleus separately (Fig. 6); c) crosscorrelations between the nucleus and coma for the same lines (Figs. 7, 8). Crosscorrelations were calculated by the formula:

$$K(\tau) = \frac{1}{T}\sum_{k=1}^{N} C_k \delta(t - \tau_k), \tag{4}$$

where $\tau_k = |t_{1j} - t_{2i}|$, $C_k = A_{1i}A_{2j}$.

ANALYSIS

The method of smoothing and the choice of the parameters are the same as in (3). As our results show, in all the cases we have a good agreement between all the lines. It says about a common mechanism for time variations of all the lines and the chemical homogeneity of the nucleus. We propose a mechanism, when gases of the parent molecules, which generate such species as CN, CH, C_2, NH_2, are ejecting from the active regions of the nucleus.

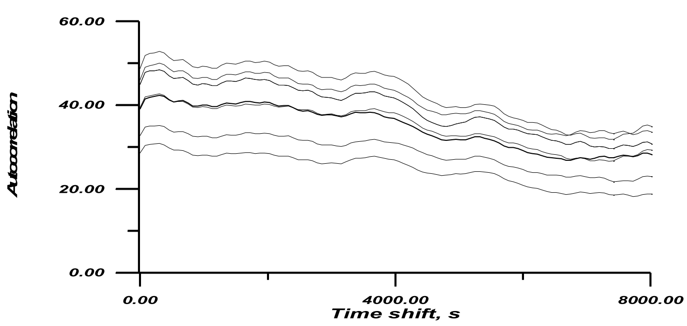

Figure 1: Autocorrelations of CN lines for nearnuclear region

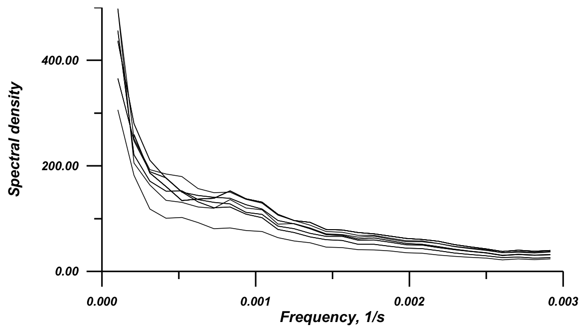

Figure 2: Fourier transformations of CN lines for near-nuclear region

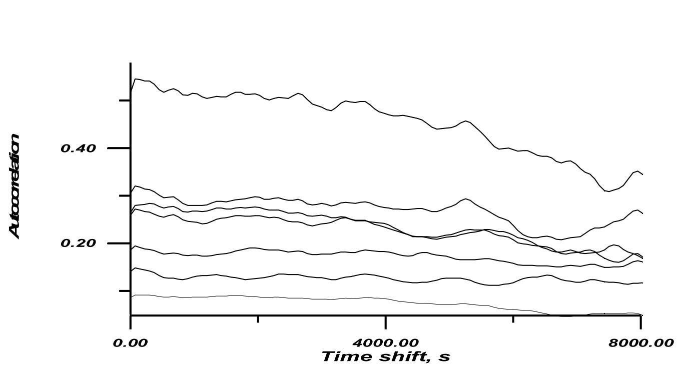

Figure 3: Autocorrelations of CN lines for coma

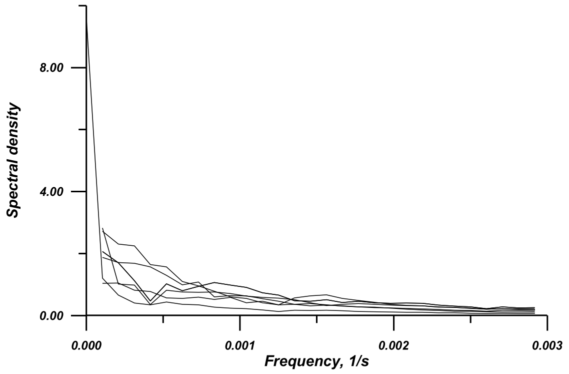

Figure 4: Fourier transformations of CN lines for coma

Fourier transformation of the crosscorrelation functions confirms the similar time behavior of all the lines studied. This analysis confirms the conclusion about the uniformity of the chemical composition of comet material ejected from the active regions. The synchronic behavior of the lines studied can be explained by variations in the rates of evaporation which are much shorter then the axial rotational period and are equal to $2^{\mathrm{h}}20^{\mathrm{m}}$ and $\sim 40^{\mathrm{m}}$ (?), respectively. The presence of these periods is connected with the mechanisms of evaporation and ejection. Their stability should be examined additionally, because their time variations presented here are tentative estimates.

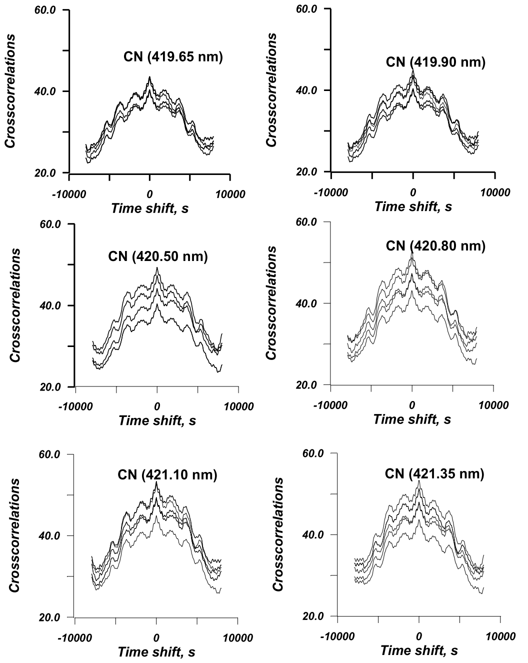

Figure 5: Crosscorrelations of CN lines for nearnuclear region

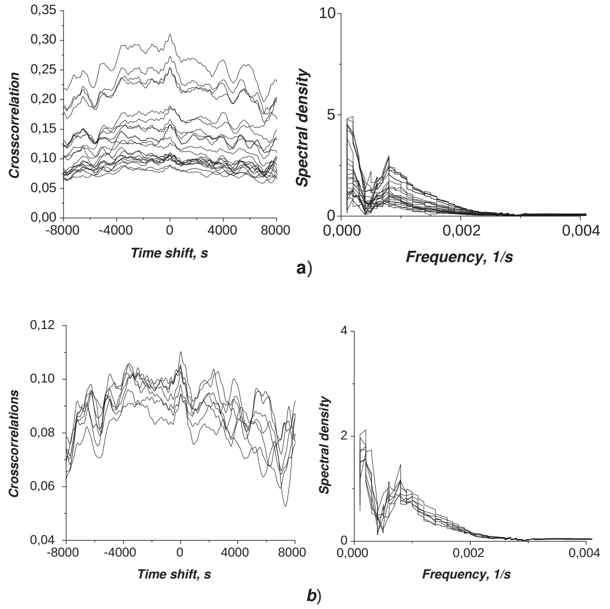

Figure 6: Crosscorrelations and Fourier transformations of CN (419.65 nm) line with: a) C_2 lines; b) NH_2 lines for coma

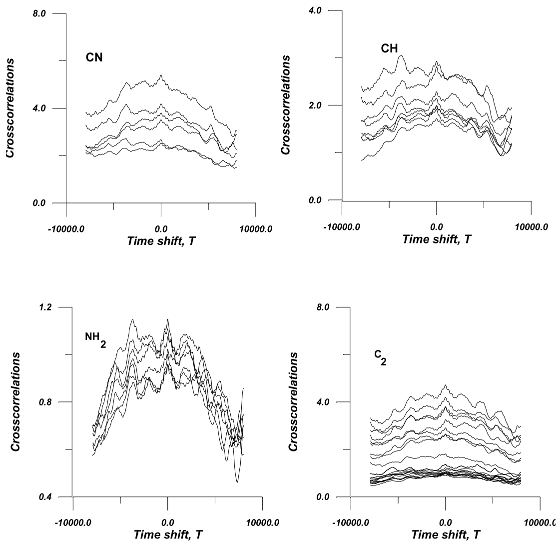

Figure 7: Crosscorrelations between the nucleus and coma for investigated spectral lines

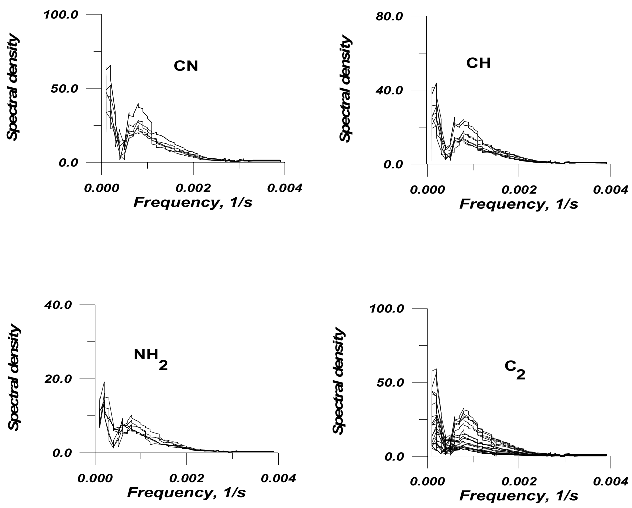

Figure 8: Nucleus – coma Fourier transformations for all investigated lines

REFERENCES

[1] *Afanasyev V. L., Lypovetsky V. D, Nazarchuk H. K., Shulman L. M.* Spectral observations of comet Halley with 1982i 6-m telescope // Comet. Circular.–1986.-N 352.–P. 1–4.

[2] *Bendat J. S, Piersol A. G.* Engineering applications of correlation and spectral analysis.–Moscow: Mir, 1983.–312 p. (in Russian).

[3] *Borysenko S. A., Nazarchuk H. K., Shulman L. M.* Time variations of some lines in comet Halley spectra and investigation of their correlations // Kinematics and Physics of Celestial Bodies.–2000.–**16**,–N 1.–P. 32–39.

[4] *Gaskarov D. V., Shapovalov V. I.* Small sampling.–Moscow: Statistics, 1978.–248 p. (in Russian).

NEW PHENOMENA IN THE EVOLUTION OF INTEGRAL BRIGHTNESS AND OUTBURST ACTIVITY OF COMETS

V. S. Filonenko[1], **K. I. Churyumov**[2]

[1]*Astronomical Observatory, Kharkiv National University*
35 Sumska St., 61022 Kharkiv, Ukraine
e-mail: filonenko@astron.kharkov.ua
[2]*Astronomical Observatory, Taras Shevchenko National University*
3 Observatorna St., 04053 Kyiv-53, Ukraine
e-mail: klim@aoku.freenet.kiev.ua

For the first time the idea that comets may be considered as the indicators of the solar activity was proposed by L. Capocci in 1826 and O. Bruhns in 1867. But despite more than one hundred fifty years of a research of this problem the mechanism of the Sun-comets relationships is still unknown. The new ideas about influence of the solar activity on light curves and outburst activity of comets obtained by authors are discussed in the present paper.

A lot of visual observational data was compiled by authors with the aim to study cometary light curves and their relation to the solar activity, as well as appropriate conditions in the interplanetary space. As a result of this work a catalogue of more than 400 real brightness outbursts of comets observed during 1927–1994 was compiled.

We have compiled a detailed light curve of Comet Halley (using near 5000 estimations of visual integral magnitude obtained during July 1985 – June 1986 by observers of the IHW and SOPROG nets). The linear correlation between the fluctuations of cometary integral brightness and the variations of solar activity indexes was found. The correlation coefficient is 0.62 ± 0.22. The comparison of light curve of Comet Halley with the changes of velocity of solar wind near the comet measured by spacecraft VEGA-1 showed that there was a reliable statistical dependence between them. The correlation coefficient is 0.71 ± 0.13. These results refute the conclusion, which was made by S. V. Orlov, about absence of influence of solar activity on the integral brightness of this comet during its apparition 1909–1910.

The study of light curves of one of short-period Comet Tempel 2 during its three different apparitions (1967, 1983 and 1988 years) gave a chance to find a new phenomenon in flare activity of this comet. It has been found that peaks and minimums of the brightness occurs at the same heliocentric distances of the comet in different apparitions. We showed that the found phenomenon is typical for 129 comets observed during 1847–1975.

So, we can formulate a new observed property of cometary flare activity: outbursts of all the observed comets are most probable at the distinct heliocentric distances. This new fact has to be added to the observational criterions for selection of a physical mechanism of cometary outburst activity.

We proposed a quantitative index of cometary outburst activity:

$$I = \bar{A}\nu = \frac{\sum \Delta m_i}{T}\,,$$

where $\bar{A} = (\sum \Delta m_i)/N$ is the average amplitude of outbursts (Δm_i is the amplitude of an individual outburst, N is the number of the outbursts), $\nu = N/T$ is the frequency of outbursts, and T is the time interval of continuous observations of a comet. Since the total amplitude of brightness outbursts $\sum \Delta m_i$ corresponds to the total energy, which was released during the outbursts, then the index I characterizes, in fact, the power of outburst activity.

The study of the 280 outbursts in 27 cometary light curves showed that comets can be divided into two groups depending on the values of the I index: a) the group of low and middle outburst activity ($I \leq 1$), and b) that of high outburst activity ($I > 1$). We can assume that only small-amplitude outbursts ($\Delta m \leq 1^m$) correlate with the level of the solar activity. High-amplitude brightness outbursts seem to have another trigger mechanism. A periodicity in the cometary outburst activity with quasi-period $6\overset{d}{.}8 \pm 0\overset{d}{.}6$ has been discovered. This quasi-period is equal to 1/4 of the Kerrington period of the Sun rotation. This is a new argument for influence of the solar activity on nonstationary active processes in cometary nucleus.

PHOTOELECTRIC MONITORING OF COMET C/1995 O1 (HALE-BOPP) IN LISNYKY

K. I. Churyumov, V. V. Kleshchonok, F. I. Kravtsov

Astronomical Observatory, Taras Shevchenko National University
3 Observatorna St., 04053 Kyiv-53, Ukraine
e-mail: klim@aoku.freenet.kiev.ua

We present results of the narrowband electrophotometric observations of Comet Hale-Bopp near perihelion which were made with the AZT-14 telescope at the Lisnyky station of Astronomical Observatory of the Taras Shevchenko National University of Kyiv. The standard set of IHW cometary filters was used. The comet's nucleus gas production rates Q of C_2 and C_3 were calculated on the basis of the stellar magnitudes of the comet for these filters. We used the Haser model for neutral cometary atmosphere for calculations. The values $Af\rho$, which are the characteristics of the dust nuclear production rate, were estimated too. Comet Hale-Bopp reached the maximum of gas (C_2 and C_3 molecules) and dust $Af\rho$(BC) production close to perihelion.

1. INTRODUCTION

One of the most informative methods of comet exploration is the photoelectric observation with narrow band filters. These data (the absolute fluxes both in emission bands and the continuum, gas and dust sublimation rate and their variations as a result of changes in heliocentric distances, nucleus rotation and comet activity, comparative chemical composition, outbursts of brightness, periods of rotation of nuclei and space orientation of rotation axes *etc.*) are obtained, as early as 1976 for more than 85 comets (A'Hearn *et al.*, 1995). The Astronomical Observatory of the Taras Shevchenko National University of Kyiv (AO KU) obtained a set of narrow band interference filters from M. A'Hearn (A'Hearn, 1982), one of the coordinators of the International Halley Watch photometric net, and joined the international cooperative work on creating the observational base of narrow band photoelectric photometry of comets. During 1982–1995 the collaborators of the AO KU participated in narrowband and UBVR electrophotometric and polarymetric observations of 9 comets: Austin (C/1982 M1), Churyumov-Gerasimenko (67P), Halley (1P), Hartley-Good (C/1985 R1), Giacobini-Zinner (21P), Thiele (C/1985 T1), Brorsen-Metcalf (23P), Levy (C/1990 K1) and Hale-Bopp (C/1995 O1) (Churyumov *et al.*, 1990; Churyumov and Rosenbush, 1991). The data on narrow band photometric and polarymetric observations of Comet Halley and Giacobini-Zinner were sent to the International Archives of these comets (both comets were the first to have been explored with space probes).

2. OBSERVATIONS AND PROCESSING

Electrophotometric observations of Comet Hale-Bopp (C/1995 O1) were made by the authors at the Lisnyky observing station of the AO KU with an electrophotometer installed at the AZT-14 reflector, which has a 50-cm diameter of the mirror. During observations the standard narrowband interference filters of the IHW, except the CN-filter (its bandpass shifted noticeably for the last 12 years) were used.

Altogether more than 500 observations of Comet Hale-Bopp were obtained for the period March 13 – April 27, 1997. The comet's nucleus gas production rates Q of C_2 and C_3 were calculated on the basis of the stellar calibration of these filters. The calculations were made by using the Haser model for neutral cometary atmosphere (Haser, 1957). The values $Af\rho$, which characterize the dust nucleus production rate (A'Hearn, 1991; A'Hearn *et al.*, 1995), were estimated too. Comet Hale-Bopp reached the maximum of gas (C_2 and C_3 molecules) and dust $Af\rho$(BC) production near the perihelion. The mean values of the production rates in the vicinity of the perihelion are $\log Q(C_2) = 28.4$; $Q(C_3) = 27.2$; $Af\rho(\mathrm{BC}) = 6.0$. These values are close to those obtained by other observers, *i.e.*, T. Farnham *et al.*, 1997. Discrepancies between $Af\rho$ values for the BC and RC filters show that the cometary continuum is more red than the Sun and increases with time according to the law

$$\log(Af\rho(\mathrm{BC})/Af\rho(\mathrm{RC})) = -0.00066(\Delta t - 0.061),$$

where Δt is the time (in days) from perihelion. This dependence is evidence for the presence of a dust in the near nucleus region of the comet that is more red than the Sun. It is possible to describe similar discrepancy for UC and BC filters as $\log(Af\rho(\text{UC})/(Af\rho(\text{BC})) = 0.0045(\Delta t - 0.0055)$.

This dependence indicates that a cometary dust which is more blue than the Sun is present near the nucleus. The maximum near perihelion in $\log(Af\rho)$ is absent. The variation of phase angle φ of the comet cannot explain the observed dependences because in the beginning of the observations on March 13, 1997, $\varphi = 47^{\circ}.2$, and the maximum of $\varphi = 49^{\circ}.1$ was on March 23, 1997 and in the end of observations on April 30, 1997. In both cases the sum of mean-square errors is approximately 1.5 times smaller for the temporal law than for a linear dependence with phase. Probably, the observed dependences are explained by changing color characteristics and sizes of the dust particles in the shells constantly being formed in the nucleus region of the comet. The both large dark particles being more red than the Sun occur in the shells simultaneously, as well as small light particles, which are more blue than the Sun. This fact, probably, is seen under the question (Churyumov *et al.*, 1999; Churyumov *et al.*, 2000).

3. CONCLUSION

1. Altogether more than 500 narrowband photoelectric observations of Comet Hale-Bopp were obtained at the Lisnyky observing station of the AO KU for the period March 13 – April 27, 1997.
2. Mean values of the gas and dust production rates near perihelion are $\log Q(\text{C}_2) = 28.4$; $Q(\text{C}_3) = 27.2$; $Af\rho(\text{BC}) = 6.0$.
3. In the dust shells simultaneously occur both large dark particles, more red than the Sun, and small light particles more blue than the Sun.

REFERENCES

[1] *A'Hearn M. F.* Photometry and polarimetry network // The Comet Halley Archive summary volume / Ed. Z. Sekanina.–Pasadena: Jet Propulsion Laboratory, 1991.–P. 193.

[2] *A'Hearn M. F., Millis R. L., Schleicher D. G., et al.* The ensemble properties of comets: results from narrowband photometry of 85 comets, 1976–1992 // Icarus.–1995.–**118**.–P. 223.

[3] *A'Hearn M. F., Schleicher D. G., Feldman P. D., et al.* Comet Bowell 1980b // Astron. J.–1984.–**89**.–P. 579–591.

[4] *A'Hearn M. F., Vanysek V.* Circ. Spectrophotometry of comets at optical wavelengths // Comets / Ed. L. L. Wilkening.–Arisona: Univ. of Arisona Press, 1982.–P. 433.

[5] *Churyumov K. I., Kleshchonok V. V., Kravtsov F. I.* Narrowband electrophotometry of comet Hale-Bopp (C/1995 O1) near perihelion // Earth, Moon and Planets.–1999.–**78**, N 3.–P. 155–160.

[6] *Churyumov K. I., Kleshchonok V. V., Kravtsov F. I.* Narrowband electrophotometry observations of comet Hale-Bopp (C/1995 O1) // Astron. Vestnik.–2000.–**34**, N 5.–P. 465–471.

[7] *Churyumov K. I., Rozenbush V. K.* Peculiarities of gas and dust production rates in comets P/Halley (1986 III), P/Giacobini-Zinner (1986 III), P/Hartley-Good (1985 VII) and P/Thiele (1985 XIX) // Astron. Nachr.–1991.–**312**, N 6.–P. 385–392.

[8] *Churyumov K. I., Rozenbush V. K., Rspayev F. K., Gorodetsky D.* I. Some results of the narrowband photometry of comet P/Halley (1986 III) // Astrophys. J.–1990.–**356**.–P. 687–692.

[9] *Farnham T., Schleicher D., Lederer S.* Comet C/1995 O1 (Hale-Bopp) // IAU Circ.–1997.–N 6589.

[10] *Haser L.* Distribution d'intensite dans la tete d'une comete // Bull. Acad. Roy. Belg. Classes des Sciences, Ser.–1957.–**5**, N 43.–P. 740.

WATER PRODUCTION OF COMETS DERIVED FROM OBSERVATIONS OF [OI] (6300 Å) AND H_2O^+ (6150 Å): COMETS C/1998 U5 (LINEAR) AND C/1999 J3 (LINEAR)

K. Jockers[1], T. Bonev[2], P. Korsun[3], N. Karpov[4], A. Sergeev[4], and V. Tarady[4]

[1] *Max-Planck-Institut für Aeronomie*
D-37191 Katlenburg-Lindau, Germany
e-mail: jockers@linmpi.mpg.de

[2] *Institute of Astronomy of Bulgarian Academy of Sciences*
Tsarigradsko Chausée 72, 1784 Sofia, Bulgaria

[3] *Main Astronomical Observatory, NAS of Ukraine*
27 Akademika Zabolotnoho, 03680 Kyiv, Ukraine

[4] *International Center for Astronomical and Medico-Ecological Research*
27 Akademika Zabolotnoho, 03680 Kyiv, Ukraine

The gas production rates of comets C/1998 U5 (Linear) and C/1999 J3 (Linear) are determined from observations obtained at the 2m-RCC telescope of Pik Terskol Observatory. In case of Comet C/1998 U5 the water production rate is derived from a classical Fabry-Perot interferogram of the [OI] $^1D \rightarrow {}^3P$ transition at 6300 Å. The interferogram shows the cometary [OI] line well separated from the night glow line because of the comet's radial velocity of 21.7 km s^{-1}. The high spectral resolution of the interferogram allows to resolve the cometary [OI] line with respect to neighbouring NH_2 lines. The [OI] emission is detected up to distances of 30,000 km from the nucleus. The water production rate amounts to 1.0×10^{28} molecules s^{-1}. An H_2O^+ column density map of Comet C/1999 J3 (Linear) is used to infer the total gas production rate of this comet using the MHD similarity law. This method is based on the theory of comet-solar wind interaction. Assuming average solar wind behavior we determine a gas production rate of 1.6×10^{28} molecules s^{-1}.

INTRODUCTION

There is now general agreement that water is the main constituent of comets. For the first time water was detected convincingly in 1986 in Comet Halley with the Kuiper Airborne Observatory [10], shortly before the in-situ measurements by the GIOTTO space probe [8]. Spacecraft observations of water have been reported in [4] (Infrared Space Observatory) and [11] (Submillimeter Wave Astronomy Satellite). Besides of these direct, but expensive observations from the stratosphere and from space, ground-based, more indirect determinations of the cometary water production still remain of value, like observations of OH at 18 cm [3] or 3090 Å [5], and observations of [OI] at 6300 Å ([6], [12]). In this paper we derive the water production rate of Comet C/1998 U5 (Linear) from a Fabry-Perot interferogram of the [OI] line at 6300 Å. In the interferogram the cometary [OI] emission is not blended by adjacent NH_2 lines, and, because of the Doppler shift caused by the comet's radial velocity, the cometary emission is well separated from the [OI] night glow. A second method to derive the water production in comets, proposed in [13], is based on the MHD similarity law of the solar wind-comet interaction. We apply this method to observations of H_2O^+ column densities in the coma of Comet C/1999 J3 (Linear).

H_2O PRODUCTION DERIVED FROM AN [OI] FABRY-PEROT INTERFEROGRAM OF COMET C/1998 U5 (LINEAR)

Comet C/1998 U5 (Linear) was observed with the Two-Channel Focal Reducer of the Max-Planck-Institute for Aeronomy at the 2m-RCC telescope of Pik Terskol Observatory on Nov. 20, 1998 (for a description of instrument, filters and etalon see [7]). At this time the comet's heliocentric distance was 1.32 AU, its geocentric distance 0.48 AU, and its radial velocity 21.7 km s^{-1}. Two exposures of the comet were taken. The first one of 30 min duration was through a solid fused silica Fabry-Perot etalon with spectral resolution $\lambda/\delta\lambda \approx 30,000$ and an interference prefilter with central wavelength 6308 Å and 31 Å FWHM (full width at half maximum). The second exposure of 15 min duration was through a filter transmitting a red continuum window at 642 nm. It was used to remove the continuum from the first image. The resulting continuum–free interferogram is shown in Fig. 1. The fringe system of the atmospheric night glow at 6300 Å is most prominent. Because the etalon is tilted by 4° the fringes are not circles. The tilt avoids reflections between etalon and filter and increases the number of recorded fringes (adapts the resolution of the etalon to the pixel size of the CCD). A second, more diffuse fringe system is caused by atmospheric OH emission at 6306.87 and 6306.98 Å. The cometary emissions are spatially localized. The strongest line is due to the cometary [OI] 6300 Å emission. Other cometary lines in the interferogram come from the 0,8,0 band of the NH_2 molecule [1]. The cometary [OI] line appears unblended. It is shifted from the airglow line because of the radial velocity of the comet of 21.7 km s^{-1}.

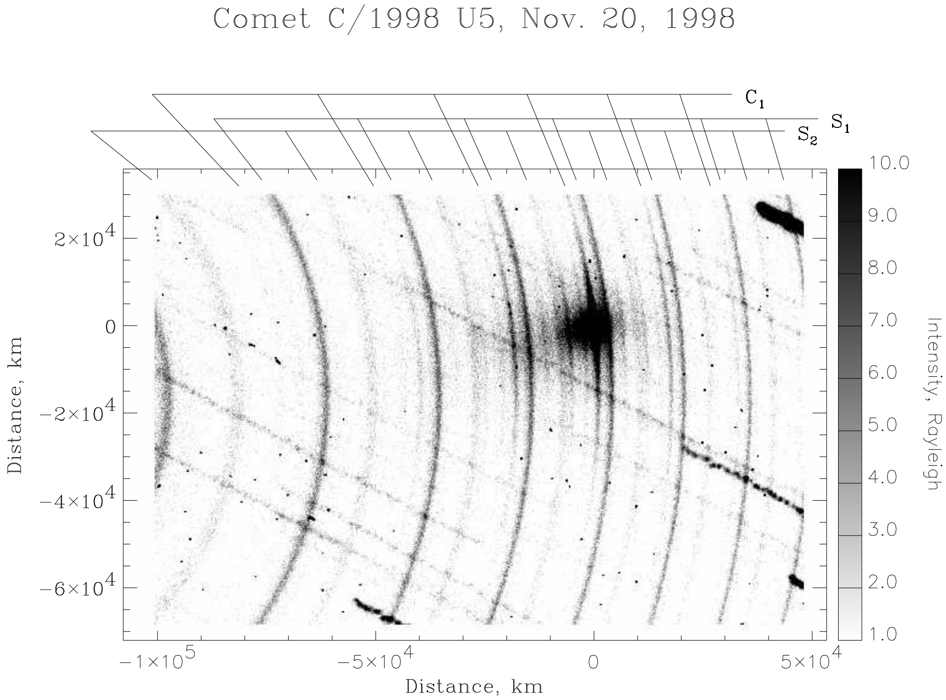

Figure 1: Fabry-Perot interferogram of Comet C/1998 U5 (Linear) in a wavelength range around 6300 Å taken Nov. 20, 1998 (see text)

With the help of observations of spectroscopic standard stars the relative intensities have been transferred to Rayleighs. Intensities in Rayleighs extracted from the interferogram are plotted in the left panel of Fig. 2 as a function of projected distance R_C from the cometary nucleus. The oxygen atom originating from dissociation of water into H_2 and O is created in the ^{1}D state. When it decays into the ^{3}P state it emits a single $\lambda =$ 6300 Å photon. Therefore, in the absence of quenching by electron collision the observed [OI] distribution is proportional to the H_2O distribution. Therefore, for distances less than the scale length of water (1.5×10^5 km at a heliocentric distance of 1.3 AU) the cometary [OI] intensity must decrease $\sim R_C^{-1}$, as observed. According to [6] the water production rate Q_{H_2O} equals 16 times the total luminosity of the [OI] emitting water vapor cloud in photons s^{-1}. If we integrate the fitted $1/R_C$ distribution out to the scale length of 1.5×10^5 km we obtain $Q_{H_2O} = 1.0\times10^{28}$ s^{-1}.

H_2O PRODUCTION DERIVED FROM AN H_2O^+ COLUMN DENSITY MAP OF COMET C/1999 J3 (LINEAR)

Comet C/1999 J3 (Linear) was observed with the Two-Channel Focal Reducer on Sept. 17, 1999, when its heliocentric distance was 0.98 AU and its geocentric distance 1.03 AU. An H_2O^+ image (exposure time 10 min) of the comet was obtained through an interference filter transmitting the short wavelength half of the 0,10,0 band of H_2O^+ (center wavelength 6149 Å, FWHM 32 Å). Like in case of the [OI] emission, a second exposure of 10 min duration through a filter transmitting a red continuum window at 642 nm was used to remove the continuum from the H_2O^+ image. The remaining H_2O^+ image was transferred to absolute intensities with the aid of observations of standard stars. To calculate column densities we assumed equal total intensities of both subbands of the 0,10,0 band of H_2O^+ and used the g-factor provided in [9]. Fig. 2 shows in the right panel

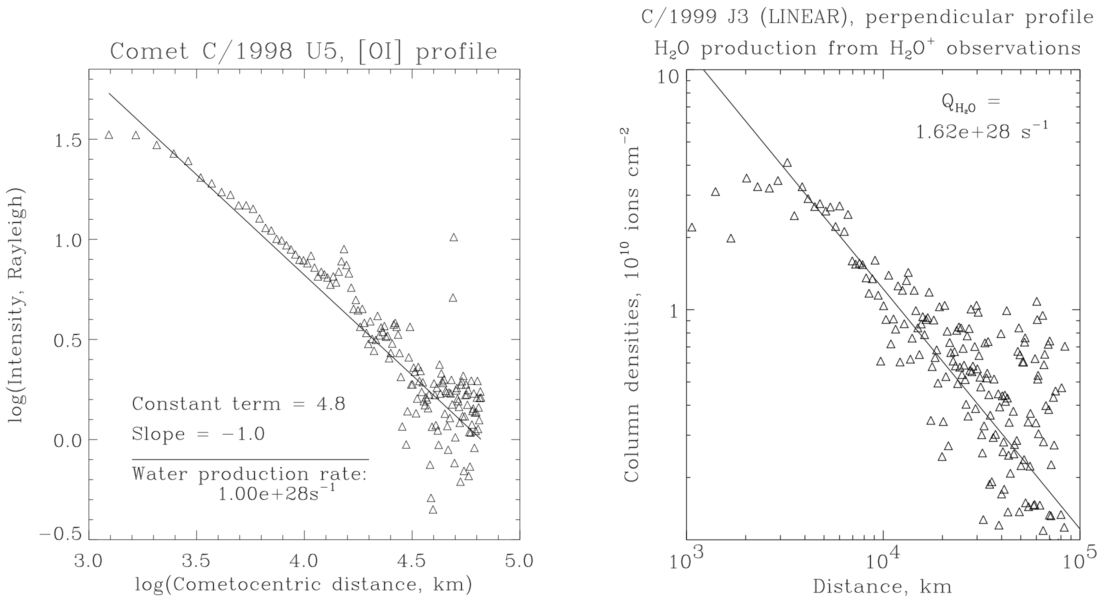

Figure 2: Two ways to derive the water production rate of a comet: Left side: Comet C/1998 U5 (Linear): Fabry-Perot interferometry of the [OI] line at 6300 Å. The intensity of the [OI] line emission is plotted versus sky projected distance R_C from the nucleus. Right side: Comet C/1999 J3 (Linear): MHD similarity law. The profile of H_2O^+ column densities through the cometary nucleus perpendicular to the solar-antisolar direction is shown. In both cases a slope $\sim R_C^{-1}$ has been fitted to the data

the column density profile, extracted along the perpendicular at the comet nucleus with respect to the comet-Sun line. Again a curve $\sim R_C^{-1}$ has been fitted.

In [13] a method was devised to derive water production rates from H_2O^+ column density maps using the MHD similarity law. If σ denotes the ionization rate, m_C the average mass of a cometary ion, Q the total gas production rate, w the outflow speed of neutrals from the nucleus (usually assumed = 1 km s^{-1}), and $\rho_\odot$ and $u_\odot$ the solar wind density and speed, we can define the interaction scale length R_I as follows:

$$R_I = \frac{\sigma m_C Q}{4\pi w \rho_\odot u_\odot}. \tag{1}$$

Then we can make the MDH equations dimensionless by introducing the following dimensionless variables:

$$\mathbf{x}' = \mathbf{x}/R_I,\ t' = tu_\odot/R_I,\ \rho' = \rho/\rho_\odot,\ n' = nm_C/\rho_\odot,\ \mathbf{u}' = \mathbf{u}/u_\odot,\ p' = p/\rho_\odot u_\odot^2. \tag{2}$$

$\mathbf{x}$ and $\mathbf{u}$ are the position and velocity vectors, t the time, ρ and n the mass and number densities, and p the pressure. The dashed quantities are the dimensionless ones. In the hypersonic limit (negligible solar wind thermal pressure), if magnetic field and sources or sinks of momentum and energy are absent, and if the neutral density follows an R^{-2} law, the resulting dimensionless equations do not depend on any dimensional quantities. As the interaction scale length R_I linearly depends on the total gas production rate Q we can say that the comet's "size" linearly increases with its production rate. Let us briefly discuss the conditions of validity of the similarity law with the aim to arrive at a practical way to use it to derive a production rate. The solar wind is a high Mach number flow, *i.e.*, $p_\odot = 0$ is satisfied. Similarly, the main effect of the comet on the solar wind flow is its mass addition to the flow. Since the initial momentum and energy of a cometary particle is small as compared to the momentum and energy of a solar wind particle the comet does not change the momentum and energy balance appreciably. As demonstrated by numerical calculations, the effect of the omnipresent solar wind magnetic field is smallest on the upstream side of the comet, whereas it leads to a flattening of the tail which increases with increasing distance downstream of the nucleus. Therefore, for the derivation of the production rate we use a cut through the nucleus perpendicular to the radius vector. A serious restriction comes from the requirement of a distribution of the neutral water source $\sim R_C^{-2}$. This condition becomes invalid if $R_I \geq R_D$, the dissociation scale length of water. At a heliocentric distance of 1 AU, with $R_D = 8.6\times10^4$ km, ionization rate $\sigma = 10^{-6}$ s^{-1}, $m_C = 20$ amu (to account for other, more heavy cometary ions) , $w = 1$ km s^{-1}, number density $n_\odot = 7$ cm^{-3}, and $u_\odot = 400$ km s^{-1} (in the absence of knowledge about the solar wind conditions average values of the solar wind number density and speed are assumed), a correction for the finite dissociation length scale must be applied for $Q > 10^{29}$. Because of lack of space we must refer to [13] for the details. A further correction must be applied to account for phase angles $\neq 90°$. Then, the essence of the derivation of a production rate using the similarity law rests in a comparison with a well measured comet, which is taken as reference. This comet is Comet Halley, of which we have spacecraft measurements. The production rate is obtained from $Q = 5\times10^{-11}\sqrt{C_2}$ [13], where the constant C_2 is derived from a fit of the function $C_2 R_C^{-1}$ to the measured profile through the nucleus (see Fig. 2, right panel). If R_C is measured in cm, Q is in units 10^{29} molecules s^{-1}. In this way we find for Comet C/1999 J3 a total gas production rate $Q = 1.6\times10^{28}$ molecules s^{-1}.

DISCUSSION AND CONCLUSION

Two methods of the determination of gas production rates have been applied to cometary observations obtained at Pik Terskol Observatory. The idea of the first method (study of [OI] emission) dates back to the early era of cometary exploration [2]. The use of a solid fused silica etalon in a focal reducer is a simple technique which allows to obtain the [OI] 6300 Å line well separated from the nightglow line (if the radial velocity of the comet exceeds 15 km s^{-1}) and from NH_2. As compared to [12] our method is more sensitive at the expense that we do not get an image of the [OI] emission but can sample the emission only along the etalon fringes. The second method is quite new. It deepens our understanding of the comet-solar wind interaction. Combination of both methods may in the future allow to explore the changing solar wind conditions at comets with ground-based astronomical observations.

REFERENCES

[1] *Arpigny C., Magain P., Manfroid J., et al.* Resolution of the [OI] and NH_2 blend in comet P/Halley // Astron. and Astrophys.–1987.–**187**.–P. 485–488.

[2] *Biermann L., Trefftz E.* Über die Mechanismen der Ionisation und der Anregung in Kometenatmosphären // Z. Astrophys.–1964.–**59**.–P. 1–28.

[3] *Colom P., Gérard E., Crovisier J., et al.* Observations of the OH radical in comet C/1995 OI (Hale-Bopp) with the Nançay radio telescope // Earth, Moon and Planets.–1997.–**78**.–P. 37–43.

[4] *Crovisier J., Leech K., Bockelée-Morvan D., et al.* The spectrum of Comet Hale-Bopp (C/1995 O1) observed with the Infrared Space Observatory at 2.9 astronomical units from the Sun // Science.–1997.–**275**.–P. 1904–1907.

[5] *Farnham T. S., Schleicher D. G., A'Hearn M. F.* The HB narrowband comet filters: standard stars and calibrations // Icarus.–2000.–**147**.–P. 180–204.

[6] *Fink U., Hicks M. D.* A survey of 39 comets using CCD spectroscopy // Astrophys. J.–1996.–**459**.–P. 729–743.

[7] *Jockers K., Credner T., Bonev T., et al.* Exploration of the solar system with the Two-Channel Focal Reducer at the 2m-RCC telescope of Pik Terskol observatory // this issue.–P. 13–18.

[8] *Krankowsky D., Lämmerzahl P., Herrwerth I., et al.* In situ gas and ion measurements at comet Halley // Nature.–1986.–**321**.–P. 326–329.

[9] *Lutz B. L.* Fluorescence efficiency factors for ionized water vapors // Astrophys. J.–1987.–**315**.–P. L147–L150.

[10] *Mumma M. J., Weaver H. A., Larson H. P., et al.* Detection of water vapor in Halley's comet // Science.–1986.–**232**.–P. 1523–1528.

[11] *Neufeld D. A., Stauffer J. R., Bergin E. A., et al.* Submillimeter Wave Astronomy Satellite observations of water vapor toward Comet C/1999 H1 (Lee) // Astrophys. J.–2000.–**539**.–P. L151–L154.

[12] *Schultz D., Li G. S. H., Scherb F., Roesler F. L.* The $O(^1D)$ distribution of comet Austin $1989c_1$ = 1990V // Icarus.–1993.–**104**.–P. 185–196.

[13] *Wegmann R., Jockers K., Bonev T.* H_2O^+ ions in comets: models and observations // Planet. and Space Sci.–1999.–**47**.–P. 745–763.

NEGATIVE WAVELENGTH GRADIENT OF POLARIZATION OF COMET 21P/GIACOBINI–ZINNER AS AN INDICATOR OF ORGANIC MATTER IN ITS DUST PARTICLES

N. N. Kiselev[1], **K. Jockers**[2], **V. K. Rosenbush**[3]

[1] *Astronomical Observatory of Kharkiv National University, Kharkiv, Ukraine*
e-mail: `kiselev@astron.kharkov.ua`

[2] *Max-Planck-Institut für Aeronomie, Katlenburg-Lindau, Germany*

[3] *Main Astronomical Observatory, NAS of Ukraine*
27 Akademika Zabolotnoho St., 03680 Kyiv, Ukraine

An unusual behaviour of the polarization of light scattered on dust particles in Comet 21P/Giacobini–Zinner is discussed. CCD imaging polarimetry of Comet Giacobini–Zinner was carried out at the 2-m telescope of the Pik Terskol Observatory (Northern Caucasus) on November 20, 1998 and January 25, 1999 using a two-channel focal reducer of the Max-Planck-Institute for Aeronomy (Germany). Narrow-band continuum filters centered at 4430/44 Å (blue continuum) and at 6420/26 Å (red continuum) were used. The comet was also observed in a wide-band red (7228/1140 Å) filter with the 70-cm reflector at the Observatory of Kharkiv National University on November 19–22, 1998. We have found that the degree of polarization of dust in the Comet Giacobini–Zinner in the blue continuum is in a good agreement with that of dust in the comets C/1987 P1 (Bradfield), C/1990 K1 (Levy), C/1996 B2 (Hyakutake) and C/1998 U5 (Linear) that were observed at the same phase angles. At the same time, permanently the polarization of Comet Giacobini–Zinner in the red continuum is about 2% less than in the blue continuum. Comets Bradfield, Levy, Hyakutake and Linear U5 display the usually observed in dusty comets increasing of the polarization with the wavelength. Contrary to all other comets, the wavelength gradient of the continuum polarization of Comet Giacobini–Zinner is negative. No other comet observed previously showed a similar wavelength dependence of polarization. First we checked if the reduced polarization of Comet Giacobini–Zinner in the red filters could be explained by the gas contamination and were convinced that it could not. We also checked if the inversion of polarization color in local parts of the coma could not produce a negative spectral gradient of the polarization for the whole coma of this comet and it could not as well. Thus, it seems reasonable to assume that the observed anomalous spectral dependence of polarization is caused by properties of dust particles. In particular, one of possible interpretations is connected with a high abundance of organic matter in the dust. The Draconid meteors associated with this comet support the presence of organic matter in the large dust grains of Comet Giacobini–Zinner, which is depleted in carbon species in the gas phase.

CN AND NH_2 ATMOSPHERES OF COMET C/1999 J3 (LINEAR)

P. P. Korsun[1] **and K. Jockers**[2]

[1] *Main Astronomical Observatory, NAS of Ukraine*
27 Akademika Zabolotnoho St., 03680 Kyiv, Ukraine
e-mail: korsun@mao.kiev.ua

[2] *Max-Planck-Institut für Aeronomie, Kaltenburg-Lindau, Germany*

Observations of Comet C/1999 J3 were made at the 2-m telescope of the Pik Terskol Observatory on September 19, 1999. Narrow-band CCD images of the CN, NH_2, and dust atmospheres have been recorded using the two-channel focal reducer of the Max-Plank-Institute for Aeronomy. To fit distributions of the CN and NH_2 molecules in the comet atmosphere Monte Carlo model was adopted. Model calculations were successful with photodissociation lifetimes equal to $\tau_{\mathrm{CN}} = 1.5\times10^5$ s and $\tau_{\mathrm{CN}parent} = 3.2\times10^4$ s for CN and its parent, $\tau_{\mathrm{NH_2}} = 1.0\times10^5$ s and $\tau_{\mathrm{NH_2}parent} = 5.0\times10^3$ s for NH_2 and its parent, respectively. These results are in agreement with HCN as the main source of the CN radicals and NH_3 as the main source of the NH_2 radicals in the atmosphere of Comet C/1999 J3 (Linear). The gas-production rates of CN, Q(CN)=3.8×10^{25} mol^{-1}, and NH_2, Q(NH_2)=2.6×10^{25} mol^{-1}, have been determined as well. These values are about 0.24% and 0.16%, respectively, of the water production rate.

OBSERVATIONS AND DATA REDUCTION

Observations of Comet C/1999 J3 were made at the 2-m telescope of the Pik Terskol Observatory on September 19.004, 1999, when the comet was close to its perihelion. The 2-channel focal reducer of the Max-Planck-Institute for Aeronomy equipped with CCD detectors was used to study its neutral atmospheres (Jockers, 1997). Observed sky fields were 7.8×7.8 arcmin with a pixel size of 1.0 arcsec and 7.8×5.2 arcmin with a pixel size of 0.8 arcsec in the blue and red channels, respectively. The interference filters IF390 ($\lambda_0 = 389.4$ nm, FWHM = 10.5 nm) and IF662 ($\lambda_0 = 662.1$ nm, FWHM = 5.9 nm) were chosen to isolate the emissions of the CN and NH_2 molecules. The corresponding underlying continua were estimated using observations through interference filters IF642 ($\lambda_0 = 641.6$ nm, FWHM = 2.6 nm) and IF443 ($\lambda_0 = 443.2$ nm, FWHM = 4.4 nm).

Original CCD frames were bias subtracted, flat-fielded and cleaned from cosmic events. Star trails were also removed from the comet images. The cometary atmosphere filled the available sky field to a large extent. Nevertheless, the night sky level was estimated and subtracted. The absolute intensity scale for cometary counts was determined from observation of the standard star 15 UMa. Its flux was taken from Voloshina *et al.* (1982).

TIME SCALES AND GAS PRODUCTION RATES

For the analysis of our data we have taken the random walk model, which is based on Monte Carlo simulation. The details of the algorithm were described by Combi and Smyth (1988). Adequacy of our calculations was tested by comparison of the observed surface distribution of the analyzed species with the calculated one. The Chi-square goodness-of-fit test has been adopted for this purpose.

CN molecule. Although CN is the second species detected in comets, so far there is no agreement among researchers regarding the nature of its parent. The most plausible hypothesis is that the HCN molecule is the major contributor of this radical in the cometary atmosphere.

According to the theoretical prediction provided by Huebner and Link (1999), lifetimes for HCN and CN decrease from 7.94×10^4 s and 3.15×10^5 s to 3.19×10^4 s and 1.34×10^5 s from the solar activity maximum to minimum.

We satisfactorily fitted the CN atmosphere observed with lifetimes equal to 1.5×10^5 s for CN and 3.2×10^4 s for its parent. Taking into account that we made our observations in September 1999, when the Sun was close to the maximum of its activity, we can conclude that there is an excellent agreement between the observed and calculated data. So, we think that just HCN is the dominant source of CN in the atmosphere of Comet C/1999 J3 (Linear).

NH_2 molecule. Previous observations of the NH_2 surface brightness distributions in comets were mainly obtained from long-slit spectra. Because the NH_2 emission bands are weak and in many cases blended with features of other species, it is very difficult to interpret them. Nevertheless, in 1989 Tegler and Wyckoff (1989) came up with a proposal that NH_3 is the parent of NH_2.

According to Huebner and Link (1999) there are several possibilities for the NH_2 parent, *i.e.*, NH_3, to be dissociated into NH_2 and other particles, but the reaction displayed below is the dominant one under solar irradiation

$$\mathrm{NH_3} + h\nu = \mathrm{NH_2(X^2B_1)} + \mathrm{H}.$$

About 96% of NH_2 appears in the cometary atmosphere in this way. In this reaction life times for NH_3 and NH_2 are decreased from 5.65×10^3 s and 4.65×10^5 s to 5.00×10^3 s and 2.94×10^5 s when the solar activity varies from low to high.

We interpret here the two-dimensional NH_2 atmosphere. Our computed surface profiles are in reasonably good agreement with the observed ones, if we adopt theoretical values for the time scales of NH_2 destruction, $\tau_{NH_2} = 1.0\times10^5$ s, and $\tau_{NH_2 parent} = 5.0\times10^3$ s for destruction of its parent, the NH_3 molecule. So, we conclude that NH_3 is probably the dominant source of NH_2 in the coma of Comet C/1999 J3 (Linear).

Gas production rates. The total number of the analyzed molecules in the cometary coma, N_{obs}, is related to the total flux of the observed band measured at the Earth by

$$\mathrm{N}_{obs} = \frac{4\pi\Delta^2\mathrm{F}_{obs}}{g}, \quad (1)$$

where g is the fluorescence efficiency factor of the observed band, Δ is the geocentric distance of the comet, and F_{obs} is the total flux of the observed band. The fluorescence efficiency factor (g–factor) is assumed to vary as r^{-2}, where r is heliocentric distance in AU.

As we know the model amount of the analyzed molecules, N_{mod}, and model production rate, Q_{mod}, from the model experiments then

$$\mathrm{Q}_{obs} = \frac{\mathrm{N}_{obs}}{\mathrm{N}_{mod}}\mathrm{Q}_{mod}. \quad (2)$$

The g-factor for CN has been taken from A'Hearn *et al.* (1995). We used the value of 2.4×10^{-13} erg s^{-1}mol^{-1} valid for the heliocentric velocity of Comet C/1999 J3 (Linear) at the moment of observation. According to equation (2) we have Q(CN)=3.8×10^{25} mol^{-1}.

To determine the gas production rate for NH_2 we use the g-factor for the (0,7,0) band as computed by Tegler and Wyckoff (1989), *i.e.*, 1.26×10^{-14} erg s^{-1}mol^{-1}. It should be noted that this value was doubled in our calculations, because according to C. Arpigny statement only half of the population of NH_2 molecules contributes to the odd, *e.g.*, (0,7,0) transitions, while the other half contributes to the even, *e.g.*, (0,8,0) transitions. This correction leads to the NH_2 production rate $Q_{NH_2} = 2.6\times10^{25}$ mol s^{-1}.

The water production rate for this comet has been determined by Jockers *et al.* (2001) from H_2O^+ observations. Using MHD similarity law the value of 1.6×10^{28} mol s^{-1} was found. Comparison with our data evidences that Q(CN)/Q(H_2O)=0.24% and Q(NH_2)/Q(H_2O)=0.16%. These results are in agreement with available data for previously observed comets.

REFERENCES

[1] *A'Hearn M. F., Millis R. L., Schleicher D. G., et al.* The ensemble properties of comets: results from narrowband photometry of 85 comets, 1976–1992 // Icarus.–1995.–**118**.–P. 223–270.

[2] *Combi M. R., Smyth W. H.* Monte Carlo particle – trajectory models for neutral cometary gases. I. Models and equations // Astrophys. J.–1988.–**327**.–P. 1026–1043.

[3] *Huebner W. F., Link R.* Interactive atomic and molecular database // BAAS.–1999.–**31**.–P. 6101.

[4] *Jockers K.* A two-channel focal reducer for small (diameter ≥1 m) F/8 telescopes // Experimental Astronomy.–1997.–**7**.–P. 305–318.

[5] *Jockers K., Bonev T., Korsun P., et al.* Water production of comets derived from observations of [OI] (6300 Å) and H_2O^+ (6150 Å): comets C/1998 U5 (Linear) and C/1999 J3 (Linear) // this issue.–P. 262–265.

[6] *Tegler S., Wyckoff S.* NH2 fluorescence efficiencies and the NH3 abundance in Comet Halley // Astrophys. J.–1989.–**343**.–P. 445–449.

[7] *Voloshina I. B., Glushneva I. N., Doroshenko B. T., et al.* Spectrophotometrija yarkih zvezd.–Moscow: Nauka, 1982. (in Russian).

DISCOVERY OF HIGH–SPEED SODIUM CLOUDS IN JOVIAN MAGNETOSPHERE AS A RESULT OF ITS INTERACTION WITH THE COMET SHOEMAKER–LEVY 9 MATTER

V. V. Prokof'eva[1] **and V. P. Tarashchuk**[2]

[1] *Crimean Astrophysical Observatory, Ministry of Ukraine for Education and Science*
Naukove, 98409 Crimea, Ukraine
e-mail: prok@crao.crimea.ua

[2] *Main Astronomical Observatory, NAS of Ukraine*
27 Akademika Zabolotnoho St., 03680 Kyiv, Ukraine
e-mail: vera@crao.crimea.ua

The spectral monitoring of Jupiter was performed at the Crimean Astrophysical Observatory during July–August 1994. More than 210 spectra were received on July 20, when the Comet SL 9 Q fragments were falling onto Jupiter and the weather condition was favourable. Their analysis allowed to discover a new phenomenon when comet matter interacted with Jovian magnetosphere. We observed sodium D-line emission splashes of different intensity before explosion of the Q fragments in the planet atmosphere.

OBSERVATIONS

The spectral observations were performed at the 0.5-m meniscus telescope with a diffractional spectrograph having the inlet circular 6 arcsec diaphragm and a digital recording TV complex. The spectrograph covered 5700–7400 Å with a resolution 20 Å. The exposition time was of 26 sec [1]. We had a possibility to inspect the diaphragm location on the planet disk continuously. We registered the spectra from the spots along the $-45°$ latitude, disk centre, east and west limbs of equator, and the places near the northern pole.

The spectra of July 20 were compared with those on July 19, when the Na D-line was observed only as an absorption line and its average equivalent width was of 1.3 Å, *i.e.*, practically equal to that value of solar D-line. On July 20, when the Q fragments were falling, the spectral observations lasted 4 hours ($17–21^h$ UT). The emission with variable intensity in the spectral range 5850-5940 Å is present in all the spectra.

The 5890–5896 Å emission could belong only to the Na D-line because no other species could produce this emission under the considered circumstances. It had an unusual time behaviour and Doppler shift. Its typical view was the sequence of the fast flashes. This Na emission had the following characteristics:

1. The mean equivalent width was equal to 2.5 Å with maximum value up to 5 Å.

2. The emission was recorded at different places of the planet disc. The dimension of luminous region was estimated as 140,000 km or more.

3. The most powerful Na flashes were observed during 1.1 hour, when the distance of the Q fragment from the Jovian centre was about $3R_j$. The typical characteristic time of the flashes was near 1 minute. The intensity of flashes steeply decreased at 0.5 hour before the mean impact moment of the Q fragments.

4. The sodium emission had a Doppler shifts up to 30 Å corresponding to the velocity 1500 km/s. We note that the brighter blue shift component was presented during all the time, but the red shift component was partly blended by a water absorption band.

5. During the moments when intensive sodium emissions were observed, the lithium 6807 Å emissions were also recorded. The Doppler shift was near to that of Na. Correct measurement of lithium emissions was very uncertain because of the presence of blends of another species in this place of a spectrum.

The brightest flashes were observed, when the Q2 and Q1 fragments passed the region of magnetosphere at a distant $3R_j$ from the planet centre. Thus, the appearance and behaviour of this sodium emission was connected with the Q fragments, which were disintegrated into at least 7–8 parts and were surrounded by extended coma with splinters and dust particles of different sizes [2].

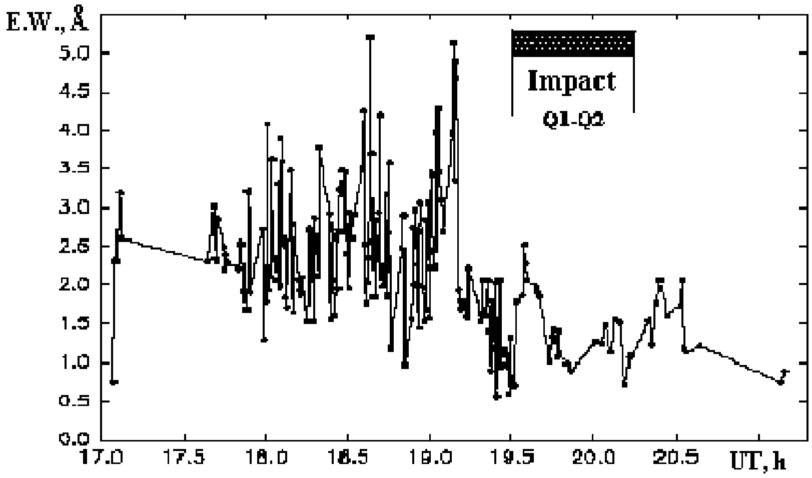

Figure 1: Equivalent width (E. W., Å) of the sodium emission D-line blue shift component versus time UT, 1994 July 20. The moments of the Q1–Q2 impacts are shown with black band

DISCUSSION

The sodium and its compounds exist in comet matter. The Na escaped from dust and surfaces of numerous splinters owing to sputtering, when they were crossing the magnetosphere. The intense flux of magnetospheric fast electrons, protons and ions existed just in the region about $3R_j$. These particles bombarded dust and surfaces of splinters. Due to the sputtering sodium was released first of all and nearly 10% of the atoms were ionized. The electrons, atoms and ions which emerged in this process were drawn into subsequent ionization process according to the mechanism of the critical ionization velocity. Increasing density of energetic electrons intensified the sodium ionization. The developing of local electric fields in plasma caused acceleration of Na ions. The processes of sputtering, ionization of Na atoms, accelerations of ions and recombination were developing simultaneously.

Plasma became unstable and this caused occurrence of lower-hybrid oscillations and noncollisional transfer of energy. Ions and electrons were involved in further processes. The geometry of the Q fragments passing through the inner magnetosphere was such that the Io's electric current tube could promote acceleration of Na ions in the longitudinal electric fields up to 1500 km/s. Recombination of sodium ions occurred due to charge exchange process. Thus, clouds of high-speed sodium atoms were produced and developed in the process of the interaction of comet dust with inner Jovian magnetosphere.

REFERENCES

[1] *Prokof'eva V. V., Tarashchuk V. P.* // Kinematics and Physics of Celestial Bodies.–1996.–**12**, N 5.–P. 82.

[2] *Prokof'eva V. V., Tarashchuk V. P., Lyuty V. M., Metlov V. G.* // Astron. Lett.–1996.–**22**.–P. 771.

SURFACE PHOTOMETRY OF COMETS: OUTLOOK FOR SMALL TELESCOPES

Yu. V. Sizonenko

Main Astronomical Observatory, NAS of Ukraine
27 Akademika Zabolotnoho St., 03680 Kyiv, Ukraine
e-mail: sizon@mao.kiev.ua

The small telescopes of observatories in Ukraine have one useful characteristic, which can give a new life for these instruments. With wide angle astrographs and cameras one can obtain the images of extended sky objects for different purposes, in particular for studies of surface brightness distributions. The examples of successful use of the results of surface photometry of comets are presented.

INTRODUCTION

One can consider what small telescopes can't compete with giant telescopes on the ground and in space. However, some of these telescopes have characteristics which are useful for study of extended sky objects. Observatories in Ukraine have some telescopes with a short focal length and sufficient aperture (for example, DShA, SBG, AFU and others), which can be used to obtain the images of such objects, in particular, images of comets. We supply below some examples of successful study of comets by means of images obtained with small telescopes.

SYNCHRONIC BANDS OF COMET C/1975 R1 (WEST)

We observed the Comet West early spring 1976 on Peak Terskol, Northern Caucasus. The images of comet were obtained with camera AFU–75 (210/735). On the pictures one can see the five bright bands formed the dust tail of Comet West. The synchrone–syndine analysis shows that the axes of bands are classic synchrones. We obtained photometric scans along the directions, which are *loci* of synchrones. The distributions of brightness in synchronic bands have been compared with the calculated distributions of brightness. To calculate the distributions we used the modified Finson–Probstein method. The results of our study are as follows: the size distributions of comet particles are obtained; the rate of dust production is computed and the duration of rise of dust emission is determined; the dependence of dust ejection velocity on particle size and heliocentric distance of the nucleus is derived. We estimated the duration of rises of dust emission used the measures of the width of the synchronic bands.

So, we have found the basic characteristics of dust particles ejected during active processes in nucleus of Comet West and the characteristics of these processes using images of the comet tail obtained with a very modest telescope.

EXTENDED SOURCE OF C_2 MOLECULES IN THE COMA OF COMET C/1995 O1 (HALE–BOPP)

The images of Comet Hale–Bopp were obtained with the double astrograph (400/2000) at the Main Astronomical Observatory of NAS of Ukraine in Kyiv in January–April 1997. Some of them were taken through special filters which allow to isolate the $C_2(\nu = +1)$ emission and nearby continuum. After subtraction of "cont" image from "C_2" image according to a special procedure we obtained the brightness isophotes. The isophotes on April 21.77, 1977 have one additional center of brightness near the nucleus. The secondary peak of brightness is shifted by $\Delta\alpha = 1.15$ arcmin and $\Delta\delta = 0.25$ arcmin relatively to the nucleus. The angle from the projected solar direction to the secondary peak direction is about 60°. On March 13.04, 1997 there is no secondary peak of brightness, but one can see a prominence in the outward isophotes. The angle between the sunward direction and to the prominence is of 60°.

It was suggested [1] that a portion of the C_2 emission in the coma of Comet Hale–Bopp was formed by the destruction of small organic dust grains. The small particles (0.1–0.3 μm) reflect light with the wavelengths 0.4–0.5 μm weekly. Therefore, there is no significant contribution to the dust brightness from the grains and at same time we can see the additional brightness of C_2 emission in the regions, where the dust grains release the C_2 parent molecules.

CONCLUSIONS

So, we have found the basic characteristics of the dust particles ejected during active processes in the nucleus of Comet West and the characteristics of these processes using the images of the comet tail obtained with a very modest telescope. Also we have given new arguments, which support the hypothesis [1], by using our small telescope. We hope to take new images of the bright comets in future with telescopes of our observatory and new detectors of light.

Acknowledgements. The research described in this paper was made possible in part by a Grant of the Ministry for Science and Technology of Ukraine.

REFERENCES

[1] *Sekiguchi T., et al.* Observations of C_2 Molecules in the Coma of Comets at Mitaka // Abstracts Book of the First International Conference on Comet Hale–Bopp.–1997.

THE COMET HALE-BOPP NUCLEUS: HOW FAST ITS AXIAL ROTATION WAS?

L. M. Shulman

Main Astronomical Observatory, NAS of Ukraine
27 Akademika Zabolotnoho St., 03680 Kyiv, Ukraine
e-mail: shulman@mao.kiev.ua

After the First International Conference on Comet Hale-Bopp (Canaries, 1998) many astronomers agree with the value of the period of axial rotation of its nucleus, which was obtained by observers by a comparison of the two sequential pattern of the dust arcs. It was noted that the pattern had been repeated each ~12 hours. The value $11^{\mathrm{h}}.35$ was taken as the period of axial rotation. Before the conference on Canaries, just after the first HST observations published by Weaver, Sekanina found a much longer period $\approx 8^{\mathrm{d}}$. Later Shulman obtained from the observation of Kidger *et al.* another value of the period, namely $\approx 4^{\mathrm{d}}$. The possible reasons of this discrepancy are discussed. It is shown that the short period is probably obtained by a misidentification of the same arc on two sequential images and, as a result, a severe overestimation of the radial velocity of dust in the arcs. To obtain the short period (a half of day) one must take the projected velocity of the arc ~ 1.6 km/s. This value can hardly be realistic because it exceeds the gas H_2O expansion velocity by the order. If one takes a more realistic expansion velocity the long period should be automatically obtained.

HOW THE LONG PERIOD WAS OBTAINED

Since 1995 August till October Kidger *et al.* [1, 2, 3, 4] observed three spiral jets. It was the beginning of activity of this comet and it is essential that only a single jet was observed each time. The Spanish astronomers have observed a series of consequent images of the comet. One could see that there was a spiral jet which was moving outward from the nucleus of the comet. The most probable suggestion is that the jet was a dust outflow from the nucleus swept by its axial rotation into a spiral. It means that the projected velocity of expansion could be determined by a simple geometric calculation. Let X and Y are the co-ordinates of a point of the jet in the image plane. Let the jet was produced by a single active region on the rotating nucleus. The circumstances of the dust ejection are defined by the next angles: ϕ is the nucleocentric latitude of the active region; ϕ_o is the nucleocentric latitude of the observer; θ_0 is the positional angle of the central meridian of the comet "disk"; $\lambda(t) = \omega(t - t_0)$ is the longitude of the active region in the moment t, t_0 is the moment when the active region passes the central meridian. It is convenient to choose the coordinate system in the picture plane with its Y-axis directed along the central meridian. If the active region was ejecting dust with the velocity $v(\tau)$ in the moment of ejection τ then an earth observer has to see, in the moment t, the curve whose equation may be written in these coordinates as follows:

$$X(t,\tau) = (t-\tau)v(\tau)\cos\phi\sin(\omega(\tau - t_0)), \tag{1}$$

$$Y(t,\tau) = (t-\tau)v(\tau)\left[\sin\phi\cos\phi_o - \cos\phi\sin\phi_o\cos(\omega(\tau - t_0))\right], \tag{2}$$

where τ is the parameter, which should be excluded to get the $Y(X)$ function on the moment of observation t. The rotational component of the velocity ωr_n as well as the repulsive acceleration by solar radiation are neglected.

This parametric curve can be described in the polar coordinates in the picture plain by the equations:

$$X = \rho\cos\theta, \quad Y = \rho\sin\theta, \tag{3}$$

where $\theta = \theta_{obs} - \theta_0 + \pi/2$ is the polar angle of the point in jet, θ_{obs} is the observed positional angle of the same point, ρ is the projected distance in the picture plain.

It is defined by the relationship

$$\rho(t,\tau)=\sqrt{x^2+y^2}=V_{pr}(\tau)(t-\tau)=(t-\tau)v(\tau)\times$$

$$\left[(\cos\phi+\cos\phi_o)^2-\frac{1}{2}\sin 2\phi\sin 2\phi_o\cos(\omega(\tau-t_0))+\cos^2\phi\cos^2\phi_o\sin^2(\omega(\tau-t_0))\right]^{1/2}, \tag{4}$$

where V_{pr} is the projected velocity and

$$\tan\theta(\tau)=Y/X=\frac{\tan\phi\cos\phi_o}{\sin(\omega(\tau-t_0))}-sin\phi_o\cot(\omega(\tau-t_0)). \tag{5}$$

Here x and y are the observed rectangular coordinates which are measured to the East and to the North, respectively. One can see that the ejected dust moved from the nucleus with an approximately constant velocity and the projected velocity can be calculated directly from the measured coordinates of points in the jet.

After the calculation of the $V_{pr}(\theta)$ and $\tau(\theta)$ the next step is to use the Eq. (5) and obtain all the set of parameters: ω, ϕ, ϕ_o, t_0. Two of these parameters, namely ϕ and ϕ_o, control the shape of the jet. One can easy estimate the axial rotation period $P=2\pi/\omega$ because the nucleocentric angle covered by the jet approximately corresponds to a half of the period. We have obtained the following values.

Parameter of the nucleus and source of dust	quantity	value
The observer passed the central meridian of the nucleus at	t_0	Oct 24.46
Positional angle of the central meridian	θ_0	130°
Nucleocentric latitude of the source	ϕ	68°
Nucleocentric latitude of the observer	ϕ_o	55°
The period of rotation	P	$3^{\rm d}.96$

One can easy calculate the space velocity of ejected dust as a function of time. The result is plotted below in Fig. 1. One can see that we have here a steep invisible increase of the velocity, then the velocity slowly decreases and finally steeply goes to zero after the local sunset in the vicinity of the active region. The maximal

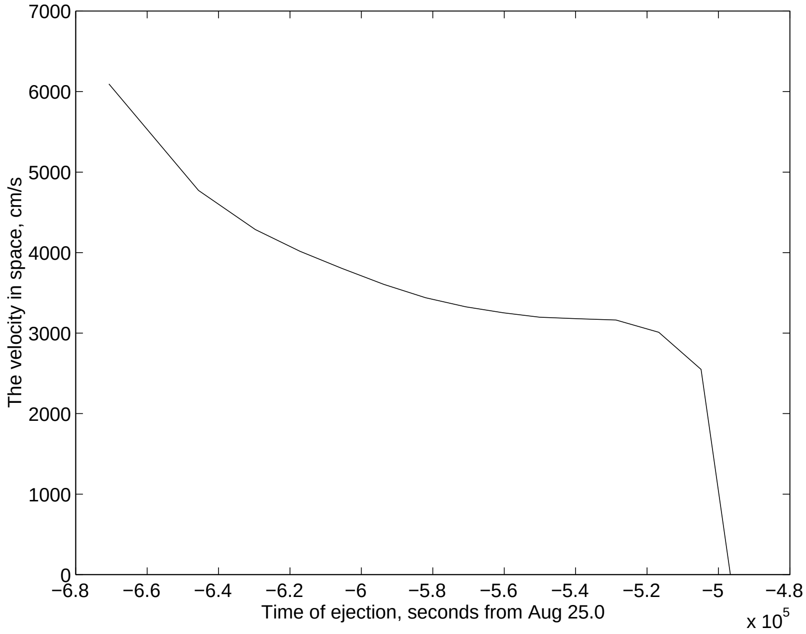

Figure 1: The projected velocity of dust in the August jet

value of the velocity ~60 m/s agrees with the radioastronomical data [8] which gives the CO velocity ~500 m/s. The CO was probably the propellant that dragged the water ice grains which formed the jet. So, the long four day period is in accordance both with the direct observed kinematics of the spiral jet and with the data on the movement of the gas which accelerated the grains. The modelled picture fits well observations as one can see in Fig. 2 below.

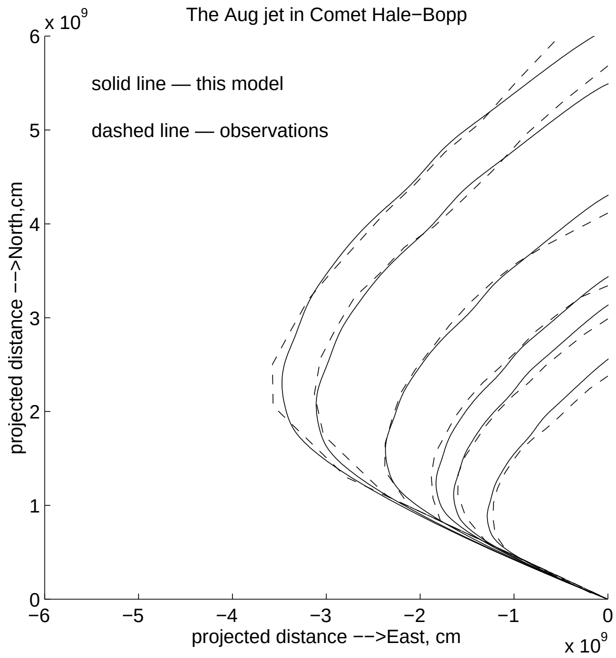

Figure 2: Comparison of this model with observations

HOW TO GET A SHORT PERIOD?

The mentioned short period (half a day) has been obtained much later when the comet approached the Martian orbit. That time it produced many jets and arcs. Several arcs were often observed simultaneously. Farnham *et al.* [5] have found the period 11.35 ± 0.05 hours from the movement of dust arcs from March 25 through April 1, 1997. The same value has been found by Licandro *et al.* [9] from a 16 days series of narrow band near infrared images of this comet obtained during April 1997. Two possible reasons may be proposed to explain this discrepancy. One of them is the spinning up of the nucleus by the angular momentum of ejected matter. Another reason is the existence of more than one active regions on the surface of the nucleus (N_{ar}) which were able to produce dust arcs.

One can expect in this case that the rotation period found from the periodicity of the arcs is only a part of the real period: $P_{obs} = P_{real}/N_{arcs}$. Both the reasons can do together. So, there may be a difference between the periods of 1995 and 1997, *i.e.*, $P_{obs}(1997) = (P_{real}(1995) - \Delta P)/N_{ar}$. The discrepancy disappears if we take $N_{ars}(1997) = 8$ and $\Delta P = P_{real}(1995) - P_{real}(1997) = 4.24$ hours so the angular velocity in 1997 exceeded its 1995 value by 4.5%. Surely, such a small difference may be simply an error of data processing. One can see that in the case of self-spinning up there should be a specific appearance of the arcs. Generally, they would not be approximately equidistant because there is no reason for the active regions to be separated by an equal interval of the nucleocentric longitude. The authors cited above [5, 9] paid their attention to the fact that all the pattern repeated approximately each 12 hours. Hence, the atmosphere of a comet is not rotating with its nucleus as a solid body and, therefore, any periodicity of the pattern cannot be considered as an effect of spinning of the nucleus.

There is the third possible reason to obtain a period of rotation which is many times shorter than the real period. If one have two multi-arc images of a comet it is possible to determine the velocity of their expansion and here is a real possibility to make a mistake. It is necessary to identify the same arc in two subsequent images. There is no individual features which could help to make this identification and, therefore, one can take two different arcs in two images as two positions of the same arc separated approximately by one day. The real velocity of expansion is given by the relationship

$$V_{real} = \frac{R_2 - R_1}{NP_{real}}\,, \tag{6}$$

where $R_{1,2}$ are two nucleocentric distances of the same arc, N is the number of revolutions between both arcs, P_{real} is the real rotation period. In the case of misidentification one should get a false estimation of the velocity

$$V_{false} = \frac{R_2 - R_1}{\Delta t}\,, \tag{7}$$

where $\Delta t \approx 86400$ s is approximately one day interval between two images. If the difference between the nucleocentic distances of two opposite edges of the same arc is

$$\Delta R = VP\frac{\psi}{2\pi}\,, \tag{8}$$

where ψ is the angular size of the arc, then one can get a false period using the relationship (7)

$$P_{false} = \frac{\Delta R \cdot 2\pi\Delta t}{\psi(R_2 - R_1)} = \frac{\Delta t}{N}\,. \tag{9}$$

So, the misidentification can give a false period which can be equal to an integer part of a day: one day, a half a day, one third of a day and so forth. This consideration does not depend on the conditions of projection because both the distances and velocity are projected and so the function of angles is self-eliminated. May be the authors of [9, 5] implicitly took N = 2 and so got their 11.35 hour period.

Note that this approach cannot give the real period because any real period fits the relationships (6) and (8). So, one has to obtain the velocity in another way, namely from the kinematics of an individual arc. It is important to remember that physical nature of the arcs was different from those observed when the comet was at a heliocentric distance about 7 AU. When the comet crossed the Jovian orbit water vapour became the main constituent of its atmosphere. So, instead of icy grains propelled by CO we had then usual mineral dust dragged outward by water vapour. If we take the half day period of rotation then the arc should expand with a velocity 1–2 km/sec. This value exceeds by the order the possible velocity of dust grains accelerated by gas outflow. Even gas itself cannot have its velocity more than 100–200 m/sec. One can see that the short period of rotation is not real.

The discrepancy between our 4 day and Sekanina's 8 day periods can be explained by the circumstances of the observations. Sekanina [6] used the Hubble Space Telescope data, which were the images of the inner circum-nuclear region, where it was very easy to take the spiral jet produced during two revolutions as that produced in one period. Sekanina simply determined the double period interval as the period.

REFERENCES

[1] *Kidger M., et al.* // IAU Circ.–1995.–N 6220.

[2] *Kidger M.* // IAU Circ.–1995.–N 6240.

[3] *Kidger M.* // IAU Circ.–1995.–N 6244.

[4] *Kidger M.* // Astronomer.–1995.–**32**.–P. 155.

[5] *Farnham T., et al.*// First International Conference on Comet Hale-Bopp (Tenerife, Feb 2–5, 1998). Abstracts, 1998.–P. 8.

[6] *Sekanina Zd.* Activity of Comet Hale-Bopp (1995 O1) Beyond 6 AU from the Sun, Preprint JPL D-13271, 1995.

[7] *Shulman L. M.* Cometary Nuclei.–Moscow: Nauka, 1987. (in Russian).

[8] *Biver, et al.* // Science.–1997.–**275**.–P. 1915–1919.

[9] *Licandro J., et al.* // Astrophys. J. Lett.–1998.–**501**.–P. 221–225.

SEARCH FOR INTERSTELLAR METEOROIDS

S. V. Kolomiyets

Kharkiv State Technical University of Radioelectronics
14 Lenin Av., 61166 Kharkiv, Ukraine
e-mail: kometa@kture.kharkov.ua

A possibility is discussed that there are interstellar meteoroids among those detected by ground based instrumentation. It appears that about 0.2–10% of the total number of the meteoroids have hyperbolic orbits. There are different points of view on possibility to detect a meteoroid having an infinite orbit. One may expect theoretically that many of the recorded hyperbolic meteoroids are interstellar. Hence, some hyperbolic orbits may be either erroneous or belong to the meteoroids which were born in the Solar System. A criterion of selection of the real interstellar particles is given in the present paper. The Kharkiv catalogue of orbits of meteoroids with the masses greater than 10^{-6} g, which produce faint radiometeors, was used.

DATA ON HYPERBOLA AND THE ACCURACY OF THE ORBITS DETERMINATION

The most of meteors observed instrumentally belong to the Solar System. Nevertheless, the Solar System is not closed. It is permeable for the particles and even large bodies flying inward and outward. Since a meteoroid with a hyperbolic heliocentric velocity may have an usual geocentric velocity [1, 11] then a possibility to record a hyperbolic meteor is no more connected with a great error of determination of its velocity. Presence of interstellar particles in the observation data is not proved till now because the accuracy of measurements and calculations is not good enough to check the reliability of these data. This problem is known as the problem of hyperbolic meteoroids but really it is the problem of hyperbolic orbits of dust grains in the Solar System. No one exact enough orbit of a small body is distinctly classified as really hyperbolic.

It is supposed that 80% of the particles recorded by the Pioneer-8 and Pioneer-9 spacecrafts caused by a stream of the β-meteoroids with the masses $10^{-15}-10^{-12}$ g. Unfortunately, the accuracy of determination of orbits was rather poor because the speed was determined with an accuracy $\pm 10\%$ and direction of the velocity with that of $\pm 27\%$ [22]. Nevertheless, the dust experiments on board of the Ulysses and other spacecrafts detected a significant flux of the β-meteoroids with interstellar hyperbolic orbits in the mass range $10^{-16}-10^{-8}$ g [17]. Effect of accuracy of the data on the percentage of hyperbola was investigated in the papers [1, 15, 21]. It occurs that there are 1–2% of hyperbola in precise photographic data [8] and up to 10% in less precise ones as well as in radio meteor catalogues [5, 6, 11]. There are hyperbolic orbits in television meteor catalogues: almost 15% in the Japanese one that includes the observations in 1990–1994 and 12% in the Canadian catalogue.

The root-mean-square errors of photographic and radio measurements are given in Table 1. The values for radio meteors [11] are averaged taking into consideration the tails of error distribution functions. The accuracy of individual orbits is sometimes better. One can meet such minimal values as follows: $\sigma V_g < 1.5$ km/s, $\sigma Z < 0\overset{\circ}{.}5$, $\sigma A < 0\overset{\circ}{.}5$, $\sigma V_h < 1$ km/s. It is shown in the papers [11, 16, 23] that the accuracy of catalogues of the orbits of radio meteors is not worse than that of photographic catalogues and sometimes exceeds it. The accuracy of catalogued orbits can be improved by increasing the accuracy of computations (if initial parameters are known), *i.e.*, taking better algorithm and constants [1, 11].

An error may be either positive or negative. Therefore, hidden hyperbola may be present among the near parabolic ellipses ($e < 1$ and $e \sim 1$). The work [1] shows the dependence of the number of hyperbola on the accuracy of computations. It occurred that 24.8% (1975) and 24.3% (1976) hyperbolic orbits became elliptic after a recalculation with the changed constants. The type of an orbit may be changed because the root-mean-square error of eccentricity σe increases with decreasing of e [23].

The growth of the number of hyperbolic orbits with increasing of the volume of data may be either real or a result of accumulation of erroneous data. Analysis of formation of hyperbolic orbits in the Solar System shows that their number cannot exceed some percent. The less is the mass of a meteoroid the more mechanisms to transform its orbit into a hyperbola exist but it is more difficult to detect such a body. Having more data one can study the distribution of hyperbolic orbit even each orbit is not very precise. Unfortunately, the accumulated at present time observation data on bodies with hyperbolic orbits are very non-uniform and insufficiently comprehensive to make any ultimate significant conclusions. According to Öpik the Pultusk famous meteorite

Table 1: Root-mean-square errors of meteoroid velocities, coordinates of the radiants and orbital elements obtained by different techniques

Technique of observation	σVg km s^{-1}	σA °	σZ °	$\sigma\alpha$ °	$\sigma\delta$ °	σe	$\sigma(1/a)$ AU^{-1}	σi °	$\sigma\omega$ °
1. Photographic in Odesa [3]	0.6	–	–	0.5	0.5	0.052	0.054	2.12	2.46
2. Radar in Kharkiv (observations of the Geminids meteor stream) [9]	2.0	–	–	2.7	2.4	0.028	0.15	5.6	4.3
3. Radar in Kharkiv (calculation with analytical formulas, average values for elliptic orbits) [23]	1.4	–	–	–	–	0.25	0.12	6.6	–
4. Radar in Kharkiv (individual hyperbolic orbits) [11]	2.4	1.8	4.2	–	–	0.205	0.253	7.0	7.6
5. Radar in Obninsk [16]	–	–	–	–	–	0.04	0.08	3.0	4.0

is a single body with confidently determined hyperbolic velocity. It is also worthy to mention 98 hyperbolic comets of the Marsden's catalogue and hyperbolic orbits in other comet catalogues. Several catalogues of hyperbolic meteoroids have been published. There are among them the Vsekhsvyatsky's catalogue consisting of 78 orbits [24] and the Simakina's catalogue consisting of 38 hyperbolic orbits [20]. There are also observed data on hyperbola determined by photographic and radio techniques in Kyiv, Kazan and Kharkiv. The radar system AMOR is working daily in the Southern Hemisphere and gives a possibility to study the characteristics of groups of non-bound particles in the inner Solar System. Meteor investigation with Arecibo radar system in 1997 confirmed the existence of hyperbolic meteoroids with masses $10^{-11} - 10^{-6}$ g.

MECHANISMS OF THE HYPERBOLIC ORBIT FORMATION OF METEOROIDS

Since both interstellar particles and those leaving the Solar System can have hyperbolic orbits it is rather complicated to analyze data on such orbits. The problem of interstellar meteoroids has already become a component of the problem of hyperbolic orbits. So, it is difficult to reveal the peculiar motion of the Sun in distributions of all hyperbolic orbits. According to the theory of capture [18] the captured into the Solar System bodies will have elliptic and near parabolic orbits. It makes the search of interstellar particles more complicated. When processing cometary orbit data one often can succeed in passing from an observed oscillating hyperbolic orbit to the primary elliptic one after accounting planetary perturbations. The observational selection is an additional difficulty when studying of distributions of cometary orbits.

The density of the interstellar comets in the Galaxy disk is estimated as one comet per cube with a side of 9 AU. It is not far from that density which ensure a noticeable probability to observe an interstellar comet. According to the Vsekhsvyatsky's estimates an interstellar meteor must be observed practically every day. In this case the meteoroids with $e \gg 1$ must be present among the observed bodies [24]. According to other estimates [4, 12], on the contrary, the eccentricities of gravitationally focused interstellar meteor orbits must be concentrated around unity. The orbits, which became hyperbolic due to perturbations from the nearest planets [21], are expected to have eccentricities $e \sim 1$ as well. A possible mechanism of the origin of hyperbolic meteoroids is a collision of two asteroids [1]. Meteoroids born in explosions caused by such collisions can get hyperbolic orbits. It is supposed in the work [13] that such meteoroids ($10^{-3} - 10^{-4}$ g) could have their orbital inclinations $i < 90°$ and heliocentric velocities $V_h > 57$ km/s.

There are many other criteria to evaluate the efficiency of a hyperbolic orbit formation mechanism in the Solar System. One of the criteria is the number of nodes of the testing orbit. A hyperbolic orbit on the contrary to an elliptic one can cross the ecliptic plane only once. For the hyperbolic meteoroids having two nodes one can find the perturbation forces in the ecliptic plane, which could transform into hyperbola their initial, probably a non-hyperbolic orbit. In Kharkiv it is proposed to use the radius vectors of ascending and descending nodes when applying this criterion. The results of measurements in Kharkiv has been checked in this way. Such suspicious orbits have been found among the data of 1975–1976. They are transformed by planetary perturbations of Mars (4 orbits), Jupiter (3 orbits) and Saturn (2 orbits). The idea that any planet of the Solar System is able to transform an orbit into hyperbola is proved in [2] by estimation of the incoming flux of the particles whose hyperbolic orbits are the result of transformation of their initial orbits in spheres of influence of planets.

There are another mechanisms which can change an orbit of a meteor body (especially of a small mass $M \ll 1$ g) in the Solar System: non-gravitational effects (*e.g.*, light pressure), perturbations from the Sun and the Moon within the sphere of the Earth attraction. Recent astronomical discoveries qualitatively confirmed the hypothesis on origin hyperbolic meteoroids by volcanic eruption on satellites of planets as well as elsewhere in the Galaxy [14, 17, 24]. Data available on Geminga show a direct connection between the matter released during the Supernova explosion and discovered micrometeoroid streams of the Arecibo particles and the Ulysses ones.

There is a hypothesis on a possibility to detect the interstellar particles by a kinematic considerations. If interstellar bodies are present among the observed meteoroids with hyperbolic orbits, then their interstellar velocity distribution must correspond to the distribution of radial velocities of the nearest stars. The velocity of the Sun is about 19.4 km/s. Parabolic velocity of bodies in the Solar System is believed to be 42.1 km/s. It gives 46.6 km/s as the lowest limit of the heliocentric velocity of interstellar meteoroids. Therefore, if the heliocentric velocity of a meteoroid exceeds the parabolic velocity more than by 10 km/s this body may be of interstellar origin. Moreover, a concentration of meteor radiants to the apex of the Sun ($\lambda = 272°$, $\beta = 57\overset{\circ}{.}5$) should be observed for interstellar meteoroids. For a particle entering the Solar System from interstellar space and coming to the Earth (*i.e.*, moving from the apex) the distributions of interstellar meteoroids on the orbital eccentricity and the perihelion distance have been calculated in the paper [12] for different longitudes of the Earth (observation dates). It has turned out that the most convenient observation periods for detection of interstellar meteoroids were in March and September. Eccentricities of such interstellar particles' orbits should not exceed the value 1.1.

ANALYSIS OF THE KHARKIV RADIO METEOR OBSERVATIONS

More than 230 thousand orbits of the meteoroids with the masses $> 10^{-6}$ g have been registered in Kharkiv [23] with the Meteor Automatic Radar System (MARS) form January 1972 till December 1978. In order to enhance reliability of further analysis we carefully select 159787 orbits according to the special technique. The hyperbolic meteoroid orbits in Kharkiv were studied by samples of different volumes selected of the mentioned multitude by a criterion $a < 0$, $e \geq 1$ and $a > 0$, $0.9 < e < 1$. All the 7911 selected orbits cover a 6 year period with the following numbers of orbits: in 1972 – 475; in 1973 – 1802; in 1974 – 1884; in 1975 – 1448; in 1976 – 1004; in 1977 – 752; in 1978 – 546. Other samples of orbits observed in 1975–1976 have also been studied [1, 2, 10, 11, 15]. There have been selected 1350 hyperbolic orbits among the 54000 orbits observed during 1975 and 950 hyperbolic orbits among the 46000 ones observed during 1976. The orbits selected according to this criterion in the Kharkiv works [1, 2, 10, 11, 15] were called near parabolic and those selected by an additional criterion $e > 1 + 2\sigma e$ were called hyperbolic. This selection gave 436 hyperbolas of the total number of 1350 orbits of 1975. Among all the near parabolic orbits there are orbits for which analytically determined heights of the meteor trails are in the range of 69–121 km. There were 640 (1975) and 461 (1976) such orbits. A list of 533 elliptical orbits (data of 1975 with $0.9 \leq e < 1$) were used. It was compiled using the Kharkiv elliptical orbit catalogue.

The Kharkiv database contains information obtained for the same period of time and by the same facilities. High statistic representativeness of the data allowed to estimate season variation of the number of observed hyperbolic orbits. The number of such orbits changes during a year approximately as the total number of orbits with a minimum in the first half of the year. The percentage of hyperbolic orbits changes during a year from 1.2 to 4.8, the averaged annual percentage of hyperbolic orbits is 2.8% of the total number of orbits. One should compare the distributions of orbital parameters of meteoroids with that of other bodies (as well as the parameters obtained by different methods) with regard to the above mentioned observational selection. The difference between the distributions of hyperbolic and elliptic meteoroids by their azimuth, zenith distance and the radiant inclination is unessential [11, 23]. The distribution of geocentric velocity V_g for meteoroids with hyperbolic orbits is only slightly shifted to larger velocities in comparison with the distribution V_g for all orbits. The physical factor of noticeability of radio meteors is a function of the observed velocity and the zenith distance of radiant. The geometric form factor is a function mainly of the radiant inclination in continuous day-and-night observations [9]. So, with regard to the stated above analogy of distributions for all the meteors and the meteoroids with hyperbolic orbits, one can conclude that it is possible to use the Kharkiv data to compare different parameters of hyperbolic and elliptic orbits.

Fig. 1 shows the distributions of hyperbolic orbits on some parameters (an example for possible interstellar meteoroids). The distributions of all different samples hyperbolic meteor orbits on the eccentricity are investigated. Among 7911 orbits 28 ones are the eccentricity above 5 and 2300 orbits are $1 < e < 2$, fifteen orbits (1975) have $5 < e < 7$ [11]. The distributions by e both according to the Kharkiv data with $e > 1 + 2\sigma e$ [11] and the catalogue [24] are similar with the main maximum between 1.3 and 1.5. But the distribution on e of all the hyperbolic meteoroids as well as that of the hyperbolic orbits by Fig. 1 are different from them and have the main maximum at $e = 1.0$ to 1.1.

When analyzing a distribution on heliocentric velocity it is worthy to mention that rather many orbits have errors of individual estimates less than the average value of $\sigma V_h = 2$ km/s. According to the Kharkiv data the tail

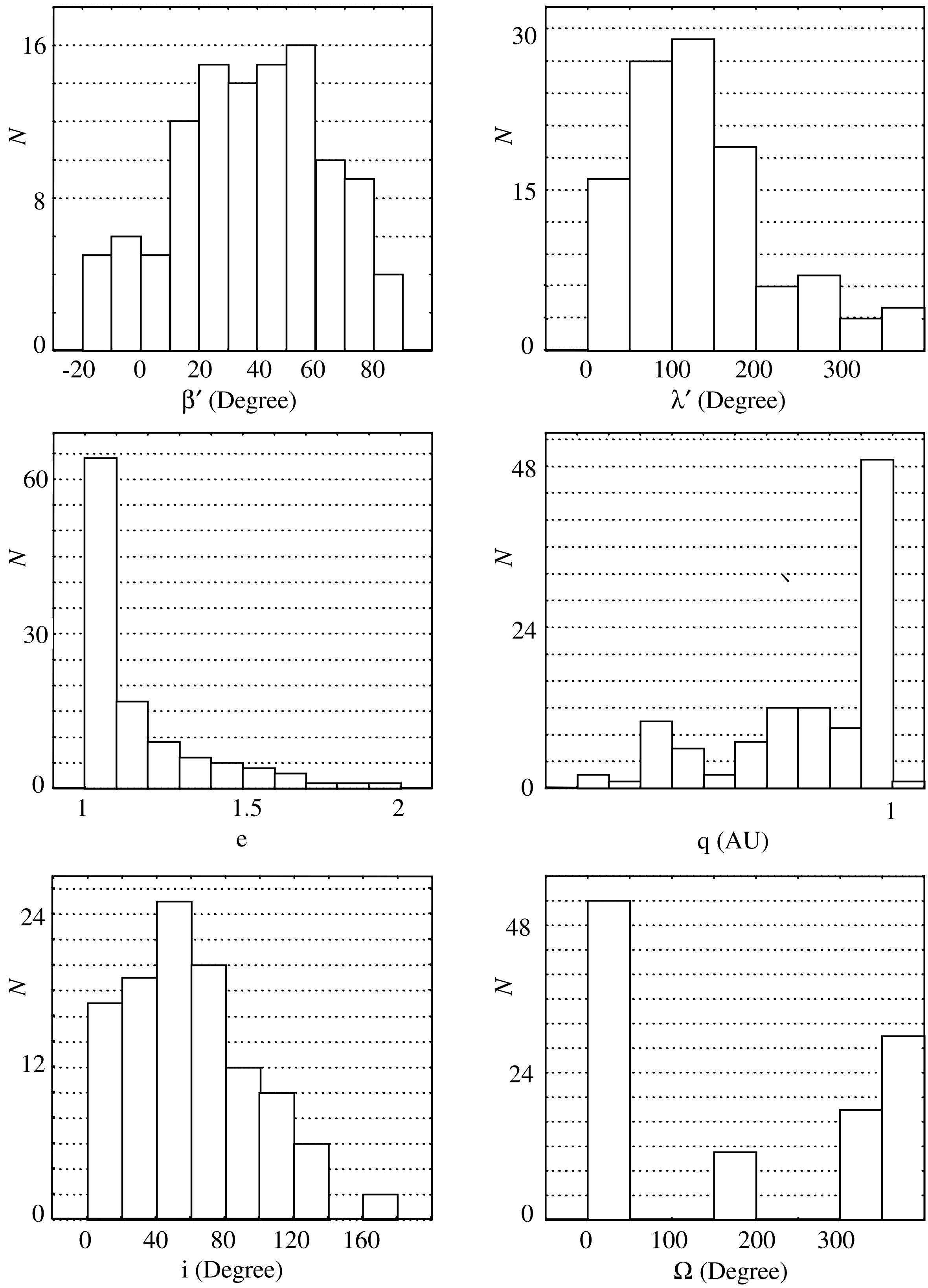

Figure 1: Distribution of a number (N) of hyperbolic meteor orbits ($1 < e < 2$) on heliocentric radiant coordinates (λ', β') and on elements of orbits: the eccentricity e, the perihelion distance q, inclination i, the longitude of the ascending node W

of the velocity distribution function extends up to $V_h \sim 90$ km/s, but the main maximum of distribution of V_h is in the range from 40 km/s to 50 km/s as well as for hyperbolic orbits. The difference between distributions of the Kharkiv data and the Vsekhsvyatsky's catalogue [24] can be explained by the fact that in the catalogue [24] the data is very non-uniform and the selection of observations wasn't taken into account. In the distributions on V_h and e based on the Kharkiv data in 1975–1976 the form and physical factors of selectivity were taken into account by a weighted processing. For hyperbolic and elliptic orbits the distributions of q are different. Elliptic orbits have an almost uniform distribution with a little excess in an interval from $q = 0.9$ to 1.0. Hyperbolic orbits show a sharp increase of the number of orbits when $q \to 1$, the most of orbits are concentrated in an interval of 0.9–1.0. It is known that for parabolic orbits q and ω are connected by the relationship $q = \sin^2(\omega/2)$ and if $q \to 1$ then the argument of perihelion $\omega \to 180°$. The distribution of ω is given in the work [11]. The main maximum lies near $\omega = 180°$. The connection between the distributions of q and ω can be used to test whether the most of orbits are real or the majority of them are a result of errors.

The distributions of near parabolic, hyperbolic and elliptic orbits on longitude of perihelion are compared. The distributions are different that can be an evidence of reality of hyperbolic orbits. The statistics of directions to aphelion and perihelion [10] was used. It was initially assumed that near parabolic and hyperbolic orbits belong to comets. According to celestial mechanics there should be a concentration of perihelion directions of long period comets to a point with the coordinates $\lambda_\pi = 246°$ and $\beta_\pi = 66°$. The search of this feature was carried out. For many hyperbolic orbits of the Kharkiv data $i < 90$. However, the obtained distributions of coordinates of perihelions λ_π and β_π for about parabolic and hyperbolic orbits hardly show the mentioned concentration distinctly. But if the interconnection of aphelion and perihelion directions is taken into account, an analysis only one coordinate of the perihelions permits to suppose that a part of particles on hyperbolic orbits are flying to meet the Solar System and penetrate it.

The distribution of elongation of the radiant from the Sun is a weighty argument in favour of reality of hyperbolic orbits in the Kharkiv data. These distributions for hyperbolas and ellipses with $0.9 < e < 1.0$ are essentially different [1]. The distribution of radiant coordinates (λ', β') of hyperbolic orbits in the ecliptic heliocentric coordinate system can testify for the conclusion about the concentration of meteor radiants to the apex of the Solar peculiar motion.

A possibility to locate interstellar meteoroids according to [12] has been studied as well. It is possible that there are certain number of interstellar meteoroids among those observed 20 days before and 20 days after March 21 during a seven years interval (1972–1978) when 111 meteoroids with the hyperbolic orbits having $1 < e < 2$ was found. Distribution of their parameters is given in Fig. 1.

The research carried out in Kharkiv gave many evidences of existence of hyperbolic orbits. They stimulate us to search for interstellar meteoroids in future. This search today has much more prospects because increasing volume of data but as well as before it is limited by accuracy of meteoroid data. New criteria of choice of interstellar meteoroids are necessary and the problem of such criteria has not been solved yet.

REFERENCES

[1] *Andreyev G. V., Kashcheyev B. L., Kolomiyets S. V.* Contradictions in the problem of hyperbolic meteors // Meteor studies.–1987.–N 13.–P. 93–104.

[2] *Andreyev G. V., Kashcheyev B. L., Kolomiyets S. V.* Hyperbolic meteoroid flax near Earth orbit // Abstracts for IAU Symp. 160: Asteroids, comets, and meteors 1993, Belgirate (Novara), Italy, June 14–18, 1993.–P. 12.

[3] *Babadzanov P. B., Kramer Y. N.* Some results of investigations of instantaneous meteor photographs // Physics and dynamics of meteors.–Dordrecht (Holland): D. Reidel Publ. Co, 1968.–P. 128–142.

[4] *Belkovich O. I., Potapov I. N.* Expected distribution of some of the orbits elements of interstellar particles in the solar system // Astron. Vestnik.–1985.–**19**, N 3.–P. 206–210. (in Russian).

[5] *Davies J. G., Gill J. C.* Radio echo measurement of the orbits of faint sporadic meteors // Mon. Notic. Roy. Astron. Soc.–1960.–**121**, N 5.–P. 437–462.

[6] *Elford W. G., Cervera M. A.* Meteor velocities: a new look at on old problem // Earth, Moon and Planets.–1995.–**68**, N 1–3.–P. 257–266.

[7] *Everhart E.* Intrinsic distributions of cometary perihelia and magnitudes // Astron. J.–1967.–**72**, N 8.–P. 1002–1011.

[8] *Jaccia L. G., Whipple F. L.* Precision orbits of 413 photographic meteors // Smithsonian. Contrib. Astrophysics.–1961.–**4**, N 4.–P. 97–129.

[9] *Kashcheyev B. L., Lebedinets V. N., Lagutin M. F.* Meteoric phenomena in the earth's atmosphere. Investigation meteor.–N 2.–Moscow: Nauka, 1967.–260 p. (in Russian).

[10] *Kashcheyev B. L., Kolomiyets S. V.* Statistics of perihelion directions of nearly parabolic and hyperbolic orbits of meteor bodies // Meteor studies.–1984.–N 11.–P. 81–89.

[11] *Kashcheyev B. L., Tkachuk A. A., Kolomiyets S. V.* On the problem of hyperbolic meteors // Space Physic Problem.–1982.–**17**.–P. 3–15.

[12] *Kazantsev A. M.* The possibility to detect interstellar meteoroids // Kinematics and Physics of Celestial Bodies.–1998.–P. 82–88.

[13] *Kazantsev A. M., Sherbaum L. M.* Hyperbolic meteors and Jupiter // Bull. Kiev. Univ. Astronomy.–1982.–**24**.–P. 72–74. (in Russian).

[14] *Kramer Y. N.* Dust particles, dust aggregates and other interstellar meteoroids // Abstracts book. Intern. Conf. METEOROIDS 1998, Tatranska Lomnica, August 17–21, 1998.–P. 440–441.

[15] *Kolomiyets S. V.* Change of the calculated shape of meteoric bodies orbits as dependent upon accuracy of calculations // Meteor studies.–1986.–N 12.–P. 75–86.

[16] *Lebedinets V. N.* Dust in the upper atmosphere and space. The meteors.–Leningrad: IEM, 1980.–248 p. (in Russian).

[17] *Mann I.* The out of ecliptic distribution of interplanetary dust and its relation to other bodies in the solar system // Earth, Moon and Planets.–1995.–**68**, N 1–3.–P. 419–426.

[18] *Radzievsky V. V., Tomanov V. P.* To the question about the origin nearly parabolic comets // Astron. Zh.–1980.–**47**, N 5.–P. 1094–1099. (in Russian).

[19] *Sarma T., Jones J.* Double-station observations of 454 TU meteors // Bull. Astron. Inst. Czechosl.–1985.–**36**, N 9.–P. 103–115.

[20] *Simakina E. G.* About hyperbolic meteor orbits // Astron. Vestnik.–1968.–**11**, N 3.–P. 153–157. (in Russian).

[21] *Stohl J.* On the problem of hyperbolic meteors // Bull. Astron. Inst. Czechosl.–1970.–**21**.–P. 10–17.

[22] *Weidensehilling S. J.* The distribution of orbits of cosmic particles detected by Pioneers 8 and 9 // Geophys. Res. Lett.–1978.–**5**, N 7.–P. 606–608.

[23] *Voloshchuk Yu. I., Kashcheev B. L., Kruchinenko V. G.* Meteors and a meteoric substance.–Kyiv: Naukova Dumka, 1989.–296 p. (in Russian).

[24] *Vsekhsvyatsky S. K.* Eruptive Processes in galaxy and hyperbolic meteors // Space Physics Problems.–1978.–**13**.–P. 141–146. (in Russian).

A COOLED PHOTOMULTIPLIER WITH AN InGaAs PHOTOCATHODE DEVELOPED FOR THE SPECTROPOLARIMETRY OBSERVATIONS

A. P. Vid'machenko, P. V. Nevodovsky

Main Astronomical Observatory, NAS of Ukraine
27 Akademika Zabolotnoho St., 03680 Kyiv, Ukraine
e-mail: nevod@mao.kiev.ua

The observations with a cooled InGaAs-photocatode photomultiplier were carried out in the Main Astronomical Observatory of the NAS of Ukraine. Astronomical objects were observed at the telescope AZT-2. We used an astronomical spectropolarimeter with the cooled photometric head and a photomultiplier tube with the InGaAs-photocathode working in the one-electron mode (Fig. 1).

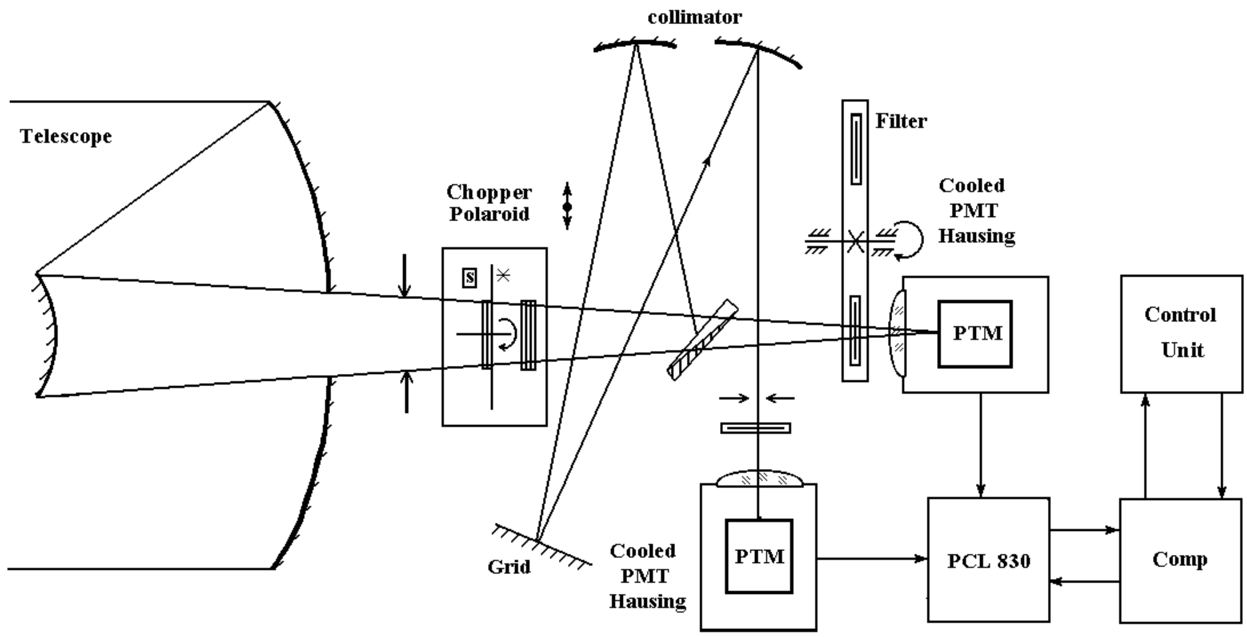

Figure 1: Structural scheme of our spectropolarimeter

The astronomical spectropolarimeter was developed and manufactured in the Main Astronomical Observatory. The device has two optical channels and can work in the modes of photometry, spectrometry, polarimetry or their combinations.

The spectral characteristics of photomultipliers with various photocathodes are presented in Fig. 2.

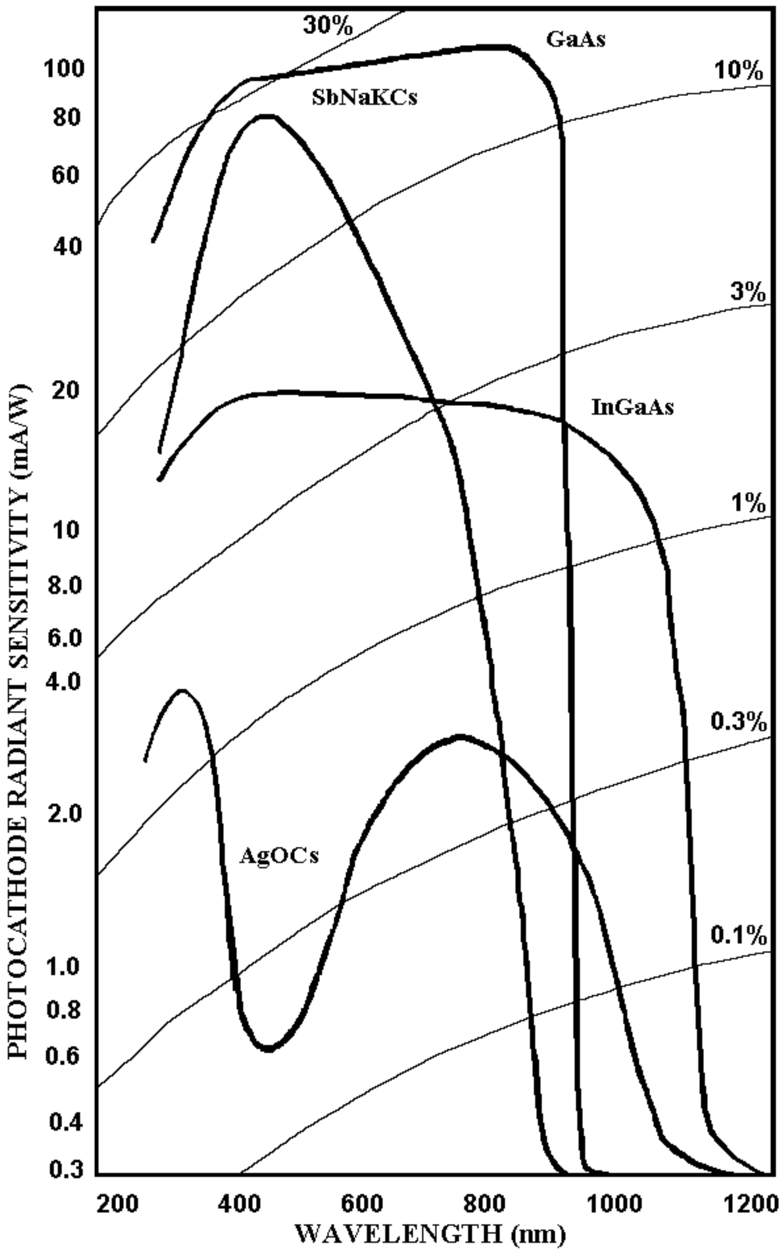

Figure 2: Reflection mode photocathodes

Advantages of a photomultiplier with the InGaAs-photocathode are:
1. Wide spectral range – 350–1060 nm.
2. Short anode pulse rise time – 3 ns.
3. A good quantum output in the near infrared (on $\lambda = 1060$ nm) – 0.2%.

Existing problem of photomultipliers with the InGaAs-photocathode are:
1. Large dark noise $\sim 100\times10^3$ pulses per second (at $T = 20^\circ$ C).
2. Small factor of amplification – 100×10^3.
3. Lateral optical input.
4. Monocrystal photocathode.

Features of work of our photomultiplier with the InGaAs-photocathode are:
1. Thermoelectric cooling of the photomultiplier for reduction of thermal noise.
2. One-electronic mode of operations of the photomultiplier.

OBSERVATIONS

1. Photometry
Object of photometric researches: β Ori, τ Ori and χ Ori.
Time of exposition: 20 s.
Photometry mode: "star" – "background".

2. Spectrometry
Object of spectral researches: Jupiter.
The spectrum of the whole disk of the planet (Fig. 3) repeats the variation of its reflectivity in visual range (the methane bands at 619 and 727 nm).
A possibility of research of celestial object with the astronomical spectropolarimeter in a range of wavelength 340–1070 nm is proved.

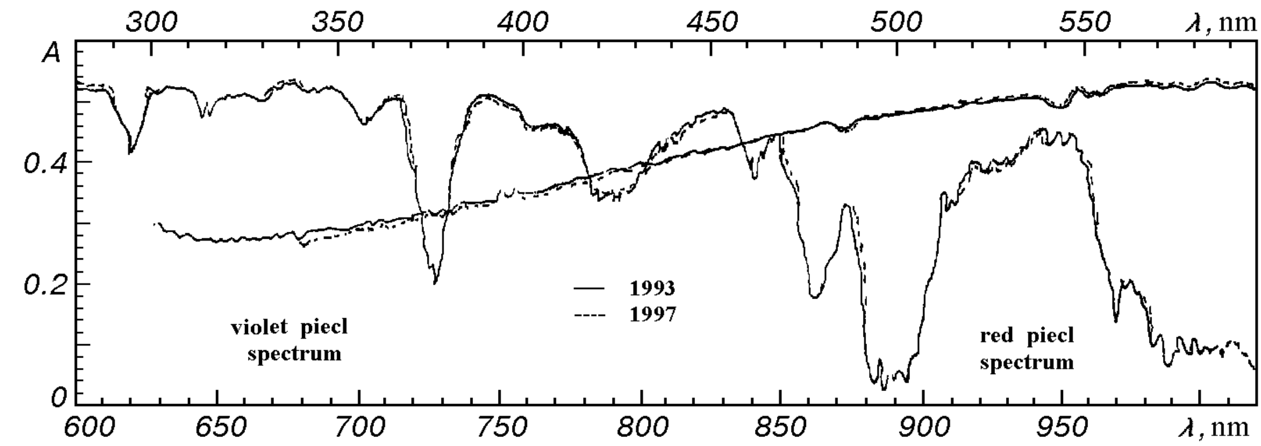

Figure 3: Spectrum of the whole disk of the Jupiter

3. Polarimetry
The spectropolarimetric measurement of Jupiter's disk was carried out.
Range of measurement: 340–1070 nm.
The Instrumental polarization of light for the system "telescope – polarimetry" is as follows:

$$Q = 0.012 + 0.016\%, \quad U = -0.031 + 0.016\%.$$

RADAR INVESTIGATIONS OF THE SOLAR SYSTEM OBJECTS AT EXTREMELY LOW FREQUENCIES

E. P. Abranin[1], A. A. Konovalenko[1], O. M. Ul'yanov[1], V. V. Zackarenko[1], Y. I. Belov[2], A. N. Karashtin[2], G. P. Komrakov[2], Y. V. Tokarev[2], P. Rodriguez[3], K. van't Klooster[4]

[1] *Institute of Radio Astronomy, NAS of Ukraine*
4 Chervonopraporna St., 61002 Kharkiv-2, Ukraine
e-mail: oulyanov@rian.ira.kharkov.ua

[2] *Scientific Research Institute of Radio Physic, Russia*

[3] *Naval Research Laboratory, USA*

[4] *ESTEC, Netherlands*

The first discussion on the use of a radar to study the Solar System has been introduced by F. J. Keer [14], and F. G. Bass and S. Ya. Braude [3]. The research of the Sun with a radar technique became to be of particularly king interest. The next step in this trend was made in Massachusetts Institute of Technology by El Campo array [1, 2, 4], [10]–[13]. The first results with reflected signal from the Sun were obtained on El Campo array

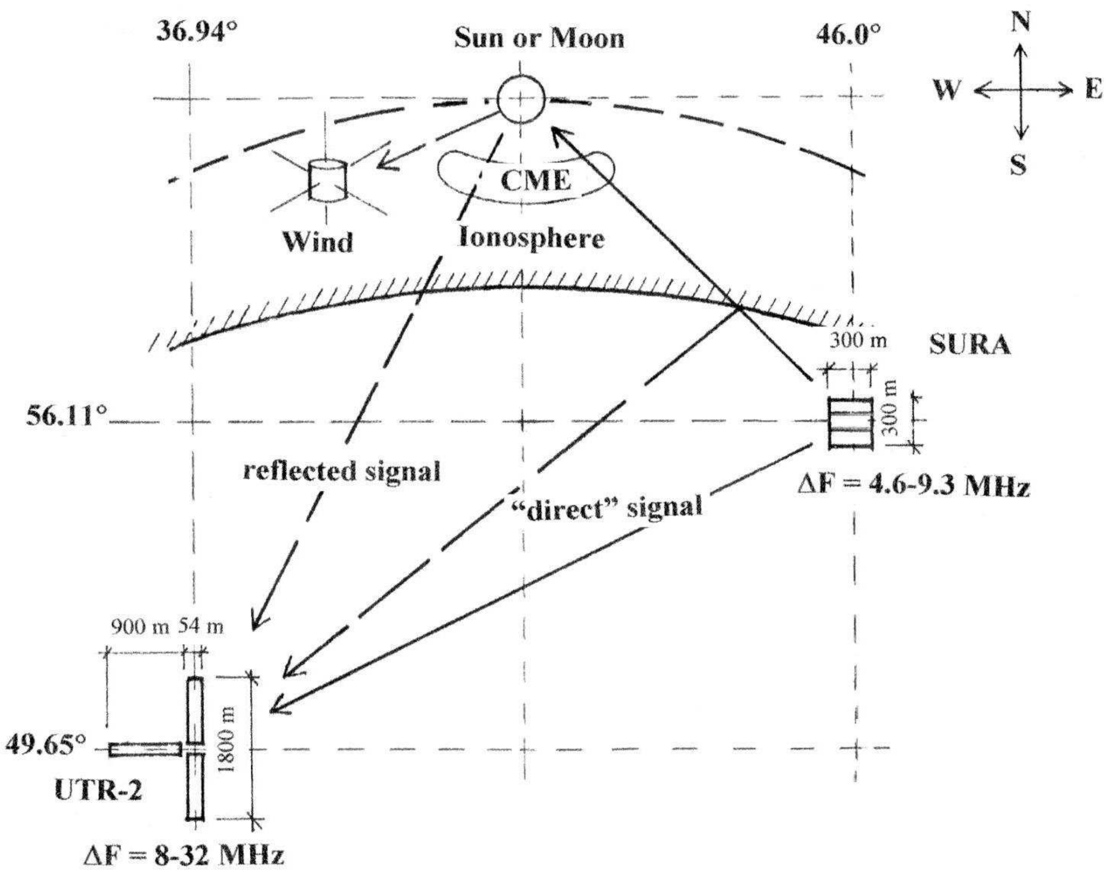

Figure 1: The general scheme of the using of the bistatic Radar SURA–UTR-2 in the radiolocation experiments

Table 1: El Campo – SURA – UTR-2 Radar System Comparison

N	Parameter	Dimension	**El Campo**	**SURA**	**UTR-2**
1	Transmitted power	P_{Tr}, [kW]	500	750	–
2	Transmitted antenna gain (Sun direction)	G_{Tr}, [dB] k	32 1585	18 63.1	–
3	Receiving antenna area (Sun direction)	A_R, [10^3m^2]	35.688	–	45.6 [1] 112 [2]
4	Transmitter frequency	F_T, [MHz]	38.25	8.913; 8.953	–
5	Ionospheric losses	L, [dB]	~ 2	~ 4	~ 4
6	The background temperature	T_B, [K°]	$\sim 2.5\times10^3$	–	$\sim 5\times10^5$
7	Temperature of the quite solar corona	T_S, [K°]	1×10^6	–	1×10^5
8	Antennas Temperature	T_A, [K°]	$\sim 1.55\times10^5$	–	$\sim 4.78\times10^5$ [2]
9	Scattering cross-section (typical value)	σ/π R_Θ^2, [m^2]	3.0	–	Unknown (estimation >3)
10	Doppler resolution	Δ F, [kHz]	10	–	<1
11	Total bandwidth	Δ BW, [kHz]	200	–	120
12	Radiometric gain	G_R	38	–	Unknown (same James)
13	Beam width (Sun direction)	NS°× EW°	0.592×6	22.8×6.3[3] 6.3×6.3[4]	1.15×31.69[2] 1.15×1.03[5]
14	Latitude	Lat, [deg]	29.189 N	56.116 N	49.654 N
15	Longitude	Long, [deg]	96.2 W	46.0 E	36.942 E
16	Signal to Noise ratio	S/N, [dB]	10	–	>-10 (estimation)

[1] – for East-West array;
[2] – for North-South array;
[3] – for one SURA section;
[4] – for three SURA sections;
[5] – for pencil beam lobe of the UTR-2;
$R_\Theta=7\times10^8$ [m] – the radius of solar photosphere.

in 1961. This program was prolonged up to 1969 and the sequence of the successful events were analyzed and interpret by I. M. Gordon and N. N. Gerasimova [5]–[8].

One of the reasons that stimulated our interest to follow research is the incoming satellites population in the Earth surrounding and the necessity to predict the Cosmic Weather, disturbances of nearest interplanetary plasma and Geomagnetic disturbances [9, 15]. In this paper we show only preliminary results on Sun and Moon radiolocation, which were obtained in the framework of the contracts N F61708–97–W0230 and N F61775–98–WE088 between the EOARD and Institute of Radio Astronomy of the NASU in 1996–1997.

The main task of this project is the preparation and realization of radar investigations of the Sun with the goal to detect the coronal mass ejections (CMEs). CMEs are ones of the most important and interesting phenomena in the solar physics and solar terrestrial relations. According to the preliminary estimations a high frequency radar can be one of the most effective means for detection of these phenomena. This technique is the most effective if it has to be applied for a bistatic configuration, for example, when the Russian SURA high frequency transmitter and the Ukrainian UTR-2 receiving antenna array (Fig. 1) are used.

The preliminary estimates of the radiolocation potential (see in Table 1) show a good possibility of registration of reflected signal from the Sun at 9 MHz. The comparison between El Campo and SURA–UTR-2 radars was made for the quite Sun conditions at the time on June 22. In our estimations we used the parameters similar to Jesse James parameters, but we didn't know the cross section and radiometric gain values. We supposed these values are to be similar to James parameters.

Our estimations show (see rows 16 in the table) that an expecting signal to noise ratio is more than –10 dB. But we know that our detection limit in similar radio astronomy observations (for example in pulsars observations) reaches the level of –15 dB. Unfortunately, we were not to be sured that the real Sun reflected signal was obtained. The best spectra where the presence of the reflected signal is the most probable were obtained on July 21, 1996. During the other séances of the Sun radiolocation a reliable registration of the reflected signal was absent.

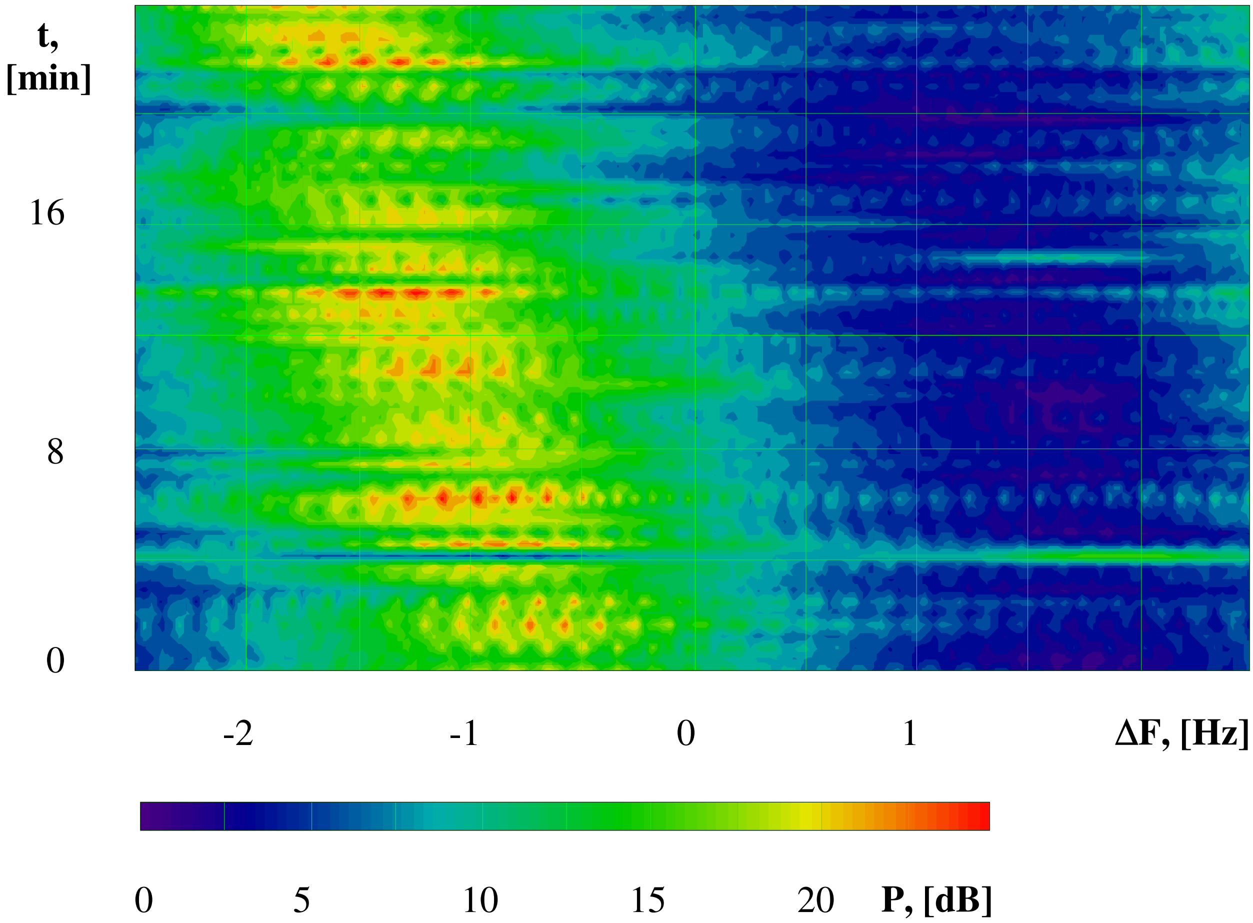

Figure 2: Dynamic Cross Correlation Function between the SURA "direct" and Moon reflected signals (The Moon radiolocation session from July 14, 1996).
Parameters of the SURA transmitter signal:
central frequency of the transmitter $F_C = 8.920$ MHz $\rightarrow$ $\Delta F = 0$;
total transmitter power $P_{S3} = 210$ kW (only third SURA section);
modulation by "ON-OFF" code with period $T = 5$ sec; "ON" duration $\Delta\tau = 1.2$ sec

The absence of the reflected signal in our data can be explained if we suppose that the cross section is to be significantly less than $3\pi R_{\Theta}^2$ (where R_{Θ} is the radius of the solar photosphere), or radiometric gain is to be considerably less than 38 dB, or the result losses are to be more than 8 dB at 9 MHz. The little scale plasma turbulence in the top of solar corona at 9 MHz may be considered as a physical evidence for the first hypothesis (cross section is significantly less than $3\pi R_{\Theta}^2$). From another side the radiometric gain decreases when the reflected signal looks like a noise signal and its scale of Doppler shifts is very broad. It means that the signal is reflected from solar plasma inhomogeneities, which have different light velocities. Our result can be explained more easy by ionosphere losses, refraction and scattering in interplanetary plasma. These questions require an additional examination because we have no possibility to compare our calibration data for the Moon (Fig. 2) and the same Jesse James data (if Jesse James used such a calibration).

During performance of the Sun radiolocation, the solar activity was daily to be patroled. These observations allowed to reveal a correlation between parameters of the reflected signal and different types of solar activity. Unfortunately, registration of the signal reflected from the Sun is impossible when the solar activity is highly strong at 9 MHz.

CONCLUSIONS

Special facilities and detection procedures were developed and introduced in regular operation at the SURA–UTR-2 radio telescopes for the Sun and the Moon radar experiments. These facilities allowed us to reduce interference effects and to reach the sensitivity maximum. Methods to check the ionospheric conditions with the Sun and Moon radar experiments simultaneously were developed. The signal reflected from the Moon was detected with a high reliability.

The Sun radar experiments require to follow its at the transmitter frequency up to 20–25 MHz. A new transmitter should be situated near the working radio telescopes. The CMEs detection at extremely low frequencies can be successful only in the periods of a low Sun activity. The probability of CMEs existence is higher in the period of a high Sun activity, but in this period there are another problems for the study at low frequency range due to increasing the critical frequencies in ionosphere. The very interesting phenomenon was detected on September 17, 1997, when the Sun burst type III with 1000 solar flux units density at 12 MHz has been cut off after 10 MHz. This phenomenon supports our point of view. So, the requirements for detection of CMEs and appearing CMEs are in contradiction to the results at the lowest frequencies.

The necessary attribute in the CMEs locations is the monitoring of solar activity. The main task of this monitoring is to put conditions when the ionosphere is transparent and the Earth-Sun information channel exists at low frequencies. The combinations of active and passive methods of CMEs detection will be very useful in future investigations.

We plan to compare results of ground-based solar patrols and satellite observations with the results of our analysis. Undoubtedly, the solar radar experiments must be continued to develop this technique.

Acknowledgements. The work is supported by contracts N F61708-97-W0230 and N F61775-98-WE088 and INTAS grants INTAS97-1964, INTAS_CNES97-1450.

REFERENCES

[1] *Abel W. G., Chisholm J. H., Fleck P. L., James J. C.* Radar Reflections From the Sun at VHF // J. Geophys. Res.–1961.–**66**.–P. 4303–4307.

[2] *Abel W. G., Chisholm J. H., Fleck P. L., James J. C.* A VHF solar radar system // I. R. E. International Convention Record.–1962.–Part 5.–P. 58–66.

[3] *Bass F. G., Braude S. Ya.* On the question of reflecting radar signals from the Sun // Ukr. J. Phys.–1957.–**2**.–P. 149.

[4] *Chisholm J. H., James J. C.* Radar evidence of solar wind and coronal mass motions // Astrophys. J.–1964.–**140**.–P. 377–379.

[5] *Gerasimova N. N.* Comparison of results of radar studies of the corona with solar activity // Sov. Astron.–1975.–**18**.–P. 482.

[6] *Gordon I. M.* Interpretation of radio echo from the Sun // Astrophys. Lett.–1968.–**2**.–P. 49.

[7] *Gordon I. M.* Radar exploration of the sun and physical processes of the solar corona // Astrophys. Lett.–1969.–**3**.–P. 181.

[8] *Gordon I. M.* Plasma theory of radio echoes from the Sun and its implications for the problem of the solar wind // Space Sci. Rev.–1973.–**15**.–P. 157.

[9] *Gurevich A. V., Karashtin A. N., Babichenko A. M., et al.* HF magnetosphere sounding at SURA // Proc. 21st Remote Sensing Society Ann. Conf., Southampton, UK, 1995.–P. 1333–1340.

[10] *James J. C.* Radar studies of the Sun at 38 Mc/s // Astrophys. J.–1966.–**146**.–P. 356–366.

[11] *James J. C.* Radar studies of the Sun // Radar Astronomy / Eds J. V. Evans, T. Hagfors.–New York, McGraw-Hill Book Company, 1968.

[12] *James J. C.* El Campo solar radar data and system design notes // Report edited by Massachusetts Institute of Technology, Center of Space Research (TR-70-2).–1970.–P. 1–83.

[13] *James J. C., Ingalls R. P.* Radar observations of Venus at 38 Mc/sec // Astron. J.–1964.–**69**.–P. 19–22.

[14] *Kerr F. J.* On the possibility of obtaining radar echoes from the sun and planets // Proc. IRE.–1952.–**40**.–P. 660.

[15] *Rodriguez P.* High frequency radar detection of coronal mass ejections // Proc. 16th NSO/Sacramento Peak International Workshop on Solar Drivers of Interplanetary and Terrestrial Disturbances, Sunspot, NM, October 16–20, 1995.

THE SUBSURFACE ULTRAWIDEBAND RADAR STUDY
OF A SURFACE LAYER OF THE SOLAR SYSTEM PLANETS

N. V. Bondarenko and Yu. V. Kornienko

Institute of Radiophysics and Electronics, NAS of Ukraine
12 Ak. Proskury, 61085 Kharkiv, Ukraine
e-mail: nbondarenko@bndr.kharkov.ua, urikor@ire.kharkov.ua

Radar experiments are widely used for remote sensing of planetary surfaces. However, the traditional (single wavelength) radar techniques are rather inefficient for study of subsurface structure. Under Earth conditions the use of ultra wideband (video pulse) radar turns out to be more productive for these purposes. Future applications of an ultra wideband radar located on a surface are examined in this paper for purposes of studying of a subsurface vertical structure to a depth of some hundreds meters.

INTRODUCTION

Radar experiments are widely used for remote sensing of planetary surfaces. However, the traditional (single wavelength) radar techniques are rather inefficient for study of subsurface structure. Under the Earth conditions for these purposes the use of ultra wideband (video pulse) radar (UWBR) turns out to be moreproductive. The methods used for the video signal detection are not optimal and make difficulties in the signal accumulation under the low signal-to-noise ratio.

In this paper the future applications of UWBR located on a surface are examined. We use here the lunar surface as an example. The new theory of the optimal video signal reception presented here allows obtaining more reliable estimations of distance to underground objects.

UWBR spans the wavelength range from 30 cm to of about 6 m. Emitted pulses are of about 30 cm long ($\sim$ 1 ns). Their repeating frequency is of about 1 MHz. In Fig. 1 the emitted pulses (a) and their representation in frequency domain (b) are shown. The Fourier spectrum of the single emitted pulse is presented in Fig. 1b as a dash line.

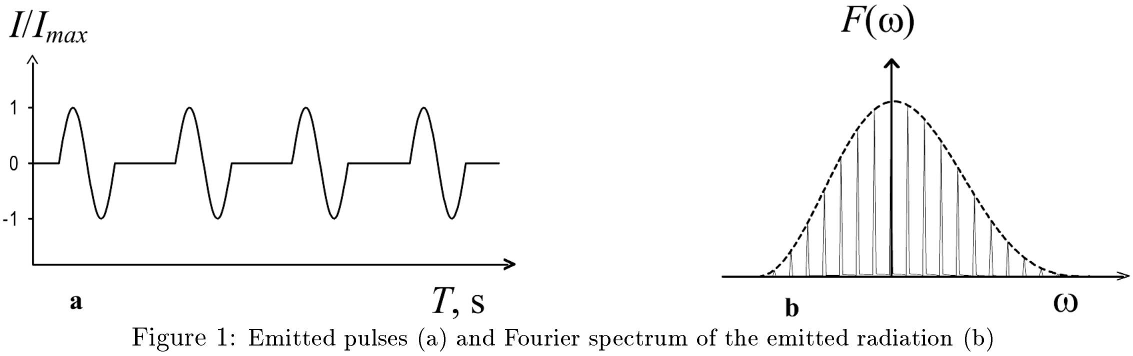

Figure 1: Emitted pulses (a) and Fourier spectrum of the emitted radiation (b)

THE THEORY OF OPTIMAL VIDEO SIGNAL RECEPTION

The upper layer of the lunar surface is a medium with dispersion and absorption. Hence, the shape of a received pulse differs from that of the emitted one. This leads to difficulties in the analysis of the received information. New theory of optimal video signal reception is free of this difficulty [1]. All calculations are carried out in the frequency domain. The theory uses the approach based on the theory of optimum statistical solutions and the classic theory of probability. Key assumptions used in the theory of the optimal video-pulse reception are those both the distance x to the object under study and detection noise ($|n\rangle$) are random. Detection noise is a stationary Gauss process with spectral density $I(\omega)$. Probability of a noise realization is: $p_N(|n\rangle) \approx e^{-\langle n|\hat{\beta}|n\rangle/2}$, where $\hat{\beta}$ is an operator which is diagonal in the frequency domain; its eigenvalues are $1/I(\omega)$. We used the $|u_0\rangle$ notation for the initial pulse and $|v\rangle$ for the received one. A reception pulse is described as $v(t) = u_1(t) + n(t)$, where $|u_1\rangle$ is the scattered pulse at the radar. $u_1(t) = e^{2i\hat{K}x}\hat{S}u_0(t) = \hat{G}(x)u_0(t)$, $\hat{K}$, $\hat{S}$ being operators, which are diagonal in the frequency domain; eigenvalues of the operators are $\varepsilon(\omega)^{0.5}\omega/c$, and $s(\omega)$, respectively. The $\hat{K}$ operator describes absorption in the medium and the $\hat{S}$ operator characterizes the scattering from the object under study. The most probable distance to the object can be found through the maximum of the logarithmic function of plausibility:

$$L(x) = 2\left\langle v\middle|\hat{\beta}\hat{G}\,(x)\middle|u_0\right\rangle - \left\langle u_0\middle|\hat{G}^+\,(x)\,\hat{\beta}\hat{G}\,(x)\middle|u_0\right\rangle. \tag{1}$$

The distance estimate obtained with this theory is not biased. The standard deviation of the estimate depends on the spectral density of both pulse and noise. It does not depend on the pulse shape and, therefore, on any pulse distortion in the medium.

APPLICATION OF UWBR FOR STUDY OF THE LUNAR SURFACE

Absorption in the lunar soil limits the penetration depth of a pulse. Absorption length l_e at the wavelengths of interest λ (30 cm – 6 m) is shown in Fig. 2 for (a) regolith (the density ρ is 1.0 g/cm^3), and for (b) rocks (ρ = 3.32 g/cm^3). These curves were obtained using the data for permittivity of lunar soils from [3] and the specific loss tangent data from [2]. At a 6 m wavelength the absorption length l_e is of about 160 m. Therefore, the objects located at a depth up to hundreds meters under the lunar surface can be found by UWBR. The upper limit for object detection is specified by the shortest wavelength. It is of about 30 cm.

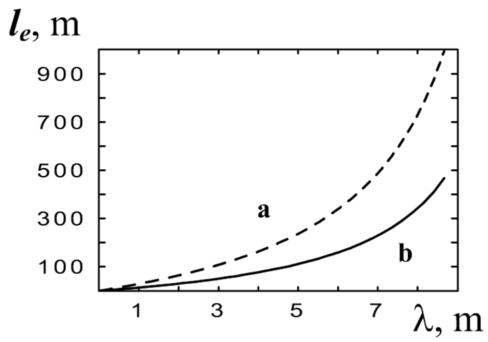

Figure 2: Absorption length for (a) regolith (ρ = 1.0 g/cm^3), and for (b) rocks (ρ = 3.32 g/cm^3)

According to the seismic data [3], the depth range from 30 cm to hundreds meters can be roughly divided into two layers: the upper, regolith layer, extended up to 10–20 m depth, and a layer of fractured bedrock ("megaregolith") extended up to 1 km depth [3]. The upper (regolith) layer has a stratified structure too. The deposits consist of rock fragments of different size [3]. The difference in average density leads to the difference of permittivity of some layers within the regolith. Such interfaces can be considered as objects for UWBR.

CONCLUSION

UWBR can feel interfaces up to hundreds meters deep under the lunar surface. It can provide with information about the regolith-megaregolith interface, some deposits inside the regolith layer, and the structure of the upper part of the megaregolith layer. With UWBR, some isolated objects (rocks) can be detected.

In addition, the UWBR has the following advantages.

- UWBR located on the surface needs much less power than remote radar equipment.
- The video pulse equipment is rather simple in comparison with a conventional radar providing a wide frequency range.
- Distance estimations obtained by the theory of the optimal video signal reception do not depend on the shape of the received signals.

REFERENCES

[1] *Kornienko Yu. V.* Optimal filtering of reflected signal in the medium with dispersion and attenuation // Radioph. i Elektr.–1999.–**4**, N 2.–P. 74–77. (in Russian).

[2] *Gary B. L., Keihm S. J.* Interpretation of ground-based microwave measurements of the Moon using a detailed regolith properties model // LPSC IX.–1978.–P. 2885–2900.

[3] *Heiken G., et al.* Lunar sourcebook.–1991.–P. 61–120, 285–356, 475–594.

THE OPTICAL PARAMETERS OF THE 2-m TELESCOPE AND SEEING AT THE PEAK TERSKOL OBSERVATORY

G. Z. Butenko[1], V. I. Kuznetsov[1], L. I. Snezhko[3], V. M. Andruk[2], V. G. Parusimov[2], A. V. Sergeev[1], and Yu. S. Ivanov[2]

[1] *International Center for Astronomical and Medico-Ecological Research*
27 Akademika Zabolotnoho St., 03680 Kyiv, Ukraine
e-mail: butenko@mao.kiev.ua

[2] *Main Astronomical Observatory, NAS of Ukraine*
27 Akademika Zabolotnoho St., 03680 Kyiv, Ukraine
e-mail: andruk@mao.kiev.ua

[3] *Special Astrophysical Observatory of Russian Academy of Sciences*
Karachayevo-Cherkesk Republic, Zelenchuk region, 357147 Nizhnii Arkhyz, Russia
e-mail: snezhko@sao.ru

We present the Hartmann images to attestate the Cassegrain focus optics of the 2-m telescope of the Peak Terskol Observatory of the International Center for Astronomical and Medico-Ecological Research of the NASU/RAS. The Cassegrain focus optics is a classical Ritchey-Chretien system with compensated coma and spherical aberration. The astigmatism corrector compensates for the system field astigmatism. Star images formed by the system with the astigmatism corrector are characterized by $d_{0.8} = 1''\!.3$, which does not meet the present-day requirements. The constant coma followed by the spherical aberration are dominating. The astigmatism is the least distortion of the image. Eliminating the Zeidel aberrations gives $d_{0.8} = 0''\!.7$, which coincides with manufacturer attestation. An additional adjustment should be made to achieve this image quality. Local wavefront errors including triangular astigmatism are small, which testifies that the unloading and fastening of the mirrors are of a high quality.

1. PROBLEMS AND INVESTIGATION PROCEDURE

Investigation of the optics of the 2-m mirror telescope constructed by “Carl Zeiss Jena” (FRG) and installed on the Peak Terskol was performed in accordance with the plan of joint ventures between the Special Astrophysical Observatory (SAO) of the Russian Academy of Sciences and the International Center for Astronomical and Medico-Ecological Research (IC AMER) of the NAS of Ukraine. The problem of a complete testing of the 2-m telescope optics in the Cassegrain focus is divided into the following parts:

– agreement between the actual optical system and the calculated one;
– position of the best image plane and the image quality in this plane throughout the whole field;
– the quality of adjustment of the optical system and possibilities of its further improvement;
– the estimate of the quality of unloading and fastening of the mirrors.

Hartmann’s method [11]–[13] was chosen as a quantitative technique for optical investigation of the 2-m telescope.

The investigation and the attestation of the optics of the IC AMER 2-m telescope were performed by the procedure [2]–[10] developed beforehand and based on the simultaneous reduction of two extrafocal photographic films (the Hartmann images) obtained before and after the focus. This procedure has many advantages such as a lower requirement on the accuracy of coordinates of apertures of the Hartmann diaphragm, a lower effect of experimental systematic errors on the results of investigations together with the possibility for estimating the accuracy of the data obtained and the reliability of the wave front topography obtained.

2. OBSERVATIONAL DATA AND THE SOFTWARE

The observational data were obtained during three nights in 1998: June 19/20, June 29/30, June 30/July 01; and six nights in 1999: July 16/17, July 17/18, July 18/19, July 19/20, July 21/22, July 22/23. The established Hartmann diaphragm (156 nonvignetted apertures in rectangular grid nodes) and a special mounting for obtaining the Hartmann images with the “Zenit” photocamera instead of the established free-shot cassette were used for the test observations.

251 Hartmann images were obtained. The preliminary and final reductions of the Hartmann images were made using the two-coordinate measuring "Askorecord" machine and the automatic digital ADMP-XY microphotometer [1], respectively.

FORTRAN-, PASCAL- and MIDAS-programs were prepared for reduction of digital images.

Figure 1 gives an example of image reduction by program package MIDAS/ROMAFOT.

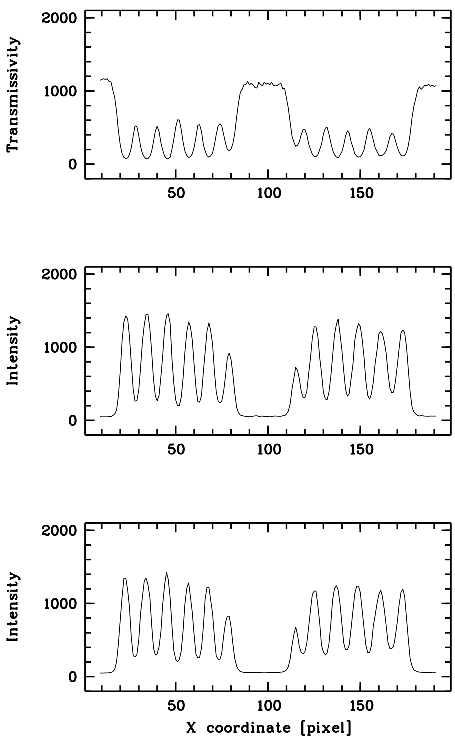

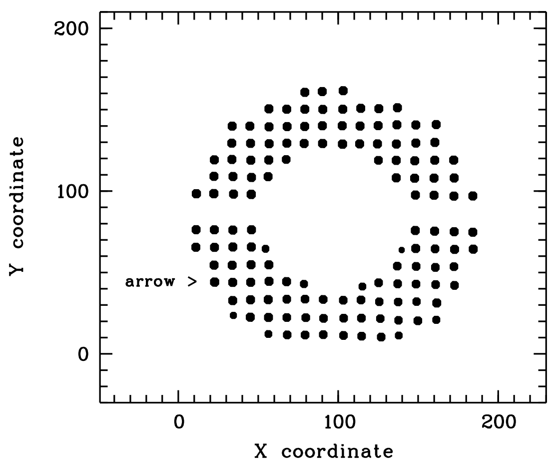

Figure 1: On the left: the section of one of serieses of the Hartmann diaphragm image on the photographic film after photometric measuring with the use of ADMF-XY (the upper row), after artificial spreading dynamical region of instrumental parameters (the mean row), as well as after filtering and smoothing (the lower row).
On the right: the restored Hartmann diaphragm after reduction with the use of MIDAS/ROMAFOT

3. THE SYSTEM WITHOUT THE ASTIGMATISM CORRECTOR

The optical system of the Cassegrain focus for the 2-m telescope is a simple two-mirror system in this case.

Figures 2, 4, 6 show the variations of the Zeidel aberrations throughout the system field for the secondary mirror position located by the focussing device reading equal to 37.45 mm.

The field astigmatism is characterized by the amplitude linear increase and by the position angle change with the point position varying in the field dominates in the wave front.

Figure 8 illustrates the variations of the Zeidel aberrations in the system without the astigmatism corrector in the field center for varying distance between the system mirrors. Figure 6 shows the constant coma A_{31} to dominate and the astigmatism A_{22} to be in the field center in the wave front (Figure 4). The variable spherical aberration A_{41} changing its sign at the focussing device reading equal to 33–34 mm is clearly seen. The coma amplitude is also minimized in this area (Figure 8).

So, Figures 2, 4, 6 show the aberration of a two-mirror system with the Cassegrain focus as a classical Ritchey-Chretien system with noncompensated astigmatism.

Initial distribution of energy throughout the image formed by the system without the corrector is characterized by $d_{0.8} = (1.34 \pm 0.05)''$. The image can be significantly improved by eliminating the constant coma, so that $d_{0.8} = (0.84 \pm 0.02)''$. The image is scarcely affected by astigmatism. All of the Zeidel aberrations being eliminated, the image size is $d_{0.8} = (0.79 \pm 0.02)''$. Therefore, having eliminated the Zeidel aberrations, we can obtain substantially the manufacturer value of the image quality.

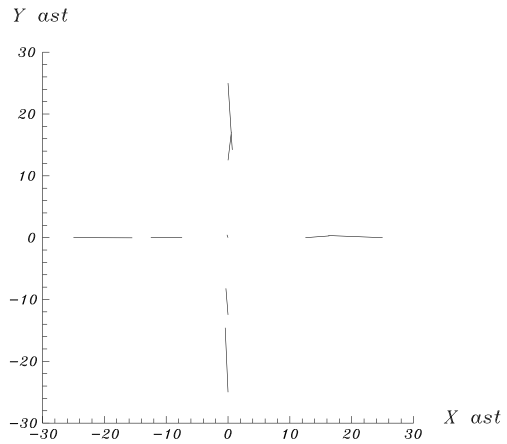

Figure 2: Astigmatism variations throughout the field in the system without the astigmatism corrector

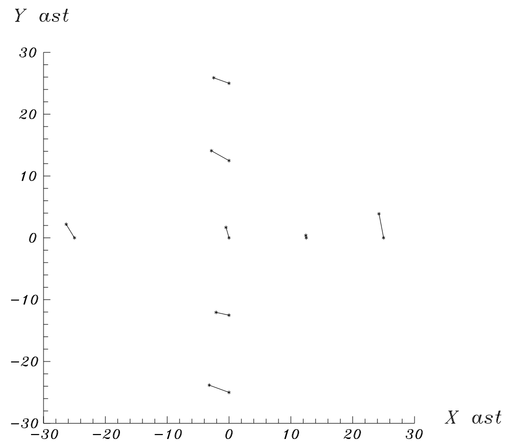

Figure 3: Astigmatism variations throughout the field in the system with the astigmatism corrector

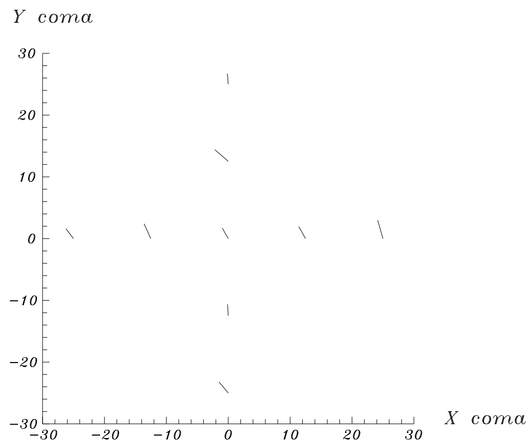

Figure 4: Coma variations throughout the field in the system without the astigmatism corrector

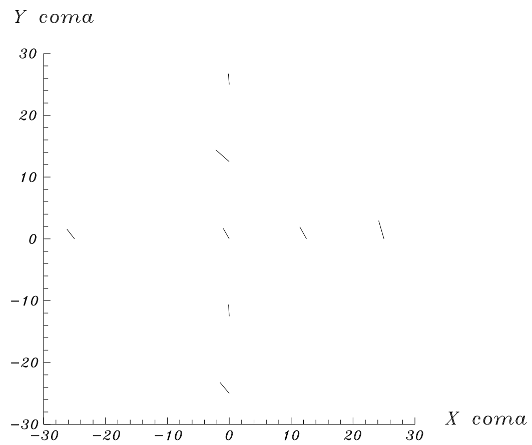

Figure 5: Coma variations throughout the field in the system with the astigmatism corrector

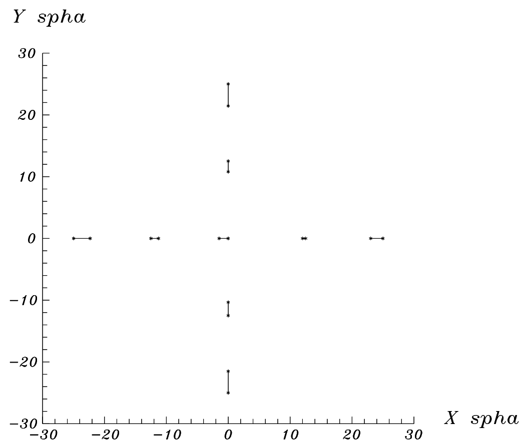

Figure 6: Spherical aberration variations throughout the field in the system without the astigmatism corrector

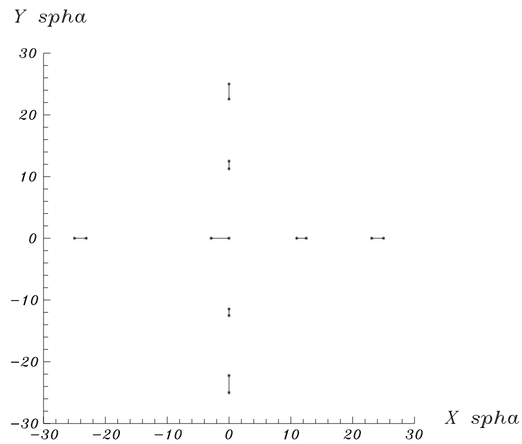

Figure 7: Spherical aberration variations throughout the field in the system with the astigmatism corrector

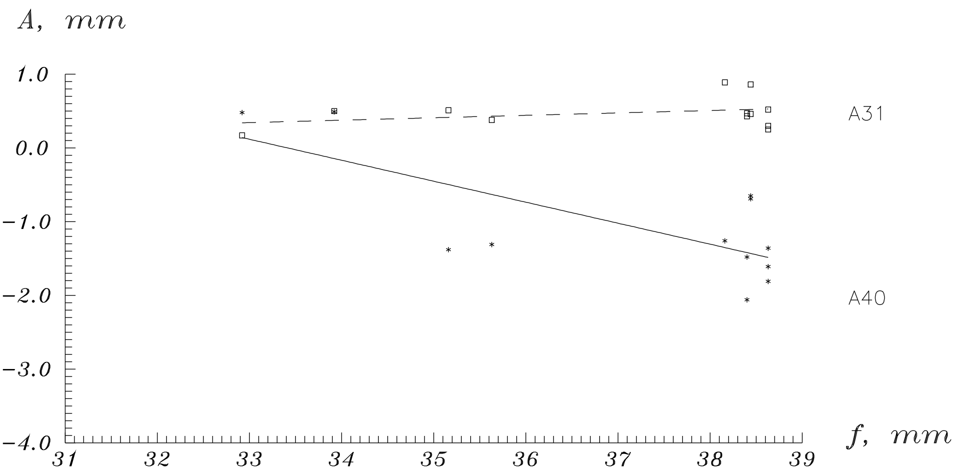

Figure 8: Dependence of amplitude of coma and spherical aberration on the focus position

In general, the investigation of the optical system without the astigmatism corrector by Hartmann's method proved the following:

– the system of the Cassegrain focus of the 2-m telescope is a Ritchey-Chretien system in which coma and spherical aberration are compensated and field astigmatism is present;

– the initial concentration of energy in the image on the axis is $d_{0.8} = 1\farcs3$, which does not meet the present-day requirements;

– we can reach the value $d_{0.8} = 0\farcs8$ by eliminating the Zeidel aberrations, primarily the constant coma and the spherical aberrations, which is in good agreement with the manufacturer attestation results.

4. THE SYSTEM WITH THE ASTIGMATISM CORRECTOR

Theoretically, the astigmatism corrector is a powerless element, that is why it is connected in the efficient paraboloid circuit when Hartmann's method is used.

Figures 3, 5, 7 show the variations of the Zeidel aberrations in the system field with the astigmatism corrector for the focusing device reading equal to 37.27 mm.

The following inferences can be made from the analysis of Figures 3, 5, 7:

– the field astigmatism is not revealed in the system with the astigmatism corrector, *i.e.*, the astigmatism corrector performs its functions;

– the amplitudes of the Zeidel aberrations in the system field with the astigmatism corrector do not exceed that for the field center;

– the constant coma A_{31} is the dominating aberration and astigmatism is minimal;

In all, the following conclusions can be made from the attestation of the system with the astigmatism corrector:

– the astigmatism corrector compensates for the field astigmatism completely;

– all of the Zeidel aberrations are present in the field center of the wave front; the wave aberrations in extraaxis points of the field do not exceed their values for the field center;

– the image produced by the optics is characterized by the low energy concentration, $d_{0.8} = 1\farcs3$. But the image can be drastically refined by eliminating the Zeidel aberrations, basically coma and spherical aberration, $d_{0.8} = 0\farcs7 - 0\farcs8$, which is in good agreement with the manufacturer attestation results.

5. ADJUSTMENT PROBLEMS

The constant coma is the principal cause of image degradation. It can be eliminated by the corresponding displacement/inclination of the system secondary mirror.

Figures 2–8 visualize the variations of the amplitudes of the coma and the spherical aberration for the axis motion of the mirror together with the field astigmatism in the system without and with the astigmatism corrector. The field astigmatism symmetry indicates that the system is centred quite well. The amplitudes of the variations A_{40} and A_{31} show that the spherical aberration and the coma caused by the astigmatism corrector can be compensated.

The results of our study testify that the additional adjustment of the Cassegrain focus system optics is necessary.

6. SEEING PROBLEMS

The photographic films with exposures less than 0.5 sec were obtained in the course of the Hartmann imaging and were reduced by the automated measurement procedure.

The trains of vibrations of aperture images are seen to be unaveraged in the Hartmann images of 0.5 sec exposures. They affect also the value of the Zeidel aberrations, especially astigmatism. In the course of the analysis of vibration of the aperture images the image quality was visually estimated by $5''$ and improved to $3''$ towards the end of the series of observations. This is caused by decrease in the difference in temperature between the observing hut space and environment. That is why before observational process the observing hut has to be ventilated for the time interval sufficient for the difference in these temperature values to get minimal.

7. CONCLUSION

We consider the attestation of the Cassegrain focus optics to be accomplished. The Cassegrain focus system is shown to be a classical Ritchey-Chretien system. The image quality estimate equal to $0\overset{''}{.}7$ throughout the field can be reached by additional adjustment, which is in good agreement with the manufacturer attestation results.

REFERENCES

[1] *Parusimov V. G.* The Automatical Digital Two-Coordinate Microphotometer for Introducing Photographic Images into an Computer // Astrometry and Astrophys.–1981.–**45**.–P. 86–99. (in Russian).

[2] *Salukvadze G. N., Snezhko L. I.* The investigation of the optics of AZT-11 // Bull. Abast. Astroph. Obs.–1980.–**53**.–P. 191–228. (in Russian).

[3] *Snezhko L. I.* The Investigation of the Optics of large Telescopes // Candidate Dissertation, Zelenchuk.–1980. (in Russian).

[4] *Snezhko L. I.* The application of Hartmann's method to the investigation of the main mirror of the LAT // Astron. Zh.–1980.–**57**.–P. 869–877. (in Russian).

[5] *Snezhko L. I.* The estimates of the reliability of results of investigation of astronomical optics by Hartmann's method // Astron. Zh.–1979.–**56**.–P. 1094–1099. (in Russian).

[6] *Snezhko L. I.* On the accuracy of Hartmann's method in studies of aspherical wave fronts // Optics and Mechanic Industry.–1980.–N 9.–P. 1–3. (in Russian).

[7] *Snezhko L. I.* The application of the Hartmann diaphragm to investigation of star image forming // Astron. Circ.–1978.–N 1002.–P. 6, 7. (in Russian).

[8] *Snezhko L. I.* The attestation results of the second main mirror of the LAT by Hartmann's method // Pis'ma v Astron. Zh.–1980.–**6**.–N 10.–P. 667–670. (in Russian).

[9] *Snezhko L. I.* The determination of the effective focal distance in the Ritchey-Chretien systems by Hartmann's method // Astron. Circ.–1980.–N 1117.–P. 2–4. (in Russian).

[10] *Snezhko L. I.* The analysis of Hartmann's method foundations // Astrophys. Investigations. Proc. SAO.–1981.–**14**.–P. 3–14. (in Russian).

[11] *Hartmann J.* Bemerkungenüber den Bau und die Justierung von Spectrographen // Zts. f. Instrkunde.–1900.–**20**, N 2.–P. 51.

[12] *Hartmann J.* Objektivuntersuchungen // Zts. f. Instrkunde.–1904.–**24**, N 1.–P. 1, 33, 97.

[13] *Lehmann H.* Anwendung der Hartmannsehen Methode der Zoneprüfung auf astronomishe Objektive // Zts. f. Instrkunde.–1902.–**22**, N 4.–P. 103, 325.

THE INTERFEROMETRIC METHOD FOR IMAGE FORMATION, AND CONSTRUCTION OF THE APERTURES FOR THE INTERFEROMETRIC TELESCOPE BY THE RANDOM SEARCH METHOD

Yu. V. Kornienko

Institute of Radiophysics and Electronics, NAS of Ukraine
12 Ak. Proskury, 61085 Kharkiv, Ukraine
e-mail: urikor@ire.kharkov.ua

In the context of the interferometric method for image formation, the problem of an optimal synthesis of input and output aperture is considered. Results obtained with the random search method are presented.

The problem of enhancing the resolution of astronomic images still remains an actual problem of observational astronomy. As it is known, the fundamental resolution limit of an astronomical instrument is determined by the diffraction of the light wave at the input aperture. However, this limit can hardly be achieved in ground-based observations due to phase distortion of the wave front in its propagation through the Earth atmosphere caused by random inhomogeneities of the refraction index. Some time ago, the digital processing of distorted images was expected to solve the problem of removing the effects of the atmosphere. But little by little, it became clear that the losses of information caused by atmospheric distortions are nonrecoverable in traditional observations, therefore, the efforts should be paid to suppress atmospheric distortions directly in the process of forming the astronomical images.

A number of ideas was suggested how to form the astronomical image so that the effects of phase distortions during the observation would be reduced or eliminated. Among them, the interferometric method of forming

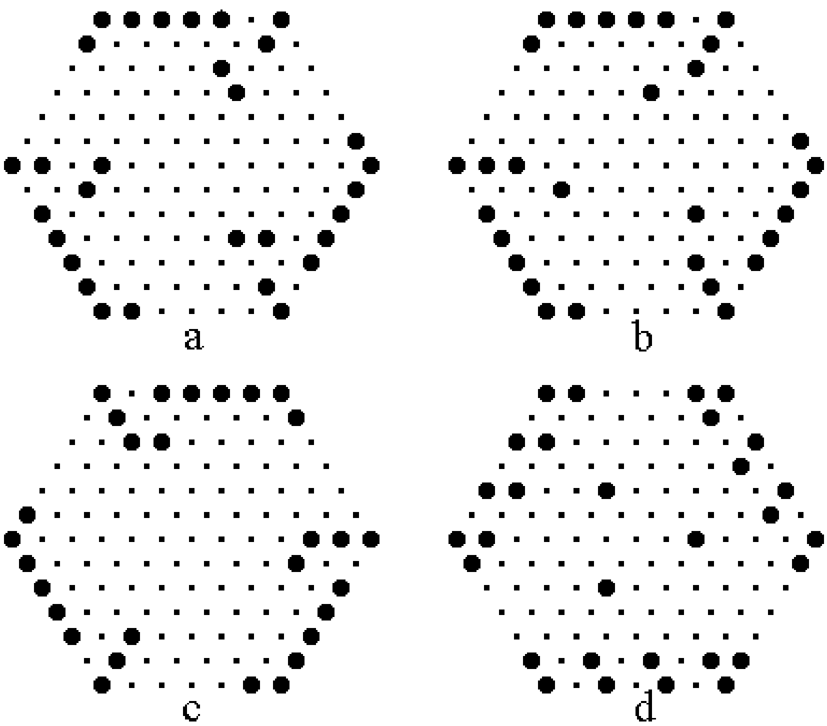

Figure 1: Examples of the configurations of the input aperture (radius – 6, elements – 30)

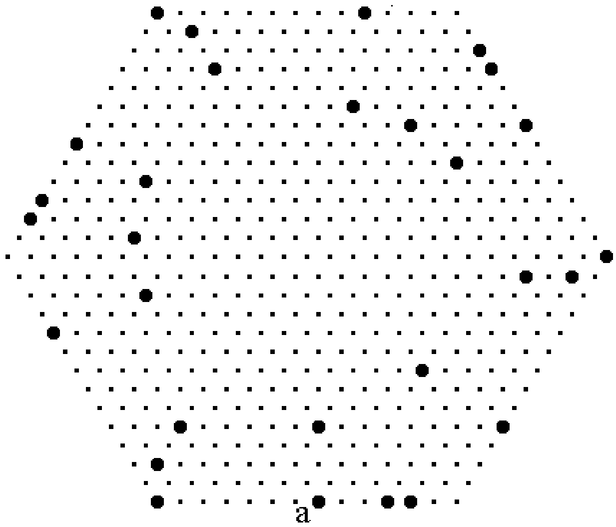

a

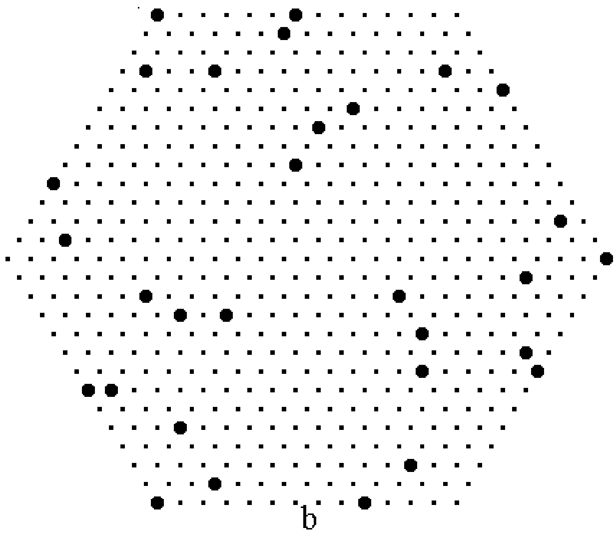

b

Figure 2: Examples of the selected configurations of the nonredundant apertures (radius – 13, elements – 30)

images [1, 2] is perhaps the most drastic one. It is based on the fact that, according to the van Zittert-Zernicke theorem, the relation between the brightness distribution over the observed object and the coherence function of the wave field which comes from the object is described by the Fourier transform. The coherence function depends on a couple of points in the aperture plane. However, this dependence is of a special character: the coherence function depends not on the radius-vectors of the individual points but only on the difference between them. Hence, while measuring the coherence function for different couples of points with the similar value of the connecting vector, one should obtain the same results differing only due to measurement errors and phase distortion in the propagation medium. It means that the information on the object brightness distribution is encoded by the field of the incoming incoherent wave with some redundancy, which results in a certain noise-immunity of coding and enables one to restore the information distorted by the atmospheric effects. In the radio astronomy, the idea of eliminating phase distortions according to the van Zittert-Zernicke theorem was suggested in [3]. Still for a long time it remained unclear how to apply it to the optical wave range.

This problem was solved when the authors of [1, 2, and 4], and later in [5], suggested an optical scheme of an interferometer (interferometric telescope) that permits the parallel measurements of the coherence function values for all the points of frequency plane accessible by the given aperture with a redundancy sufficient for eliminating unknown phase distortions. Although this method was found to overcome the terrestrial atmosphere effects, it also remains valid in designing orbital telescopes since the phase distortions inevitably occur in space due to construction deformation in the attempts to built as large optical system as possible.

When designing an interferometer, a proper configuration of the input and output apertures has to be selected. There is freedom of choice in this point. Nevertheless, various aperture configurations are not quite equivalent neither from informational nor from technical and constructive points of view. Hence, we have to select the optimal configuration both for the input and output apertures. The most complex problem is the optimization of the output aperture which is to be nonredundant and, for the given number of elements, be of the minimal achievable size. Thus, in this case, we deal with the problem of designing of a nonredundant aperture with the maximal possible number of elements in the given regular domain of a rectangular or hexagonal lattice.

The question about the limiting possibilities to construct nonredundant apertures with the maximal number of subapertures in the given domain of a rectangular or hexagonal lattice is not solved yet. There exist efficient regular methods of designing such apertures [6, 7], however, it is not clear to what extent they are approaching the ultimate possibilities. The upper estimates were obtained for the maximal possible number of the elements $Q(n)$ in a rectangular nonredundant aperture with a side n for some values of n (*e.g.*, [8]), still no detailed data on the behavior of this function were reported. There is even less information on the function $H(r)$ that determines the maximal possible number of elements in a nonredundant hexagonal mask of a radius r.

For small values of n (up to 5 or 6) and r (up to 2 or 3), this problem can be solved by a direct trying of all full nonredundant masks and choosing the maximal ones. It requires a certain amount of calculations that is large enough but still available with the up-to-date computational technique. The scope of calculation grows rapidly with the increasing of the aperture size, which restricts this possibility for large values of n or r not only presently, but also in future.

In this view, a compromise can be found in a random search for the full nonredundant masks and choosing those ones which contain the maximal number of elements k. This way never ensures finding of masks with the maximal k, while it does not exclude such a possibility. The latter can be sometimes inherent in some regular methods of constructing the masks. The results of the random search enable one to judge indirectly about the number of maximal nonredundant masks for the given n or r when studying the probability of re-obtaining the same masks.

The aim of the present paper was to clear up what the maximal achievable number of elements for squares with a side n not exceeding 20 and for hexagons with a radius r up to 15. The excess of the obtained values of k over n or $2r+1$ is shown in Fig. 1, and the examples of the selected configurations of the nonredundant apertures are illustrated by Fig. 2.

As it was expected, a ratio of the number of masks with the maximal found k to the full number of the selected nonredundant masks for the given n or r decreases dramatically with the growing n or r, and, as a result, a search of maximal masks for $n > 30$ or $r > 15$ becomes rather complicated. At the same time, for most of values for n and r presented in Fig. 1, the determined values of k can be assumed to be the maximal possible ones, *i.e.*, they coincide with the corresponding values of the $Q(n)$ and $H(r)$ functions.

REFERENCES

[1] *Kornienko Yu. V., Uvarov V. N.* Signal accumulation at observation of an astronomical object through the turbulent atmosphere // Comptes Rendus of Academy of Science of Ucraine.–1987.–Ser. **A**, N 4.–P. 60–63. (in Russian).

[2] *Roddier F.* Redundant versus nunredundunt beam recombination in an aperture synthesis with coherent arrays // J. Opt. Soc. A.–1987.–**A4**, N 8.–P. 1396–1401.

[3] *Jenison R. C.* A phase sensitive interferometer technique for the Fourier transform spatial brightness distributions of small angular extent // Mon. Notic. Roy. Astron. Soc.–1958.–N 118.–P. 278–384.

[4] *Kornienko Yu. V.* Interferometric approach to the problem of turbulent atmosphere effects in astronomical observations // Kinematics and Physics of Celestial Bodies.–1994.–**10**, N 2.–P. 98–106. (in Russian).

[5] *Kornienko Yu. V., Leyferov V. A., Pugach V. V.* Informational efficiency of a multibeam interferometer in the observation of an object throughthe inhomogeneous medium // Radiofisika i Electronika.–1987.–**2**, N 1.–P. 132–136. (in Russian).

[6] *Kopilovich L. E.* Multi-beam optical interferometer: the output aperture optimization // Kinematics and Physics of Celestial Bodies.–1998.–**14**, N 2.–P. 138–142.

[7] *Kopilovich L. E.* Non-redundant apertures for optical interferometric systems: maximization of the number of elements // J. Modern Optics.–1998.–**45**, N 11.–P. 2417–2424.

[8] *Kornienko Yu. V.* Construction of Nonredundant Apertures for an Interferometric Radiotelescope by the Method of Random Search // Physics and Engineering of MSMW: 3rd Intern. Kharkiv Symp., Kharkiv, Ukraine, Sept. 15–17, 1998.–P. 578–580.

HARDWARE SELECTIVITY OF A RADAR–TRACKING RECORDER OF ORBITS OF INDIVIDUAL RADIOMETEORS

A. A. Kuhtin

Kharkiv State Technical University of Radioelectronics, Kharkiv, Ukraine
e-mail: `ort@kture.kharkov.ua`

A method is offered which reduces the selectivity of a radar-tracking recorder of orbits of individual radiometeors by comparison of the distributions of elements of orbits meteoroids received by it with the modeled distributions constructed by the results of measurement of number of radiometeors, *i.e.*, by the primary experimental material, least deformed by the hardware selectivity.

INTRODUCTION

The proposed method is based on the data obtained with the automated radar-tracking system (MARS) [1], designed for registration of reflections from meteoric traces and definition of orbits of meteoric bodies. The given method is acceptable for similar radar-tracking systems used for observation of radiometeors as well.

As well as all other methods of registration of meteor phenomena in the Earth atmosphere the radar-tracking method has an essential selectivity being sensitive to parameters of the registered phenomena and, particularly, to characteristics of meteoroids. The account of the notice factors actually determines a inverse problem of radiometeoric astronomy. Along with complication of the equipment and methods of processing the reflected signals this influence of hardware selectivity sharply grows to estimate it theoretically is practically impossible. One of probable ways to take into account the effect of hardware selectivity is described below.

FINDING OF WEIGHT FUNCTIONS

This research of the hardware selectivity of a multistation radar-tracking system of definition of orbits was made by a comparison of the distributions of orbits, received by it with the modelling distributions constructed by results of measurement of number of radiometeors. For this purpose a method of imitation modeling is proposed to recalculate the number of radiometeors in distributions of elements of their orbits using the beforehand known law of distribution radiants of orbits of radiometeors on the sky. This law was obtained by the analysis of more than 200 thousand meteoric bodies registered at the MARS station. The comparison of the modeled distributions with distributions obtained by registration of individual orbits, allows to calculate one-dimensional weight functions (Figure 1d), which is useful to reduce the raw data for the hardware selectivity – to pass from "seen" distributions to "true".

An important feature of such an approach is that here all the factors of selectivity are not divided, as it is usually done, into physical, geometrical, astronomical bases and hardware. It is important because, for example, the physical and astronomical factors are hardly independent, because the estimations of both first and second order depend on the meteoroid velocity. The same is true to other factors. In the offered method the selectivity of the radar-tracking recorder of orbits is taken into account by an estimation of the uniform factor, which includes all noticeable factors but not as independent but all their connections.

In Figure 1 the following distributions are displayed. Figure 1a and Figure 1b contain the information about really registered on station MARS and modelling distributions of the semi-major axis – eccentricity (a, e). On these distributions only one meteor (either registered, or generated) corresponds to each point. The number of meteors in the modelled distribution is 600 thousand, in the really registered distribution it is about 2.5 thousand. In Figure 1c one can see the distributions of number of meteors on semi-major axis of orbits. The dot-dashed line shows the distribution registered on MARS, the continuous line – the modelled distribution. Figure 1d, as it was already marked, gives the one-dimensional weight function received for semi-major axises a. This function can be used for the traditional transition from an observed distribution of elements of orbits to true one.

The weight functions are made in the following way. We have the observed distribution of orbits of meteoric bodies over the celestial sphere received by counting of them. On the other hand, having the heliocentric velocities from the analysis of the station MARS data meteoroids, one can made a modelled distribution of the orbits of meteoroids, if after simulation an orbit of a meteor fits to the condition of crossing the orbit of the Earth [2].

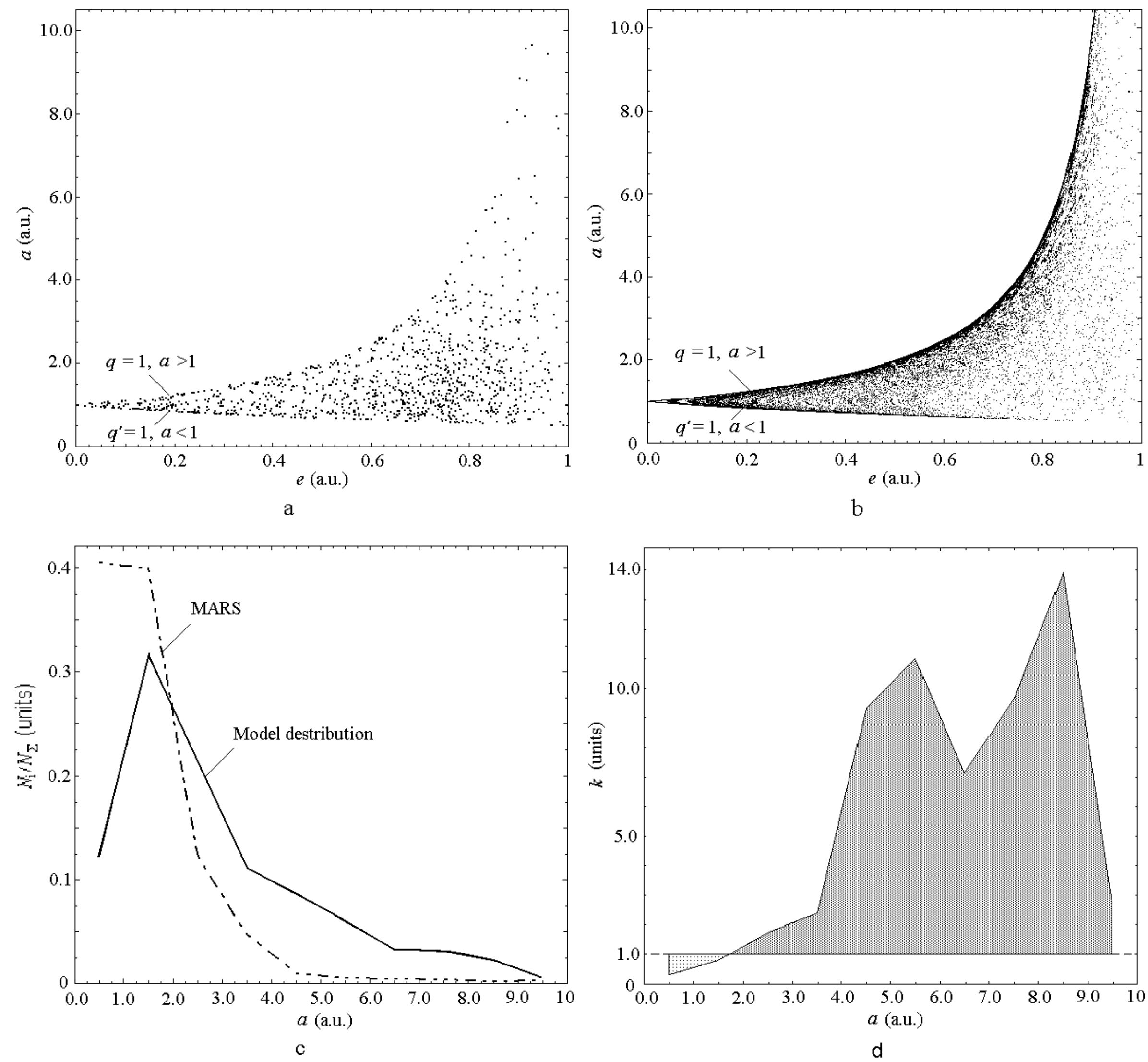

Figure 1: Different distributions

$$0.983 < R = \frac{q\,(1+e)}{1 \pm e\cos\omega} \leq 1.017, \tag{1}$$

where R is the radius-vector of the orbit of the Earth, q – perihelion distance, e – eccentricity, ω – argument of perihelion, then the elements of the orbit of this meteor were included in the database.

There were also distributions in the different axes: eccentricity – perihelion distance (e, q); inclination – perihelion distance (i, q); inclination – semi-major axis (i, a), inclination – eccentricity (i, e). The weight functions to correct eccentricity, perihelion distance, an inclination distribution were obtained as well.

REFERENCES

[1] Results of researches under the international geophysical projects // Meteoric researches.–N 4.–Moscow: Owls. Radio, 1977.

[2] Results of researches under the international geophysical projects // Meteoric phenomena in an atmosphere of the Earth.–Moscow: Nauka, 1967.

INFORMATIONAL EFFICIENCY OF A MULTY–BEAM INTERFEROMETER IN THE OBSERVATION OF AN OBJECT THROUGH THE TERRESTRIAL ATMOSPHERE

Yu. V. Kornienko and V. Pugach

Institute of Radiophysics and Electronics, NAS of Ukraine
12 Ak. Proskury, 61085 Kharkiv, Ukraine
e-mail: pvv@ire.kharkov.ua

A consideration of the influence of the registration noise on the accuracy of the image reconstruction of a remote sensing object being observed with a multibeam interferometer (the evolution of the stellar Michelson interferometer concept) through a thin layer of the medium having random refraction index inhomogeneities is given. This accuracy appears to decrease due to phase distortion but this effect is rather small. It is concluded that the interferometric imaging method has a high degree of resistance to phase distortion in the atmosphere.

The aim of this study is to estimate quantitatively the information efficiency of a multi-beam interferometer [1] and its immunity to phase distortions.

The set of equations for undisturbed phases of Fourier components of an image consists [2] of equations of the kind

$$\varphi_\nu + \delta_i - \delta_k = \psi_{ik}, \tag{1}$$

where φ_ν is the required actual value of phase of the ν-th Fourier component; δ_i and δ_k are the phase distortions at the i-th and k-th subapertures of the interferometer; and ψ_{ik} is the phase of the Fourier component. The parameters of the solution can be chosen arbitrarily, *i.e.*, like a constant additions to the phase distortions φ and the total phase front inclination (two components). In order to avoid this uncertainty, we complement the set of Equations (1) by equating these parameters to zero:

$$\lambda \sum \delta_i = 0, \quad \mu \sum x_i \delta_i = 0, \quad \mu \sum y_i \delta_i = 0, \tag{2}$$

where x_i and y_i are the coordinates of the i-th aperture.

Let us present the derived set in the form

$$A\,|X\rangle = |Y\rangle, \tag{3}$$

where X is the vector whose components are the required undisturbed phases φ and atmospheric phase distortions δ; Y is the vector consisted of the measured values of ψ; A is the matrix of the coefficient that is completely determined by the interferometer geometry, *i.e.*, by the spatial arrangement of its subapertures. (All its components are equal to 1, −1 or 0). The right-hand side of this set, being a result of the experiment, contains random errors which are assumed to be normally and independently distributed with the same variance. This problem can be optimally solved using the least squares method. First, we multiply both sides of (3) by the A^+ – matrix conjugated with A and derive the system

$$M|X\rangle = |Z\rangle \tag{4}$$

with the most probable value of the vector X being its solution. Here $M = A^+A$, and $|Z\rangle = A^+|Y\rangle$.

If the interferometer aperture consists of n subapertures and transmits l spatial frequencies, then the vector X consists of $l+n$ components (l phases of the image Fourier-components and n phase distortions), the vector Y consists of $n(n-1)/2+3$ components, the matrix A of $n(n-1)/2+3$ lines and $l+n$ columns, the vector Z of $l+n$ components and the matrix M of $l+n$ rows and the same number of columns.

Let the right-hand side of (3) are to be known with the error $|\eta\rangle$. It results in an error $|\xi\rangle$ in the solution of system (4) that, due to its linearity, satisfies the equation

$$M|\xi\rangle = A^+|\eta\rangle, \tag{5}$$

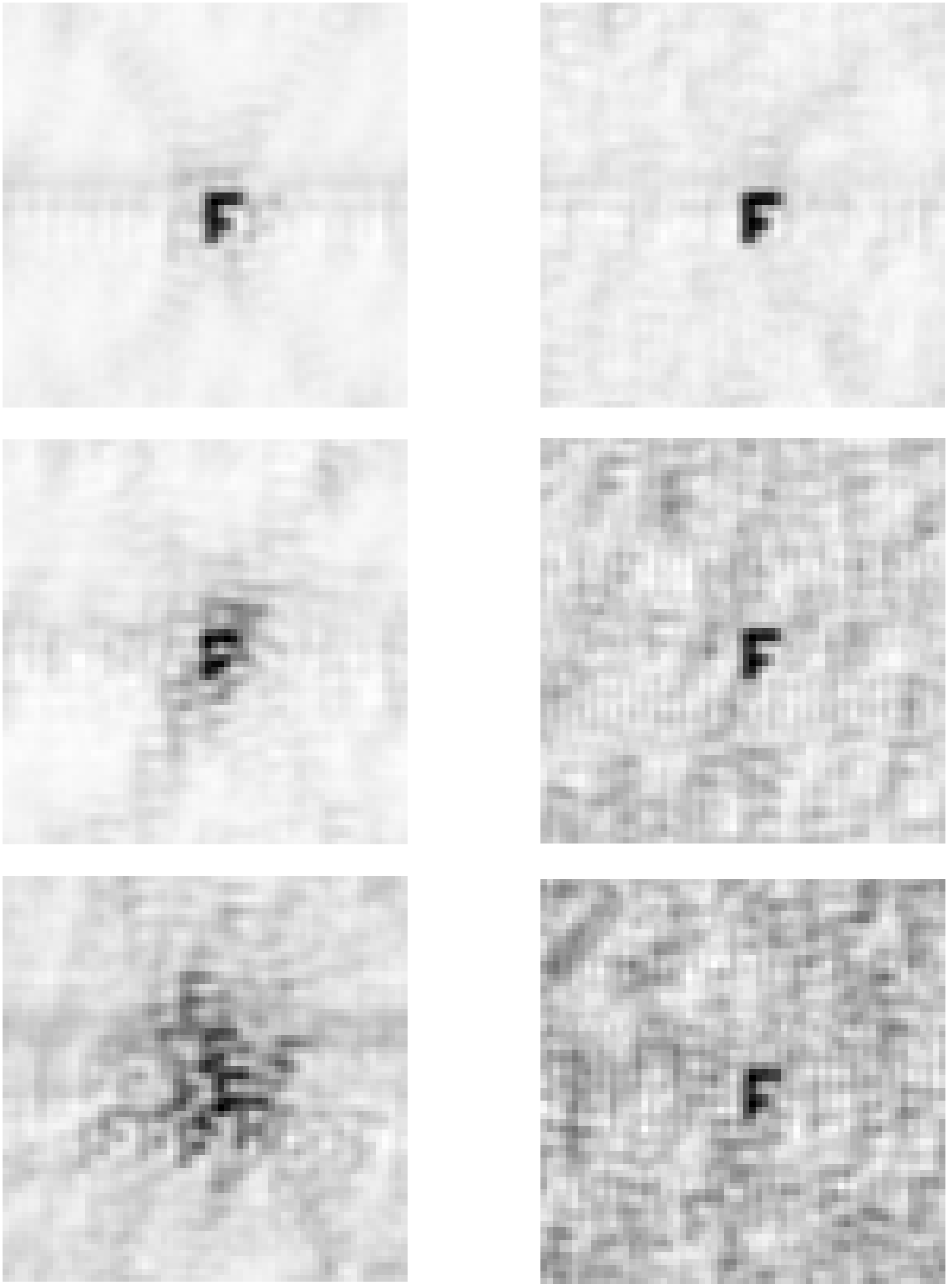

TELESCOPE INTERFEROMETER

Figure 1: The results of computer simulation of an observing through the Earth atmosphere a stretched object using both a traditional and an interferometric telescope for various wave front disturbances

which gives

$$|\xi\rangle = M^{-1}A^{+}|\eta\rangle. \tag{6}$$

Therefore, the covariation matrix of these errors has the form of

$$C = M^{-1}A^{+}\,\overline{|\eta\rangle\langle\eta|}\,AM^{-1}, \tag{7}$$

where the dash means the averaging over the ensemble of the recording noise realizations. Matrix $\overline{|\eta\rangle\langle\eta|}$ is the auto-covariations matrix of the errors $|\eta\rangle$. By the assumption accepted about the statistical properties of $|\eta\rangle$ this matrix is equal to DE, where E is a unity matrix, and D is the error variance of the vector $|\eta\rangle$ components. For this reason and due to (7),

$$C = DM^{-1}, \tag{8}$$

where D characterizes the intensity of the detection noise, and M^{-1} describes the dependence of the X value error on the interferometer geometry. However, among all the unknowns in system (4), we will restrict our interest to those ones that are related to the object of observation, *i.e.*, φ.

The matrix of their error covariation is

$$C_{\varphi} = DG, \tag{9}$$

where G is a sub-matrix of M^{-1} obtained by crossing out all rows and columns related to the unknowns δ. Since the errors are normally distributed, the desired Fisher matrix F is inverse to C_{φ} and equal to G^{-1}/D.

Matrix $H = G^{-1}$ depends only on the interferometer geometry and characterizes the interferometer efficiency in observation through the atmosphere. We shall call it a matrix of the interferometer information efficiency.

The direct calculation of this matrix for several simplest geometries of the interferometer has shown [3, 4] a surprisingly high immunity of the method suggested in [1] to the effects of atmospheric distortions. However, it remains unclear to what extent it is true for other configurations of the input aperture. To answer this question, a method of analytical calculation of matrix F should be found, which is however associated with certain difficulties, since for rationally designed interferometers [5, 6] containing tens of subapertures, the number of elements of this matrix reaches the values of the order of 10^5 to 10^6. The results of investigation in this area are briefly presented in [7].

Here we show the results of computer simulation of an observing through the Earth atmosphere a stretched object using a traditional and interferometric telescope for various wave front disturbances. The results are demonstrated in Fig. 1.

REFERENCES

[1] *Kornienko Yu. V., Uvarov V. N.* Signal accumulation at observation of an astronomical object through the turbulent atmosphere // Comptes Rendus of Academy of Science of Ukraine.–1987.-Ser. **A**, N 4.–P. 60–63. (in Russian).

[2] *Roddier F.* Redundant versus nunredundunt beam recombination in an aperture synthesis with coherent arrays // J. Opt. Soc. A.–1987.–**A4**, N 8.–P. 1396–1401.

[3] *Kornienko Yu. V.* Interferometric approach to the problem of turbulent atmosphere effects in astronomical observations // Kinematics and Physics of Celestial Bodies.–1994.–**10**, N 2.–P. 98–106. (in Russian).

[4] *Kornienko Yu. V., Leyferov V. A., Pugach V. V.* Informational efficiency of a multibeam interferometer in the observation of an object throughthe inhomogeneous medium // Radiofisika i Electronika.–1997.–**2**, N 1.–P. 132–136. (in Russian).

[5] *Kopilovich L. E.* Multi-beam optical interferometer: the output aperture optimization // Kinematics and Physics of Celestial Bodies.–1998.–**14**, N 2.–P. 138–142.

[6] *Kopilovich L. E.* Non-redundant apertures for optical interferometric systems: maximization of the number of elements // J. Modern Optics.–1998.–**45**, N 11.–P. 2417–2424.

[7] *Kornienko Yu. V.* Construction on Nonredundant Apertures for Interferometric Radiotelescope by Method of Random Search // Physics and Engineering of MSMW: 3rd Intern. Kharkiv Symp., Kharkiv, Ukraine, Sept. 15–17, 1998.–P. 578–580.

A HARDWARE–SOFTWARE COMPLEX OF THE INFRARED FOURIER SPECTROMETER FOR AIR POLLUTION MONITORING

A. A. Veles, A. V. Morozhenko, M. G. Sosonkin, A. V. Shavrina, I. G. Kesselman

Main Astronomical Observatory, NAS of Ukraine
27 Akademika Zabolotnoho St., 03680 Kyiv, Ukraine
e-mail: veles@mao.kiev.ua

On the basis of a experimental laboratory model, the principles of implementation of a hardware-software complex Fourier spectrometry, data collection and processing are compiled and justified. This complex can be used as for the ground based and moving platform observation as for flight experiments. A mathematical algorithm and a program code for fitting the observed and modelled spectra were developed for express-analysis of Fourier-transform spectra with the goal of control of any dangerous gas compound pollutions.

On the basis of a laboratory model the main principles of implementation of a hardware-software complex (see Fig. 1) of control, data acquisition and processing for the infrared Fourier spectrometer [1] designed for on-board experiments are justified and developed taking into account the demands of safety, speed and energy consumption.

The preference of an IBM compatible in comparison with a specialized digital signal processor as a nucleus of the system is justified. The development of interface components for an usual personal computer has a number of advantages. First of all, the standard hardware and software (compilers, library) are used. Secondly, a safety of the system is enhanced whilst the platforms for development, testing and using are coincident.

The interface of data processing and device control systems are made and the requirements to the software and resources of PC are elaborated.

The four main functions are given to the program part:
- registration of the signals arriving from the interface card of the Fourier spectrometer;
- mathematical data arrays processing;
- visual representation of the data;
- the processing of any user's input.

The results of test measurements of main characteristics for our model Fourier spectrometer have shown

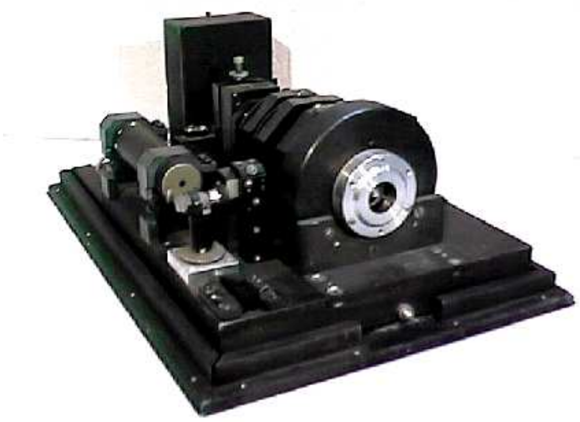

Figure 1: IR Fourier spectrometer general view

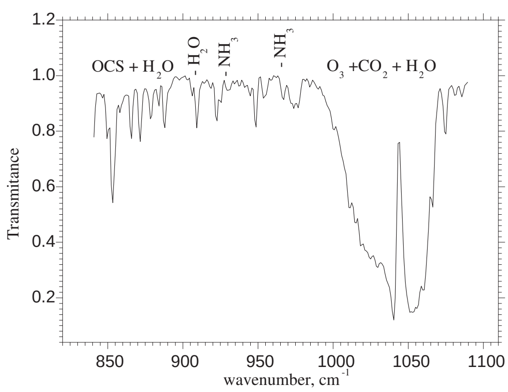

Figure 2: Solar spectra. 800–1100 cm^{-1} region, $hw = 2$ cm^{-1}

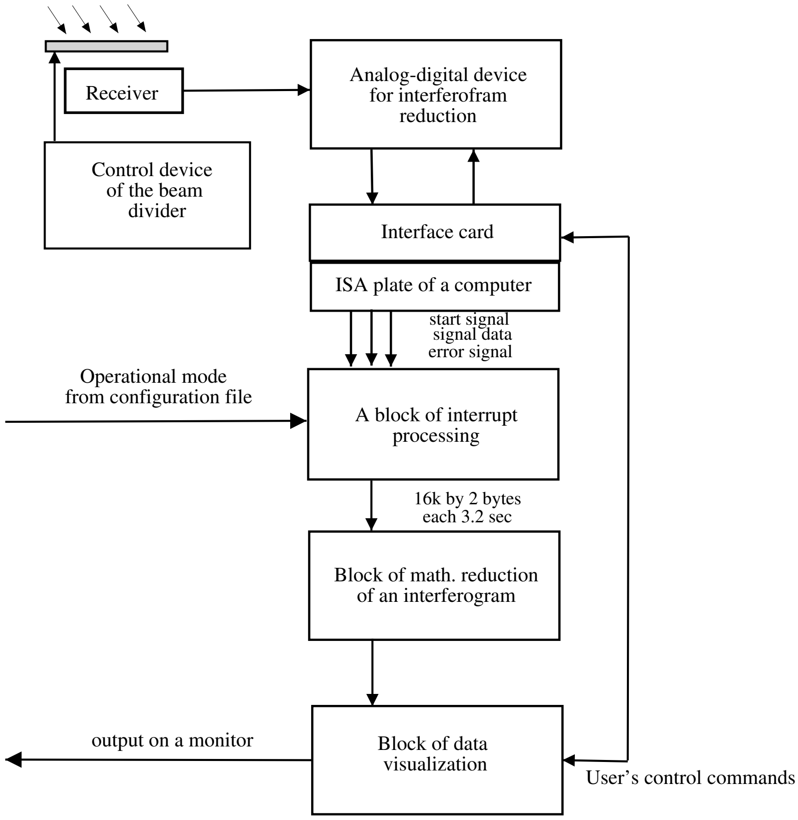

Figure 3: Block-scheme of the Fourier spectrometer's interface

an availability of its continuous work in a real time mode along 500–1000 scans without any failures. The capacity of available computer (Pentium 150 MHz) is quite enough for simultaneous registration, transformation, visualization and processing of a signal.

A block of interrupt processing provides continuous processing of hardware interrupt requests, coming from the spectrometer interface card. It combines the consistently arriving signals in a data array and processes faulty situations.

Block of mathematical processing
• interferogram appodization (by cosine, gaussian);
• fast Fourier transform code (16384 points in 0.04 sec);
• smoothing of a spectrum (on ≥ 3 points).
The storage of a spectrum is carry out separately on beam divider directions. The calculation of average values and their dispersions is possible for any data array length.
The calculations of 100% intensity line for two accumulated spectra.

A block of data visualization ensures
• the representation of two data arrays as diagrams (interferogram + spectrum, spectrum + spectrum, 100% intensity line + spectrum);
• the change of a scale (increase, reduction);
• graphic cursor.

REFERENCES

[1] *Bell R. J.* Introductory Fourier transform spectroscopy.–New York – London: Academic Press, 1972.–398 p.